Modelling Fluid-Structure Interaction Problems with Coupled DEM-LBM

Rodrigo Guadarrama Lara

Submitted in accordance with the requirements for the degree of
Doctor of Philosophy

The University of Leeds

School of Chemical and Process Engineering
Institute of Particle Science and Engineering
Faculty of Engineering

February 2017

The candidate confirms that the work submitted is his own, except where work which has formed part of jointly-authored publications has been included. The contribution of the candidate and the other authors to this work has been explicitly indicated below. The candidate confirms that appropriate credit has been given within the thesis where reference has been made to the work of others.

The work in Chapter 4, sections 4.1.2, 4.2.2 and 4.2.3 of the thesis has appeared in a publication as follows:

Rodrigo Guadarrama-Lara, Xiaodong Jia, Michael Fairweather, 'A meso-scale model for fluid-microstructure interactions', Procedia Engineering 102 (2015) 1356-1365

I was responsible for Abstract, 1. Introduction, 2. Simulation and experimental techniques, 3. DEM and LBM software validation, 4. Coupled code implementation and test cases, 5. Results and conclusions. The contribution of the other authors was assisting in writing the paper.

The work in Chapter 5, Figure 5-6 has appeared in a publication as follows:

Yanjun Guan, Rodrigo Guadarrama-Lara, Xiaodong Jia, Kai Zhang, Dongsheng Wen, Lattice Boltzmann simulation of flow past a non-spherical particle, Advanced Powder Technology, Available online 4 April 2017, ISSN 0921-8831.

Acknowledgements

I thank my supervisors Dr X Jia and Prof M Fairweather for their time, support, advice and patience. Through their teaching and experience I have learnt more than I expected. Thank you for trusting me and for the constructive talks.

Thanks to Dr Anren Li for his time, collaboration and unconditional support.

Thanks to Neil Smith who did not hesitate in allowing me the use of his lab equipment.

Thanks to Simon Welsh and his team in the Graduate School Office in the Faculty of Engineering; particularly Suzanne Bramwell for her support when I needed urgent documents.

Thanks to my colleagues Rafid Abbas, Ahmed Al-Saadi, Mohammadreza Alizadeh, Nicolas Delbosc, Jabbar Gardy, Yanjun Guan, Michael Johnson and Mehrdad Pasha for their time, willingness, support and friendship.

Thanks to people in CONACYT, especially Samuel Manterola and his team.

Last but not least, thanks to my family in Mexico and Slovenia. I appreciate your support given from the very first moment you knew I was starting this journey. Thanks for believing in me, for your words and the good vibes.

A mis padres Irma y Enrique

Porque a pesar de que me alejé físicamente por un momento, siempre me han apoyado cada que decido perseguir un sueño y me han hecho sentir su inmenso amor y apoyo. Gracias infinitas!

Los amo

To Suzana

Moja ženkica, what can I say, you know everything about me. You've been with me in the ups and downs in this journey, and we've learnt a lot together. Thanks for being there always, walking next to me and pushing me up the hill…literally!

Ljubim te

Abstract

When studying the properties and behaviour of particulate systems, a multi-scale approach is an efficient way to describe interactions at different levels or dimensions; this means that phenomena taking place at one scale will inherently impact the properties and behaviour of the same system in a different scale.

Numerical representation and simulation of fluid-structure interaction (FSI) systems is of particular interest in the present work. Conventional computational fluid dynamics (CFD) methods involve a top-down approach based on the discretisation of the macroscopic continuum Navier-Stokes equations; cells are typically much larger than individual particles and the hydrodynamic force is calculated for all the solid particles contained in singular a cell. Unlike traditional CFD solvers, the lattice Boltzmann method (LBM) is an alternative approach to simulate fluid flows in complex geometries in a mesoscale level. In LBM the fluid is deemed as a collection of cells, each one containing a particle that represents a density distribution function with a velocity field. The distinct element method (DEM) is in charge of handling the motion of particles and calculating the interparticle contact forces. The two methodologies LBM and DEM were selected among the available approaches to be combined in a single computational code to represent FSI systems.

The key task to undertake was the implementation of a coupling code to exchange information between the two solvers LBM and DEM in a correct and efficient manner. The calculation of hydrodynamic forces exerted by the fluid on the particles is the major challenge in coupled FSI simulations. This was addressed by including the momentum exchange method, based on the link bounce-back technique, together with the immersed boundary method to deal with moving particles immersed in a fluid.

In addition, in order to better understand the dynamics of FSI systems in a mesoscale level, the present work paid special attention to the accurate representation of individual particles displaying irregular geometries instead of the preferred spherical particles. This goal was achieved by means of X-ray microtomography digitisation of particles, allowing the capture of complex micro-structural features such as particle shape, texture and porosity. In this way a more realistic particle representation was achieved, extending its use to the implementation into computational simulations.

The DEM-LBM coupling implementation carried out was tested quantitatively and qualitatively based on theoretical models and experimental data. Different cases were selected to simulate the dynamic process of packing particles, particle fluidisation and segregation, particles sedimentation, fluid permeability calculations and fluid flow through porous media.

Results and predictions from simulations for a number of configurations showed good agreement when compared with analytical and experimental data. For instance, the relative error in terminal velocity of a non-spherical particle settling down in a column of water was 4.2%, showing an asymptotic convergence to the reference value. In different tests like the drag on two interacting particles and the flow past a circular cylinder at Re = 100, the corresponding deviations from the references published were 20% and 8.23% respectively. The extended Re range for the latter case followed closely the reference curve for the case of a rough cylinder, indicating the effects of the inherent staircase-like boundary in digital particles.

Three dimensional simulations of applications such as fluidisation and sedimentation showed the expected behaviour, not only for spherical particles but also considering complex geometries such as sand grains. A symmetric array of spheres and randomly mixed particles were simulated successfully. Segregation was observed in a case configured with particles with different size and density. Hindered settling was also observed causing the slow settling of the small particles.

Incipient fluidisation of spherical and irregular geometries was observed in relatively large computational domains. However, the minimum fluidisation velocity configured at the inlet was commonly 10 times larger than the calculated from the Ergun equation.

Table of contents

List of figures

List of tables

Nomenclature

Latin characters

A	area	m^2
a	acceleration	m/s^2
bf	body force driving the fluid in LBM	dimensionless
c_D	drag coefficient	dimensionless
D_P	pore diameter	m
d_p	particle diameter	m
E	Young's modulus	Pa
F_D	drag force	N
g	gravitational acceleration	m/s^2
m	mass	kg
r	radius	m
r_{hy}	hydrodynamic radius	m
Re	Reynolds number	dimensionless
ts	time step	s
u	velocity	m/s
u_0	settling velocity of a sphere in infinite fluid	m/s
u_{rel}	relative velocity between fluid and solid	m/s

Greek characters

β	Richardson and Zaki correction factor	dimensionless
δ	Blasius boundary layer thickness	m
ε	porosity, voidage or void fraction	dimensionless
η	Blasius similarity variable	dimensionless
ρ	density	kg/m^3
μ	dynamic viscosity	kg/m s
ν	kinematic viscosity	m^2/s
τ	relaxation parameter	dimensionless
ϕ	sphericity	dimensionless

Subscripts

DEM	indicates parameter in DEM system units
f	indicates parameter of the fluid
LBM	indicates parameter in LBM system units
p	indicates parameter of the particle
phy	indicates parameter in physical system units

Abbreviations and acronyms

2D	two dimensions or two-dimensional
3D	three dimensions or three-dimensional
AR	Aspect Ratio
BB	Bounce Back
BE	Boltzmann Equation
BGK	Bhatnagar, Gross and Krook model
CAD	Computer Aided Design
CFD	Computational Fluid Dynamics
KC	Kozeny-Carman equation
CT	Computed Tomography
DDF	Density Distribution Function
DEM	Distinct Element Method
FBR	Fluidised Bed Reactor
FEM	Finite Element Method
FSI	Fluid Structure Interaction
LBM	Lattice Boltzmann Method
LEFM	Linear Elastic Fracture Mechanisms
LGCA	Lattice Gas Cellular Automata
LU	Lattice Units
MES	Mean Empty Space
MIP	Mercury Intrusion Porosimetry
MRT	Multiple Relaxation Time
NMR	Nuclear Magnetic Resonance
NS	Navier-Stokes equation
PSD	Particle Size Distribution
RGB	Red, Green and Blue colour scale
R&D	Research and Development
SEM	Scanning Electron Microscope
SRT	Single Relaxation Time
SVL	Structure Vision Ltd
VED	Volume Equivalent Diameter
XMT	X-ray Microtomography
pw	pixel width

1. Introduction

In our everyday activities we see and use products made of different materials, for example stainless steel, paints, ceramics, polymers; we even use them for medical treatments in form of tablets or purchase packed products such as food, powdered detergents, sand or soil. Evidently these materials are transformed by means of different methodologies and processes to deliver a wide variety of products.

The importance and effectiveness of such products lies in a basic and small element, a particle. The analysis and characterisation of this single element is very important to assess, predict and in some cases control particle interactions and chemical reactions occurring in different processes.

The following sections in this chapter explain the main objectives of the work carried out in this project and the motivations behind it.

1.1. Relevance of particles packing and fluid-structure interaction modelling

Packed beds are formed by a collection of millions of stacked particles placed in a container. In a particle packing process, larger geometries tend to pack poorly compared to smaller ones. In the interest of reducing bed voidage and produce tight packed structures, it is important to select the optimal packing methodology taking into consideration factors that could affect the final packing density, in this way avoiding flaws in the final structure. Unfortunately packed structures may still present internal damage originated by fatigue, crack growth, or even corrosion when particles interact with a fluid flowing through the pores (Beaudoin 1985). For instance, in the cement industry, the quality of the final product is affected by particle size. In order to determine the rate of chemical reactions, the surface area of the particles must be taken into account since such reactions primarily occur in fine particles rather than in large ones. When structural damage is present, even the smallest crack can develop in a stable way causing micro-structural flaws, mechanical instability and potential leaks of fluids.

The structure of a material can be described through its microstructure and crystal structure. The former is of interest in the present work because it will help to characterise and describe the physical appearance and state of materials in a scale

between nanometres to centimetres, scale named as mesoscale hereafter. The crystal structure covers a much smaller scale considering the position and arrangement of atoms in a material.

Micro-structural changes may also originate when the container to particle diameter ratio is reduced. This is known as wall effect, which can be explained as the increased bed porosity or voidage near the container walls. The importance of this effect lies on the design of packed bed reactors for optimal heat transfer and fluid flow. In more complex cases, such as particle segregation, fluidisation and sedimentation, continuous monitoring is required to understand stratification and concentration changes, as well as measurements of particles' velocities and the evolution of bed formation (Bux et al. 2015).

In carbon capture and storage (Turnbull et al. 2017) gas is injected in underground geological reservoirs and any leakage to the surface is considered one of the major hazards. Measuring crack propagation in solid structures is not an easy task. For this reason, non-destructive and safe methodologies are important and necessary to model and predict fluid flow through cracks and mass transport. Moreover, it is desirable to predict potential behaviours in order to reduce costs and mitigate risks.

When a solid particle is completely immersed in a fluid, either a liquid or gas, the FSI can be described as the true interaction of a movable solid object with the surrounding fluid. From this perspective, a constant mutual interaction at the interface between the solid and the fluid varies through time, thus representing a complex system to study considering that the fluid may cause deformation of the structure, which in turn will modify the boundary conditions of the fluid.

1.2. Motivation and objectives

In a particulate system such as a packed bed, knowing the features of particles and calculating interparticle forces is important to control the packing process and bed mechanical properties. In practice, it is difficult to track all the velocities and forces for each one of the particles involved in the system. Moreover, it is not possible to have access to the particles within the bed and to visualise internal voids or flaws in the structure.

The particle-fluid interaction phenomenon can be found in industrial equipment, for instance in centrifuges, elutriators, cyclones and settling chambers. From a general

point of view, microstructural changes in matter caused by internal and external forces influence global properties of a structure such as density, heat transfer, porosity and permeability. Assessing these changes is paramount in a decision-making process in order to predict the behaviour of particles forming a structure and to prevent undesirable effects. For this reason, the particle-fluid interaction is a very important matter of study when it comes to design and performance assessment of industrial equipment.

Numerical methodologies are an effective approach used for evaluating the mechanical properties and behaviour of different materials, and computing the translational and rotational motion of a large number of particles for a wide range of applications. In this way different scenarios can be proposed and tested, e.g. packing processes of different materials with different size distributions, or addition methods at different pouring rates. Without numerical simulations experimental investigation may be limited to carry out due to costs, availability of equipment, site accessibility, potential hazards and likely to be performed only at small scale.

Numerical studies of particulate systems are reported in the literature (Yuan et al. 2016; Sexton et al. 2014). However the majority consider discs or spheres as the basic particle to generate packed beds. This is a common and valid approach since spheres are easy to represent and computations of their properties are known. On the other hand, with the fast development of computational capabilities and the wide variety of tools available for particle modelling, it is important to study packed beds trying to represent them as close as possible to the real ones.

In different research areas of science a multi-scale approach is an efficient way to describe systems that show interactions at different levels, i.e. phenomena taking place at one level will inherently impact the properties of the system in another level or scale.

For the study of discrete particles and their mutual interactions there is a well-known and popular numerical method called the discrete element method, initially developed for general problems in rock mechanics. The key approach in DEM simulations is based on the fact that particle-level mechanics have a direct impact on the global properties of granular assemblies such as bed voidage and structural hydraulic conductivity.

Regarding fluid flow studies, CFD is a branch of fluid dynamics created in order to analyse and solve problems related to fluid flow making use of specialised software improving calculations accuracy and reducing time to allow users the study of complex physical phenomena. In traditional CFD simulations, the energy, mass and momentum equations are solved by the Navier-Stokes (NS) equations where the density in the system is locally conserved.

In recent decades, the LBM has attracted the attention of people studying turbulent fluids and multi-phase flow in porous media. It was firstly developed from lattice gases where the particles reside on the nodes of a discrete lattice and stream from one lattice to another according to their discrete velocity field. LBM has been recognised as an attractive and easy-to-implement alternative approach to simulate fluid flows in complex geometries where the fluid is replaced by a collection of particles represented by a density function.

The main objective of the present work is to develop and implement a coupling algorithm to combine DEM and LBM to study FSI systems modelled in three dimensions (3D). The DEM-LBM coupled model is expected to reproduce FSIs more accurately by calculating and taking into account local fluid velocities affected by the presence of solid objects, which are likely to continuously interact and translate in the fluid. Furthermore, the use of non-spherical particles in computational simulations is a further attempt to represent FSI systems in a more realistic way.

There exist algorithms that help researchers to represent particles to be used in computational simulations. The available methodologies have been combined in some cases in the attempt to achieve the representation of more complex geometries (Džiugys & Peters 2001). In this work X-ray microtomography (XMT) was used to obtain digital images of non-spherical particles and packed beds. This equipment served as a very attractive way to capture physical features inherent to every individual particle, and in this way to represent solid particles and packed structures in a more accurate way. Although spheres and different regular geometries are commonly used in research to represent solid particles (Farr 2013), in the present work the intention is to also use irregular geometries with complex shapes that are more likely to be present in selected processes. Additionally, the nature of both DEM and LBM computational meshes allows to easily implementing the digitised particles from XMT into the DEM-LBM environment.

To contribute to a better understanding on the dynamics of FSI systems, the DEM-LBM coupled model aims to provide a different approach to study these systems. Instead of analysing a system in a large scale using the NS equations, a different perspective was followed by using a bottom-up approach where the collection of interactions taking place at a mesoscopic level results in the dynamic behaviour at the macroscopic level. Experimental data was used not only to validate the model but also to find practical applications in industry and R&D areas such as the fluidisation and sedimentation of particles. Furthermore, the proposed use of XMT technique aided to assess the effect of particle shape in particulate systems. In this way, the combined DEM-LBM-XMT methodology adopted in the present work was expected to provide a powerful and non-invasive alternative tool to study and represent different FSI systems.

The in-house computational programme DigiPac was initially validated in a stand-alone mode having tested two of its modules based on DEM and LBM, called DigiDEM and DigiFlow respectively. The module based in DEM was tested by packing spherical and sand particles to assess their packing density and compare the results obtained with experimental data. The corresponding module based in LBM was also tested by predicting the permeability of solid structures. The second stage consisted of the implementation of the coupling code and testing it numerically by means of simple cases using a single spherical particle in order to be sure that the results compare with analytical data. The final tests find applications in industry like particle bed fluidisation, particles segregation and hindered settling of particle.

1.3. Thesis outline

The thesis continues in chapter two which includes the pertinent literature review of the relevant methodologies on which the present work is based, namely DEM, LBM and the coupling method. Chapter three describes into detail the methodologies employed, the description of the software DigiPac used in this work and an introduction to XMT.

Chapter four is the first chapter of results comprised by the stand alone validation of the existing modules based on DEM and LBM. Chapter five include initial cases to test the coupled DEM-LBM. Chapter six presents selected application cases involving multi-particle systems.

Chapter seven is the final chapter devoted to discuss the findings, reflexions, concluding remarks of the project and ideas for future work.

2. Literature review

In this chapter the relevant methodologies DEM and LBM are introduced. Experimental and numerical modelling research documented in the literature are discussed as well as different discrete particle representation techniques and existing solid-fluid coupling methodologies for the study of fluid-structure interaction problems.

2.1. DEM for dynamic simulations of particulate systems

DEM is a well-established methodology originally developed by Cundall & Strack (1979) to describe the movement and interactions of assemblies of circular discs and spheres based on Newton's laws of motion for every discrete particle. Since then, DEM has been widely used to simulate different phenomena and processes (Cleary & Sawley 2002; Lemieux et al. 2008; Langston & Kennedy 2014). The discrete approach in DEM permits to follow the properties of individual particles in a multi-particle system to study mechanical properties of granular materials at a microscopic level. The overall behaviour of the system at a macroscopic level (large scale, greater than centimetres), i.e. visible to the naked eye, can still be captured since it is governed by constitutive particles interacting at a microscopic level.

In computational simulations the particle shape commonly used is a sphere given its simplicity for numerical representation, contact detection and force calculation. However, in recent investigations researchers have introduced non-spherical particles into their work to assess the effect of irregular shapes in different systems (de Bono & McDowell 2015; Dong et al. 2015; Delaney et al. 2015; Jin et al. 2011; Lu et al. 2015). It has been demonstrated that in order to obtain more accurate simulations, it is important to correctly describe and represent particles showing irregular shapes. To do so, different methodologies are available. The most representative are described in the following paragraphs.

The sphero-polyhedron approach was created and developed with the intention of handling complex geometries. Pournin & Liebling (2005) named the particles spherosimplices. In principle, the initial particle geometry is a polyhedron that first is eroded and then dilated with circular (2D) or spherical (3D) elements, resulting in a polyhedron with rounded edges. Every particle is then defined as a sphero-polyhedron with defined features such as edges, faces and vertices in a triangular mesh.

The way in which overlap between two polyhedral is detected is similar to other methodologies available. For example, if vertices are the feature to be used, the distance between two vertices corresponding to two different particles is simply the distance between two points. When this distance is less than zero then an overlap is detected. Other distances are found when using two features; for instance, the distance between a vertex and an edge is found by tracing a perpendicular line from the vertex to a selected edge. A similar approach of tracing a perpendicular line is used to find the distance between a vertex and a face. The process of finding such distances involves a linear or quadratic system of equations. The force between two interacting polyhedral is found using a pair of features and the total force is the summation of all the present pair combinations. In practice, researchers using this methodology only consider interactions between vertices and faces, and between edges. More details of this methodology can be found in Mirtich (1997), Alonso-Marroquín (2008) and Galindo-Torres (2013).

In the sphere assembly method, also known as composite particle model in Zhao et al. (2015), or multi-sphere method in Kruggel-Emden et al. (2008), non-spherical particles are represented by randomly built clusters of spheres that overlap, or by simply placing spheres next to each other to form different particle shapes. The forces between spheres within the clusters are neglected. The disadvantage of this methodology is that for the representation of realistic angular particles and irregular geometries like sand grains, a large number of spheres must be used to build only one particle, thus making it computationally expensive. A similar approach bonding different geometries have been used in the literature merging two spheres with a cylinder (Langston et al. 2004). Other researchers have opted to simply use different geometries like cubic particles (Fraige et al. 2008), ellipses (2D) and ellipsoids (3D) (Li & Ng 1995), or sphero-disc particles (J. Li et al. 2004). A concise review including a classification of particles representation was presented in Džiugys & Peters (2001). In this work it was highlighted that the major problem when dealing with irregular geometries that have no analytical solutions is the contact detection and the particles overlap calculation. The procedure is not straightforward and extra computational effort is required.

Another approach to generate a wide range of shapes is using superquadrics, known as well as superquadratics or superellipsoids (Williams & Pentland 1992). These shapes are 3D representations of particles using ellipsoid-like shapes defined by a set of formulae. Depending on the power used in the equation describing the particle

shape, round or sharp corners can be obtained. Alternative algorithms to generate different shapes include the polar shape (Hogue & Newland 1994; Oakeshott & Edwards 1994), and the skeleton shape (Džiugys & Peters 2001).

A different technique is known as the virtual space method (Džiugys & Peters 2001), which consists of a mesh of regular cells to represent a particle. Analogous to a collection of pixels in digital imaging, a shape is constructed by filling in different cells known as pixels (2D) or voxels (3D). For computational memory saving and increased efficiency, in some cases only the pixels representing the overlap between two particles are filled in.

Figure 2-1 below presents the most popular techniques used in the literature to represent particles.

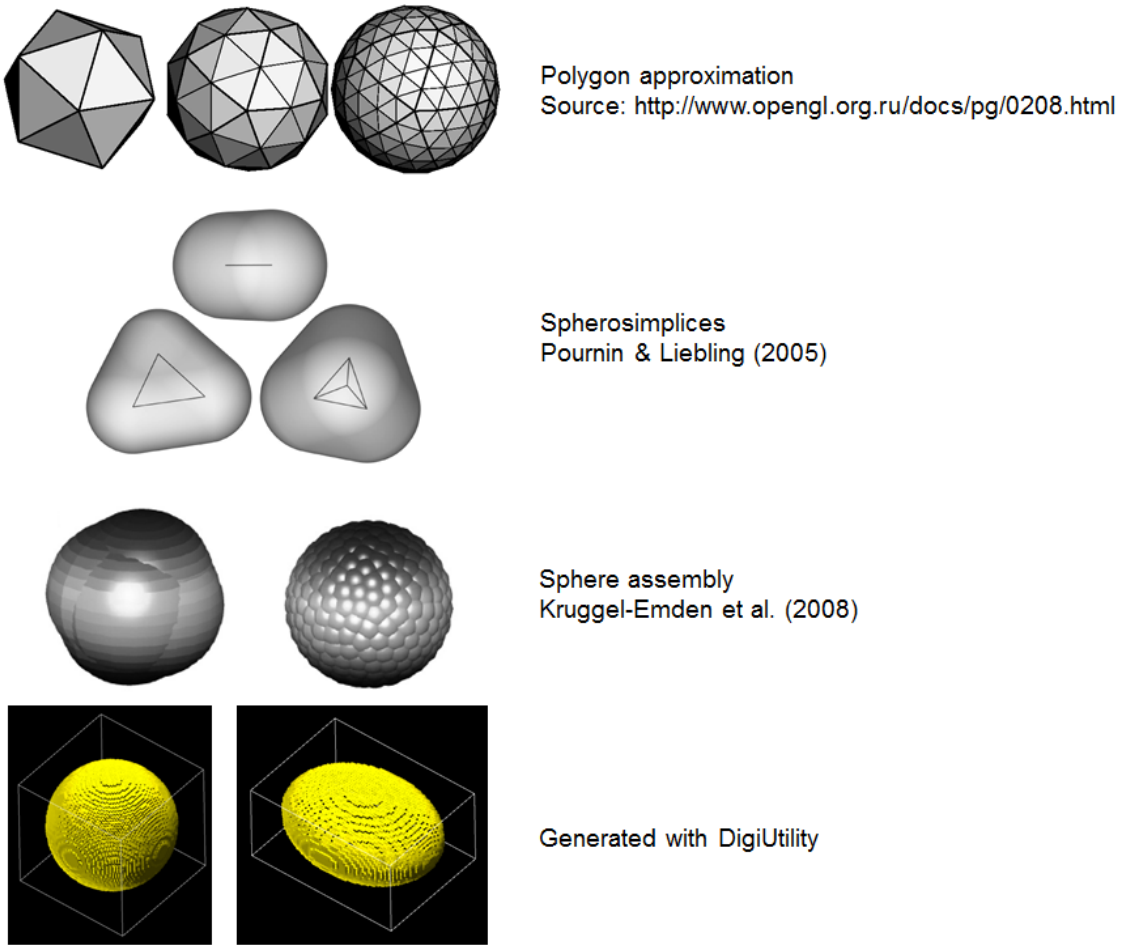

Figure 2-1 Representation of particles in a computational environment

Once a methodology is selected to represent different discrete particles, they can be used to study phenomena present in nature or in a range of applications. For instance, particle packing is an area of great interest for researchers. The packing process results in an assembly of particles forming a powder to be used in different processes.

In powders mutual interactions are present among all the particles, between the particles and a fluid (if present), and between the particles and the walls of the container accommodating them. These interactions depend on the type of contact originated by the phases involved, for example, mechanical friction and cohesion between solid particles, viscous friction present at particle-fluid interface, buoyancy, fluid adsorption, and chemical reaction.

Powders do not exhibit uniform characteristics and behaviour; that strongly depends on the process that is carried out on them. For example, different interaction dynamics will produce a characteristic behaviour if the powder is taking part in one of the following processes:

- Granular flow in hoppers or screens
- Grinding or milling to improve its properties for further processing
- Mixing to make a higher quality product
- Compressed in moulds to obtain a preformed solid
- Granulation to obtain larger grains
- Fluidisation to improve contact between the powder and the fluid

It is important to identify the properties and characteristics of the particles in order to achieve the desired features in the powder to be used in a determined process. For this reason, researchers have showed interest not only in experimenting with solid particles but also in the numerical modelling area to analyse the properties of individual particles, to produce packed structures using different computational algorithms and to further test and study the effects of particle shape and size on the powder behaviour and in the aforementioned processes. Furthermore, modelling could extend the research studies to hypothetical cases difficult to reproduce and measure in experiments.

Early ideas to computationally generate packed structures started in the 1960's by trying to represent the structure of liquids as a collection of molecules closely packed (Bernal 1964). Problems arose when inhomogeneous packed structures were systematically generated due to particularities in every algorithm developed. Substantial discrepancies in the geometry of packed structures were found when they were compared to packings generated in the laboratory. Additionally, shaking of a packed structure was possible to carry out in the laboratory to collectively rearrange the particles and thus increase the packing density, but with the limited algorithms and computational capabilities those days, the incipient algorithms produced loose structures.

First attempts employed regular geometries like cylinders and spheres; powder representations were made of clusters with only a few particles, which significantly limited the description of an ideal random packing. One of the algorithms trying to overcome these problems was further developed by Finney (1976). For a random packed structure of 500 mono-sized spheres, when the distance between two spheres of same radius was smaller than the diameter, both spheres moved equally away until the scenario where they only just touched. In turn, the 'away' move might originate further overlaps that vanished after repeating the basic constraint of the algorithm.

In reality, this model is based on an ideal representation of dynamic systems with elastic collisions, i.e. the total kinetic energy before particles collide is exactly the same after collision with no loss of energy. Since there is no other force added to the system, the interparticle dynamics depends only on the overlap condition. Trajectories are assumed to be linear and constant all the time; potential particle collisions are controlled by a prediction based on the knowledge of particle's position and its linear motion, but if a particle changes direction then the potential collision event is simply discarded.

Subsequently different techniques were developed for the analysis of the dynamics of particulate systems, such as the statistical sampling Monte Carlo method, the cellular automata method and the discrete element method.

Researchers have used the Monte Carlo (MC) method to pack spheres (Li & Ng 2003; De Lange Kristiansen et al. 2005; Foteinopoulou et al. 2015; Soontrapa & Chen 2013). Although it has been proven useful for determined studies and has shown capable of

producing fair packing densities compared to experimental data, this methodology does not allow large overlaps and interparticle forces are not calculated. In MC method the translation of particles is governed by random generated vectors. If a particle finds another particle along a vector, then simply another random vector is generated. The principle to generate a packed structure lies on addition constraints, i.e. if after a predefined number of attempts a particle cannot find a place into the domain, that particle is simply discarded and a new one is generated. Furthermore, the dynamic process of packing is hampered by the fact that the particles are not allowed to explore the whole domain and accommodate freely. This factor affects the efficiency of the MC method as the packing density increases.

The algorithm called collective rearrangement (Nolan & Kavanagh 1992; Bertei et al. 2014) follows a similar principle of initially placing the particles randomly but uniformly distributed in the computational domain according to an initial value of porosity. This algorithm is a simplification that does not simulate the dynamic process of packing. Small overlaps are allowed but the forces are not calculated based on the dynamics of the system; instead, forces acting on particles are simply considered to be equal in magnitude and in opposite direction. Moreover, particles with no contacts are fixed and are not affected by future contacts.

The cellular automata (CA) method was originally conceptualised back in the 1940's by Stanislaw Ulam and John von Neumann and years later presented in text by Edmundson (1969). In CA a dynamic system is constructed with a regular lattice in which time and space are discrete. Rules of local interaction among cells in the lattice are imposed; as time progresses all cells are updated simultaneously according to these rules. There are many alternatives to define rules that will affect the overall behaviour of the system. All the rules have in common a principle specifying that the current value or state of one cell will be modified at the next time step depending on the state of the predefined finite number of its neighbouring cells. For instance, rules can be defined to allow particles to stick together to large particles instead of small ones; or particles may slide down faster if there are no particles in the near vicinity. If the rules are appropriate, the system will be stable towards convergence. CA has been used to model diffusion, aggregation, transport and deposition of particles due to gravity. Stephen Wolfram (Wolfram 2002) published a book in which he introduced a classification of CA rules. These rules describe the evolution of stable and oscillating patterns originated into the system throughout the simulation time. Works on

simulations of particulate flows involving CA have implemented three dimensional (3D) models and developed complex rules to account for the particles features and physical system parameters (Wang et al. 2012; De Korte & Brouwers 2013; Marinack Jr. & Higgs III 2015).

Regarding DEM, this methodology has been the base of a wide range of research focused on particle interaction systems. The main reason is the availability of data for trajectories and forces acting on every particle at any given time. Compared with experiments, the modelling of packed beds with a methodology like DEM permits to easily measure the velocity of every particle in the system and to visualise all the internal particles forming a packed bed. In this sense, DEM is a powerful and well established approach that several researchers have included in their work.

But let us start from the beginning with the first published paper describing the details behind DEM. Cundall and Strack applied the numerical model to study the mechanical behaviour of assemblies of discs and spheres (Cundall & Strack 1979). The advantage of this model lies on the fact that calculations are based on the Newton's laws of motion and interactions in multi-particle systems that can be easily modelled as a result of small overlaps allowed between particles. Cundall's first programme developed was a two-dimensional model called *BALL* and it was capable to model assemblies of discs.

About a decade later, Cundall (1988) presented a comprehensive study of a 3D version of DEM, moving towards more complex systems. The relevance of this publication is that Cundall reflected on the importance to develop an algorithm that would detect and categorise contacts in a 3D multi-particle system successfully. The ideas reported in his publication have encouraged a number of scientists to work on new ideas to develop and implement algorithms capable of dealing with a large number of particles of different geometries in a more efficient way.

The particles' contact dynamics is governed by their mutual interactions and for this reason a force-displacement law is the core to make DEM work. The most used force-displacement laws are known as Hertz contact model and linear spring-dashpot. The Hertz contact model (Hertz 1896) is a non-linear elastic contact model that makes use of two spring-dashpot settings for the normal contact and frictional interaction between two particles. The linear spring-dashpot uses a similar representation for the normal

contact but the model incorporates a slider for the tangential force; in both models an overlap between particles is required to compute the corresponding forces.

As one could imagine, as the system domain grows with thousands of particles interacting, the computation time increases significantly. The task to find neighbouring particles for potential contacts in every time step is exhaustive and some researchers have developed algorithms to specifically tackle this problem (Domínguez et al. 2010; Awile et al. 2012).

Zhao et al. (2006) and Perkins & Williams (2001) developed and implemented different contact detection algorithms in DEM. In Zhao's work, the main purpose was to develop a new 3D computational code to simulate the interaction of polyhedral particles. One of the new concepts introduced was the way in which the neighbour search was implemented consisting of two different levels. To start, the whole 3D domain was discretised in equal cubic regions; for a particle i there was a cube list that registered in which cubes was particle i located. A second list registered the particles contained in each cube. A sensitivity analysis was included to find the optimal cubic size and the effect on code execution time. The work developed derived from the necessity of enhancing the code performance. This made evident the flexibility of DEM to implement algorithms that have significantly improved speed and effectiveness of the simulations, providing more accurate results, and reducing computational time, as expressed in Zhu & Yu (2006).

Given the significant improvements made to DEM algorithms, researchers have explored and found different areas of application for such numerical tool. For instance, Mishra & Rajamani (1992) implemented an algorithm in DEM to model the dynamics of spherical particles in tumbling mills to predict the torque required to drive a ball mill and its power draft. The results obtained showed a relative good agreement compared with experimental tests carried out. However, particles were represented as discs and the inaccuracy on the parameters describing the particles interaction, such as the friction coefficient, might have been the cause that led to unexpected final predictions. Further research was concentrated in the analysis of packed structures generated with mono-sized spheres or variations in the particle size distribution (PSD) and the container-to-particle aspect ratio (AR). Results from simulations have been compared with experimental data already reported in the literature. For instance, in Mueller (1997) the quantitative analysis compared the void fraction of experimental and modelled

structures; four deterministic algorithms produced fair trends that agreed with the experimental data, however the sequences followed to generate the packed structures did not allow particle addition randomness and the increase of AR showed a significant deviation from the experimental data. Effects on void fraction and coordination number by variation of the PSD and AR in random packings of spheres have been addressed by Jia et al. (2011) and Lochmann et al. (2006). No significant influence on the packed bed was found for the mono-sized spheres case, but when the bed was generated using a bimodal distribution, a large AR produced a more lose structure. For a Gaussian distribution the influence is notorious depending on how wide is the range of particle size. The highest void fraction was found for a particle size ranging from 1 to 5 mm. The direct comparison of different packed structures revealed how packing density changed when the PSD was modified, however no experimental validation was included in their work which was crucial to be more confident of the findings discussed.

Specific modelling requirements have been addressed for particular case studies, for example to evaluate particle deformations developed due to a compaction process. In the work presented by Munjiza (2004), the methodology followed focused on the necessity of simulating the compaction process of real non-spherical powder. Particles were digitised from 2D images obtained from Scanning Electron Microscope (SEM), thus giving polygonal approximations to represent the particles. In the work presented by Lewis et al. (2005), DEM was used as base model to develop a two-stage contact detection algorithm. The simulations included powder made of irregular shapes and sizes, finding that these physical characteristics together with specific material properties have an important impact on the resulting compaction and deformation of a product. The importance of the compaction processes of powder and granular materials was highlighted by emphasising the need of proper and efficient particle scale modelling. An important implementation derived from this work is the adaptation of the finite element method (FEM) to account for the deformation of particles.

3D DEM models have been developed with the intention of producing more realistic simulations. Parallel programming together with the fast evolution of computational capabilities, increment of memory and high-performance processors, have permitted researchers move towards the detailed representation of non-spherical particles and the construction of more complex systems involved in granular flow. Such is the case of the work presented in Cleary & Sawley (2002) and Langston et al. (2004). Their findings have shown that using particle shapes different than the traditional circular

geometries has a significant effect on the overall behaviour of the system under study. In Farsi et al. (2016) the particle shape influence on packed columns and voidage formation was studied using numerical simulations for a specific application. The performance and efficiency of catalysts in fixed bed reactors was investigated using a DEM-based programme to involve small irregular geometries originated from catalyst fragmentation. The problem presented lies in the fact that such small particles modify the bed voidage and reduce its permeability, which in turn has an impact in the lifetime of the reactor. Combining the Finite Element Method with DEM, cylindrical pellets were represented by means of a tetrahedral mesh. The columns generated were compared to digital images obtained from X-ray computed tomography (CT) in terms of axial and radial packing densities.

Applications of DEM have been extended to the nuclear and metal industries. For instance, Suikkanen et al. (2012) modelled packed beds of nuclear fuel spheres to assess the core load and the effects on power profile due to the neutron dynamics. Three different simulated packed structures were analysed showing a higher density at the bottom and near the centre according to the results obtained from the axial and radial profiles. It was also observed that the higher the average packing density of the structure, the better the arrangement of the particles near the walls. For future applications, a region of the packed structure could be selected to simulate fluid flow through the bed and detect local hot spots in the core. Moreover, having a record of the position of every fuel pebble could be very useful to predict the local fuel burn up and aid in the design of future fuel load cycles. Langston & Kennedy (2014) quantified two modelling parameters that compare to porosity and connectivity in real experiment measurements based on mono- and bi-sized beds of spheres. With a full-scale DEM model they predicted the pore fraction of the packed beads and assessed the changes in connectivity due to further addition of small spheres. In this way, their findings provided relevant information for the manufacture of porous metals in order to achieve the desired heat-transport characteristics. Nevertheless, particle interstitial fluid effects were neglected.

Combined experimentation with modelling has been also practiced to produce data readily available to be fed to the DEM model and to compare the results obtained from the two different methodologies. Such is the case of the research reported by Oger et al. (2008) and Al-Raoush & Alsaleh (2007). In the first one, experimental studies were formulated to understand the aeolian sand transport. Test cases were designed varying

the angle of incidence and colliding velocity of a bead hitting a static bed of particles; modelling was carried out in 2D and 3D. The second paper reported on the development of an algorithm to generate random packings of polydisperse spheres and the validation process through the structural analysis of physical parameters obtained from 3D CT. It is noteworthy that the use of CT and XMT has increased in different research areas around the globe for the study of packed beds, micro-structure analysis and modelling validation (Jia et al. 2007; Suzuki et al. 2008; Navvab Kashani et al. 2016).

Validation work is crucial to test the confidence in the algorithms developed for DEM. It is a very important stage in which the algorithm is challenged to produce sensible results compared with experimental data and/or numerical analysis. When the data generated by the model does not compare then the algorithm must be modified and tested again for a selected number of basic cases. This might be a tedious and time consuming task but the developer must ensure that the model, once validated, can be applied for a range of configurations with the certainty that reliable results will be produced.

Zou & Yu (1995) have carried out experiments packing spheres in cylindrical containers to study the thickness effect that affects the micro- and macro-structure of the bed near the wall of the container. Different cases were configured varying the cylinder-to-sphere diameter ratio and their findings in terms of packing density and bed porosity have been used to validate packed structures generated with DEM. Similar studies in Delaney et al. (2012) and Jia et al. (2012) have reported validation work using different PSD for spherical particles. Gan et al. (2004) and Jia & Williams (2001) based their research on the packing of non-spherical particles. Different authors have proposed some validation cases, for instance Asmar et al. (2002) produced the code DMX and introduced 8 different tests based on simple cases such as single falling sphere hitting a wall and two particles in contact to verify the code and evaluate the normal, damping, cohesion and friction forces. Chung & Ooi (2011) also proposed 8 different tests to benchmark DEM codes only for spherical particles. They used the commercial codes PFC3D and EDEM to compare results with experiments, analytical solutions, and numerical results from FEM. Besides designing the basic cases involving single sphere interactions, some of the tests focused on the investigation of energy dissipation after collisions.

Given the success and popularity of DEM, some authors have spent time collating information about the different modelling techniques. An interesting review is presented in Zhu et al. (2007) and Zhu et al. (2008). In this series, the theoretical developments of DEM since its first appearance are summarised, including particle-particle and particle-fluid interaction models coupled with CFD. Recently Lisjak & Grasselli (2014) published a summary of techniques focused on the modelling of fractures in solid rocks and their propagation. Besides the well-known DEM, they discussed a finite-discrete element method technique called continuum-discontinuum methodology. This combination of FEM with DEM has as starting point the representation of the solid structure as a whole; then fractures are generated following a fracture criterion handled by FEM. The fractures may further develop or new ones may appear in the structure.

The comprehensive research and analysis carried out by Zhu and Lisjak provided sound arguments to conclude that numerical representations based on DEM are an efficient way to represent and examine particulate systems, reaffirming the relevance of employing this methodology for studies in the industry and R&D areas.

Considering the literature review presented about the evolution and expansion of DEM, it is clear that much work has been carried out to increase the capabilities of the methodology given the continuous use, application, learning and documentation of a wide sector of the scientific community. It is concluded that the key of DEM's popularity and extensive use lies in the fact that the methodology is based on physical rules easy to understand and implement. Furthermore, it has been proven that DEM works correctly and efficiently in different test cases ranging from single sphere to multi-particle systems of real irregular geometries taken from the nature. DEM is also flexible and versatile, allowing in this way the representation of a wide range of configurations to study their mechanical properties. Part of the research included in this literature review has made it clear that on one hand, DEM can be applied to generic cases and successfully produce accurate results for most of the existent codes. On the other hand, the numerical method is application dependent, meaning that further adaptations and modifications should be implemented in order to first validate such implementations, and then simulate specific configurations based on the area of interest of the user.

The detailed data produced by DEM for every particle at every time step makes the method advantageous over experiments since the micro-dynamics of powders can be

retrieved easily, including the data inside the system that cannot be physically visualised or measured. Real systems may contain millions of particles. However, the study of a representative fraction of the entire volume is likely to provide a significant insight for researchers. For these reasons it is encouraging to continue using DEM to further study specific applications that have not been studied yet, or those that should be studied in more detail, for example the ones including an extensive use of non-spherical particles. The motivation to extend its capabilities lies on the idea of producing a more powerful numerical tool that can be coupled with fluid dynamics algorithms to represent more complex systems. Further details of DEM are included in chapter 3.

2.2. LBM for computational fluid dynamics

The study of fluids in motion is relevant in different research and industry applications involving mix of solutions, mass transport, heat transfer and particle coating, to name a few. Fluid dynamics provide substantial information about the behaviour of liquids and gases moving in and through determined spatial configurations. The CFD field of study brings together disciplines such as fluid mechanics, mathematics and computer modelling to study fluids in motion and the interactions with its surroundings. In order to describe the physical characteristics and properties of fluids in motion, it is necessary to make use of equations that govern the fluid behaviour. It is here where computer science plays its role to solve these equations by means of numerical methods to accurately represent the fluid.

Thanks to the rapid development of computational software, CFD is nowadays a robust and well-established tool to solve numerical methods such as finite difference (FDM), finite element (FEM) and finite volume (FVM). Generally speaking, the first step of a CFD solution is to discretise the flow domain into computational cells. The equations of motion are to be solved for a number of fluid nodes in the generated computational mesh. There are two ways of discretising the flow domain, but the volume discretisation is preferred over the surface flow discretisation (known as boundary element method).

The finite methods are used to solve partial differential equations that correspond to the macroscopic balance equations of conservation of mass, momentum and energy. FDM is used to estimate and solve the governing equations written in terms of fluid nodes data. Algebraic equations are constructed from interpolations between fluid nodes in

FEM, whereas in FVM equations are derived by integrating the equations of motion over the volume (Green & Perry 2008).

In the present work it is relevant the case when solid particles are immersed in a fluid to study FSI systems. The selection of the method to interpret and represent the fluid-solid interface depends on the application but it is ideal to achieve an optimal balance between computational efficiency and accuracy, particularly for complex FSI systems.

For instance, Lagrangian methods are capable of tracking the solid-fluid interface and are mainly used when it is not expected to have significant perturbations in the domain. If such condition was not satisfied for high Reynolds (Re) number fluids, a slight modification of the domain might potentially produce mesh elements degeneration. As a result, a partial or complete remeshing of the domain would be necessary, making the method computationally expensive. On the other hand, the advantage of these methods lies on the easiness to represent the interface allowing a good approximation because the solid-fluid interface always matches the mesh. As such, the numerical accuracy is determined by the mesh size. In this way, boundary effects are treated considering the grid points that lie on the boundary.

Francis Harvey Harlow has worked on the development of CFD algorithms known as *particle in cell* and *marker and cell* methods (Harlow (1964)). The *particle in cell* method is a mesh-free technique in which the capture of the interface is achieved by using particles having velocity equal to that of the fluid. For every particle, the Lagrangian equation is satisfied at the location of the particle in a determined moment in time. In the *marker and cell* method (Harlow et al. (1965)), the liquid domain is constructed with the aforementioned characteristics of the particles. A different method is the surface marker method developed by Aulisa et al. (2004). In this case the interface of the particle is tracked at its exact location, having a reduced computational effort.

Unlike CFD, a different treatment is followed in approaches known as pseudo-kinetic models. Instead of representing individual particles in motion, a collection of them is used to describe a fluid in a mesoscopic level. One of those approaches is the LBM for fluid flow representation and FSI studies. The fluid interpretation in LBM lies on the premise that the macroscopic behaviour of a fluid is the result of its microscopic behaviour at a particle level. Chapman (1916) & Enskog (1917) independently

developed a multi-scale analysis known as the *Chapman-Enskog expansion* in which the macroscopic NS equations are recovered from the Boltzmann equation (BE). In this way, the computation of the macroscopic transport coefficients is possible through the microscopic definition of the fluid.

LBM is a much simpler numerical scheme and a highly-parallel algorithm regarded as an alternative numerical method to traditional CFD solvers based on the discretisation of the macroscopic continuum NS equations. LBM approximations are constructed in a way to similarly give the macroscopic behaviour of the NS equations. LBM is implemented on a regular mesh, meaning that no re-meshing is needed as solid particles move in the fluid. Most of the LBM implementations have seen their major use in research areas, although its use in commercial codes has increased gradually.

LBM was proposed more than two decades ago and it is based on the molecular description of the fluid. The Lattice Gas Cellular Automata (LGCA) is the LBM predecessor and was initially used by Hardy et al. (1973) for fluid studies. It was Frisch et al. (1986) who used LGCA for the NS equation in a rather simple system to simulate a 2D fluid. Also known as the FHP (named after initials of the authors), the model uses a hexagonal mesh where only two possible collisions may take place, 2-particles and 3-particles collision. Every time step, particles located at the centre of each cell propagate and collide with neighbouring particles according to predefined collision rules. The conservation of mass and momentum is easily satisfied since all particles have the same mass and speed, and net momentum for all collisions is zero. Early fluid simulations based on the LGCA can be found in Rothman (1988) and Papatzacos (1989).

A couple of years later McNamara & Zanetti (1988) used the basic principles of LGCA to implement what we know now as LBM. The main modifications were the use of real values instead of Boolean to represent the population of particles, and the pre-averaging of the particles population function to eliminate the inherent statistical noise in LGCA. Early works reported attempts to solve the inherent drawbacks of the methodology due to the non-linearity of the governing equations and statistical noise. Similar to McNamara & Zanetti, Higuera et al. (1989) proposed a linearised collision term to address the issues of statistical noise and have numerically stable results. In this way, LBM gained major interest and the evolution of the methodology has been

based on the discretisation of the BE in both time and space and the treatment of the collision operator (He & Luo 1997).

Different LBMs exist nowadays and the selection depends on the application of interest, desired model accuracy and available computational capabilities. An interesting review of different available models was presented by Succi (2015). It has been made clear that accuracy entails a higher and more complex level of programming of the collision rule, which makes it more expensive computationally speaking. However, the simplest version of LBM is known as the Bhatnagar-Gross-Krook LBM model (BGK-LBM) which made use of a collision operator rule proposed by Bhatnagar et al. (1954). This model has been used to solve the BE proposed in 1872 by Ludwig Boltzmann. Since the BE is a non-linear integral differential equation, the BKG model replaces the collision term with a much simpler term to derive the transport equations for the macroscopic variables, i.e. collisions are not defined explicitly but the model relates closer to the continuous kinetic theory. However, in the attempt of achieving a simpler model, BGK-LBM (also known as single relaxation time model SRT) is restricted to laminar fluid flows at low Reynolds numbers, and users of this model must bear in mind that accuracy might be compromised.

Qian et al. (1992) gave the *D2Q9* name to a 2D model with 9 velocities in a squared mesh and keeping the uniform particle mass as unit. With the BGK model, the LBM numerical stability relies on the relaxation parameter that describes the rate at which the particle distribution functions relax towards local equilibrium after collision. Zou & He (1997) contributed significantly to the LBM implementation of the bounce-back boundary condition applied to straight boundaries.

Considering the different model developments and the applications that the methodology is able to handle, a classification of the available LBM models in terms of the fluid characteristics is listed below:

- Single component-single phase. The simplest single-fluid models that have been implemented (e.g. Poiseuille flow or creeping flow past a fixed cylinder or sphere)
- Single component-multiphase. For systems in which phase separation takes place (e.g. water present in liquid and vapour form)
- Multi component-multiphase. Used for systems having more than one fluid component (e.g. oil-water flow through porous media for permeability studies)

It is not the intention of this chapter to provide an in-depth review of the models just listed; instead, the following discussion is focused on research reporting the use of LBM for FSI applications relevant to the present work, such as fluid flow through porous media, fluidisation and sedimentation of particles (in section 2.3). However, the reader is referred to the book by Sukop & Thorne Jr. (2007) which includes a clear and easy to follow explanation of LBM, further bibliography, and more details of the models listed above.

To improve the accuracy and numerical stability of LBM, parameters such as relaxation time, lattice refinement and boundaries treatment have been the focus of researchers in recent years. Some authors have considered that the BGK-LBM has the issue of having only one single relaxation parameter to characterise the collision of particles, which translates into having all functions relaxing towards equilibrium at the same rate. In real physical terms that is not the case, and different relaxation rates would be expected. For that reason, it was d'Humières (1992) who initially developed the multiple relaxation time collision model (MRT) for LBM to overcome the aforementioned issue. In general, MRT-LBM has been considered to be more stable than BGK-LBM since more than one relaxation parameter can be controlled independently. The BGK-LBM has become very popular due to its simplicity and implementation easiness, but it has also been criticised for its inaccuracy to efficiently handle boundary conditions and for not being reliable and numerically stable at low fluid viscosities.

A number of researchers have opted for the use of MRT-LBM. For instance, a multiple relaxation time collision model is implemented in LBM by Mussa et al. (2009) to simulate a 2D fluid flow past two cylinders in which a mesh refinement was also considered. Wang et al. (2014) carried out MRT-LBM simulations of the phenomenon known as drafting-kissing-tumbling (DKT) in which two vertically aligned spheres sediment in stagnant fluid. Due to a wake generated by one of them, the sphere settling down behind catches up increasing velocity, touching the wake-generating sphere and switching positions. The effect of the interparticle distance and different particle size was assessed as well.

Luo et al. (2011) carried out a comparison of the three different collision models available, SRT, two relaxation time (TRT), and MRT. It was not surprising that their results found from TRT and MRT yielded more accurate and stable simulations using a configuration of a 2D lid-driven square cavity flow. However, in addition to an important

insight in the use of MRT, their work provided the first comprehensive comparative work of the different collision terms available in LBM. The authors found that at least three independent relaxation parameters are necessary: “one for the shear viscosity ν (or the Reynolds number Re), one for the bulk viscosity ζ, and one to satisfy the criterion imposed by the Dirichlet boundary conditions which are realized by the bounce-back type boundary conditions”. Furthermore, the analysis of the authors extended to the discussion on the selection of the optimal value or range for the relaxation parameters. This is worth noting because published research related to LBM rarely offers information about this parameter, and it is commonly limited to only comment that the value must be larger than 0.5 to avoid having a zero viscosity in LBM units (this is rather a simplistic conclusion by merely observing the equation to obtain such viscosity).

Regarding the correct modelling of boundary conditions in LBM, different researchers have tried to correctly implement moving interfaces immersed in a fluid (Strack & Cook 2007; Noble & Torczynski 1998). It was Peskin (1977) who originally proposed the immersed boundary method (IBM) derived from studies on cardiovascular flows. This method was used to represent a solid object immersed in a fluid by a collection of discretised points located on the solid-fluid interface. The FSI takes place at such points, i.e. the immersed structure exerts a force on the surrounding fluid whilst the structure is translated, movement originated by the fluid pressure. The force applied on the fluid by the solid object is the result of the addition of local-force contributions. Under this scheme the objects are deemed as moving solid boundaries. The entire simulation can be performed on a fixed grid. Unlike the conventional approach of defining a surface grid for the boundary and then for the fluid and the solid, in IBM the grid is generated without considering the surface grid which can be seen as the boundary of the solid intersecting through the grid. The governing equations are discretised to incorporate the appropriate boundary conditions given the fact that the grid does not conform to the solid boundary but the advantage is that there is no need of coordinate system transformations. If a fluid is passed through the structure it will fill all the available empty spaces and the permeability of the structure near the wall will show an increment due to the wall effect mentioned. The no-slip condition applied on the interface is attained by including a force density term obtained from the virtual boundary method (Goldstein et al. 1993), the direct forcing method (Fadlun et al. 2000), or the momentum exchange method (MEM) (Ladd 1994a).

The hydrodynamic interactions between the solid and fluid phase using the MEM have been described comprehensively in (Ladd 1994a; Ladd 1994b; Nguyen & Ladd 2002; Chen et al. 2013). When a particle of any shape is placed on a regular LBM mesh, interacting links are formed between nodes belonging to the fluid and nodes belonging to the particle. As a consequence, boundary nodes are generated halfway on the interacting links and it is on these boundary nodes where the FSI is calculated.

The IBM-LBM scheme has been used to describe FSI systems in Feng & Michaelides (2004), Dash et al. (2014), Prestininzi et al. 2016, Chen et al. (2014) and Eshghinejadfard et al. (2016). Furthermore, combining DEM with IBM-LBM has been tested in Cui et al. 2014 and Han & Cundall (2013) and found to be an effective methodology to numerically study and describe the phenomenology taking place in FSI systems, not only for fluid flow through complex solid geometries but also for the interrelated effects between particle-particle, particle-wall and particle-fluid interactions. More details about work in the literature covering FSI and coupling numerical methods are included in next section 2.3.

Another area that researchers have explored numerically using LBM finds its application on permeability predictions in porous structures. There exist experimental studies and analysis available in the literature that assess the transport processes and hydrodynamic conductivity in porous media (Dullien et al. 1977; Van Brakel & Heertjes 1977; Berryman & Blair 1987). The truth is that difficulties have arisen at the moment of interpret and represent the internal pore network of solid structures. The pore disposition within a structure is very complex; in the past assumptions were made to treat pores as straight tubes or spherical chambers interconnected by cylindrical links. As an initial approach these interpretations provided preliminary insights, but it was customary to develop a different approach considering the continuous technological advances in measurement equipment and software. As such, researchers have tried to take advantage of different tools, methodologies and techniques to move their investigations forward. For this reason, more realistic representations of porous structures are important to evaluate fluid dynamics in complex systems. Moreover, since different experimental methods are available (Franke et al. 2006; Reimers et al. 2004; Wilson et al. 2008; Huettel & Rusch 2000), a single technique cannot be applied to study all the different structures present in nature due to the large variety of samples, environments or the facility to carry out measurements in-situ.

For this reason different techniques have been used to study properties of porous structures. For instance, in Maosong et al. (2004); Tueckmantel et al. (2012) and Rezaee et al. (2012), for the analysis of hydrocarbon and oil recovery, and tight gas sand reservoir. A relationship was established between permeability and pore throat size through mercury injection porosimetry (MIP) and nuclear magnetic resonance (NMR) analysis. Findings showed that a reduction of the pore throat size reduces significantly the permeability of the reservoir. Schmitt et al. (2013) studied the permeability in porous seal rock samples by means of a combined MIP and nitrogen gas adsorption technique to obtain porosity data and pore-size distribution comparing the results with empirical models. Similarly, Bolton et al. (2000) adopted as well the MIP technique for fluid flow evaluation and studied the effects of fractures present in fine-grain sediments.

Zhou et al. (2010) studied the pore-characterisation of cement-based structures. The authors discussed the limitations of the MIP technique in which is evident the underestimation of large pores and the overestimation of small ones. For that reason the authors attempted to provide improved MIP measurements by doing pressurization-depressurization cycles instead of continuous steps that only increase pressure when injecting mercury into the sample. Knowing the limitations of MIP, researchers have tried to combine different techniques to complement a widely used methodology that still presents some drawbacks. Some authors have tried microscopy to analyse a large number of 2D images taken of the pore network (Abell et al. 1999; Gómez-Carracedo et al. 2009). In Tsakiroglou & Payatakes (1990, 2000) microscope digital images of rock samples were studied to observe the pore network and pore size distribution. However, the pore network modelled contained only spherical chambers with cylindrical inter-connections.

Promising attempts involving computed tomography have been reported widely in the literature. The use of state-of-the-art equipment has aided to actually visualise the 3D pore network of solid structures, and well-defined pore shapes to quantify porosity. This technique was introduced for rock analysis in order to gain a better insight and achieve more realistic interpretation and representation of porous solids. In different studies (Peng et al. (2012); Weber et al. (2010); Rigby et al. 2011; Fusi & Martinez-Martinez 2013) it has been established the advantage of using this alternative tool to observe and calculate porosity. Understanding that no methodology is flawless, Bossa et al. (2015) studied and discussed the restriction of CT image resolution employing both

micro- and nano-CT. It was highlighted the difficulty of micro-CT to detect the smallest pores that represent a significant part of the total porosity. On the other hand, nano-CT requires a much smaller region of interest to be able to capture the smallest pores, meaning that a very small sample is studied, which puts in doubt if such sample is representative of its parent. The authors nonetheless provided insight from their tests reporting that the measured porosity and pore connectivity depend directly on the sample size used and image resolution (pixel size at the moment of scanning the sample). The nano-CT helped them to detect ≈60% of the entire pore volume of the sample, confirming that a decrease in pixel size increases pore connectivity due to a larger amplification resulting in better visualisation of the network.

Another combination of techniques further exploring the properties of porous media has brought together experimentation, CT and numerical simulation. Soil aggregates were studied in Dal Ferro et al. (2012) using a combined MIP simulation programme with XMT technique for the analysis of porosity and pore-size distribution. Numerical methods were used to observe pore distribution curves and to represent and quantify the properties of the pore network. However the capabilities of the method were only able to generate cylindrical links among the pores.

When no experimental data is available, researchers use numerical analysis and/or computational simulations to represent and study systems present in nature. The most basic porous structure for permeability studies is generated with spherical particles. Vidal et al. (2009) carried out studies using a Monte Carlo based software to generate a porous structure with polydispersed spheres and predict its permeability as a function of polydispersity using LBM. Spheres polydispersity was also studied in Sarkar et al. (2009) considering two different size distributions, finding that no significant change in drag force is originated for different distributions as long as the size range remains constant. Pan et al. (2001) and Rong et al. (2013) used LBM as well for permeability calculations and the study of fluid flow in fixed clusters of spheres. DEM was used exclusively for clusters generation; permeability predictions were carried out in LBM. The effect of porosity on fluid flow was assessed, confirming its non-uniformity at a pore scale. In Beetstra et al. (2006) studies on clusters of mono-sized spheres varying the distance between the particles were carried out using LBM. Findings report the clustering effect producing lower drag coefficient due to the inter-particle distance. In Machado (2012) a 2D domain was used to evaluate the influence of increasing mass flow rate in pressure drop in highly porous solid structures using small squares fixed in

the system. The authors compared LBM simulation predictions with calculations from the Ergun equation and experimental data from micro-power plants for energy storage. Cho et al. (2013) studied the permeability and local fluid behaviour around differently arranged fixed structures representing fibrous porous media with a combined 3D MRT-LBM. Having generated symmetrical arrays of cylinders and spheres, Khabbazi et al. (2013) used the BGK-LBM to assess the permeability of fibre-like structures. From the predictions a correlation was developed to obtain the Kozeny-Carman constant for structures varying in porosity. Bogner et al. (2015) used TRT-LBM to study the flow dynamics in static structures with different porosities generated by randomly accommodating mono-sized spheres. Although their results showed good agreement at low Re compared to the widely used Wen & Yu correlation (Wen & Yu 1966), deviations were significant when compared to other available correlations. Their work could be regarded more as a qualitatively assessment of the local flow in porous networks. Zhang et al. (2016) reported on the geometrical effects on permeability in a 2D pore network with two-phase immiscible flows.

A step further in studies employing LBM has been taken in the field of non-zero velocity particles and non-spherical geometries. Hölzer & Sommerfeld (2009) tested a drag correlation using a 3D LBM. Besides a sphere, they used an ellipsoid, cube, cuboid and cylinder. Only for a sphere the rotation of the object and the effect on the fluid was studied for different angular velocities; for the other particles, the angle of incidence was modified varying their fixed positions. Their findings of drag coefficient agreed well with previous studies carried out by different authors (Haider & Levenspiel 1989; Comer & Kleinstreuer 1995; Pitter et al. 1973; Jones & Knudsen 1961; Saha 2004), showing that as the particle geometry departs from spherical, the drag coefficient becomes higher, confirming that drag is strongly dependent on particle shape and angle of incidence.

The use of LBM has been successfully used as an additional study analysis tool in applications such as the efficiency of a newly designed heat exchanger (Borquist et al. 2016), heat transfer in fractal porous media (Cai & Huai 2010), micro-voids formation in electronic chips encapsulation (Ishak et al. 2016), gas flow in micro channels (Yuan & Rahman 2016), heat transfer behaviour in particulate suspensions (Mccullough et al. 2016).

The motivation to use LBM lies in the understanding that the behaviour and physical properties of a fluid at a macroscopic level can be recovered from the physics taking place in a mesoscopic level. The advantage of using LBM is the mathematical approach in which the propagation-collision dynamic of the particle density functions is treated as a collection of fluid particles rather than evaluating individual interactions that would require a more complex and time consuming approach. From the literature discussed in this section, LBM is not only limited to simulate fluid flow through porous structures that remain fixed in a computational domain, it can also be coupled with other algorithms to study FSI systems in which one or many solid particles are immersed in the fluid and interact with each other, translating and rotating as result of hydrodynamic and contact forces. Although it has been used in its majority for R&D and academic purposes, its popularity and evolution has made LBM an attractive solver also in industrial applications.

The next section includes discussion about available coupled methodologies to simulate FSI, focusing in LBM and DEM which are relevant for the present work. More details about LBM can be found in the next chapter in section 3.2.

2.3. Coupling models for fluid-structure interaction simulations

Having presented in the previous sections the relevant numerical methodologies for solid and fluid solvers, this part focuses on the methodologies that make possible the coupling of such solvers. In order to enhance the capabilities of numerical simulations and represent more accurately and dynamically FSI phenomena, coupling algorithms and methodologies have been developed for years and reported in the literature.

In FSI systems one or more solid objects or structures interact with a fluid. The fluid in question may be a gas or a liquid, with the possibility of both being present. Depending on the system configuration the fluid may surround the solid or flow through pores and cracks of a structure. Some configurations are commonly reported in the literature. One of them is a single solid object or array of objects fixed and immersed in a fluid. The objects remain motionless but the fluid flows around them and FSI takes place at the interface (Qu et al. 2013; Hooper & Wood 1984). In some cases the single object rotates along one axis but it does not actually translate (Al-Mdallal 2015; Karabelas et al. 2012). A similar configuration may differ by simply varying the particle geometry (Krueger et al. 2015; Chen et al. 2015). A different configuration is when the fluid flows through the pore network of a structure. This structure may be represented as a unique

solid porous object (Zhang et al. 2016) or generated by a collection of solid objects of the same or different geometry clumped together (Eshghinejadfard et al. 2015) or as an array of objects (Yazdchi & Luding 2011). The coupling methodologies for these two configurations have addressed the way in which the solid boundary is represented and handled by the fluid solver. The accurate representation and treatment of the boundary are the main features to consider in the coupling methodology.

A fully coupled configuration is the one in which a solid object is allowed to freely move in the fluid with the hydrodynamic and external forces governing the rotation and translation of the object. Furthermore, more than one object immersed in the fluid will provide a system in which the interparticle forces play an important role as well. In this case, the coupling algorithm should be implemented paying attention to the exchange of information between the fluid solver and the solid solver, in addition to the method to correctly represent the solid boundary in the fluid.

Fluid flow around a fixed object such as a sphere (Liao 2002; Tsutsui 2008; Almedeij 2008) or a cylinder (Catalano et al. 2003; Qu et al. 2013; Singha & Sinhamahapatra 2010; Chakraborty et al. 2004) are common cases used to study simple FSI systems and to benchmark and validate computational coupling algorithms. In the laminar regime, symmetric fluid streamlines pass the solid object and no turbulence is observed. For non-spherical geometries the flow pattern is affected by the particle shape and surface roughness (Laín & Sommerfeld 2007; Shih et al. 1993).

The FSI complexity increases when more elements and features are involved, e.g. a two-phase flow in a porous structure, like in an oil well or an engine; or a system with thousands of small particles being transported by a fluid, like the erosion of a river bank or the fluidisation of particles in a reactor. In some cases, the stress exerted by the fluid may even cause particle or structural deformations originating non-linear responses. In turn, these responses will modify the fluid-solid interface making it a more challenging problem. These are some examples of FSI problems that are a matter of interest to researchers in both industry and academia.

In numerical modelling the analysis of FSI systems entails the discretisation of both solid and fluid phases. The *conforming mesh* and *non-conforming mesh* methods are used in computational solvers to generate a mesh that will represent the elements involved in the system, to define the solid-fluid interface and to perform the

corresponding calculations. The selection of one over the other depends on the desired accuracy to represent the computational elements and calculations. It is also application oriented depending on the features of interest under study. The main difference is that in the *conforming mesh* approach vertices of one cell must intersect other cells only at vertices, and not at other feature such cell edges or faces. On the other hand, the preferred *non-conforming mesh* has the advantage of allowing local cell refinement where needed without the constraint of matching cell vertices. For example, complex solid geometries give raise to complex fluid flows around them. A fluid could be represented by combining large square or rectangular cells representing simple flow regions whereas refined triangular cells could be used for complex flow at the boundaries of an object.

There is another difference in terms of how to compute the FSI between the two phases. Two approaches known as *monolithic* or *direct*, and *partitioned* or *iterative* approach can be used to solve the fluid and solid phase. In the monolithic approach both the fluid and solid governing equations are reformulated and later combined in the same mathematical framework to be linearised and solved with a single algorithm. The difficulty of this approach is the interpretation of the new system of equations since there are two different systems of reference, one for the solid and another for the fluid. On the contrary, in the partitioned approach the sets of equations to solve the solid and fluid phase are treated separately by independent algorithms. Therefore, a coupling algorithm to exchange information between the two solvers is implemented and conversion factors are calculated to keep consistency between the two solvers.

The first step to follow in order to simulate the hydrodynamic forces interacting with solid particles immersed in a fluid is the incorporation of adequate boundary conditions in the Boltzmann model. The most popular and easy to implement is the link bounce-back method (LBB) (Zou & He 1997). LBB methodology has been adapted to the LBM environment resulting in different methods, one of them being the momentum exchange method (MEM) (Ladd 1994a). To give an idea of the fundamental interpretation in this method Figure 2-2 presents a simple sketch of MEM for LBM in a regular mesh.

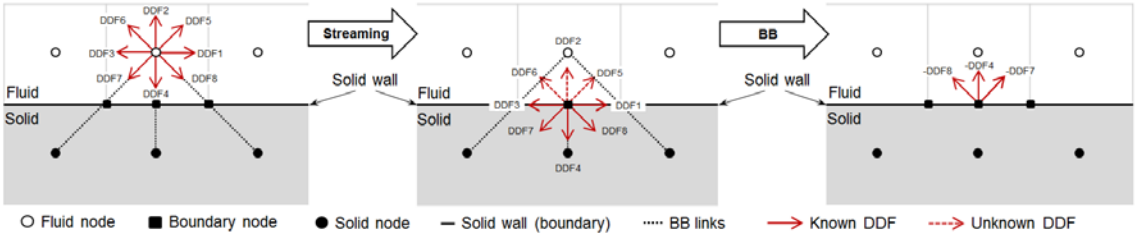

Figure 2-2 Bounce-back in LBM environment for no-slip boundary condition

It is observed that BB links are generated between fluid and solid nodes near a solid wall (image on the left). The density distribution function (DDF) is represented by a particle in the centre of the lattice. The DDF is interpreted as the probability of the particle to propagate to a neighbouring lattice with one of the possible velocity vectors or to remain at rest. The DDF define the density and velocity at each lattice node and indicate the number of particles at a determined time t that are located within a physical space in a particular position x and having a particular velocity e.

For instance, the density distribution function 4 (DDF4) is moving towards the solid wall. After streaming (image in the middle), DDF2, DDF5 and DDF6 are unknown. To find them, these DDFs are reflected or “bounced back” in the opposite direction, resulting in -DDF4, -DDF7 and -DDF8. The LBB ensures conservation of mass and momentum at the boundary with no tangential velocity on the solid wall. The idea behind this technique is that the fluid is exerting a force on the solid wall through every BB link formed between fluid and solid nodes, and the total hydrodynamic force is the summation of all the forces along the BB links.

The stress integration method (H. Li et al. 2004; Connington et al. 2009) was reviewed in Yu et al. (2003) and compared to MEM. In this method the hydrodynamic force is calculated in a similar way integrating all the stress contributions along the surface of the particle. The main disadvantage is that it requires a large number of extrapolations between fluid data, making it more complex to implement and computationally expensive for 3D systems. He & Doolen (1997) studied the stress applied on curved geometries. They had to define an adapted coordinate system in order to place as many nodes as possible close to the boundary to calculate a velocity gradient. Given the nature of LBM, the velocity is not the primary variable and the calculation of the gradient may result in loss of accuracy. In Mei et al. (2002) a similar comparison of MEM and stress integration was carried out. The authors highlighted that for a 2D flow

past a cylinder configuration almost half of the computational code was dedicated to calculate the hydrodynamic force when using the stress integration method.

When MEM is applied to moving boundaries (solid objects immersed in a fluid), the technique dictates that the solid boundary must be placed halfway on links generated between solid and fluid nodes. Some authors argue that this action impacts negatively the accurate representation of the boundary and statistical noise is introduced. Nevertheless, Ladd has extensively discussed and tested MEM for LBM (Ladd 1994a; Ladd 1994b). Initially MEM was regarded as a shell model since the object was not precisely a solid particle; the object was represented more like a boundary having fluid on both sides, i.e. inside and outside of the closed boundary. The same MEM principle was applied to every DDF on both interior and exterior fluid of the boundary. Later on, most of the authors employing MEM switched to the corrected version that does not include internal fluid. The argument was simple, using the MEM shell model originated *'undesired'* motion of the boundary from internal fluid sites and, in order to avoid that, heavy particles should be configured, which limited MEM use. The MEM has been tested by different authors and some of them have adjusted the methodology to specific needs (Chen et al. 2013). Furthermore, the achievable accuracy combining LBM with MRT has shown hydrodynamic interactions within 1% of a numerical solution using small spherical particles (Dünweg & Ladd 2009). Despite being only first-order accurate, MEM is still a popular technique to simulate FSI due to its inherent simplicity and robustness. However, the disadvantage is the presence of large force fluctuations at the solid interface.

Aidun et al. (1998) started to apply MEM without fluid inside the boundary. The modification they proposed was the addition of an external force applied to the particle known as *impulse force*. Such force would play the task of moving the boundary with the purpose of covering and uncovering fluid sites. A similar idea adding a binding force to particles forming a cluster was used by Cui & Sommerfeld (2015). By simply using imbalanced forces, the hydrodynamic force exerted by a fluid governed by LBM would cause spherical particles to detach from a much larger sphere and be carried away by the fluid flow. As long as the frictional force between particles is larger than the hydrodynamic force, small particles remained attached to the cluster. Some authors like Yin et al. (2012) have claimed that the momentum exchange is not necessary to calculate FSI and have criticised the fluid-solid node status change. However, what prevailed in their modifications was the BB concept.

Different authors have used the extrapolation (Ziegler 1993) and interpolation method (Filippova & Hänel 1997; Yin et al. 2012; Abdelhamid & El Shamy 2014) to deal with immersed boundaries using LBM. BB links are also formed in a similar manner as in MEM for extrapolation and interpolation. The extrapolation method consists of setting the equilibrium function on solid boundary nodes considering zero velocity and density extrapolated from the corresponding fluid nodes. The interpolation method does not require the redefinition of the solid boundary to conform to the mesh as performed in MEM. As such, curved boundaries are treated explicitly with second-order accuracy. Since the original location of the boundary is retained (unlike MEM in which boundary is redefined halfway of every BB link), some authors consider that the interpolation method provides a more accurate and stable BB condition for all the boundary nodes. The interpolation method follows the BB approach and relies on the momentum exchanged in every link formed between fluid and solid nodes near the particle boundary. The main difference is that the interpolation is carried out on the original location of the particle boundary and not at the middle of the link. An adjusting parameter must be calculated every time the boundary translates to know the fraction of the BB link falling on the fluid part of the cell, and the corresponding fraction falling on the solid part of the cell. Even when the boundary is treated at its exact location, fluid nodes are necessary to obtain additional data and carry out the corresponding interpolation. Problems arise when a solid particle approaches a solid wall or when two particles approach to each other to the point that no fluid data can be obtained since the gap between the two solid objects is much smaller than the lattice.

A different technique developed to deal with non-conforming boundaries was introduced by Noble & Torczynski (1998) known as immersed boundary method (IBM). The authors modified the collision part in the lattice Boltzmann equation (LBE) to implement an additional collision term in order to produce a smooth transition between hydrodynamics and rigid body motion. The new collision term is accompanied by a volume fraction parameter that accounts for the portion of fluid mass in every boundary cell. In this way the corresponding fluid and solid fractions are obtained for cells intersected by the solid boundary and later used to weight their portions in the collision term. When the boundary cell is completely solid, the weighting factor becomes 1 and the process follows the BB approach. Their method seems to be more appropriate for cases in which boundaries immersed in a fluid do not conform to the computational mesh. For instance, in Cook et al. (2000), DEM was coupled to LBM using the IBM. Their work was on simulations of 2D configurations of particle sedimentation (ellipse

and disc). Later on in (Cook et al. 2002) particles were represented by means of superquadric elements that remained bonded to model a 2D pore throat of weakly consolidated sandstone to be eroded by fluid flowing through the throat. The authors demonstrated the capabilities of the coupled model and acknowledged that 3D simulations are preferred but the computational expenses are more significant even for small configurations like the one proposed in their work.

In general in the literature the BB condition implemented in LBM is still the most popular choice. The errors present are usually cancelled when they are averaged over boundary nodes, whereas the local errors in the interpolation technique are not. MEM is easier to implement and has showed to produce fair approximations at a reasonable computational expense. Employing the interpolation method makes more sense when non-uniform meshes are used. Since the cell velocity is dictated by the mesh holding the smaller cells, density distributions in the coarser grid would not reach a neighbouring cell in a single time step. The partially-saturated cell method produces second-order solutions and has shown to be more accurate compared to MEM but at a greater computational expense.

In the following paragraphs different methodologies coupling fluid with solid solvers found in the literature are presented. Although DEM-LBM coupling is of particular interest for this thesis, DEM coupled with traditional CFD models are also included.

In the work presented by Zobel et al. (2012), the authors constructed beds of mono-sized spheres contained in a cylinder. The shape of the container wall was varied with the intention of obtaining a more homogeneous void fraction distribution near the wall. The capabilities of DEM were used in a first stage to generate packed beds, but once obtained they remained fixed. CFD was used to measure the average velocity near the wall. The configuration can be regarded more like a fluid flow through a porous structure without actually performing the dynamics of FSI. A similar DEM-CFD model was used in Chu et al. (2011) to present the FSI in a gas cyclone application. Since DEM calculates parameters at individual particle level and CFD does at the computational cell level, the way in which the coupling worked is by means of DEM providing information of location and velocity of individual particles in order of CFD solver to compute the porosity and volumetric particle-fluid interaction per cell. Then the flow field is calculated to finally find the fluid force exerted on the particles. Although the same force is applied on all the particles contained in a computational cell, this

approach is more reliable than adding an artificial force to move individual particles. Successful representation of a gas cyclone was achieved to describe key flow features such as particles flow pattern. In Goyal & Derksen (2012) LBM was combined with FVM to simulate the flow past a cylinder and the sedimentation of a single sphere and two aligned spheres. Halfway BB was applied together with the IBM. The validation of the combined methodology was achieved in a regular mesh without applying local refinement. It was the purpose of the authors to assess this feature since adaptive grids are computationally unfeasible for viscoelastic liquids studied. More details of implementations combining DEM-CFD can be found in Kollmannsberger et al. (2009), Korevaar et al. (2014), Jing et al. (2016), and Vollmari et al. (2016); the last one involving fluidisation of non-spherical particles.

Cui et al. (2012; 2014) based their study in the fluid leakage from underground pipes covered by soil sediment which leads to a cavity generation and the potential risk of pipeline exposure, surface subsidence and collapse. The analysis was primarily based on the initial height of the bed covering the leaking pipe. Spheres were employed for the 2D simulation domain where the DEM software solved the particle interactions in the soil with a slight overlap allowed. LBM was used to model the fluid flow using the IBM to provide the interface treatment for particle-fluid interactions. The successful implementation of the coupled DEM-LBM yielded valuable results in predicting the cavity size formed by a pipe leakage depending on the bed height of the sediment. Further work should be developed in order to perform experimental tests and compare results with the ones obtained from coupled simulations using a 3D model in which particles are not circles but preferably display geometries found in real soil beds.

An application in geology such as particle erosion was studied with a coupled DEM-LBM model in Brumby et al. (2015). A 3D LBM model with 15 velocities was employed with a SRT; the no-slip boundary condition was implemented using the halfway BB and FSI treated with the IBM. Further in the report it is explained that when pouring particles randomly into the system, pairs that have overlaps were dismissed. It is rather confusing the way in which contacts were treated. After validating the coupling with the calculation of terminal velocity of a particle, simulation of onset erosion demonstrated qualitatively the presence of a shear stress at the upper part of the bed which caused some spheres to be detached and carried away.

Feng & Michaelides (2004) combined LBM with IBM and a repulsive force between particles to represent the sedimentation of 504 discs in 2D simulations; Ido et al. (2016) also combined LBM with IBM but the solid solver was based on DEM for simulations of magnetic particles in fluid. . Recently in Cao et al. (2015) LBM was coupled with a discrete external boundary force model that accounted for the solid particle interactions. A repulsive force is imposed between the particles controlled by a threshold parameter that determines when such repulsive force is generated. A validation case of a single particle settling down in quiescent fluid was followed by the settling of two spheres placed in-line to study the different stages during settling for different initial configurations. A comprehensive set of data was generated to analyse three regimes identified as repulsion, transitional and attraction. Although a 3D LBM model was used, the force imposed between particles was based on a threshold for interparticle distance instead of the natural dynamics generated by the gravitational and hydrodynamic forces.

In Qiu (2015) a combined DEM-LBM-IBM was presented to assess the fluid flow around a cylinder and fluid flow through porous media. As an incipient validation work, the coupling proved the capabilities of the combined methodology; however, the porous media was made of a symmetrical array of cylinders fixed in the domain. For this type of configurations the DEM capabilities are not used since in both cases the cylinders remained fixed avoiding interparticle contacts. Han et al. (2007) combined LES with DEM-LBM-IBM to account for turbulent regimes incorporating a Smagorinsky parameter in the Boltzmann equation. The importance of this combined methodology lies in the fact that previous work carried out by different authors followed standard formulations in which only laminar fluids can be modelled with LBM. In this case the authors correctly argue that most practical applications are turbulent in nature involving higher Reynolds numbers. The authors explained the relationship between the relaxation parameter and numerical stability for simulations without turbulent model. For small values of the relaxation parameter (close to 0.5) the fluid became unstable without the turbulent model. Once they tested their model, a fluid flow with Re = 56000 was achieved. Additional numerical validation of their model would be necessary, but the first results obtained seemed to have given a significant step further in the use of LBM for high Reynolds number with the implementation of a turbulent model. More DEM-LBM coupling implementations in 3D using spheres can be found in Han & Cundall (2013), Mansouri et al. (2009) and Wang et al. (2017).

2.4. Summary

In computational simulations there exist two principal approaches known as *continuum* and *discrete* to model and represent FSI. In a continuum approach (Eulerian) the behaviour of individual particles is neglected and the entire structure is considered as a whole in the simulation, relying on the quality of the structural mesh. In contrast, a discrete approach (Lagrangian) permits to study individual particles; in this way the micromechanics of granular materials can be better studied from a meso-scale perspective. The overall behaviour of a system at a macroscopic level can still be represented with the discrete approach since the physics are still governed at a meso-scale level by interparticle interactions.

According to the main objective to achieve on this thesis, DEM was selected to study and represent discrete particles. DEM is a well stablished method that accurately describes the performance of granular material. In addition, DEM is based on physical laws described by simple equations that can be solved analytically, making easy the understanding of the methodology and its numerical implementation. The preferred DEM model to be used was the soft-sphere model. In this model multiple contacts are allowed at a single time step unlike the approach of one collision at a time used in the hard-sphere model.

In regards to fluid solvers, the majority of CFD techniques follow a top-down approach based on the discretisation of the macroscopic continuum Navier-Stokes equations. Although these methods have been used extensively to simulate FSI, re-meshing methods to account for moving boundaries immersed in a fluid might be expensive in computational terms. LBM has become popular as an alternative to traditional CFD solvers. Instead of calculating the pressure and shear stress along the solid boundary, LBM has been proven to be accurate in representing FSI by computing the momentum exchange between incoming and outgoing DDFs along the solid boundary. In this work LBM is preferred over traditional CFD methods since the behaviour of a fluid at a macroscopic level is considered not to be very sensitive to changes occurring at a mesoscopic level. In this way, the methodology considers the physics involved at a mesoscopic level in order to represent the averaged macroscopic behaviour. Furthermore, the same mesh used by DEM to represent solid particles is used as well by LBM, avoiding in this way remeshing and taking advantage of the inherent features of coupling DEM with LBM.

For the treatment of solid boundaries immersed in a fluid with LBM, the partially saturated cells method by Noble & Torczynski (1998) has been used by different authors in the literature. Known as well as the immersed boundary method, this technique does not require modification of the computational mesh. Instead, the body force term that represents the effect of having a solid boundary in the fluid is applied at the original locations of a set of boundary points. On the other hand, the momentum exchange method has been widely used by a number of researchers due to its inherent simplicity, ease to implement and robustness. In this case the curved boundary is replaced by a boundary that conforms to the computational mesh. As such, the original boundary is modified and the fluid-structure interaction takes place at the middle point of links crossing the boundary (links generated between fluid and solid nodes near the boundary). A common feature in both IBM and MEM is that the bounce-back rule is applied at the interface to account for the no-slip condition.

It is important to consider that more robust methodologies can be combined to accurately represent FSI systems. The author believes that simulations in two dimensions or those using spheres provide a good insight and first approach to study different phenomena. However, a large number of investigations have been carried out already and more complex systems should be investigated by extending previous studies. For instance, systems in 3D involving a large number of irregular geometries have not been deeply studied. The main reason behind this idea is that non-spherical geometries are more likely to be found in nature and in different processes such as mining engineering, sintering and coating, fluidized bed reactors, and mass transport of sands and soils. For this reason the author believes that modelling FSI systems using non-spherical geometries must be further explored to account the effects of particle interlocking and resistance to flow originated by the main physical features of irregular geometries.

The approach adopted in the present work to construct non-spherical geometries for DEM is based on the image digitisation process. Similar to 2D imaging by means of a collection of pixels (squares), a 3D particle might be represented by a collection of voxels (cubes) that when all put together form the desired geometry. The advantage of representing non-spherical particles with digital images becomes obvious when the particle is located in a regular mesh. Both DEM and LBM share the same mesh and for this reason no re-meshing or any other special treatment is necessary. In this way, particles in coupled DEM-LBM can move one cell at a time or a fraction of a cell, and

the fluid surrounding the particles is updated accordingly as a function of the new positions of every particle. The advantage of LBM over methodologies such as the finite element method lays on the fact that the continuous process of body-fitting-mesh regeneration is not necessary. It is known that curved-boundary particles will display a staircase-like boundary; however resolution might be improved as particle dimensions are increased. The process to generate digital geometries to represent particles in a DEM-LBM environment is by means of computational algorithms (for regular geometries) or computed tomography (for irregular geometries). X-ray microtomography was used by the author to obtain digital images of irregular geometries found in nature such as sand grains. Following this technique almost any particle shape found in nature can be captured and used for numerical simulations.

Finally, to present a condensed summary of the literature review covered in this chapter, the following table provides a quick overview of the relevant methodologies and main features to carry out numerical representations of fluid-structure interactions. It must be understood that adaptations and modifications to different coupling methodologies are application dependant. For instance the origin of LBM was precisely an evolution from LGCA. Methodologies have emerged and authors have chosen a combination of them to solve different problems. In more recent years research has focused to address numerical stability and computational efficiency.

Table 2-1 Summary of methodologies presented in the literature review

Solid solver	
Hard-sphere model	One overlap at a time allowed between particles
Soft-sphere model	Multiple overlaps allowed for every particle
Particle representation techniques	Sphero-polyhedron (or spherosimplices)
	Sphere-assembly (or composite particle, or multi-sphere)
	Superquadrics (or superquadratics, or superellipsoids)
	Digital images (pixels and voxels)
Fluid solver	
Traditional CFD: FVM, FEM	Continuum representation of fluid
	Calculates hydrodynamic force based on volume fraction
	Multiple particles contained in a single computational cell
Alternative CFD: LBM	Discrete representation of fluid by density distribution functions (DDF)
	Calculates hydrodynamic force along the solid boundary
	More than one computational cell occupied by a single solid particle
Coupling techniques	
Momentum Exchange Method (MEM)	Original boundary modified to conform to computational mesh
	Momentum exchange takes place halfway on links generated between fluid and solid nodes along the boundary
Extrapolation and interpolation methods	Based on LBB, original boundary is retained and calculations are carried out on the exact location on the link fraction. Additional fluid nodes are required to collect data for calculations
Immersed Boundary Method (IBM)	Original boundary location is retained
	A volume fraction parameter is included to account for cells sharing fluid and solid

3. Methodologies

Introduction

This chapter presents and describes the methodologies in which the present work is based. DEM and LBM are presented followed by the coupling technique details. A flow diagram is presented to visualise the logic of the coupling code implemented. In the last part the DigiPac software is introduced providing information of the relevant modules known as DigiDEM, DigiFlow and DigiUtility. Finally, a description of the methodology used for image digitisation with X-ray microtomography is included.

3.1. The distinct element method

DEM is a methodology originally developed to describe the movement and interactions of particles in two dimensions, specifically circular discs, using a spring-damper-slider contact model. Later on, the continuous effort of researchers resulted in an extended methodology for 3D modelling and the implementation of not only spherical particles but also the use of different geometries.

In a simulation environment involving a determined number of solid particles, multiple contact points are registered by means of algorithms based on theoretical contact mechanics. The traditional model is the spring-damper model in which the repulsive force between two particles coming into collision is described as an ideal spring with its spring constant as in Hooke's law.

$$F = -kx \tag{3-1}$$

F being the force in the opposite direction of the contact, k the spring constant, and x the distance the spring is compressed during a contact.

When there are no contacts between particles, they will follow Newton's law of inertia. This is, a particle at rest will remain at rest if no external force is applied on it; and a particle in motion would remain in that state unless an external force acts on it to modify its state. When particles are added to a computational DEM environment, two main tasks are executed. The first one is to perform a contact search using a contact detection algorithm. If no contact is detected, particles will continue at rest or in motion

according to Newton's first law. When contacts have been detected, the contact force calculation process starts. Subsequently, the corresponding particle acceleration, velocity and position parameters are updated for every particle every time step. Thenceforth, the cycle starts again by searching for further contacts between the particles or carrying out the corresponding updates if contacts are still taking place.

The translational motion of a particle is calculated using Newton's second law of motion (3-2). The total force acting on a particle is the sum of different forces applied on it. For instance, a common case in which a particle might be involved is to be subject to a contact force plus the gravitational force plus any other external force applied on the particle. If many external forces are applied, they all can be summed up and presented as one single net external force. Having calculated the total force on the particle, the result is equated to the particle's mass m_p multiplied by the particle's translational acceleration a_p.

$$F_{contact} + F_{gravity} + F_{external} = m_p \cdot a_p \tag{3-2}$$

The distinct element method is an existing module part of the DigiPac package known as DigiDEM. In DigiDEM particles are considered as discrete elements that displace following the Newton's laws of motion and they interact with each other at contact points. In this DEM version when a contact between two particles takes place, a small overlap volume between them is formed. This overlap is a key parameter used to calculate the contact force in a collision by considering each particle as a spring. Although this does not happen in reality, the overlap is analogous to an elastic deformation that each particle would exhibit during collision. Calculating the contact force from particles overlap is similar to the soft-sphere model calculation but in the present work it is adapted for non-spherical particles based on the definition of the Young's modulus. The DEM version used in the present work assumes the presence of a small and elastic deformation when particles interact with each other or with a container wall; neither plastic deformation nor breakage is considered. For multi-particle systems, e.g. a particle packing process under normal conditions, such assumptions result in convenient modelling since the whole assembly of particles is not very sensitive to the precise values of individual interacting forces. However, it is considered that the geometry of the particles would be a property having a larger effect in the final assembly of particles.

The Young's modulus E is a mechanical property of linear elastic materials used to measure the stiffness of solid materials. It is a way to know how much a solid object will stretch according to a stress applied to the object. The definition of the Young's modulus is the expression relating stress (proportional to load) and strain (proportional to deformation).

$$E = \frac{\sigma}{\varepsilon} \Rightarrow \frac{stress}{strain}\left[\frac{N}{m^2}\right] \tag{3-3}$$

where the stress is defined as $\sigma = F/A$, being F the contact force and A the contact area where force is applied. Strain is defined as $\varepsilon = \Delta L/L$, being ΔL the overlap depth and L the particle size.

In DigiDEM small overlaps are essential for evaluation of contact forces. A pure Hertzian model only describes normal contact between spheres and assumes that there is no friction between the solid objects in contact. Di Maio & Di Renzo (2005) have provided evidence of poor performance of the Hertz-Mindlin model simulating small and large impact angles. Considering the relevance of irregular geometries in this work, such model is not convenient. Furthermore, the consideration of additional parameters such as restitution and friction coefficient, adhesive or repulsive force, and quantification of damping force, makes DigiDEM a more robust model.

Figure 3-1 provides an illustration of a head-to-head contact between two discs. It can be observed that when two particles collide a small overlap is allowed between them in order to calculate the contact force. The damper-spring diagram is used to model the collision; for instance, particle *j* works as a damper and a spring as seen from particle *i* perspective.

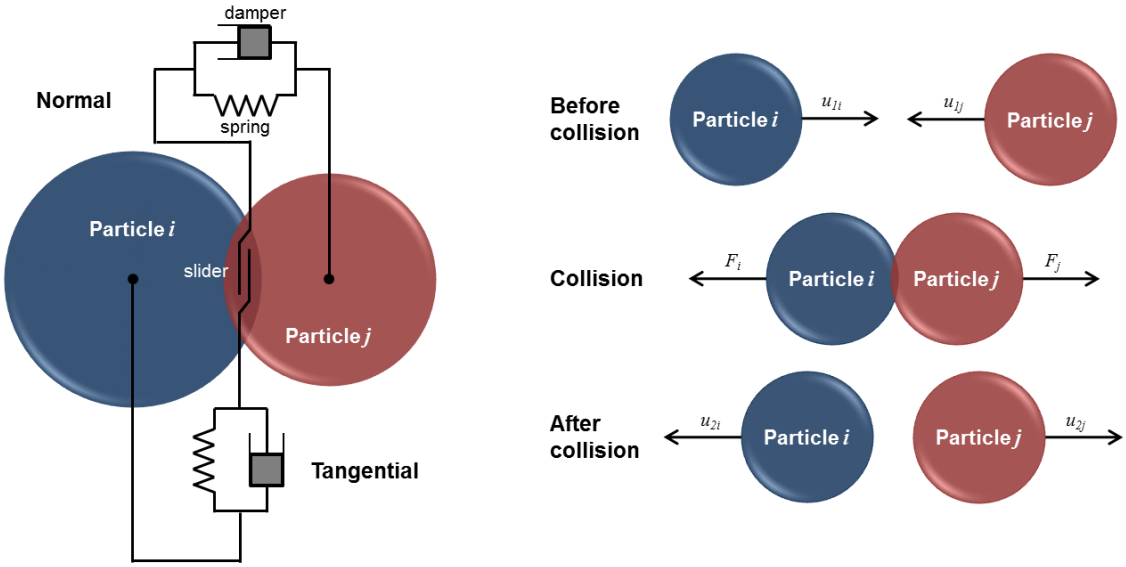

Figure 3-1 DEM spring-damper-slider model with particles overlap

From the illustration above particle i will feel an opposite force during collision which originates from 'spring' particle j. Energy loss (if any) is handled by the 'damper' part of particle j, which depends on the restitution coefficient parameter. If particle i is rotating with an angular velocity during collision, then the slider will handle this using the friction coefficient parameter. In a similar manner, particle i will work as a damper-spring model for particle j.

The following sections present the way in which the contact force is calculated during collision, consisting of two parts known as normal force and shear force. The time step calculation is an essential parameter to consider and its calculation is presented as well followed by the treatment of digital particles in *DigiDEM*.

Normal force - The normal spring contact force for a given E is calculated as:

$$F_{n-s} = \left(\frac{EA}{L}\right)\Delta L \tag{3-4}$$

It should be noticed that the overlap volume is the product of overlap depth times the contact area.

The damping force is also present in this model and it opposes to movement precisely acting as a damper. The normal damping contact force depends on the restitution coefficient and is calculated as:

$$F_{n-d} = -k_{n-d} \cdot u_{n-rel} \tag{3-5}$$

where k_{n-d} is the normal damping constant with a minus sign to indicate opposition to movement, and u_{n-rel} is the normal relative velocity between the two colliding particles. For this equation the normal damping constant is obtained from:

$$k_{n-d} = \left(2\sqrt{m \cdot kn}\right)\left(\frac{-\ln(c_r)}{\sqrt{\pi^2 + (\ln(c_r))^2}}\right) \tag{3-6}$$

where c_r is the restitution coefficient (between 0 and 1); m is the mass of the particle in kg, and:

$$k_n = \frac{EA}{L} \tag{3-7}$$

When c_r is equal to 1, an elastic contact takes place and there is no damping; if its value is 0 then all the energy is dissipated and there is no bouncing.

Having calculated the two components of a normal contact, the total force is calculated as the addition of both as $F_{tot-n} = F_{n-s} + F_{n-d}$.

When two particles are in contact, both share some data such as overlap volume and contact area. For two particles i and j in a normal collision, the contact force will have the same magnitude but opposite direction as $F_i = F_j$.

To avoid large overlaps yielding very high repulsive forces, the calculations in *DigiDEM* are carried out allowing a maximum overlap volume equal to a 10% volume of the smallest object involved in the collision.

Since the total contact force is an output and the particle mass m_p is known, a_p can be easily calculated from equation (3-2) by simply solving for this variable. The new velocity and position of the particle after contact are found by carrying out the corresponding update over time with the velocity Verlet algorithm. In the following set of equations 3-8 and 3-9, $u(t)$ is the velocity in the previous time step, and $u(t+\Delta t)$ is the velocity in the current time step (same case for acceleration). In equation 3-9 $x(t)$ is the

position of the particle in the previous time step, and $x(t+\Delta t)$ is the new position in the current time step.

$$u(t+\Delta t) = u(t) + \Delta t\left(\frac{a(t)+a(t+\Delta t)}{2}\right) \tag{3-8}$$

$$x(t+\Delta t) = x(t) + u(t)\Delta t + \left(\frac{a(t)\Delta t^2}{2}\right) \tag{3-9}$$

It is important to highlight that the calculations shown in the previous equations are carried out only if a contact is detected; otherwise particles translate and rotate with constant acceleration if initial conditions were given. Particles might also be subject to gravitational force and/or any other external forces imposed.

Shear force - The above description is for a normal contact, but when shear is present, the total shear contact force must be calculated. The shear direction is obtained from the relative velocity vector and contact vector between a pair of particles involved in a collision. Then the shear relative velocity is obtained as the dot product of the shear direction vector and the relative velocity vector.

The shear spring force has associated a constant parameter k_s calculated as:

$$k_s = \frac{k_n}{2(1+\upsilon)} \tag{3-10}$$

where k_n is the parameter previously calculated in equation 3-7, and υ is the Poisson's ratio, a parameter that relates the transversal strain (expansion) with the axial strain (compression) for a particle being stretched elastically. Then, the shear spring force is calculated as:

$$F_{s-s} = -k_s \cdot \Delta L_s \tag{3-11}$$

where ΔL_s is the shear displacement. In a similar way as done for the normal components, the shear damping force is calculated using the shear relative velocity:

$$F_{s-d} = -k_{s-d} \cdot u_{s-rel} \tag{3-12}$$

where:

$$k_{s-d} = 0.1 k_{n-d} \tag{3-13}$$

When the user is configuring a new simulation, the Young's modulus E, Poisson's ratio υ, and restitution coefficient c_r must be given as input.

In the end, the total shear force is the summation of the shear spring force and shear damping force components $F_{tot-s} = F_{s-s} + F_{s-d}$.

To convert from DEM to physical units the conversion factor is the lattice length Δx for both force and velocity. This lattice length is the same used in both DEM and LBM solvers.

Time step - Selecting the appropriate time step for simulations allows the code to register the corresponding velocities and accelerations of every particle. A small value is preferred in DEM to avoid losing data when particles travel with high velocities, potentially displacing more than one cell per time step. With the appropriate time step configured particles' parameters are not expected to change significantly in two consecutive time steps. In this way particles are only affected by forces applied on them by immediate neighbours, and it is ensured that disturbances do not propagate further. A small time step also would help to carry out accurate simulations and enable the code to capture small overlaps and sudden particle velocity changes.

To find the optimal simulation time step a parameter known as Rayleigh time step is used to ensure numerical stability and retention of particles acquiring high velocities during the simulation.

The Rayleigh time step in DEM is indicated as Δt_{DEM}. To find its value some physical properties of the particles involved in a collision are needed. Particle dimensions, density, and E are used in the calculation of the maximum time step allowed:

$$\Delta t_{DEM} = \frac{0.5\left(X_p + Y_p + Z_p\right)}{\sqrt{E/\rho_p}} \tag{3-14}$$

Where X, Y and Z are the dimensions of the particle in question and ρ_p is the particle's density. If the properties of the colliding particles are different, the maximum time step recommended would correspond to the smallest value obtained.

Common time steps values in DEM are on the order of 10^{-5} s, but in some cases for small particles of order of microns, the time step should be reduced to 10^{-6} s or even 10^{-7} s. Such a small time step for a simulation of a large number of particles ($\approx 10^5$) may require generous computational capabilities. A simulations involving a few thousands of particles, e.g. the packing process of particles plus a settling period of time, may take less than 30 minutes in an average computer with 4 CPUs and 8 GB in RAM with a 2.70 GHz processor.

Particle treatment - In DigiDEM all the particles are treated as a collection of voxels (cubes). Geometries are represented more like a digitised image of a particle; for this reason the particle's edges look more like a staircase boundary (see Figure 3-2).

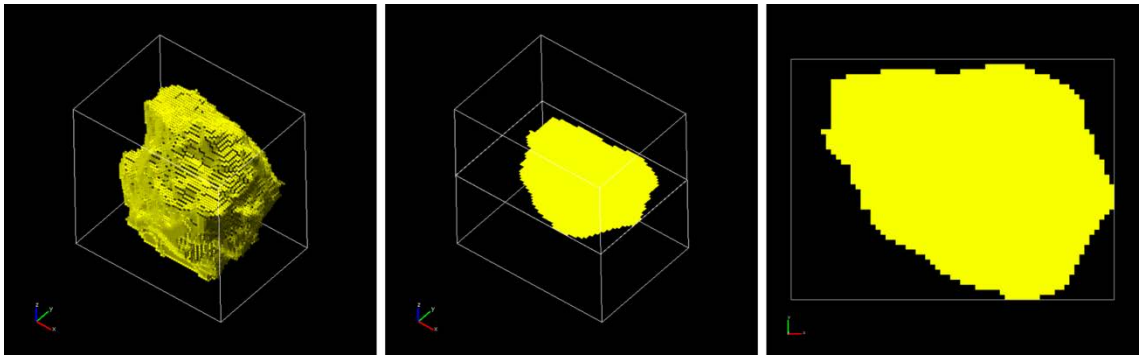

Figure 3-2 Image of a digitised particle: left 3D view; middle and right 2D view

The digital approach used in DigiDEM makes simpler and faster the collision and overlap detection. A 2D regular mesh contains cells known as *pixels*; a 3D regular mesh contains cells known as *voxels*. When working with voxels the edge length or cell width is always known because particles are placed in a regular mesh having cells of the same size. In this way the computational domain where particles interact is a regular mesh in which translation and rotation of particles is carried out as a relocation of voxels.

As shown in Figure 3-2, all particles have a bounding box that contains them. It is not physically represented in the mesh but it works as a reference to find the position of particles in the entire domain. This box has three lengths (X,Y,Z) defining the particle

size in those three directions. For instance, a sphere with diameter d_p = 20 voxels would be contained in a cubic bounding box of length = 20 voxels. The way in which computational dimensions are translated into physical dimensions is by knowing the value given to the lattice width. Analogous to the scale on a geographical map, if one lattice represents 1 mm then the sphere has a diameter d_p = 20 mm.

When particles collide the maximum overlap allowed between them is controlled by the smallest particle involved in the collision. A 10% volume of the smallest particle is equal to the maximum overlap allowed. For this reason it is important not to have very small particles in DigiDEM. For instance, a single particle may have 6 contacts at a time (one per face of the bounding box). A particle of size (5, 5, 5) voxels would see its volume dramatically reduced if it had 6 contacts in one instant. For this reason it is advisable to use particles no smaller than 10 voxels in any direction.

Working with digital particles in a DEM environment has not been widely studied. In this work two main advantages of working with particles made of voxels have been detected:

- regular and complex particle geometries can be handled without much effort since they are represented as a collection of voxels that conform to the computational mesh
- the required computational resources, such as memory and CPU time, do not increase significantly when dealing with complex digitised geometries

DEM is fairly deemed as a highly intensive algorithm. The main reason is that as the number of particles in the domain increases, the particle-contact detection procedure increases linearly. If one seeks to obtain good accuracy in the simulation, an appropriate (and probably small) time step should be chosen to avoid losing relevant data every iteration and to ensure numerical stability and smooth particles motion throughout the whole simulation. DigiDEM produces finer results due to the finer definition of the time steps which permits the particle to move in different positions inside a single computational cell; on the other hand, this represents an inherent impact in time consumption while running a simulation. An appropriate balance between number of particles and computational resources must be found. It also should be considered the application for which DigiDEM is being used; running a simulation of a few hundreds of particles, even a couple of thousands in a regular computer would not demand many resources and the desired behaviour might be observed fairly quickly.

3.2. The lattice Boltzmann method

After almost 30 years after its first appearance in 1988, LBM is now a widely used methodology to represent the fluid dynamics of particularly mesoscopic systems. Typically near-incompressible fluid flow problems are suitable for LBM, such as flow through porous media and multi-component fluids in microstructures.

LBM evolved from the lattice gas model to simulate fluid flows in the 70's. This model was based on a Boolean approach applied to particles on a regular lattice, in which only two states were possible for every particle, a particle with non-zero velocity or a particle at rest. The motion of every particle was influenced by the self-state and that one of neighbouring particles; particle motion was controlled by a propagation and collision process taking place every time step. LGCA seemed to be a revolutionary method to simulate fluid flows, however it soon revealed some problems like its inherent statistical noise and its complex collision rule. The evolution of LGCA to solve these problems resulted in LBM which in the beginning pre-averaged the noise present in LGCA. Further developments of LBM have addressed different issues throughout the years. Unlike traditional CFD models based on the direct discretisation of the Navier-Stokes equations, LBM has a different approach in which the evolution of the fluid flow stems from the dynamics of density distribution functions deemed as particle populations at a mesoscopic level. Although LBM is derived at this level it is straightforward to recover the parameters for solutions of the macroscopic Navier-Stokes equations.

The fundamental concepts behind LBM are those central to fluid mechanics, conservation of mass and momentum. The former implies that there is no mass transfer in the system; mass is not loss or created. In this way the initial amount of mass in the initial system must be conserved. LBM deals with nearly-incompressible flows, so a small variation of mass is expected but within certain limits to comply with the mass conservation principle. Momentum conservation is related to mass since momentum p is defined as:

$$p = mu \tag{3-15}$$

where m is mass and u velocity. In a collision where two particles are in motion and subsequently collide, conservation of momentum implies that after collision the total momentum of the two particles is the same as their initial momentum (assuming that no

momentum is lost in any form of energy). From the collision it is derived that momentum is related to force, which also involves particle's mass as in Newton's second law of motion.

Having in mind these basic concepts, the basic idea of Boltzmann's work was that a gas is composed of particles with mass, velocity and momentum. These particles interact following the rules of classical mechanics. If the gas is discretised it is possible to imagine having a large number of particles, and then a statistical treatment would be useful and appropriate to describe the system dynamics, namely propagation and collision. The complete form of the Boltzmann equation is a complicated non-linear integral differential equation, but with recent methods the equation can be numerically solved. As a result, LBM simplifies the initial basic idea to a number of discrete spatial positions confined to nodes on a mesh or lattice. Particles momentum is reduced to a set of velocities in different directions for a single particle mass. The model D2Q9 is introduced below in Figure 3-3 to present graphically the LBM idea. The D2Q9 model means that the mesh is a 2D lattice and that the DDFs may have any of the 9 possible velocities. Although this model is not used in this thesis, its representation is used at this stage only for illustration purposes since it is easier to include all the vectors involved in the lattice and explain from the image.

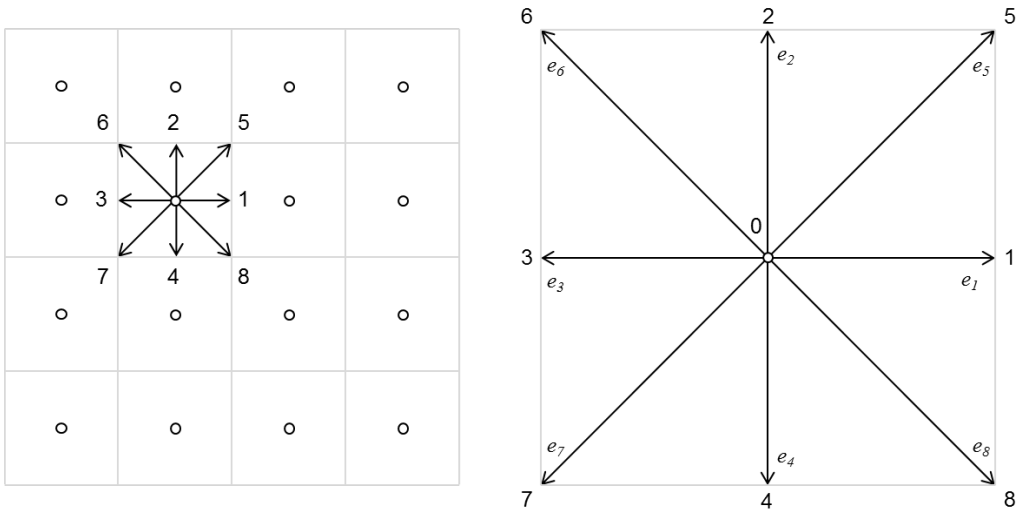

Figure 3-3 LBM 2D lattice representation showing the 9 DDFs possible velocities

In Figure 3-3 the 2D lattice representation shows the set of velocities e_i in which the sub index i = 0, 1,…, 8 indicates the velocity vector. The DDF is represented by a particle in the centre of the lattice, known as a fluid node or fluid site, and such particle

is at rest when e_i = 0. It is common practice to use a particle mass of 1 for all the fluid sites, in this way all the particles' velocities and momenta are always equivalent in LBM units. The length of the lattice is known as lattice unit (LU) represented by Δx_{LBM} and is usually taken as 1. This value is adopted because it is very convenient at the moment of defining the set of velocities, where e_1, e_2, e_3, e_4 are equal to 1 LU/s, and the diagonal velocities e_5, e_6, e_7, e_8 are equal to $\sqrt{2}$ LU/s. The velocity of e_0 is 0.

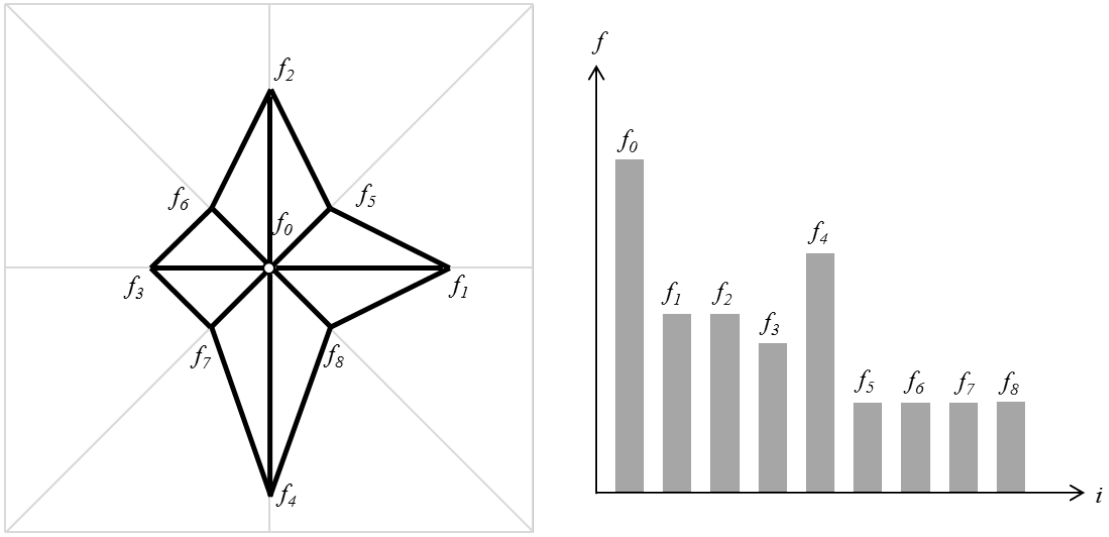

Figure 3-4 Interpretation of the DDFs in a 2D lattice in LBM
(reproduced from Sukop & Thorne Jr. 2007)

The discrete DDFs are 9 in total for the 2D model corresponding to the number of velocities (see Figure 3-4). These DDFs represent the probability of the particle to propagate to a neighbouring lattice with one of the 8 possible velocities or to remain at rest. In this way LBM reduces the possible particle positions and momenta to a few confined nodes in the lattice in the discretised time.

Having introduced the set of velocities and interpretation of DDFs in the 2DQ9 model, now the D3Q19 model is presented graphically in Figure 3-5. This model is the one used in the present work for fluid flow simulations and the one to couple with DEM. In a similar way as in the 2D model, the D3Q19 model is represented by a 3D lattice with cubes having the same lattice length of 1 LU but in this case with a set of 19 possible velocities.

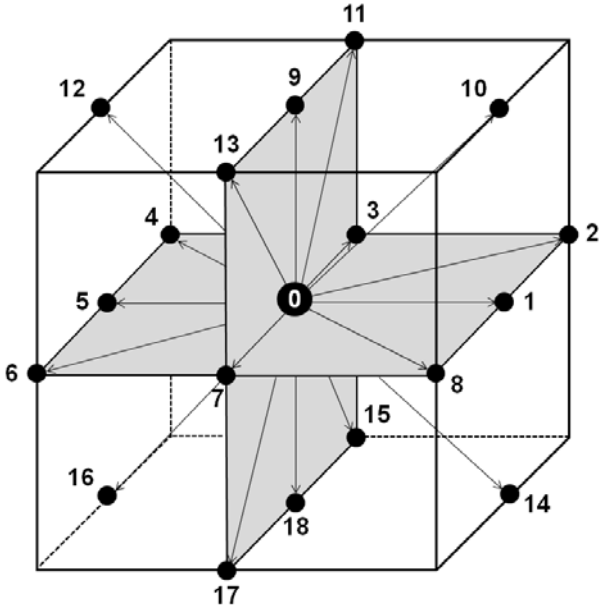

Figure 3-5 LBM D3Q19 mode showing the 19 velocity vectors in a cubic lattice

The time- and space-averaged propagation at each fluid node is modelled with the corresponding DDF. The DDFs define the density and velocity at each lattice node and indicate the number of particles at a determined time t that are located within a physical space in a particular position x and having a particular velocity e. The DDFs are allowed to move with discrete velocities from one cell to a neighbouring one in any of the allowed velocity vectors, collide with other particles, or remain in the centre of the cell with zero velocity. The continuous propagation of fluid particles every time step follows simple propagation and collision rules designed to conserve mass and momentum.

The BGK approximation to solve the Boltzmann equation is the most popular procedure to replace the complexity of the full collision term with a linearised BGK single relaxation time model. In this way, the evolution of the DDFs is described by the following equation know as LBM-BGK with SRT:

$$f_i\left(x+e_i, t+\Delta t_{LBM}\right) - f_i\left(x,t\right) = -\frac{1}{\tau}\left[f_i\left(x,t\right) - f_i^{eq}\left(x,t\right)\right] \qquad (3\text{-}16)$$

where f_i represents the DDFs; e_i is the set of velocities; Δt_{LBM} is the time interval or time step; τ is a parameter known as single relaxation time that indicates the DDFs relaxation rate to regulate the functions during collision to redistribute the DDFs meeting at each cell; f_i^{eq} is the equilibrium density distribution function. The left-hand

side in (3-16) corresponds to the streaming or propagation stage, whereas the right-hand side is used to model the collision stage in which all the DDFs relax towards local equilibrium at a single rate.

In the D3Q19 model one of the possible vectors in the propagation stage is i = 0, meaning that a portion of the DDF remains at rest in the centre of the cell with a velocity vector [0, 0, 0] in XYZ coordinates. The 19 velocity vectors in the model are presented in every column in the following table, corresponding to the velocity vectors shown in Figure 3-5.

Table 3-1 Velocity vectors in the D3Q19 model shown in Figure 3-5

i=0	*i=1*	*i=2*	*i=3*	*i=4*	*i=5*	*i=6*	*i=7*	*i=8*	*i=9*	*i=10*	*i=11*	*i=12*	*i=13*	*i=14*	*i=15*	*i=16*	*i=17*	*i=18*
0	1	1	0	-1	-1	-1	0	1	0	1	0	-1	0	1	0	-1	0	0
0	0	-1	-1	-1	0	1	1	1	0	0	-1	0	1	0	-1	0	1	0
0	0	0	0	0	0	0	0	0	1	1	1	1	1	-1	-1	-1	-1	-1

The equilibrium distribution functions are defined according to the velocity vectors. In this way, there are three different equations corresponding to the zero-velocity vector, the orthogonal velocity vectors, and the diagonal velocity vectors:

$$f_0^{eq} = \frac{\rho_f}{3}\left[1 - \frac{3}{2}u_f^2\right] \tag{3-17}$$

$$f_{1,3,5,7,9,18}^{eq} = \frac{\rho_f}{18}\left[1 + 3\left(\vec{e}_i \cdot \vec{u}_f\right) + \frac{9}{2}\left(\vec{e}_i \cdot \vec{u}_f\right)^2 - \frac{3}{2}u_f^2\right] \tag{3-18}$$

$$f_{2,4,6,8,10-17}^{eq} = \frac{\rho_f}{36}\left[1 + 3\left(\vec{e}_i \cdot \vec{u}_f\right) + \frac{9}{2}\left(\vec{e}_i \cdot \vec{u}_f\right)^2 - \frac{3}{2}u_f^2\right] \tag{3-19}$$

The macroscopic parameters of the fluid such as density ρ_f, velocity u_f and pressure p are recovered from the following set of equations. They can be considered as the transition step to go from the discrete mesoscopic LBM velocities to the continuum macroscopic velocities representing the motion of the fluid.

$$\rho_f = \sum_{i=0}^{18} f_i \tag{3-20}$$

$$u_f = \frac{1}{\rho_f}\sum_{i=0}^{18} f_i e_i \tag{3-21}$$

$$p = c_s^2 \rho_f \tag{3-22}$$

In (3-22) the parameter c_s is the speed of sound of the cell defined as $c_s = c/\sqrt{3}$, where c is the cell speed obtained from $c = \Delta x / \Delta t_{LBM}$.

Fluid flows are characterised by a dimensionless parameter known as Reynolds number, which is classified in three main regimes called laminar, transitional and turbulent. The way in which a real flow characterised by a determined Re is represented in the LBM environment is precisely using such parameter since it is dimensionless, meaning that in both physical and computational systems its value must be the same. For a fluid flow, Re is calculated using the following equation:

$$\mathrm{Re} = \frac{u_f d_p}{\nu_f} \tag{3-23}$$

The viscosity in LBM mainly depends on the relaxation parameter:

$$\nu_{LBM} = \frac{\tau - 0.5}{3} \tag{3-24}$$

Another parameter depending on the selection of τ is the time step:

$$\Delta t_{LBM} = (\tau - 0.5)\left(\Delta x^2 / 3\nu_{phy}\right) \tag{3-25}$$

A criterion that must be satisfied is that the selection of τ must ensure *Ma* ≤ 0.1, where *Ma* is the Mach number in the fluid. The highest *Ma* achievable is obtained considering the maximum fluid velocity in $Ma_{\max} = u_{f_{\max}} / c_s$. In Zou & He (1997) and Sukop & Thorne Jr. (2007) it is discussed the optimal range to select a relaxation parameter to avoid numerical instabilities. It has been found that the value must fall between $0.5 < \tau < 1.25$, being 1 a preferred value and values close to 0.5 for high Re. For this reason, the selection of the parameters should be done considering the expected Re value for

the fluid in the simulation; as long as Re is maintained, the other parameters may be modified in order to obtain a solution.

Boundary conditions - A common implementation in LBM is the bounce back boundary condition with a single relaxation parameter to specify velocity or pressure boundaries. To carry out the implementation of boundary conditions at stationary walls, the DDFs at domain boundaries should be the functions providing the desired velocity or pressure. The no-slip BC is modelled through the BB technique which dictates that the incoming DDF towards a solid boundary is reflected back to the fluid domain along the direction it came from. The BB technique ensures conservation of mass and momentum and guarantees that no tangential velocity is present at the boundary. Let us consider the following figure to explain the process.

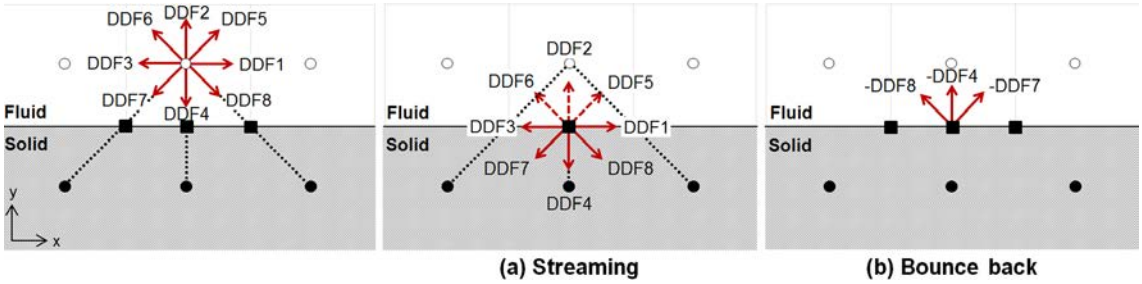

Figure 3-6 LBM 2D representation for boundary condition on a stationary solid wall

After streaming DDFs 4, 7 and 8 are known since they are coming from an internal fluid site, but DDFs 2, 5 and 6 are unknown and must be determined. DDFs 0, 1 and 3 are not affected in this case, attaining in this way the no-slip BC along the solid boundary.

Observing the unknown DDFs, 6 and 5 have velocity components in X and Y directions; DDF2 has velocity component only in Y direction, then:

$$f_5 - f_6 = \rho u_x - \left(f_1 - f_3 - f_7 + f_8\right) \tag{3-26}$$

$$f_2 + f_5 + f_6 = \rho u_y + \left(f_4 + f_7 + f_8\right) \tag{3-27}$$

$$f_2 + f_5 + f_6 = \rho - \left(f_0 + f_1 + f_3 + f_4 + f_7 + f_8\right) \tag{3-28}$$

Then, equating (3-27) and (3-28) yields:

$$\rho = \frac{f_0 + f_1 + f_3 + 2(f_4 + f_7 + f_8)}{1 - u_y} \tag{3-29}$$

The bounce-back rule applies directly to DDF2 from DDF4, so it is determined as:

$$f_2 - f_2^{eq} = f_4 - f_4^{eq} \tag{3-30}$$

Having found DDF2, DDF5 and DDF6 can be found:

$$f_2 = f_4 + \frac{2}{3}\rho u_y \tag{3-31}$$

$$f_5 = f_7 - \frac{(f_1 - f_3)}{2} + \frac{\rho u_x}{2} + \frac{\rho u_y}{6} \tag{3-32}$$

$$f_6 = f_8 + \frac{(f_1 - f_3)}{2} - \frac{\rho u_x}{2} + \frac{\rho u_y}{6} \tag{3-33}$$

For pressure (or density) boundary condition, let us consider the following image to exemplify the procedure, which follows a similar analysis as the one presented previously for BC on solid walls.

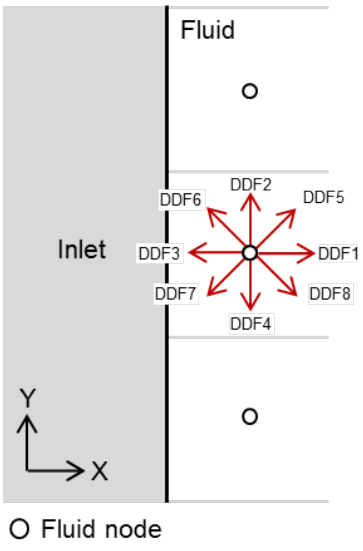

Figure 3-7 LBM 2D representation for inlet boundary condition

Assuming that pressure is specified at the boundary along Y direction as $\rho = \rho_{inlet}$ and u_y is set to zero, after streaming the data available from the fluid site are DDFs 2, 3, 4, 6 and 7; DDFs 1, 5 and 8 are unknown as well as u_x.

$$f_1 + f_5 + f_8 = \rho_{inlet} - \left(f_0 + f_2 + f_3 + f_4 + f_6 + f_7\right) \tag{3-34}$$

$$f_1 + f_5 + f_8 = \rho_{inlet} u_x + \left(f_3 + f_6 + f_7\right) \tag{3-35}$$

$$f_5 - f_8 = -f_2 + f_4 - f_6 + f_7 \tag{3-36}$$

With equations 3-34 and 3-35 the velocity is found:

$$u_x = 1 - \frac{f_0 + f_2 + f_4 + 2\left(f_3 + f_6 + f_7\right)}{\rho_{inlet}} \tag{3-37}$$

The BB rule can be applied directly to DDF3:

$$f_1 - f_1^{eq} = f_3 - f_3^{eq} \tag{3-38}$$

And now the DDFs can be found:

$$f_1 = f_3 + \frac{2}{3}\rho_{inlet} u_x \tag{3-39}$$

$$f_5 = f_7 - \frac{\left(f_2 - f_4\right)}{2} + \frac{\rho_{inlet} u_x}{6} \tag{3-40}$$

$$f_8 = f_6 + \frac{\left(f_2 - f_4\right)}{2} + \frac{\rho_{inlet} u_x}{6} \tag{3-41}$$

For fluid nodes located at the corner, i.e. adjacent to two perpendicular domain boundaries, the procedure is as follows. Taking as reference the bottom site in Figure 3-7, DDFs 3, 4 and 7 are known, u_x = u_y = 0, and DDFs 1, 2, 5, 6 and 8 are unknown. The BB rule can be applied directly so $f_1 = -f_3$, $f_2 = -f_4$ and $f_5 = -f_7$; substituting this in (3-34) and (3-35):

$$f_6 = f_8 = \frac{\rho_{inlet} - (f_0 + f_1 + f_2 + f_3 + f_4 + f_5 + f_7)}{2} \quad (3\text{-}42)$$

A similar procedure is followed for locations in the corners of the domain boundaries. The velocity BC at the inlet is handled in a similar manner as pressure.

The implementation in a D3Q19 model for flow in X direction is as follows. Consider the image in Figure 3-8 in which the velocity vectors (as presented in Figure 3-5) are displayed in 2D projections.

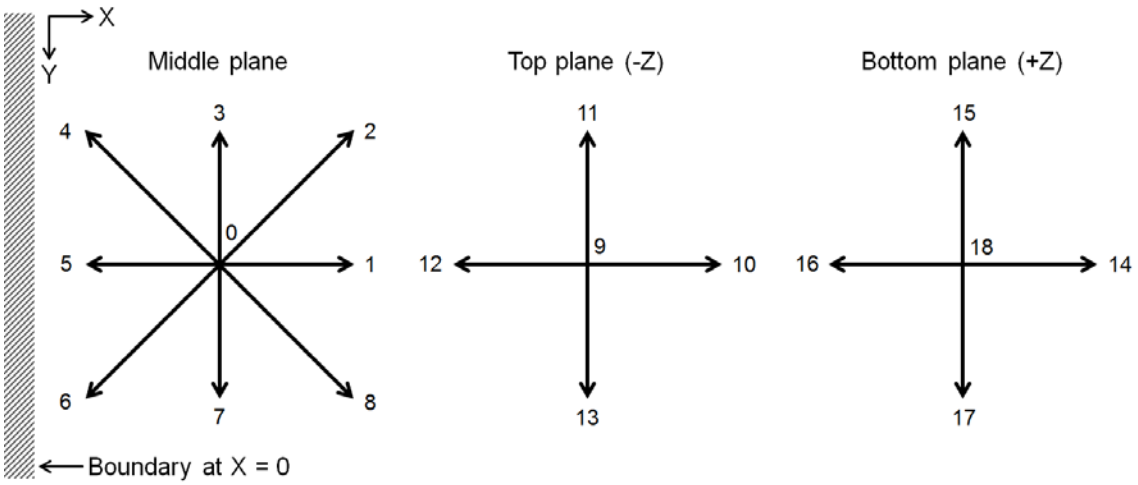

Figure 3-8 Middle, top and bottom planes displaying velocity vectors in D3Q19 model

The idea is to have DDFs at domain boundaries giving the desired pressure or velocity. Considering a site at boundary X = 0 as reference, during streaming DDFs 4, 5, 6, 12 and 16 come from an internal fluid site and hence have known values. On the other hand, DDFs 1, 2, 8, 10 and 14 are unknown and need to be determined to meet the specified boundary condition. In this particular case DDFs 0, 3, 7, 9, 11, 13, 15, 17 and 18 are not affected by boundary condition along X. From (3-21) for i's of vectors with non-zero fluid velocity in +X direction:

$$\rho u_x = \sum f_i e_i \quad (3\text{-}43)$$

Since f_i can be replaced by expressions with Q, a system of 4 equations with 4 unknowns is obtained (Q_x , Q_y, Q_z and u_x).

$$\rho = \left(f_0 + f_3 + f_4 + f_5 + f_6 + f_7 + f_9 + f_{11} + f_{12} + f_{13} + f_{15} + f_{16} + f_{17} + f_{18}\right) + \left(f_1^{eq} + \frac{Q_x}{18}\right) + \left(f_2^{eq} + \frac{Q_x}{36} - \frac{Q_y}{36}\right) + \left(f_8^{eq} + \frac{Q_x}{36} + \frac{Q_y}{36}\right) + \left(f_{10}^{eq} + \frac{Q_x}{36} - \frac{Q_z}{36}\right) + \left(f_{14}^{eq} + \frac{Q_x}{36} + \frac{Q_z}{36}\right)$$

Reducing:

$$\rho = \left(f_0 + f_3 + f_4 + f_5 + f_6 + f_7 + f_9 + f_{11} + f_{12} + f_{13} + f_{15} + f_{16} + f_{17} + f_{18}\right) + \left(f_1^{eq} + f_2^{eq} + f_8^{eq} + f_{10}^{eq} + f_{14}^{eq}\right) + \left(\frac{Q_x}{6}\right)$$

Then, for the DDFs involved having velocity component in +X direction:

$$\rho u_x = \left(f_1^{eq} + f_2^{eq} + f_8^{eq} + f_{10}^{eq} + f_{14}^{eq}\right) + \left(\frac{Q_x}{6}\right) - \left(f_4 + f_5 + f_6 + f_{12} + f_{16}\right) \tag{3-44}$$

And solving for Q_x:

$$Q_x = 6\left[\rho u_x + \left(f_4 + f_5 + f_6 + f_{12} + f_{16}\right) - \left(f_1^{eq} + f_2^{eq} + f_8^{eq} + f_{10}^{eq} + f_{14}^{eq}\right)\right] \tag{3-45}$$

In a similar way for Q_y and Q_z with the corresponding DDFs:

$$\rho u_y = \sum f_i e_i = 0 \tag{3-46}$$

$$Q_y = 18\left[\left(f_2^{eq} - f_8^{eq}\right) + \left(f_3 + f_4 + f_{11} + f_{15}\right) - \left(f_6 + f_7 + f_{13} + f_{17}\right)\right] \tag{3-47}$$

$$\rho u_z = \sum f_i e_i = 0 \tag{3-48}$$

$$Q_z = 18\left[\left(f_{10}^{eq} - f_{14}^{eq}\right) + \left(f_9 + f_{11} + f_{12} + f_{13}\right) - \left(f_{15} + f_{16} + f_{17} + f_{18}\right)\right] \tag{3-49}$$

Now, for the unknown DDFs in +X direction the equilibrium DDFs from the respective (3-18) for DDF1, and (3-19) for DDFs 2, 8, 10 and 14, are:

$$f_1^{eq} = \frac{\rho}{18}\left[1 + 3u_x + 3u_x^2\right] \tag{3-50}$$

$$f_{2,8,10,14}^{eq} = \frac{\rho}{36}\left[1 + 3u_x + 3u_x^2\right] \Rightarrow \frac{1}{2} f_1^{eq} \tag{3-51}$$

Finally the unknown DDFs in +X direction can be calculated from the following set of equations:

$$f_1 = f_1^{eq} + \frac{Q_x}{18}$$

$$f_2 = f_2^{eq} + \frac{Q_x}{36} - \frac{Q_y}{36}$$

$$f_8 = f_8^{eq} + \frac{Q_x}{36} + \frac{Q_y}{36} \tag{3-52}$$

$$f_{10} = f_{10}^{eq} + \frac{Q_x}{36} - \frac{Q_z}{36}$$

$$f_{14} = f_{14}^{eq} + \frac{Q_x}{36} + \frac{Q_z}{36}$$

For the other boundaries in -X, +Y, -Y, +Z and -Z a similar approach is followed to find the unknown DDFs.

For cases in which a fluid is not confined to a closed domain surrounded by solid walls, the fluid boundary is treated in a different way since an artificial bounding of the domain should be defined. In computational simulations is common to consider periodic boundary conditions (PBC) to represent a much larger domain to avoid long execution times and focus on regions relevant to study.

In LBM different BC can be implemented (Izquierdo et al. 2009). The present work includes PBC and outflow boundary or virtual boundary condition (VBC). For PBC DDFs reaching the boundary and going out re-enter the domain on the opposite side along its corresponding direction. For instance, in Figure 3-9 on the left-hand side, two fluid sites *A* and *B* are located at opposite boundaries along X direction. The arrows indicate the DDFs interacting in both sites; in this way the DDFs streaming out from *B* will interact with the corresponding DDFs in *A* (unlike BB previously presented on

stationary walls in which DDFs are reflected back). PBC are declared in pairs; in a cubic domain this would be inlet and outlet, and/or top and bottom, and/or left and right.

VBC is a case applied only in the direction of the flow. In this case the DDFs streaming out of the domain are simply discarded and do not re-enter or interact with the opposite boundary. Figure 3-9 shows the difference between PBC and VBC with a 2D lattice having the fluid inlet at $X = 0$ and the outlet at $X = n$. In PBC the DDFs streaming out from *A* (inlet) are taken into account to update the corresponding DDFs in cell *B* located on the opposite side (outlet), and vice versa from *B* to *A*. However, in VBC that is not the case; the DDFs in cell *A* do not affect the DDFs in cell *B*. Instead, the incoming DDFs expected at the outlet are copied from the neighbouring cell, i.e. *C* is copied to *B*. The resultant effect is similar to a fluid streaming out at the outlet.

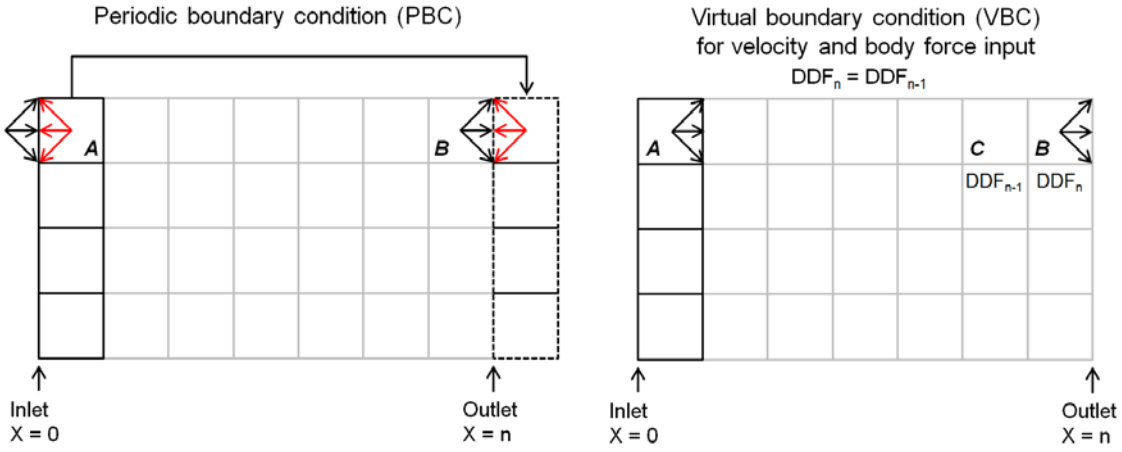

Figure 3-9 Interpretation of periodic and virtual boundary conditions

The use of VBC has significant advantages in some cases. When using PBC in a small domain, a system presenting turbulence would generate vortices that will re-enter the domain influencing the fluid at the inlet. Even in larger domains in the direction of the fluid, it takes a considerable length for the vortices to extend and disappear. If this effect is undesired then VBC are an effective solution. In this work it was observed that using VBC allowed reaching a steady-state fluid much faster compared to configurations using PBC because any turbulence generated at the outlet was not fed back at the inlet.

3.3. Coupling DEM and LBM

The selected methodology in this work choosing DEM as a solid solver and LBM as a fluid solver was thought to be adequate for the FSI applications of interest. As

previously discussed in the literature review in Chapter 2, a traditional CFD methodology to model FSI follows an Eulerian-Eulerian approach in which both solid and fluid phases are seen as a continuum phase sharing the same governing equations. However, one of the objectives in the present work was to study systems from a mesoscale level to observe the behaviour of discrete particles in a fluid, the mutual particle-fluid interactions and effects, and to collect information at a particle level, which in some experimental cases is difficult to obtain. Moreover, the idea that particle geometry and particle physical features have an important impact in the FSI behaviour makes the DEM-LBM coupling a suitable approach to study different cases involving segregation, fluidisation and sedimentation of discrete particles.

The way in which the coupling takes place is considering solid objects immersed or suspended in a fluid. These objects are deemed in the fluid solver as solid walls or boundaries (some authors called them obstacles); and these boundaries may be fixed or travel through the fluid.

The bounce-back technique is used mostly for fixed boundaries immersed in the fluid. It is simple to implement and operations are locally solved. The no-slip condition is ensured at the fluid-solid interface with no tangential velocities, and the incoming distribution functions colliding with the solid boundary are reflected back in the same direction they came from, thus accomplishing mass and momentum conservation.

A different approach should be followed when objects move in the fluid. Given the applications of interest in the present work and the way in which particles are treated in DEM, the selected methodology to couple DEM with LBM was the momentum exchange method together with the immersed boundary method. Since both fluid and solid meshes are the same, no remeshing and refinement are necessary.

3.3.1. Momentum exchange method

The link bounce-back, also known as momentum exchange method, is an extension of the BB that was developed to deal with moving boundaries. In MEM the particle-fluid interaction takes place exactly at halfway the link formed between a fluid node and a solid node. The technique is accurate when the solid boundaries of a particle conform to the computational mesh. When this is not the case, curved boundaries are adapted to yield staircase-like boundaries that conform to the mesh, as shown in Figure 3-10.

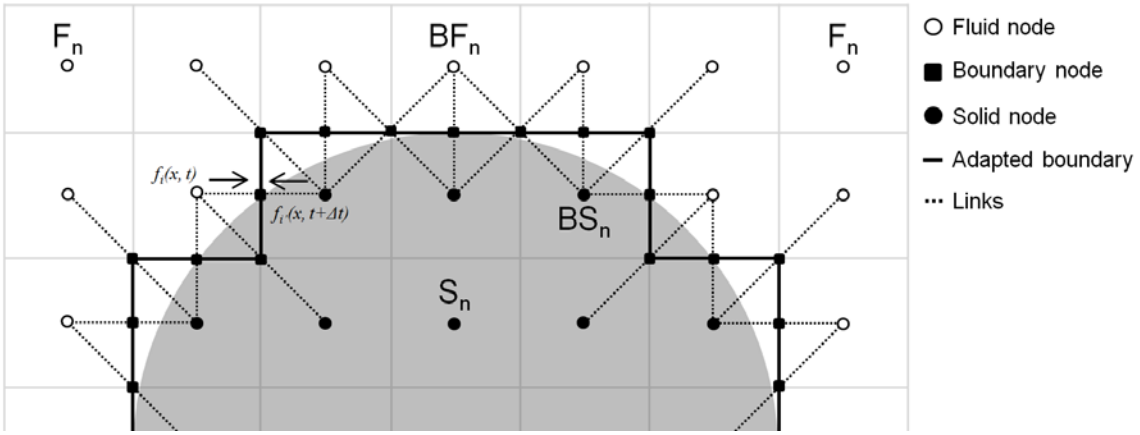

Figure 3-10 Representation of an adapted curved boundary in MEM

In the image above it is observed that solid squares representing boundary nodes are located halfway the link formed between boundary-fluid nodes (BF_n) and boundary-solid nodes (BS_n). The solid line connecting those boundary nodes depicts the adapted boundary of a curved shape, in this case half of a circle in a 2D regular mesh. Normal fluid and solid nodes that do not intervene in the momentum exchange are labelled as F_n and S_n. All the links formed contribute to the momentum exchange and the summation of all of them around the solid particle yields the total hydrodynamic force exerted on the interface.

The velocity of every boundary node is calculated from the equation:

$$u_B = u + \Omega\left[\left(x + 0.5 e_i \Delta t\right) - x\right] \tag{3-53}$$

where u, Ω and x are the linear velocity, angular velocity and position of the particle. Then this boundary node velocity is included in the normal BB equation for the BF_n:

$$f_i^{'}\left(x, t+\Delta t\right) = f_i\left(x, t\right) - 2\omega_i \rho\left(u_B e_i\right) \tag{3-54}$$

Where ω_i is a weighting function in LBM with values ω_0 = 1/3; ω_i = 1/18 for orthogonal velocity vectors i = 1, 3, 5, 7, 9 and 18; ω_i = 1/36 for diagonal vectors i = 2, 4, 6, 8, and 10 to 17. f' refers to the DDF in the opposite direction of the incoming one. For the SB_n a similar procedure is followed for BB:

$$f_i\left(x + e_i, t + \Delta t_{LBM}\right) = f_i^{'}\left(x + e_i, t\right) - 2\omega_i \rho\left(u_B e_i\right) \tag{3-55}$$

The net exchange of momentum from one link results in the force exerted on the solid particle as:

$$f_{i'}\left(x+0.5e_i, t+0.5\Delta t_{LBM}\right)=2\left[f_i\left(x,t\right)- f_{i'}\left(x+e_i,t\right)-2\omega_i\rho\left(u_B e_i\right)\right]e_i \qquad (3\text{-}56)$$

The total hydrodynamic force is obtained by applying equation (3-56) to all the links formed along the boundary and adding them all up.

In practice MEM presents two main drawbacks, one is the modification of boundaries' shape, specially curved ones. However, the summation of all the hydrodynamic forces along the interface is considered to handle that problem. The second problem is related to the total number of links generated. As particles move, some fluid sites 'disappear' and become solid sites covered by the particle; on the other hand, some solid sites will become fluid sites as the particle translates. Consistency of links may not always be kept, causing more problems for complex geometries traveling at high velocities. This discontinuity may lead to hydrodynamic force fluctuations common in lattice-based methodologies. The problem may be mitigated by applying a total force time average in the previous and next time step.

3.3.2. Immersed boundary method

The IBM was developed to overcome the two main problems inherent to MEM, i.e. a more accurate representation of the moving boundaries by means of lattice volume fraction at the solid-fluid interface, and in this way mitigate momentum exchange discontinuities.

To better understand the natural physics of a moving boundary, let us imagine an ensemble of particles represented by a DDF. The DDF streams with a constant velocity e_i towards a solid wall placed in perpendicular position to the streaming motion. The wall itself translates with a small velocity $e_i >> u_{wall}$. The force applied on the wall during collision is proportional to e_i - u_{wall}; and after the DDF collides with the wall it bounces back with a velocity - e_i + 2u_{wall}. Given that velocities in LBM are discrete, the desired BC cannot be implemented directly; however, the DDFs bouncing back from a moving or stationary wall can be modified in order to maintain consistency of the momentum transferred to the wall as in the continuous velocity case. In a single time step during an LBM cycle, the solid boundary in DEM remains fixed whereas the fluid is in motion. Since the fluid cannot flow across the solid boundary; that would mean that

an artificial pressure gradient would arise from the compression and expansion of local fluid near the boundary. When the boundary is moving the mass transfer across the boundary is recovered when the particle moves to its new position. That particle velocity is then taken into account when updating the corresponding DDFs by introducing the particle's velocity term into equation (3-54).

A collision term accounting for the solid volume fraction occupying a cell and a corresponding weighting factor were introduced in the LBE. From Figure 3-10 it is noticeable that a curved boundary on a squared lattice has two regions, a fraction that belongs to the solid particle and a fraction that is part of the fluid, both within the same lattice. In this way, the modified LBE is:

$$f_i\left(x+e_i,t+\Delta t_{LBM}\right)=f_i\left(x,t\right)-\frac{\Delta t_{LBM}}{\tau}\left(1-B_n\right)\left[f_i\left(x,t\right)-f_i^{eq}\left(x,t\right)\right]+B_n\Omega_i^s \tag{3-57}$$

Where B_n is the weighting function accounting for the total volume fraction ratio ε in every cell at the solid boundary, i.e. is the fraction of a cell covered by the solid particle. In this way the total weighting function is the summation of the volume fraction ratios in every cell:

$$B_n=\sum\left[\frac{\varepsilon\left(\tau-0.5\right)}{\left(1-\varepsilon\right)+\left(\tau-0.5\right)}\right] \tag{3-58}$$

The additional collision operator Ω_i^s is used in the BB equation to reflect back the non-equilibrium part of the DDFs:

$$\Omega_i^s=f_{i'}\left(x,t\right)-f_i\left(x,t\right)+f_i^{eq}\left(\rho_f,u_p\right)-f_{i'}^{eq}\left(\rho_f,u_f\right) \tag{3-59}$$

Equation 3-57 modifies the DDFs in boundary cells covered partially or completely by a solid. In this way, the velocity of the fluid is forced to match the velocity of the solid particle.

Having considered the above equations, the hydrodynamic force and torque that the fluid exerts on a solid particle is computed in a similar way summing up the momentum exchanged along the whole solid-fluid interface:

$$F_f = \frac{\Delta x^2}{\Delta t} \sum B_n \sum \Omega_i^s e_i \tag{3-60}$$

$$T_f = \frac{\Delta x^2}{\Delta t} \sum \left[(x - x_c) \times B_n \sum \Omega_i^s e_i \right] \tag{3-61}$$

Where x - x_c is the centroid of the solid particle.

Given the nature of the particle representation in DEM and LBM in this work, the volume fraction ratio calculation for boundary nodes is carried out by cell decomposition. In this technique each lattice cell having a boundary node covered partially by a solid particle is decomposed in sub-cells as shown in Figure 3-11.

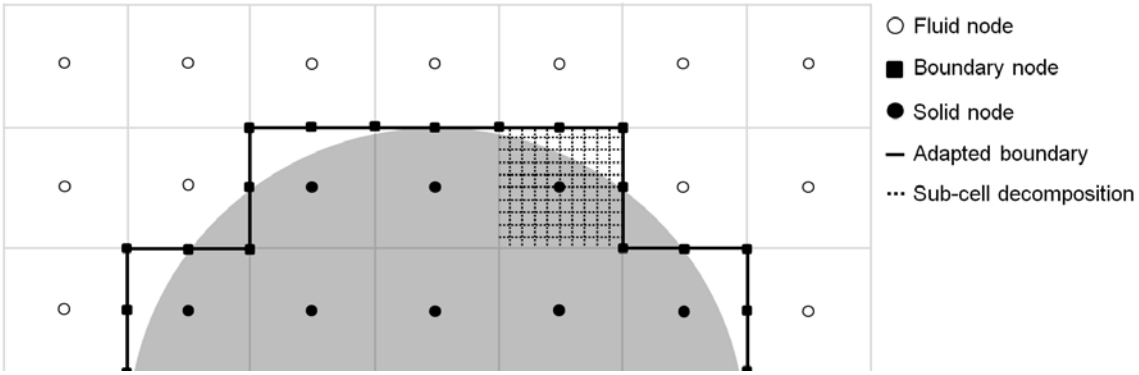

Figure 3-11 Sub-cell decomposition to compute cell volume fraction at boundaries

The vertices of each sub-cell are checked to know if they are in the solid region or fluid region; then the summation of the corresponding sub-cells in the solid region yields the volume fraction in the cell. Although easy to implement it may become computationally expensive, even more for complex geometries displaying marked angled boundaries. However, this is the best approximation considering the nature of the mesh and particle digitisation process selected.

3.3.3. Flow diagram of the coupling algorithm

The methodologies previously described were combined into a coupling algorithm to achieve the main objective of the present work. A pseudo code is presented in this section to facilitate the discussion of the functions implemented in the computational code.

Different FSI configurations are possible involving a large number of particles with different properties; for exemplification purposes a configuration in which two horizontally aligned spheres approached towards each other with a constant velocity is considered. Before the spheres are allowed to move, the first task was the fluid initialisation; once this is done, then the coupled DEM-LBM execution was initiated as shown in Figure 3-12:

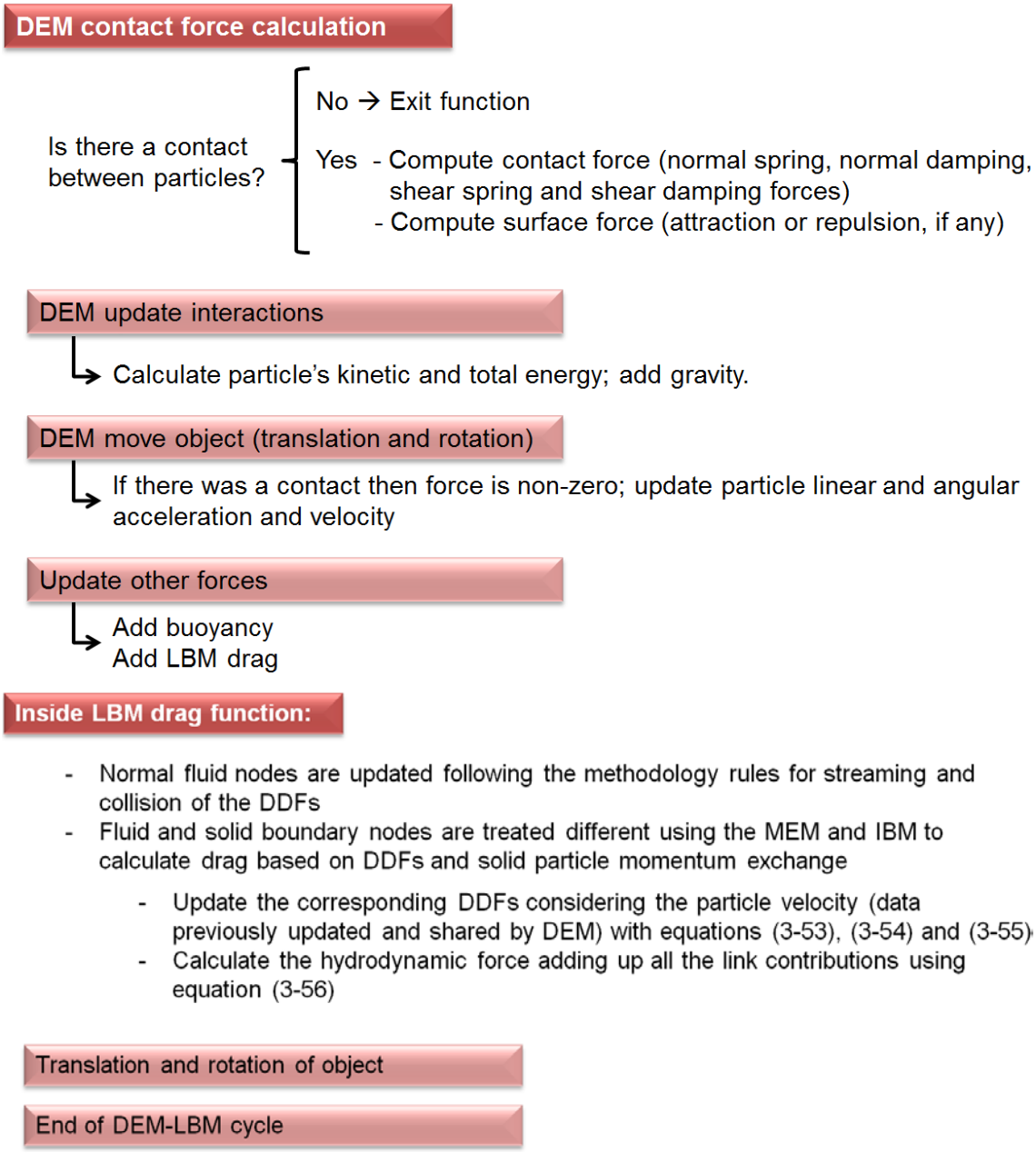

Figure 3-12 Flow diagram of relevant functions in DEM-LBM coupling algorithm

If there was no contact between solid particles, then drag force from LBM is the only force used to update objects' acceleration and velocity. Drag force and contact force

are never added. Update of acceleration and velocity is made two times per DEM-LBM cycle, one for contact force and one for LBM force. Same situation is for actual motion of solid particles.

After the initial implementation it was expected that the nature of a digitised particle would lead to stair-like boundaries, and this would cause instabilities in the coupled algorithm since: 1. When particle was in motion, boundary nodes switched from fluid to solid and vice versa; and 2. Accurate force calculation was compromised since true boundary was modified. Significant force oscillations were present in several tests as particle translated in the fluid, which increased as particle velocity increased as well. Nevertheless, the obvious advantage of the particle digitisation technique directed the efforts to further investigate solutions for the aforementioned problems.

Different ideas were found in the literature which led to the implementation of the IBM to overcome the problem of MEM placing the solid boundary halfway of the links between boundary nodes. The idea was to reduce the hydrodynamic force fluctuations by approximating more accurately the solid fraction value covered by a particle at boundary cells.

More advanced in the project, a turbulence model was incorporated into the code to allow the simulation of high Re fluids.

Turbulence model - The general formulation of LBM permits the calculation of laminar flows only. In order for the coupled model to be capable to handle a wider range of configurations, a turbulent model was implemented.

The most common turbulent model used is known as large eddy simulation (LES) (Zhiyin 2015). Sufficiently high Re fluids imply dealing with a system in the turbulent regime characterised for its non-linearity and potential instability. Such turbulent flow is likely to present eddies with different length, duration and energy. In order to address this problem LES is used to directly solve large scale eddies which are the ones that contribute more significantly to mass transport than the smaller ones. In LBM the unresolved small scale eddies are treated by means of a sub-grid model. A simple model used in this context is the Smagorinsky model (Smagorinsky 1963), which assumes isotropic energy dissipation and that the Re stress tensor depends only on the local strain rate.

The most practical way to implement the Smagorinsky model is to introduce a local eddy viscosity ν_t (or turbulent viscosity) added to the fluid viscosity. The overall effect is the mitigation of small scale eddies, which results in more stable numerical simulations. The stress tensor S_{ij} is calculated from the second-order moment on the non-equilibrium part of the DDFs as:

$$\tilde{S}_{ij} = \left(\partial_j \tilde{u}_i + \partial_i \tilde{u}_j\right)/2 \tag{3-62}$$

And the eddy viscosity is obtained from:

$$\nu_t = \left(S_c \Delta x\right)^2 \sqrt{\sum \tilde{S}_{ij} \tilde{S}_{ij}} \tag{3-63}$$

where S_c is the Smagorinsky constant. For small values of S_c, the sub-grid turbulence does not add significantly to ν_f. On the other hand, large values would see a higher diffusion of the fluid. In the present work the value used is 0.1 as this is a typical value used.

3.3.4. Scaling factors

In the coupled DEM-LBM it is very important to keep consistency with the physical units since two different frames of reference are involved, DEM and LBM. For DEM it is straightforward since the lattice length is defined by the user. In this way a simple product operation will yield the measurement in physical units. For example if the lattice length is 0.0005 m and a sphere is made of 20 voxels in diameter then the diameter in physical units is 0.01 m. However, when running a coupled simulation forces are calculated independently in each solver. For this reason it is important to correctly define the conversion factors between both solvers, and to convert the corresponding forces to physical units.

The premise to do that is that dimensionless quantities must be equal in the systems involved. For instance, Re of a fluid in LBM should match exactly Re in physical units; drag coefficient for force calculation must follow the same rule.

To start the drag coefficient c_D was set to be equal in both systems in order to find the scaling factor for force:

$$c_D = \left[\frac{2F_D}{\rho_f u_{rel}^2 A}\right]_{phy} = \left[\frac{2F_D}{\rho_f u_{rel}^2 A}\right]_{LBM} \tag{3-64}$$

Where the subscript phy refers to quantities in physical units; LBM refers to quantities in LBM units.

Another dimensionless quantity used is Re; so solving for velocity u in (3-23) and substituting it in (3-64):

$$\left[\frac{2F_D}{\rho_f\left(\frac{\mathrm{Re}^2\,\nu^2}{L^2}\right)A}\right]_{phy} = \left[\frac{2F_D}{\rho_f\left(\frac{\mathrm{Re}^2\,\nu^2}{L^2}\right)A}\right]_{LBM} \tag{3-65}$$

Considering that $L^2 = A$, simplifying and solving for $F_{D_{phy}}$:

$$F_{D_{phy}} = \frac{F_{D_{LBM}}\rho_{phy}\nu_{phy}^2}{\rho_{LBM}\nu_{LBM}^2} \tag{3-66}$$

To find the velocity in physical units from velocity in LBM units the following conversion factor is used:

$$u_{phy} = \frac{3u_{LBM}\nu_{phy}}{pw(\tau - 0.5)} \tag{3-67}$$

Time should be consistent in both DEM and LBM systems; to do so, the number of iterations corresponds to the time step calculated for each system. The information transferred from LBM to DEM includes the hydrodynamic forces and torques originated by the fluid acting on the particles. Then DEM carries out the corresponding calculations to update particles' velocities and positions considering interparticle contact forces plus the hydrodynamic forces provided by LBM. Generally LBM time step is longer than DEM time step, therefore it is assumed that hydrodynamic forces are constant until DEM time reaches the LBM time. For example, if LBM time step is 10 times the DEM time step, it is assumed that the hydrodynamic force is constant during 10 time steps. After a DEM calculation cycle, the fluid force in LBM is updated accordingly and the LBM-DEM iterative process continues.

In a DEM-LBM simulation the time step in both solvers is related as:

$$N_{LBM}\Delta t_{LBM} = N_{DEM}\Delta t_{DEM} \tag{3-68}$$

where N is the number of iterations. The following cases are possible to configure in a coupled simulation:

$\Delta t_{LBM} << \Delta t_{DEM}$ at every DEM step run $N = \frac{\Delta t_{DEM}}{\Delta t_{LBM}}$ LBM steps to update the flow

$\Delta t_{LBM} \approx \Delta t_{DEM}$ at every DEM step run one LBM step to update the flow

$\Delta t_{LBM} >> \Delta t_{DEM}$ at every $N = \frac{\Delta t_{LBM}}{\Delta t_{DEM}}$ DEM step run one LBM step to update the flow

To run a coupled DEM-LBM simulation first the fluid must be initialised. At this point a large number of LBM iterations are required in order to achieve a steady fluid before running the coupled DEM-LBM. If the simulation requires a stagnant fluid then just few hundred iterations are enough.

3.4. The DigiPac software

The DigiPac software is a package comprised by a range of modules intended for the modelling of packed structures to assess their behaviour and predict the properties of such systems involved in different processes with a broad range of applications. In the following subsections a description of the relevant modules used in the present work is presented, highlighting the main features and theory behind their functionality. Section 3.5 includes information about the XMT technique employed in the present work.

3.4.1. DigiDEM for solid particles interactions

This module represents a very useful tool for the pharmaceutical and chemical industry but it also may be used in the civil, mining and nuclear fields to predict how the particles behave in a confined space of regular or irregular geometry, how the particles segregate depending on the shaking of the container during simulation (or after the settled bed was formed), and to predict the packing density, number of contacts among the particles and the distribution profiles of the particles. This means that not only the final parameters of the structure can be calculated from simulations but also the

dynamic process of packaging. With such a powerful tool, the user can improve and optimise, for example, the storage volume of any object of arbitrary shape.

The DigiDEM module allows the user to perform simulations of packing regular geometries such as cylinders, cones, ellipses and spheres into a well-defined container, e.g. a cube or a bottom sealed cylinder. One of the attractive advantages is that the user can define different non-uniform irregular shapes to create new designs of structures and add them into a container that can be also defined of an arbitrary geometry. The user can create any shape for the particles to be packed and for the containers to hold such particles by using the available tools in the DigiUtility module which will be described in a following subsection.

Furthermore, it is possible to simulate the shaking of the container to make the particles interact inside, likewise simulate fluidisation of the particles by means of a plug flow like to characterise different materials according their size and/or density as done in the sand industry to grade materials. Structures such as an impeller can be used to set a characteristic motion to simulate the mixing of the particles inside a container, assessing some properties such as segregation and packing density.

One important consideration to have in mind is that the time step has to be very small in order for the programme to be able to capture the many number of interactions or particle movements taking place during the simulations, hence maintaining numerical stability. The accuracy achieved in the simulations by means of fine tuning of particle positions and orientations is countered by the simulation time which tends to be as large as several million time steps.

An interesting feature of the programme is that it introduces the option of importing digitised objects from Computer Assisted Design (CAD) models or 3D XMT fostering the work with voxels, similar to a pixel in 2D but a voxel is defined in three dimensions, like a cube, making it simpler and faster, and truly demonstrating that any arbitrary geometry can be considered as a particle or a container. The strength of this way of representing objects is that the translational and rotational movement is a simply and fast relocation of voxels, no matter how complex is the geometry of the object. The disadvantage lies on the size of the system desired, if too large then the user must have available a considerable amount of memory.

It is important to point out that the current version of DigiDEM is able to handle rigid and solid objects that do not change in shape nor break in order to facilitate the simulations.

One solution for the aforementioned issue is the possibility of using periodic boundary conditions for the packing container if present. Taking Figure 3-12 as reference, this feature can be implemented in any of the walls of the container and basically means that if a particle falling vertically reaches a periodic wall at the bottom, it will reappear at the top with the same characteristics it had in the previous position, namely translational and rotational velocity.

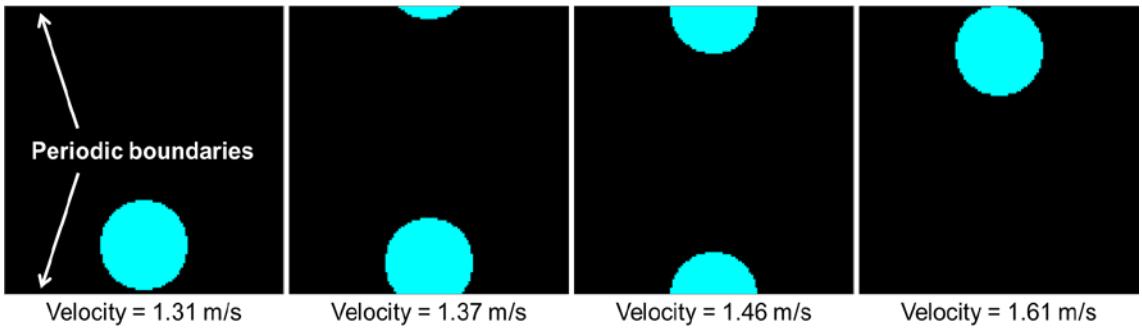

Figure 3-13 Representation of periodic walls in DEM environment

The output files produced once the desired packed structure is obtained are volume packing distribution, particles orientation distribution, coordination number for each particle, radial distribution function, mean empty space (MES) and tortuosity.

The MES is a way of measure the pore space in three directions, it is calculated by initially defining a total number of starting points; from each one of these points, a straight line is drawn in both positive and negative directions until it reaches the system boundary or a solid site, then the same procedure is followed in the three X, Y and Z directions yielding the average distance in every direction.

The tortuosity is defined as the ratio of the actual length of a flow path L_t to the straight length L_0 or thickness of the sample along the pressure gradient. The user defines how many random empty sites at one end of the volume will perform a random walk towards the other end in the selected direction. For each starting point more than one walk can be performed; in the end, the results will be averaged and divided by the corresponding domain dimension yielding the tortuosity as the squared value of this length ratio.

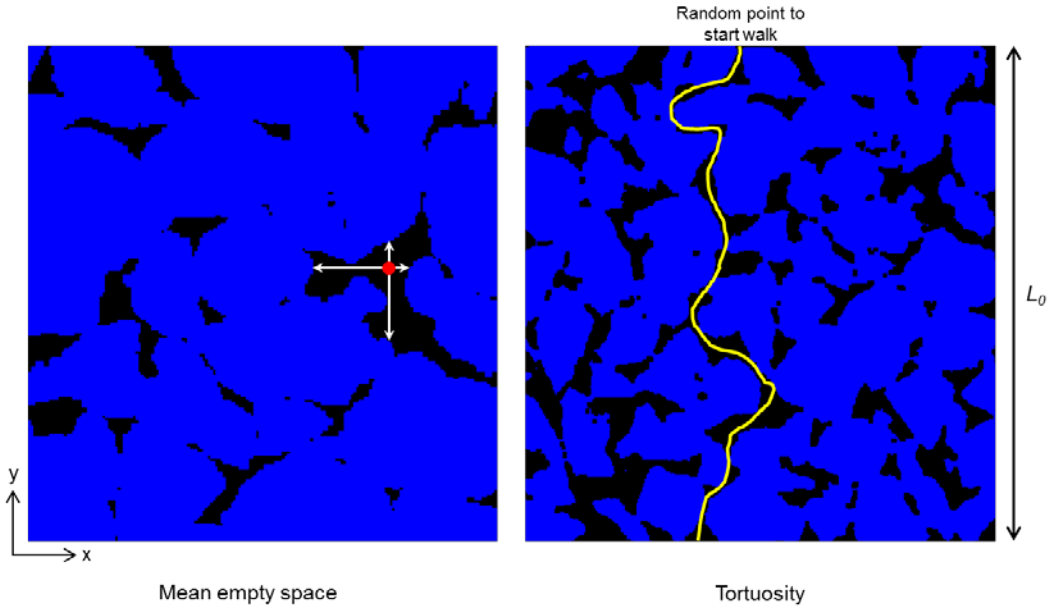

Figure 3-14 2D representation of mean empty space and tortuosity

3.4.2. DigiFlow for simulations of fluid flow through porous media and flow around a solid object

The DigiFlow module was designed to calculate the intrinsic permeability of porous structures and it is based in the LBM D3Q19 scheme previously presented in subsection 3.2.

In this module it is possible to simulate a single phase fluid for the assessment of changes in the fluid behaviour due to structural features present in the system under study.

A porous structure generated in DigiDEM or a similar image from XMT can be loaded in DigiFlow to simulate a low Reynolds number fluid flow through it (in the laminar regime). Similarly as in DigiDEM, the physical space is mapped onto a regular lattice grid having the voxel as a basic unit.

It is important to point out that in DigiFlow is considered that a flow generated by a constant pressure gradient ∇P is the same as that driven by a constant external force labelled as body force bf, for this reason, a constant force is used to drive the fluid flow and it is restricted to move along the X axis. The sample can be rotated before in DigiUtility to carry on simulations of flow in a different direction.

The prediction of the dimensionless permeability k was carried out using equation 3-69:

$$k_{LBM} = \frac{u_f \nu_f}{bf}\left(\frac{1}{d_p^2}\right) \tag{3-69}$$

where u is the Darcy (superficial) velocity of the fluid averaged over a cross section normal to the direction of the flow including the solids; this is a parameter obtained from the DigiFlow simulation. The parameter ν is the fluid viscosity in LBM units and is related to the relaxation parameter τ:

$$\nu_{LBM} = \frac{2\tau - 1}{6} \tag{3-70}$$

Both bf and τ are user input parameters.

3.4.3. DigiUtility module for particles generation and image post-processing

DigiUtility is a collection of tools that helps in the processes of creating and editing geometries to be used in other modules as well as in the post-processing stage of particle digitisation. Some of the features allow the user to generate shapes, manipulate volumes, rotation, segmentation, projections replacement, perform specific operations on selected individual pixels, and additional capabilities can be added through plugins. This module primarily operates with proprietary *.bin* format files but other formats can be loaded into this module such as *stereolithography (.stl)* files.

Predefined regular geometries can be generated such as ellipses, spheres, cubes, cylinders, torus and cones; the user only needs to input the values for the basic measurements and/or axes. A wide range of particles can be generated from basic ones, for instance spheres on sphere, agglomerate of spheres or different objects like crystals with the possibility to embed and merge two or more objects. The basic particles can be generated locally in DigiUtility from the predefined geometries or importing new ones, whether obtained from CT or designed in third party software.

In DigiUtility the user is able to perform a variety of actions on the volumes, modifying the colour values of one individual pixel or a range of them, merge volumes, clipping options, choose among different views for a better edition, calculate volume statistics, remove pixels, convert to binary, erode and dilate the surface, fill in empty spaces, obtain the packing fraction, rotate and make videos, save images, extract isolated

volumes, etc. Figure 3-14 shows three images of objects that can be generated in DigiUtility, one of them a sphere covered by spheres, where the user must provide the diameter of the large sphere, the diameter of the small spheres and the maximum numbers of spheres to be placed on the surface of the large sphere.

In short, this module is an important tool that significantly helps the user to create simple geometries and a mixture of them, producing complex shapes, as well as pre and post-processing and segmentation to extract individual particles or agglomerates if desired.

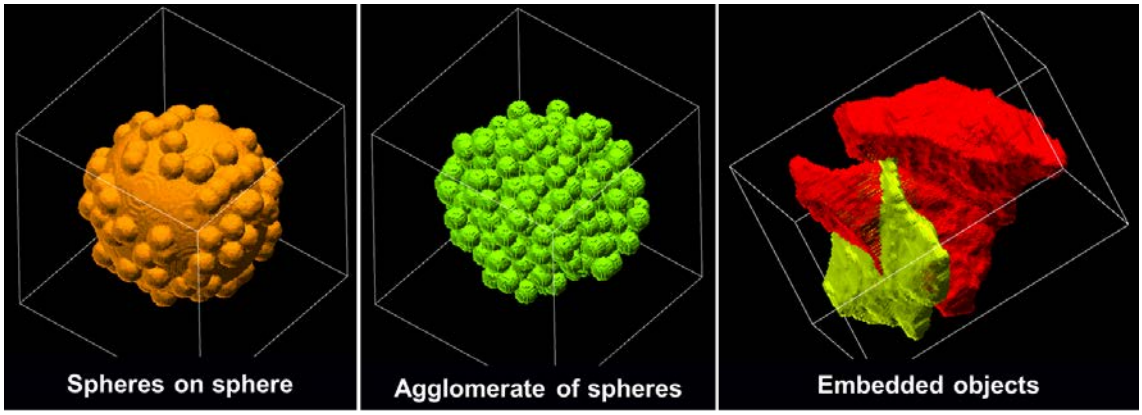

Figure 3-15 Three examples of complex geometry particles generated in DigiUtility

3.5. X-ray microtomography for particles digitisation

The image acquisition technique through XMT has been used recently on a large scale in many R&D areas apart from the well-known medical use to obtain images of internal parts of the human body such as bones.

The acquisition of 2D images is based on the principle that a shadow is projected on a surface when an object is placed between a source of light and such surface. The surface where the shadow is projected is called detector, the source of light is an x-ray source and the object of interest is the sample placed inside the x-ray scanner.

The equipment used in this work is a General Electric Phoenix Nanotom® S equipped with an x-ray tube producing a conical beam of 160 kV maximum voltage and maximum output of 15 W, the current in mA is regulated by the voltage set prior the start of the scanning process. The largest object that can be placed inside the scanner on the sample holder should be of 150 mm height x 120 mm diameter with a maximum weight of 2 kg.

The highest resolution achievable for a particular object depends on its size and on the details that the user is looking for, for example, considering that the available surface area on the detector is ~2000 x 2000 pixels, if the resolution desired is 2.5 μm per pixel, then the maximum sample size is found by multiplying the resolution by 2000 which in this case yields 5000 μm (5 mm); if the size of the object is known, the maximum resolution is obtained through the inverse operation.

Even when the sample fulfils the size requirement, the user must bear in mind that once the sample is placed inside the scanner, the sample holder will rotate 360 degrees to acquire the 2D images and while rotating, the sample may tilt to one side and “go out” of the detector, which might affect the final representation of the 3D volume. In order to avoid this, the sample should be reduced in size or resolution decreased. If the user is interested in observing features smaller than the resolution set, it will not be possible due to the pixel size unable to capture such finer details.

The total time for the sample to rotate 360 degrees and finish the image acquisition process depends directly on the initial configuration of the user before running the scan. One factor is the number of total images defined by the user, which may be large as 1440 (or more) corresponding to 4 images every degree of rotation. This should be increased only when detailed results on the surface and internal structure are sought, otherwise a total number of 1000 projections results in a process of approximately 40 minutes. The exposure time of the sample every degree of rotation can also be modified, commonly half of a second is enough to capture the shape and general details of the object of interest. Exposure time can also be increased but it represents an over exposure risk. It is recommendable to not use more than one second, only if necessary. The software is configured to warn the user if the exposure time is very large in order to avoid permanent damage to the sample.

A sketch showing a basic layout of the main elements in the scanner is shown in Figure 3-10. It can be noticed that the beam is emitted from the source, hits the object and passes through it to finally travel further towards the detector.

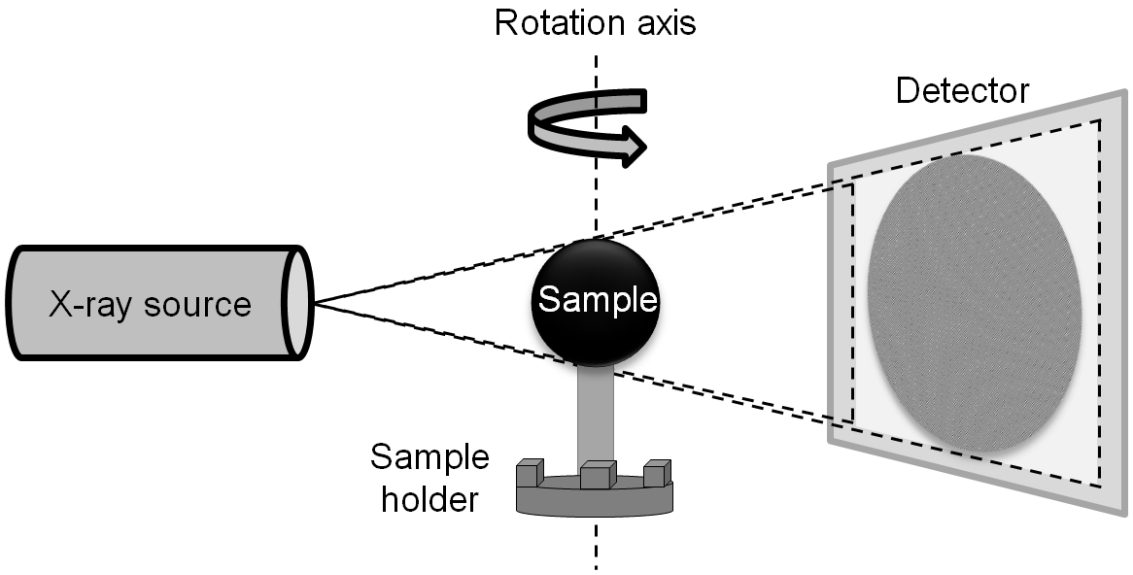

Figure 3-16 Simple diagram of the scanning process layout

Since the x-ray is interacting with the sample, its attenuation depends on the thickness and atomic number of the material of the sample. To avoid losing the x-ray before it reaches the wall due to very dense materials, the user can control the energy of the beam by increasing the voltage, which in case of the Nanotom® S is limited to a max of 160 kV; the current in mA is limited according the selected voltage. In this way, the higher the energy of the x-ray, the more material it will penetrate before is fully absorbed. For this reason is helpful to know the type of material and thickness of the sample beforehand to have an idea of the x-ray power and perhaps, reduce the thickness of the sample if necessary.

In Figure 3-17 is presented the view of a rock during the digitisation process where the surface roughness can be captured as well as the internal structure and particle shape. A wide range of grey tones is used to represent each voxel value of the surrounding air and the sample, in which darker voxels represent high density zones or high density materials and lighter correspond to low density materials or air.

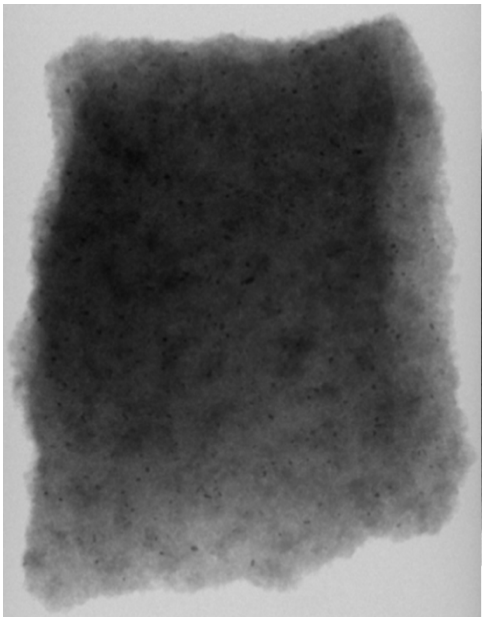

Figure 3-17 Rock 2D projection in grey scale

The XMT technique was used to obtain digitised images of irregular geometries such as sand grains and rock samples. The methodology is based on the acquisition of a large number of 2D images (hundreds or thousands depending on the desired image detail) while the sample is rotated 360 degrees. These 2D images or projections are subsequently used to construct a three-dimensional volume by stacking the projections together.

Once the volume is reconstructed, the post-processing stage follows to enhance the visualisation of the object or to focus on specific elements of interest. The file is converted to a suitable extension file to use in the post-processing step, in this case to a *.bin* file to be used in DigiUtility where the voxels colour range now is between 0 and 255. For the particular case shown in Figure 3-18, all voxels on right-hand side image were set to 100; the material composition was neglected since the authors interest lies on the accurate capture of particle size and shape. As it can be observed in the same image, the particle is contained in a bounding box, this is considered as a lattice grid for that particle where empty nodes are always represented by a black voxel equal to 0.

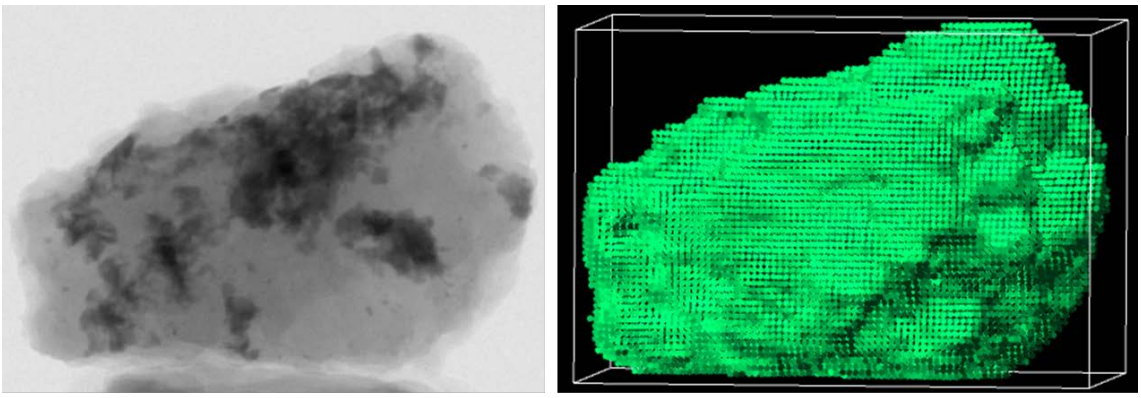

Figure 3-18 Sand grain digitisation

Practically any sample of any shape, within the maximum size constraints of the equipment in use, can be placed in the scanner; for instance, it is possible to obtain digitised images by scanning an individual particle and using it to make up a packed bed, or by scanning a packed bed made up of different particles and using it directly in LBM for fluid flow simulations in structures made of different materials such as sand, soil, rocks, powder, etc. If desired, segmentation can be achieved with the appropriate post-processing software for the extraction of individual particles which can be used as the basis of simulations of the dynamic packing process using DigiDEM. The inherent advantage of this technique is that the digital image embeds the shape, surface texture and internal structure of both regular and complex geometries.

4. Validation of the uncoupled DigiDEM and DigiFlow modules

Methodologies based on the solution of governing equations are prone to present numerical errors while approximating to the solution. The undesired effect is that significant differences and inaccuracies may exist between analytical and numerical results. In some cases even when numerical results are comparable, the visualisation of the numerical solution helps to support the interpretation of the results obtained and analyse the behaviour and phenomena taking place in a computationally simulated system. However, in some cases the qualitative interpretation may look correct but not necessarily accurate quantitatively speaking. For this reason, it was important to carry out an evaluation and validation of the current status of the DEM and LBM codes to be used in order to examine the results produced.

The main objective of this initial validation was to assess the current status of both modules DigiDEM and DigiFlow, based on DEM and LBM methodologies respectively. The use of XMT for particle digitisation required the definition of a methodology to follow in order to prepare samples, carry out the digitisation part and then do the post-processing job to generate and analyse the data. Selected parameters of packed beds obtained from XMT and from packing simulations were compared to analytical and experimental values using spheres and sand grains.

The first section includes information of the DigiDEM module used for simulations of the dynamic packing process of glass spheres and sand grains of different size. The second section presents permeability predictions from fluid flow through packed beds as worked in DigiFlow.

The second section extends to simulations of fluid flow through porous media generated with spherical particles and sand grains. A further section presents permeability predictions in sandstone compared with available experimental data provided by an external source. A comprehensive analysis was carried out in this section with the attempt to find an alternative way to calculate porosity and permeability of the samples combining XMT with LBM. Samples were scanned, digitised and processed to run in DigiFlow and predict the porosity and permeability of such samples. The numerical results were compared with the experimental ones.

The last section presents a qualitative test of the current way in which in DigiDEM it is possible to simulate a plug flow to fluidise particles.

Additional to validation, results helped to detect areas of improvement and do some code implementations and modifications for efficient data collection and faster data analysis.

4.1. DigiDEM validation cases

Two different particle shapes were selected in order to evaluate the packing density, mean empty space and tortuosity in packed structures generated from XMT scans and particle packing simulations with DEM. One of the chosen shapes was a sphere due to its symmetric geometry and ease of analysis and representation. Additionally, using spheres was considered an appropriate starting point for the validation tests since a large number of experiments and correlations reported in the literature are based on studies employing this fundamental geometry.

Sand grains were chosen as well to produce packed beds. With the intention of carrying out simulations to produce more realistic porous structures as present in nature, the use of irregular geometries such as sand grains was expected to help in doing so. With its inherent non-smooth surface, texture, roundness and angled corners, these factors definitely intervene in the final density of packed structures. Sand grains may have a relatively wide range of sphericity and this will influence the way in which they interact and orientate in a packed bed. The roughness of sand grains also plays an important role in terms of particle interlock and frictional force between particles that might hinder particle movement, ultimately affecting packing density and pore network.

A strong motivation to use sand grains was that they pose a challenge to represent accurately, even more in a computational environment where they are handled by numerical algorithms. Additionally, the necessity of carrying out experiments and numerical computations using geometries different than the traditional ones is encouraging to study more realistic granular systems with real applications in natural processes and the industry.

To start, five cases were defined for validation of DEM generating different packed structures. Three cases were labelled as A, B and C for mono-sized beds using glass beads of diameter 2 mm, 1 mm and 0.3 mm respectively. The other two cases labelled

D and E correspond to packed structures using sand grains with mean particle size of 250 μm and 300 μm.

4.1.1. Packed structures of spherical particles

The first step was to produce a column of spheres randomly placed in a plastic tube and digitise a section of the column by means of XMT. Spheres available in the laboratory were used to generate a digital packed bed; then the scanning procedure was carried out for image acquisition and later volume reconstruction of the sample. Once the 3D volume was available, the next step was post-processing of the digital volume. This was an exhausting task since it required significant time and repetitive application of different software tools and filters. In this stage the volume was cleaned by removing all the voxels corresponding to air. In other words, in a binary system of 1s and 0s, air should be 0 meaning that there is no solid object represented by that voxel. Only voxels representing the solid particle are desired to retain in the reconstructed volume. Although a dense sphere is well defined in size and shape in a tomography image, solid boundary voxels are less dense and are more challenging to identify since they tend to blend with voxels belonging to air around the object.

Different samples of sand grains already categorised by size were also available in the laboratory. The same procedure was followed to digitise packed columns of sand grains. The main difference was that sand grains displayed a wider range of shadows depending on the material density in the grain. Post-processing digital columns of sand grains was even more challenging and time consuming since it was not very easy to distinguish solid boundary voxels. For this reason different thresholds and filters were tested. Once the post-processing stage was finished, the final structure was assessed obtaining its packing density, pore network, mean empty space and tortuosity.

The XMT parameters configured for the three columns of spheres were: Tube voltage and current 150 kV, 150 μA, resolution of 9 μm per pixel, 1000 projections, X-ray focus mode 0, and 1 second for integration time of the detector.

For identification and consistency purposes, a digitised bed or any other object obtained through X-ray microtomography will be labelled hereafter as XMT; packed structures generated with simulations will be labelled as DEM.

The second part was to actually generate digital random packed beds using DigiDEM to compare the physical parameters between the XMT packed bed and the one produced with the software. Spherical particles were generated in the module DigiUtility and then poured into a tube of fixed inner diameter (I.D.). In DigiUtility the desired diameter in number of voxels was input and the object was automatically created and saved into a suitable *.bin* file to use in DEM simulations. The main features of cases A, B and C for spheres are shown in Table 4-1.

Table 4-1 Packed beds of spheres configurations

	XMT		DEM		
Case	d_p (mm)	Tube I.D. (mm)	d_p (voxels)	Tube I.D. (voxels)	I.D.-d_p ratio
A	2	10	120	600	5
B	1	10	60	600	10
C	0.3	10	18	600	33

The bed packing density is an important parameter that provides a good idea of how densely a packed bed is. Related to this parameter is the characterisation of porous media microstructure, which is also important to understand in order to predict macroscopic properties such as permeability. The pore network morphology also provides information about the mechanical behaviour of a granulate system at a microscale level, which in turn has an impact at the macroscale level.

Besides characterising the packed beds through these physical parameters, in DEM simulation it is also accounted the effect of the dynamic process of packing. Unlike hard-sphere models in which particles overlapping are moved away from each other following pre-defined rules, DEM allows the particles to move freely in the domain following the Newton's laws of motion. When particles are poured down they fall down subject to gravity and bounce on the container walls and hit other particles around. In this work particles were not placed randomly in the system, they were poured down from the top of the system with zero initial velocity and travelled down following realistic physics contact rules. The size of the spheres is not modified throughout the entire simulation.

The mean empty space is a way of measure the pore space in the sample by averaging the dimensions of the pores. It is calculated by initially defining a total number of starting points located only in pore sites, the more points the better. Then from each one of these points a straight line is measured in both positive and negative directions until it reaches the system boundary or a solid site; the same procedure is followed in all three X, Y and Z directions. Then the mean distance is obtained in every direction, and the result reported is the average of the distances in the 3 directions.

The tortuosity is a way of characterising how sinuous a pore network is, i.e. it gives an idea of how “twisty” the pores are for a flow traveling from one side of a sample to the opposite one. It is defined as the ratio of the actual length of a flow path to the ideal length of a straight path without any curve, which is basically the thickness of the sample along the flow pressure gradient. The user defines how many random empty sites at one end of the volume will perform a random walk towards the other end in the flow direction. For each starting point more than one walk can be performed. The average of the tortuous path lengths is divided by the straight path length; the value obtained is squared and reported as tortuosity. The comparison of both XMT and DEM packed structures is presented in Table 4-2.

Table 4-2 Values calculated from sphere packings

	Case	Packing density	MES	Tortuosity
XMT	A	0.455	442.104	1.204
	B	0.493	341.805	1.241
	C	0.507	292.185	1.144
DEM	A	0.428	230.625	1.380
	B	0.436	169.710	1.474
	C	0.468	109.011	1.357

From the values observed in the previous table it is clear that in general all packed structures presented a lower packing density compared to experimental data for spheres, which is around 0.64 (Scott & Kilgour 1969). However, in both XMT and DEM cases, the packing density follows an expected trend from case to case in which the smallest particles are more densely packed compared to larger ones. This can be explained by the particle size and the wall effect having larger impact in larger particles in case A compared to the smaller ones in case C. The relative errors calculated were 5.9%, 11.6% and 7.7% corresponding to cases A, B and C in this order.

Such loose packed columns were not shaken to allow rearrangement of particles. The friction coefficient and surface roughness of particles are known to affect the final packing density as well. Tangential forces arise when friction between particles is present, resulting in motion limitation and particles interlock. The surface of spheres is expected to be smooth; however the nature of digital particles implies the representation with staircase-like boundaries, which plays an important role in increasing friction. This effect can be reduced by increasing particle resolution. When particle move freely and interlock due to friction is reduced then higher packing densities can be obtained.

The tube I.D. was small enough to allow a maximum of 5 spheres along the I.D. in case A. However that is an ideal case, but in reality the limited packing space had an effect on packing density, and when the spheres were poured they did not have enough free space to freely move and rearrange. Another factor that could have affected the total voidage is the thresholding applied in the post-processing stage that could have erased more solid boundary nodes than the expected ones, resulting in a reduced overall solid fraction.

When dealing with digital images visualisation is the main assessment criterion based on the user's judgement. Although the author of this work carried out the tasks of post-processing considering different thresholding ranges, filters and analysis of structural properties, it is possible that overestimation of pore fraction was due to deletion of more voxels than planned. It is difficult to control and visualise slice by slice when a reconstructed volume is made of hundreds of 2D slices, and for that reason filters and tools were applied to the entire 3D packed structure and not on individual 2D slices.

Paying attention to the main objective of the validation, the increasing values from case A to C are a correct indicator of the expected packing density according to the particle size. Moreover, the DEM predictions also follow the same trend and the values of packing density are comparable to those ones from XMT packed beds. The MES parameter is consistent with the packing density, meaning that a low packing density will likely contain larger pores as in case A, corresponding to larger particle diameters; and a higher packing density as in case C presented pores of smaller size, corresponding to smaller particle diameters. The tortuosity is basically an indicator of the ratio of the longest tortuous path to the straight path from one side to the opposite

side of the sample. The values for all cases are consistent, indicating that the pore network morphology is similar for mono-sized packed beds.

To visually relate the results presented in Table 4-2 with the actual packed structures, Figure 4-1 includes 2D cross sections of both XMT and DEM beds with images of XMT and DEM beds. Cases A and C are presented to easily observe the difference in particle size. The plots presented in Figure 4-2 correspond to the packing density profiles of the three cases. The plots show the axial distribution over a normalised bed height. The two XMT and DEM packing density profiles are overlapped for direct visualisation and comparison. They were constructed by stacking up the per-slice solid fraction in a specified axial height. It can be observed that the DEM profile closely follows the XMT packing profile.

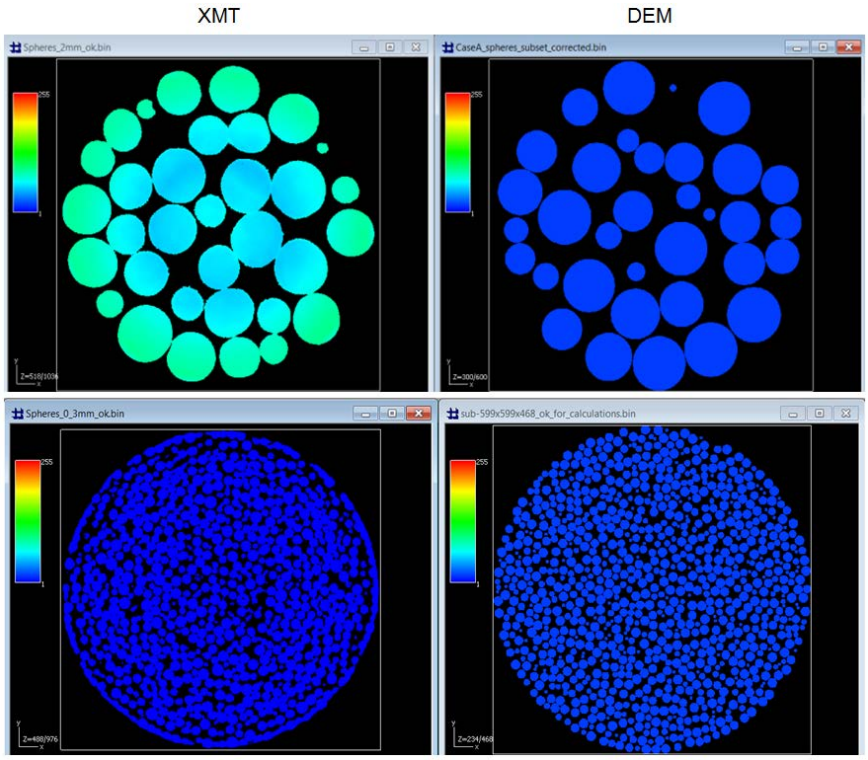

Figure 4-1 Top row: Case A XMT view (left) and DEM view (right). Bottom row: Case C

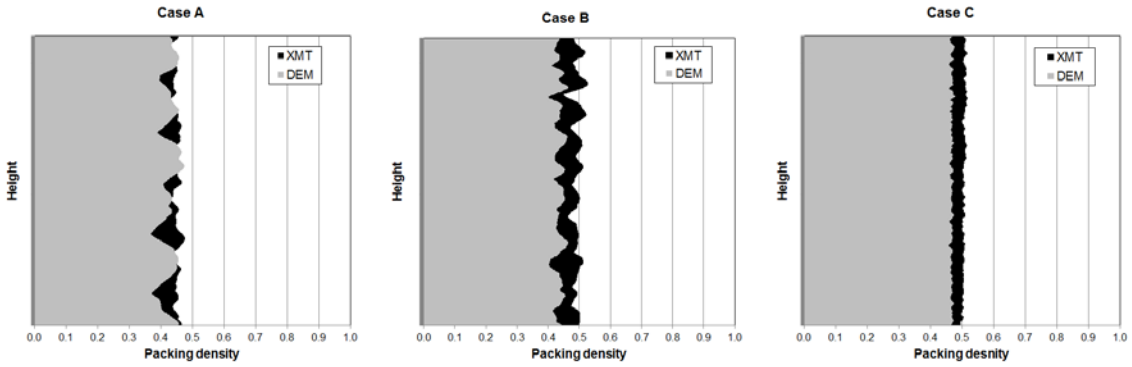

Figure 4-2 Packing density profiles of cases A, B and C

The packing fraction near the tube wall fluctuated largely in case A compared with the other cases. Oscillations were reduced as particle size was reduced. Case C showed a profile that tended to be more uniform because small particles near the wall accommodate better than large ones.

It should be noticed that the top and bottom region of the beds were cut out because packing fraction in this sections might not be uniform and it is good practice to report data considering the bulk region. That is because at the top layer of the bed particles are loose since they do not have other particles above generating pressure for compaction on them and the packing fraction fluctuates in this region. However, when a bulk region is extracted from the volume, a straight line cuts the particles, meaning that some particles in full might be included but some others are not because a fraction could have been cut off.

The density profiles in the plots presented above correspond to the results showing that DEM structures slightly underestimate the corresponding ones from XMT structures.

Such behaviour near the wall of the container is known as wall effect. The cyclic variation observed in the radial distribution is characteristic of packed beds of mono-sized spheres. This effect produces the oscillations observed in the plot, and extends up to 10 particle diameters inside the bed (Caulkin et al. 2006). Beds with small I.D. to d_p aspect ratios are more likely to be affected by the wall effect.

4.1.2. Sand grains packed structure

Two different samples of sand grains were chosen to carry out a similar comparison of the selected parameters as presented in the previous section. The mean particle sizes

chosen were 250 µm and 300 µm; hence the two study cases are referred as Sand250 and Sand300. Such samples were obtained from a wide range of available jars already categorised by size in the laboratory.

After having obtained the 3D packed structure, an exhaustive post-processing work including segmentation was carried out in order to extract individual sand grains from the packed bed to later be used in simulations to generate the corresponding DEM packed beds.

For Sand250 174 individual particles were analysed. The volume of every particle was calculated knowing the total number of voxels making up the particle, and the length of the voxel, given by the scan resolution. Then the corresponding PSD was obtained before configuring the simulation. The particles' mean lengths in the X, Y and Z axes were 270, 262 and 212 µm, respectively. For Sand300 the process carried out was similar but the total number of particles used to obtain the PSD was 30; the average particle lengths along the X, Y and Z axes were 314, 336 and 283 µm, respectively.

Figure 4-3 shows a 2D image from the XMT scanner where the tube containing sand particles from sample Sand250 is displayed on the left-hand side. In the same figure a region extracted from the DEM packed structure for analysis is displayed on the right-hand side.

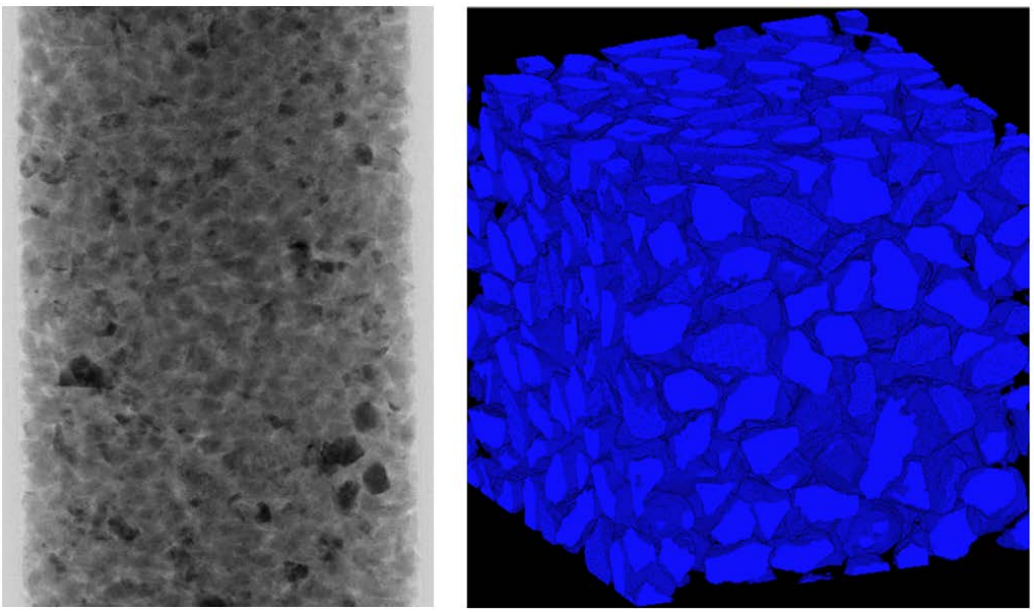

Figure 4-3 Sand250 in XMT scanner (left); region extracted from DEM bed (right)

Table 4-3 lists the values obtained for XMT and DEM packed structures.

Table 4-3 Parameters obtained from sand packaging

		Packing density	MES	Tortuosity
Sand250	XMT	0.379	170.338	1.553
	DEM	0.346	153.144	1.547
Sand300	XMT	0.387	185.628	1.595
	DEM	0.339	174.486	1.594

The values from the previous table indicate that DEM predictions follow closely the values from XMT structures, but similarly as in the cases of packed beds of spheres, the DEM values underestimate the XMT values. Some of the reasons leading to such underestimation were observed as well in the previous section reporting packed beds of spheres.

The relative errors calculated were 8.7% and 12.4% for Sand250 and Sand300, respectively. The difference between the XMT bed and the one generated in DigiDEM is related to post-processing tools and thresholds applied when removing voxels around the particles representing air. In both tests the effect observed is consistent in terms of packing density underestimation, which was interpreted as a larger deletion of boundary voxels in the DEM bed.

The MES predictions seem to be more consistent in this case compared to values from packed bed of spheres. It can be notice that as particle increases in size, it is expected that the pore space would do as well. Particle interlock originated from angled geometries of the sand grains, and friction among particles may have prevented particles to move freely in the packing space to rearrange their positions. That might have led to a reduced packing density compared to glass spheres that displayed a smoother surface compared to sand grains.

In terms of tortuosity, the paths in a pore network of packed sand grains are more sinuous compared to the paths in a packed bed of spheres. This is an important indicator that provides information about how particle shape affects the pore space within a packed structure.

Figures 4-4 shows the plots corresponding to cases Sand250 and Sand300. As observed in those cases using spherical particles, the curves compared in the plots show a small gap between XMT and DEM predictions, indicating a small underestimation of packing density in DEM. This difference is evidence that there are more empty spaces present within the extracted volume from the DEM bed. However, the trends show a very good agreement following the data captured with XMT.

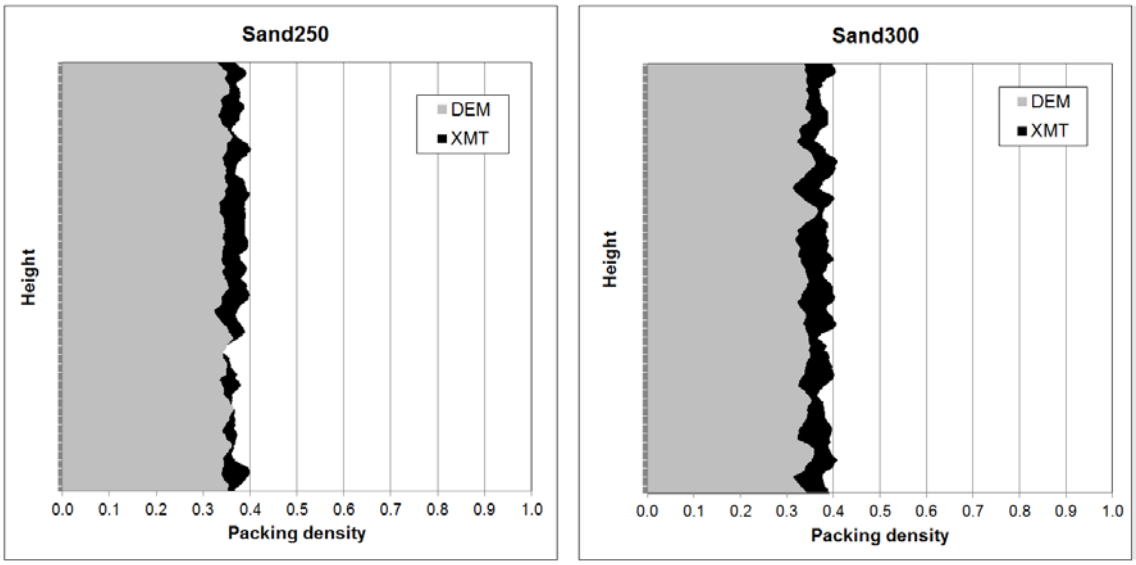

Figure 4-4 Sand250 and Sand300 density profiles comapring XMT and DEM beds

One reason leading to the aforementioned underestimation of DEM predictions could be explained as follows. A careful selection of individual sand grains was done based on the corresponding PSD before configuring DEM simulations. However, the total number of particles that would fill the entire domain is unknown beforehand. Furthermore, the number of particles for every group in the PSD is also unknown. It is possible that more large particles were added to the domain in DEM simulations, having less number of small particles in the bed which tend to occupy small voids, thus having smaller per-slice packing density. This may have leaded to reduced packing densities in DEM structures compared to XMT ones.

4.2. DigiFlow validation cases

LBM has been tested in different applications, for instance for flow past a fixed object such as circular cylinder, sphere, or a flexible string, Couette flow, Poiseuille flow, and flow through porous media. In order to make use of the methodology and apply it to the

desired configurations, it is important to test and validate the implementation to know its capabilities and limitations.

To validate the DigiFlow module, selected analytical situations are included in the following sections. For instance, a laminar Poiseuille flow in an empty channel is presented first, including tests to the three different boundary conditions to initialise a fluid. The second part includes the fluid flow in porous media characterised by its hydraulic conductivity, also known as permeability. Packed structures were generated with XMT and DigiDEM to run simulations of fluid flow through porous media. The validation was done comparing permeability values predicted from simulations with analytical ones calculated using the Kozeny-Carman equation (for a bed of spheres), and experimental data from the literature for permeability in sand grain beds. In the last section a validation test was carried out using experimental data provided of permeability in different rock samples.

4.2.1. Fluid flow in an empty duct

In this section three different configurations were tested to initialise a fluid flow for the boundary conditions implemented. Body force, pressure and velocity were tested using both periodic and virtual boundaries for each case. A superficial velocity of 10^{-4} in LBM units was targeted once a steady state (numerical convergence) was achieved.

The system domain consisted of a duct of length L = 200 voxels with a squared cross-section a = 100 voxels and solid walls in directions perpendicular to the fluid (i.e. Y and Z direction). PBC and VBC were tested in the direction of the flow, i.e. X direction. The relaxation parameter was maintained as 0.6 in all configurations for consistency; the only parameter varied was the input value at the inlet boundary.

When defining a body force value, the density distribution functions are initialised for every fluid site in the system. For pressure and velocity boundary conditions, these are defined at the inlet; every fluid site in the cross section at the inlet is initialised to result in DDFs yielding the desired pressure/velocity.

In order to achieve a steady state flow the simulations were run for a number of iterations to allow DDFs to propagate along the length of the duct until convergence was achieved. At this point, the superficial velocity in the duct was registered. The total

number of iterations varied since the way in which the fluid is initialised is different from one boundary condition to the other.

The most straightforward configuration was the one defining velocity boundary conditions with virtual boundary. Since the value given as input is the value desired, a steady state fluid was achieved in a few thousand iterations. For this case a velocity of 10^{-4} in LBM units was given as input. For the other two simulations using body force and pressure, a trial-and-error process was followed until a superficial velocity equal or close to 10^{-4} was achieved. Figure 4-5 shows the corresponding plots over the total number of iterations required before reaching convergence for the three cases tested using body force, pressure and velocity boundary conditions.

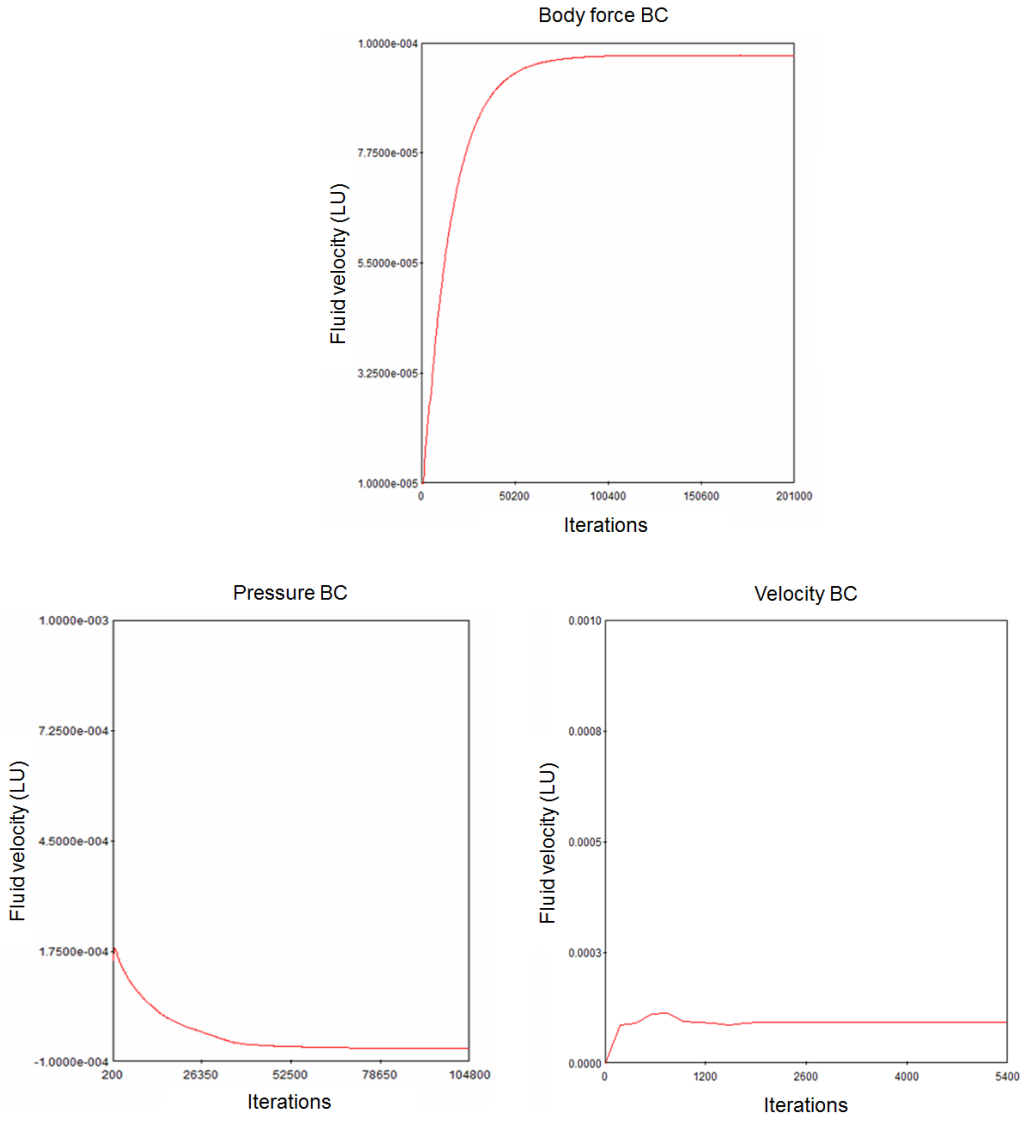

Figure 4-5 Number of iterations to reach convergence for different boundary conditions

It was found that a body force of 10^{-8} gave a superficial fluid velocity of $1.05x10^{-4}$ but at least 150000 iterations were necessary before reaching convergence. To find the pressure value to achieve a superficial velocity of 10^{-4} (or very close to this value), a trial an error process took long time since convergence was achieved about 10^5 iterations for every test case. A precise input value was not obtained due to the length to run this case but it was inferred from the following. An input value of $2x10^{-4}$ resulted in a superficial velocity of $8.27x10^{-5}$, and an input value of $3x10^{-4}$ resulted in a superficial velocity of $1.24x10^{-4}$. So, the input value should be between $2x10^{-4}$ and $3x10^{-4}$.

In Figure 4-5 it is observed that when the velocity boundary condition was imposed at the inlet, only 5000 iterations were needed to reach convergence. Using body force and fluid velocity at inlet gave similar superficial velocities in the duct, but the main difference was that using body force required 30 times more iterations to reach convergence. Such significant difference made obvious the choice of velocity boundary condition with virtual boundaries over body force and pressure to initialise the fluid in further simulations.

In a second stage the length of the duct was varied to assess the superficial velocity at convergence. The four duct lengths were 100, 200, 400 and 800 voxels with virtual boundary in the direction of the flow and a relaxation parameter of 0.6. The same input velocity of 10^{-4} in LBM units was given for all cases. As expected, convergence was reached in less than 10^4 iterations for all the cases. The following table summarises the findings.

Table 4-4 Number of iterations and fluid superficial velocity in ducts with different length

Duct length (voxels)	No. of iterations	Superficial velocity in the duct
100	1000	$1x10^{-4}$
200	2000	$9.96x10^{-5}$
400	10000	$9.83x10^{-5}$
800	10000	$9.69x10^{-5}$

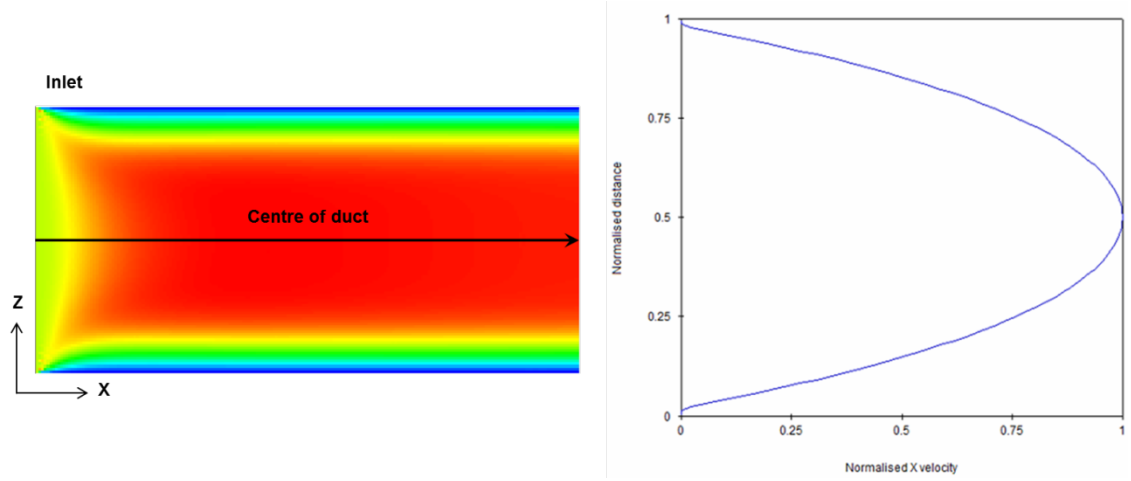

Figure 4-6 Velocity profile along X direction in a duct L = 200 voxels

From this test not only the boundary conditions implemented in LBM were assessed but also an important decision was made. Using velocity boundary condition imposed at the inlet was selected as preferred boundary condition since showed more accurate fluid superficial velocity according to the values obtained, and less iterations were needed to achieve steady state when combined with VBC in the direction of the flow.

4.2.2. Permeability in packed beds of spheres

The estimation of permeability in porous media is of practical interest in different areas such as medicine, chemical and petroleum engineering, and geology. The permeability is closely related to the morphology of the porous structure under study, and depends mainly on the viscosity of the fluid travelling in the pores and the pressure applied.

Although different methods currently exist for the theoretical and experimental estimation of permeability, it is still challenging to carry out tests in-situ and in some cases non-invasive techniques would be preferred to avoid sample contamination, extraction and resizing. If the pore network is known, it is possible to calculate the permeability by solving the NS equations for a given pressure gradient and then obtaining the mean velocity of the fluid.

In some cases it is common to find reports assuming that the permeability of a representative section from a sample means that the entire volume has a homogeneous permeability. This approach is practical for calculations; however permeability not solely depends on voidage but more importantly in the morphology of the pore network, pore volume distribution and the number of interconnections among

pores. From this perspective, it is clear that it is not simple to visualise the entire pore network and interconnections to find a correct relationship between these parameters and permeability.

Different semi-empirical and semi-theoretical approaches exist to study the fluid transport in porous media. In this work the permeability in porous media was studied taking into consideration the Kozeny-Carman equation (KC), a popular model relating permeability and porosity. The dimensionless Kozeny-Carman equation (4-1) is used in this section to assess the predicted permeability values from LBM.

$$k = \frac{\varepsilon^3}{180(1-\varepsilon)^2} \tag{4-1}$$

Packed beds of spheres of 64 voxels in diameter were generated varying the bed voidage ε. The bulk region was extracted from the packed bed, as practiced in the previous section. The volume extracted was then transferred to DigiFlow to run simulations of fluid flow through porous media and calculate the permeability of every structure. Different voidage values were targeted to visualise a trend of the effect of this parameter on the permeability of the structures.

Dimensionless permeability predictions from DigiFlow were calculated using equation 3-69, configuring parameters bf = 0.0001 and τ = 1. The results are presented in Figure 4-7 comparing permeability values from predictions and KC equation in function of bed voidage. Data points from this work were calculated using fluid velocities once a steady-state fluid through the medium was reached.

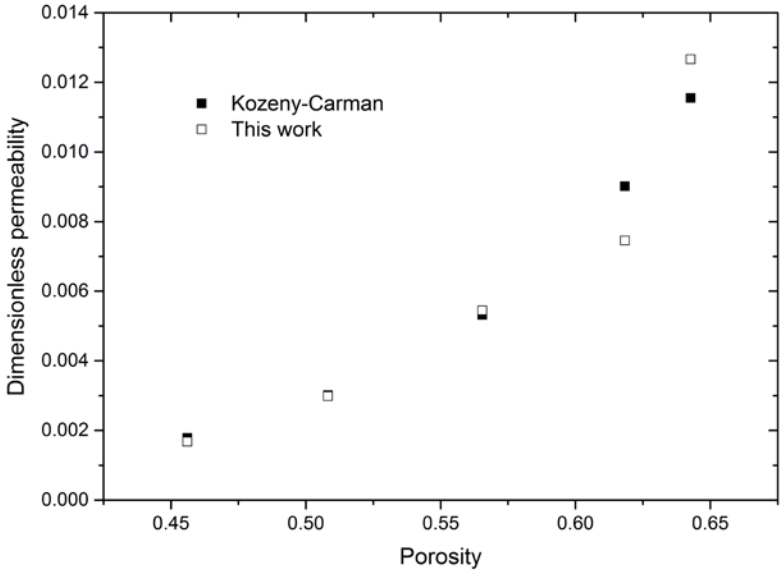

Figure 4-7 Permeability in packed beds of spheres: LBM predictions against KC values

From Figure 4-7 it is observed that for the 3 lowest porosities the predictions compare very well to calculations with the KC equation. However, the 2 high-porosity predictions present discrepancies. It is known that KC equation was derived considering a structure having capillary conduits as pores keeping constant the particle size. Although this equation has been successfully applied to estimate the permeability in random sphere packings (Carman 1937; Klemm et al. 2001), it has some limitations. This equation can be applied only to laminar flow systems with small fluid velocities in the pores. For this reason, for the two cases with high porosity, as the pore size increases, the fluid velocity in the pores does, and the presence of transitional or turbulent flow should be taken into consideration. The Re found for ε = 0.643 was close to 93, value that falls into the transitional regime. The highest relative error found was 17% for ε = 0.618.

4.2.3. Permeability in packed beds of sand grains

Packed sand grain beds were generated following the same procedure as previously described in DEM validation section. The new XMT and DEM packed beds were considered for permeability calculations in DigiFlow. Experimental data on permeability was selected from Huettel et al. (1996) and used as reference to compare with predicted values.

It was challenging to find data from experiments reporting permeability in sand grain samples in the literature. The available sand grains in the laboratory were the mean particle size reference to search experimental data in order to match particle size in digital packed beds.

Initially, the packed structures generated previously from XMT and DEM were subject to fluid flow. A representation of the structure used in DigiFlow is shown in Figure 4-8. The image on the right-hand side is the volume having a fluid flow through the pore network. The solid grains are indicated in solid blue colour; the fluid is represented by a RGB (red, green, blue) scale with warm tones (yellow, orange and red) corresponding to high fluid velocity values, and cold tones (green and blue) to low fluid velocities.

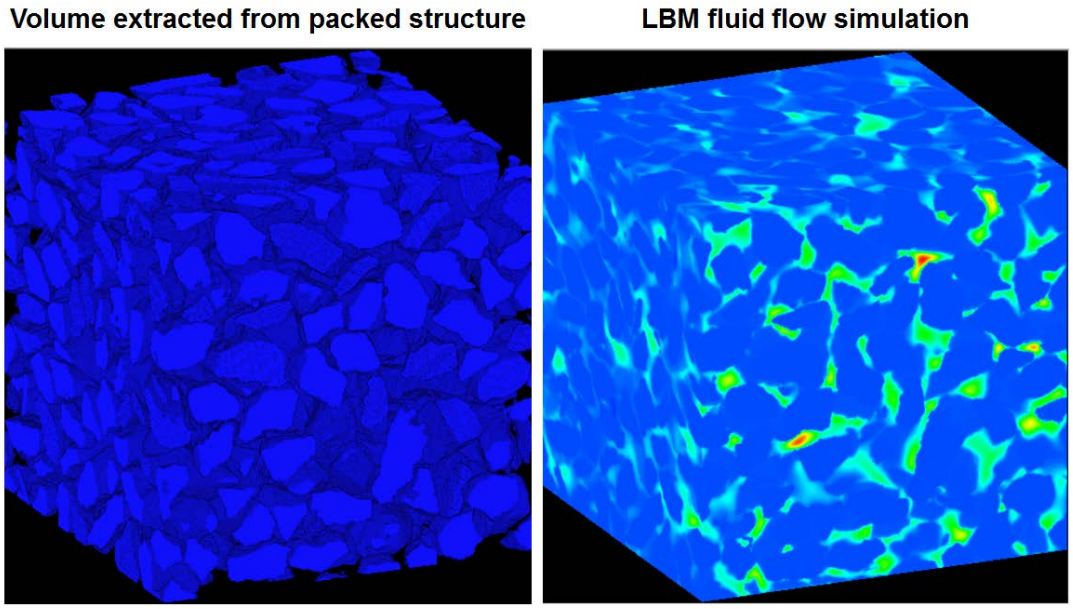

Figure 4-8 Volume extracted from a packed bed of sand grains (left) in DigiFlow (right)

The voidage and permeability data from experiments and predictions are compared in Table 4-5. According to Huettel et al., Sand250 sample was sieved, in this way the PSD reported had a smaller range compared to the one of sample Sand300 that was unsieved. This was considered when scanning the packed beds and generating the corresponding DEM structures. Different attempts were carried out and different packed beds generated since it was found that all predicted porosities were much larger than those ones reported in Huettel et al. (1996).

Table 4-5 Permeability prediction in sand beds compared with experimental data

	ε	Permeability (10^{-11} m^2)
Sand250 (Huettel et al. (1996)	0.164 ± 0.034	4.5 ± 0.1
Sand300 (Huettel et al. (1996)	0.194 ± 0.039	2.9 ± 0.1
Sand250 DigiFlow	0.492	3.22
Sand300 DigiFlow	0.463	3.28

It is important to notice the relationship between voidage and permeability from both samples. In experiments reported, Sand250 showed a smaller voidage compared to sample Sand300. The latter was unsieved, meaning that a much wider PSD was present in the bed. Sample Sand250 was sieved, this means that to some extent, smaller particles that are known to fill in small pores were removed. In contrast, Sand300 was expected to contain those small particles filling in small pores since this sample was not sieved; however the voidage measurement resulted slightly higher compared to Sand250. Now, in terms of permeability values, it was expected that a higher porosity would result in higher permeability, but experimental data did not show that trend between the two samples tested. Regarding the data obtained from DigiFlow, both predictions are consistent between each other, i.e. a similar voidage showed a corresponding similar permeability. The voidage values resulted to be higher compared to those form experimental data because samples were neither shaken nor compressed before digitisation with XMT.

The data included in Table 4-5 shows a relationship between voidage and permeability, but it is not limited to a simple comparison. A pore volume distribution evaluation complemented with analysis of the pore network, tortuosity and pore interconnection would provide an in-depth insight about the causes and effects in the packed bed. The next section provides a more extended discussion about permeability in sandstone.

4.3. Particle fluidisation and segregation in plug flow

In this section, two cases of fluidisation and segregation of particles are presented. The purpose of carrying out these tests was to assess the current option implemented in

DigiDEM to simulate a plug flow-like fluid flow. The plug flow model is a simplified approximation to represent an ideal fluid having a constant superficial velocity in the entire domain. Such assumption makes the model easy to implement and it has practical applications for models in which knowing the superficial velocity of the fluid is enough to predict the overall behaviour of the system.

In a two-phase system the presence of solid objects modifies the total number of fluid sites per cross section. In order to keep a constant velocity in every cross sectional area perpendicular to the fluid flow, the local velocities must be modified depending on the per-cross section free fractional area. For example, if half of a cross sectional area is occupied by solid sites and the other half corresponds to fluid, then all the fluid sites in that cross section will have their velocity doubled in order to maintain a constant velocity in the cross section and in the whole system.

To better understand the constant fluid velocity assumption in plug flow, Figure 4-9 shows a configuration with two spheres aligned one next to each other. A flow velocity of 1000 LU/s was configured. A cross section with no solid sites would have an effective fluid velocity of 1000 LU/s in every individual site. However, for a cross section located at the middle position of the spheres, the velocity in every fluid site will be modified according to the free area fraction in that specific cross section. For instance, if the free area fraction is 0.98, then every fluid site in that cross section will have an augmented velocity of 1020.4 LU/s in order to maintain a constant velocity of 1000 LU/s in the entire domain. The same logic is followed for every axial cross section in the domain.

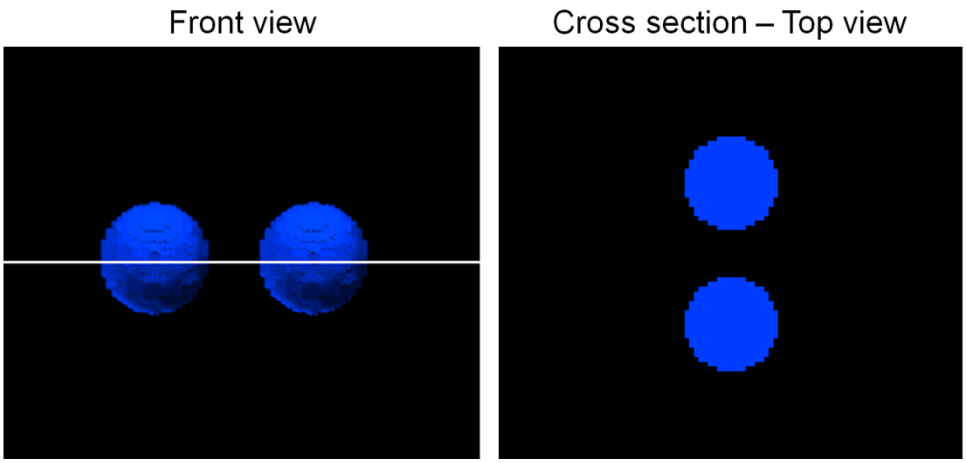

Figure 4-9 Cross sectional view of free area fraction for fluid sites

This difference becomes more significant in a multi-particle system where the free area fraction is dramatically reduced. Misleading interpretations of terminal velocity and minimum fluidisation velocity could be derived from plug flow simulations if the aforementioned effect is not taken into acount. This is because a small fluid velocity might actually fluidise the particles due to the largely augmented per slice fluid velocity. Although interstices between particles may have an effect on local fluid velocity increase, the artificial increase in plug flow comes from a different source. A case in which a particle was fluidised from a multi-particle cross section is left alone at some point, may result in the particle settling down due to per slice local fluid velocity reduction.

DigiDEM had implemented one mode for drag force calculation in plug flow simulations corresponding to the laminar regime (Stokes drag). Before running the tests, the Rayleigh drag was implemented to account for the transitional and turbulent regimes. The two equations used to calculate drag were:

Stokes $$F_{D-St} = 6\pi\mu r u_{rel} \quad (4\text{-}2)$$

Rayleigh $$F_{D-Ra} = 0.5\rho_f u_{rel}^2 c_D A \quad (4\text{-}3)$$

In both equations the relative velocity between the particle and the fluid is used. Based on the configuration of the system and the particles used in simulations, the user should know beforehand the fluid regime expected in order to select the correct mode from the configuration.

To know the mode to select, Plug Flow – Stokes or Plug Flow – Rayleigh, Re of the particle Re_p should be taken into account. Considering a single sphere travelling in a fluid with terminal velocity u_t, the drag force exerted on the surface of the sphere depends on the fluid in its immediate vicinity and on the particle drag coefficient. This parameter depends on the particle shape, orientation and Re_p. When looking at Re and the corresponding fluid regime ranges reported in the literature, it was found that information varied greatly among authors showing different limits for every regime. After evaluating different resources, a book written by Richard Holdich (2002) was selected as reference since it was considered to provide reliable data including clear descriptions and reasoning of the different regimes and the methods to calculate terminal velocities of particles and their corresponding Reynolds number. Furthermore,

the book included the Heywood tables (Heywood 1962) which have showed to be more accurate to find terminal velocities of spherical particles up to a Re of 10^5. Fortunately Richard Holdich (Holdich n.d.) developed an online tool to easily calculate terminal velocities of spherical particles by providing basic information of the system such as particle size and density, and fluid density and viscosity. The online tool provided the terminal velocity and Re_p at this velocity. Knowing that, the user can easily decide which regime to select for simulations since the Stokes upper limit is commonly set as 0.2. For larger Re_p Plug Flow – Rayleigh should be selected.

In plug flow tests particle fluidisation and separation was expected to be achieved by considering the force balance between drag and weight of the particles. Having as reference the specific weight of a sphere, the fluid velocity to make that sphere rise in the fluid was found from equation (4-2) or (4-3), depending on the fluid regime. Figure 4-10 presents a free-body diagram showing the forces acting on a sphere immersed in a non-zero velocity fluid. The gravity force F_G acts on the sphere pulling it down, whereas the drag force F_D pushes it upwards due to the viscous forces originated by the fluid in motion. Analytically the sphere would remain suspended if all the forces acting on it are balanced. For material densities much larger than the fluid, buoyancy force can be neglected and the balance of forces is only between F_G and F_D.

$$F_G = V_{sphere}(\rho_s - \rho_f)g \tag{4-4}$$

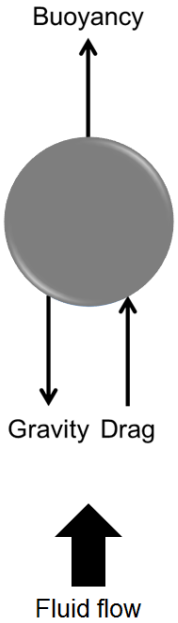

Figure 4-10 Forces acting on a particle immersed in a non-zero velocity fluid

Equating (4-4) with (4-2) or with (4-3), depending on Re_p at u_t, and solving for u, the velocity at which the balance of forces takes place is found. This serves as reference to have an idea of the minimum necessary velocity to balance the forces and indicates that any fluid velocity larger than the one found should make the sphere rise. A smaller value would cause the sphere to sink. Keeping the fluid properties equal, calculations from (4-4) show that F_G is larger for bigger particles made of same material.

For a test of fluidisation of particles with same density but different size, carrying out a similar force balance for the largest particle size to be fluidised resulted in the fluid velocity that should make all the particles rise. If only a specific size is to me fluidised, then the force balance analysis should be carried out for that specific particle size.

4.3.1. Spherical particles segregation

This case was configured to observe separation of spherical particles in a domain by fluidising only the two smallest particle sizes while the larger ones remained at the bottom. The sphere diameters selected were 6, 8, 10 and 12 mm, all of them having the same density of 1500 kg/m^3.

Calculation of the parameters F_G and u_t was carried out first for every particle size. All Re_p were well above the Stokes limit, therefore the Plug Flow - Rayleigh mode was configured for simulations.

In order to separate the spheres with diameters 6 and 8 mm from the larger ones, the terminal velocity of particle 8 mm was taken as reference. This meant that a fluid velocity greater than 0.367 m/s should fluidise spheres of diameters 6 and 8 mm. The force balance for d_p = 8 mm was carried out between F_G and F_D substituting in (4-8) a velocity of 0.4 m/s. The resulting drag force was indeed larger than the gravity force. The same procedure was followed for all particle sizes to confirm that the selected fluid velocity would fluidise only the smallest particles, taking care that drag for d_p = 10 mm was not larger than particle weight.

Figure 4-11 shows a sequence of snapshots taken at different time steps to register the evolution of the simulation. The initial *ts* is not zero because first particles were poured down from the top of the domain and allowed to settle down.

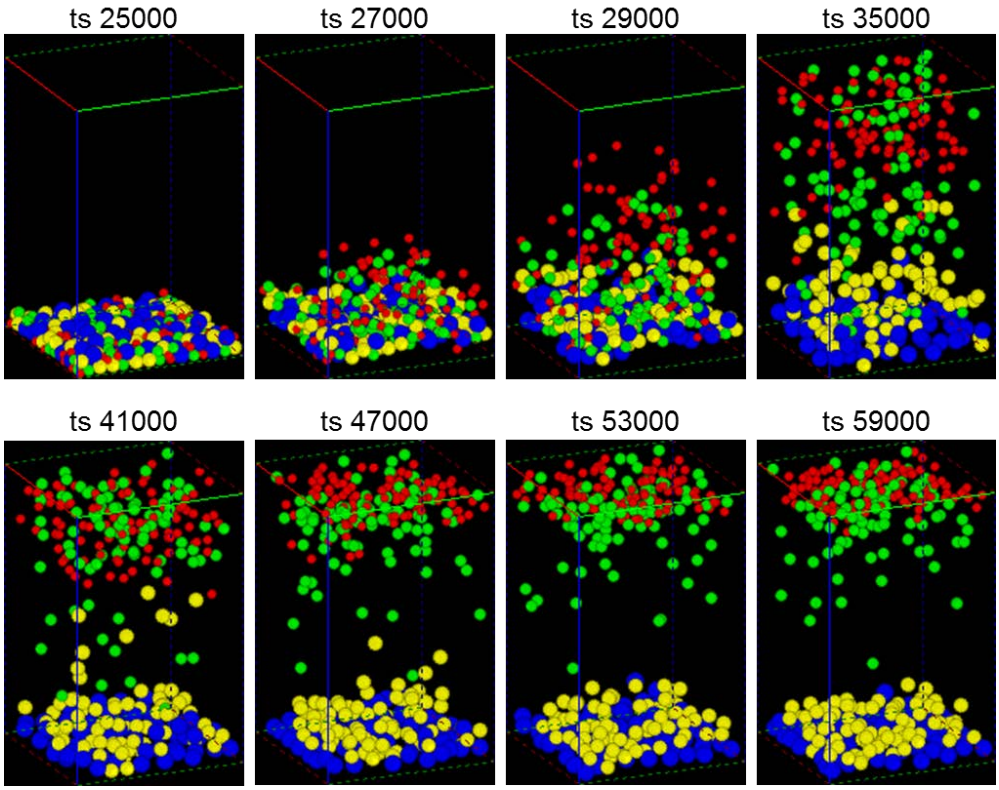

Figure 4-11 Spheres fluidisation and segregation in plug flow fluid

In Figure 4-11 the colour code corresponding to particle size is: d_p = 6 mm red spheres; d_p = 8 mm green spheres; d_p = 10 mm yellow spheres; d_p = 12 mm blue spheres. From the images it can be observed that at ts = 27000 the particles start to be fluidised, including some of the largest particles. This is an effect caused by the frictional forces between the spheres originated by the smallest spheres travelling up and even pushing upwards large spheres blocking their way. Even at ts 35000 some particles reach a significant height due to the inertial lift caused by the other particles, but they returned to the bottom after a number of steps.

Overall the behaviour observed was as expected according to the calculations carried out previous to the configuration and execution. When the fluid was switched off, the smallest particles travelled down to the bottom of the container but remained on top of the largest particles showing an obvious interface and separation by size.

4.3.2. Sand grains segregation

A similar case using sand grains was configured to observe fluidisation and segregation. Only two particle sizes were considered for this configuration. The reason

was that the same system was used as well for coupled DEM-LBM simulations. In order to obtain results in a reasonable time, a small domain with relatively a small number of particles was desired for coupled simulations since they were generally more computationally expensive.

Using the similar approach as in the previous section, the terminal velocity for the sand grains was calculated using the VED for the smallest size. The small particles to be fluidised had a ψ = 0.67, VED = 15.056 LU equivalent to 7.53 mm, and density of 1200 kg/m^3. The big particles had a ψ = 0.54, VED = 24.466 LU equivalent to 12.23 mm, and density of 3000 kg/m^3. Small particles are represented in Figure 4-12 in blue colour.

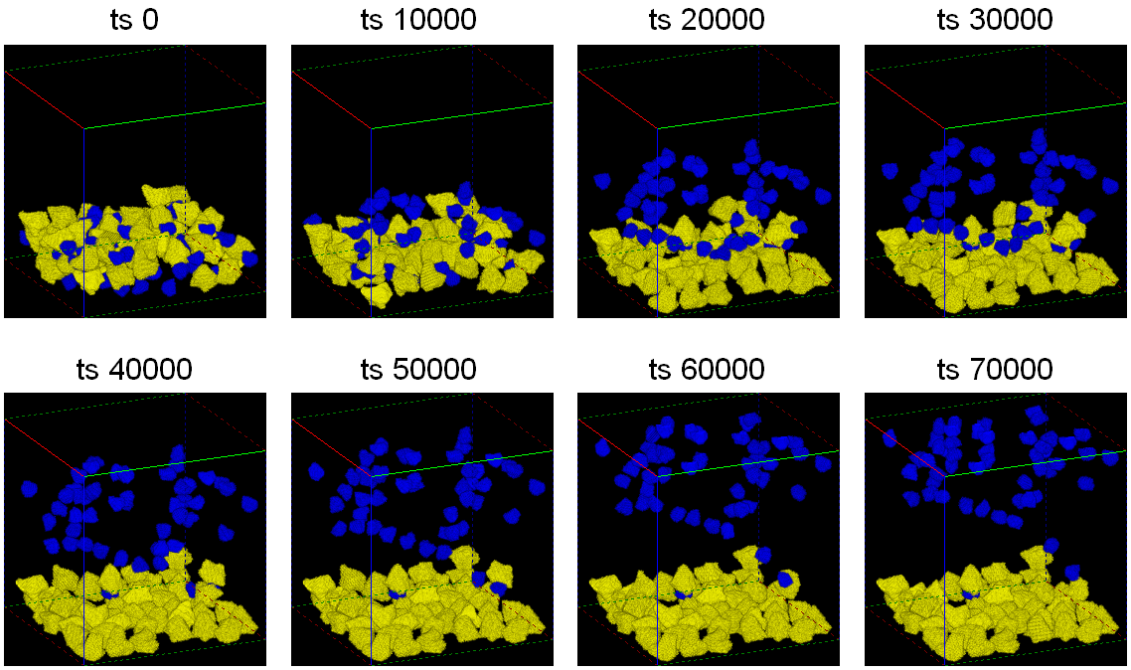

Figure 4-12 Sand grains fluidisation and separation by size and density

Friction force between particles is likely higher in this case due to the geometric nature of sand grains; additionally, cohesive and adhesive forces are present between the particles and in particle-wall interactions. Another feature to notice is that for spherical particles the area facing the upward flow is always the same, but for particles at rest with different geometries the area projected perpendicular to the flow is different. The surface facing the upwards flow may not be neither smooth nor aerodynamic; it might actually present more resistance if one or more of the faces are flat. Also to consider is the fact that when the particles were packed letting them settle down in vacuum, they arrange and orient themselves in such a way that they might fit gaps between particles, making the bed more cohesive and more difficult to expand with the fluid due to higher

friction forces caused by such arrangement and the surface roughness representing an additional opposition force.

Plug flow is a simplified model that helps to understand the behaviour of particles being dragged by a constant-velocity fluid. When more complex fluid-structure interactions are to be simulated with more accuracy, different models to represent the fluid should be employed. In this work the attempt to do so was using LBM.

5. Coupled DEM-LBM validation

In this chapter fundamental validation cases are presented for FSI using the coupled DEM-LBM one-way and two-way modes. The validation stage is very important to confirm in this way that the algorithm implemented is indeed working as intended. To do so, selected experimental and numerical data reported in the literature was taken as reference to carry out simulations following different configurations.

It is worth mentioning an interpretation that the author found from different research published in the literature. Different authors report on FSI fundamental test configurations to validate coupled DEM-LBM implementations. Such configurations normally involve only one fixed object immersed in a fluid. At first this may not seem to be a fully coupled DEM-LBM algorithm to test since only one particle is included in the system and it is not interacting whatsoever with any other solid object. Furthermore, the solid object is fixed in the system and it is only the fluid which interacts with the fixed object at the surface. In the strict sense of the fluid-structure interaction concept, there is indeed an interaction between the solid and the fluid at the interface. However, the author considers that the capabilities of DEM are not used at that stage. What it is being evaluated in those configurations is the bounce-back link method implemented (either half-link or at true location of the boundary by means of extrapolation and interpolation) to deal with boundaries in a fluid. Some authors report a DEM time step for a configuration of a single particle fixed in a domain when in fact, there is no need at that stage to define a DEM time step since the solid object is not moving. In this work the author considers a fully coupled DEM-LBM when the object is in motion. Moreover, to take full advantage of the coupling, more solid objects should be added to the system to fully assess the solid phase interaction with DEM when objects are immersed in a fluid, part covered by LBM.

Having considered that, fundamental configurations found in the literature are included in this chapter that work as benchmark to test the DEM-LBM implementation. At this stage, the mode named *one-way* implies that the presence of solid particles immersed in a fluid is going to affect it only as a boundary present in the fluid, but particle velocity data is not fed to LBM. On the contrary, in the *two-way* mode the particle velocity data from DEM is used by LBM to update the corresponding properties of the fluid and calculate the relative velocity considering the translation and rotation of solid particles.

5.1. Fluid flow past a fixed sphere

The initial case to test and validate the coupling for fluid structure interaction was the fluid flow past a fixed sphere. The sphere was placed at the centre of the domain and the empty space around it was filled with a non-zero velocity fluid. The fluid velocity BC was initially configured at the inlet boundary. Different data points were obtained varying the inlet velocity for different Reynolds numbers.

The steady-state fluid velocity field was used to calculate the drag force exerted by the fluid on the sphere. In turn, this force was used to calculate the drag coefficient from equation (3-64). The configuration parameters follow a similar test for DEM-LBM carried out by Owen et al. (2011) and Galindo-Torres (2013). The reference data for the drag coefficient in function of Reynolds number curve for a sphere come from the empirical correlation derived from experiments in Mikhailov & Freire (2013).

Bearing in mind that the projected area of a digitised particle may differ to that one of a sphere, a theoretical prediction of the error expected was calculated before running the simulations.

Let us consider a sphere of diameter 1 mm and density of 2650 kg/m^3. When dropped in a quiescent fluid with water properties (density of 1000 kg/m^3 and dynamic viscosity 0.001 Pa s), the sphere's settling velocity in an infinite medium is 0.156 m/s, yielding a Re = 156. Calculating the drag force at this velocity yields F_D = 7.94x10^{-6} N. Now, when the projected area is not a perfect circle but a circle with staircase-like boundary, the projected area used to calculate F_D changes slightly. Having all parameters equal but changing only the projected area, the F_D on a digitised sphere yields 7.98x10^{-6} N; resulting in an error of 0.59% which is acceptable knowing the implications of using digitised particles in the computational environment.

For the configuration the sphere was placed fixed in the centre of a domain with dimensions 0.96x0.24x0.24 m in X, Y and Z directions. The data used was obtained from Owen et al (2011). The relevant parameters are presented in Table 5-1; the configuration in the simulation is shown in Figure 5-1.

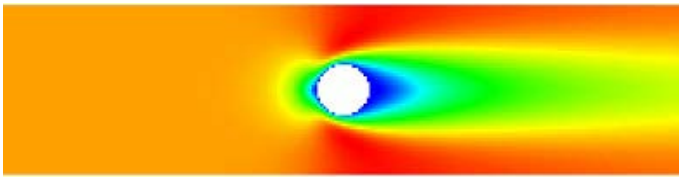

Figure 5-1 Configuration of fluid past a fixed sphere

Table 5-1 Simulation parameters for flow past a fixed sphere configuration

τ	Δx (m)	Δt (s)	v_{phy} (m^2/s)	ρ_f (kg/m^3)	d_p (m)
0.6	0.004	0.016	10^{-4}	10^3	0.072

Knowing the desired Re value, the corresponding fluid velocity was calculated and the value was set as velocity boundary condition at the inlet. The fluid was allowed to reach a steady state before reading data. Two types of boundary conditions were tested for the boundaries of the domain, periodic and virtual.

Since Δt_{LBM}, τ, u_f and ν_f are interrelated, the selection of the relaxation parameter and fluid viscosity was essential to avoid numerical problems. If the relaxation parameter was fixed as 1, the Mach number obtained was too large for LBM simulations as shown in Table 5-2 below.

Table 5-2 Calculation of *Ma* using different viscosity values with τ = 1 and Δx = 0.001 m

	viscosity (m^2/s)	***Ma***
Configuration 1	10^{-6}	42.3
Configuration 2	10^{-3}	0.0423

It is evident that when using the kinematic viscosity value of 10^{-6} m^2/s, the value of *Ma* does not satisfy the condition for LBM fluid stability. However, when the value was reduced to 10^{-3} m^2/s, the value of *Ma* is smaller than 0.1 and numerical stability in the fluid can be ensured. For this reason, in order to obtain reasonable representations the numerical fluid parameters were adjusted in a way that the cell speed is small enough when compared to $u_{f_{\max}}$ (Feng et al. 2010).

Initial results from DEM-LBM simulations are presented in Figure 5-2 along the reference data from Mikhailov & Freire (Mikhailov & Freire 2013). The solid line corresponds to experimental data whereas discrete points correspond to numerical simulations. Data points from DEM-LBM simulations follow the reference data but all the values were overestimated. The Y axis does not display log scale values (as commonly a c_D vs Re plot does) to better observe the departure of the data points from the reference curve.

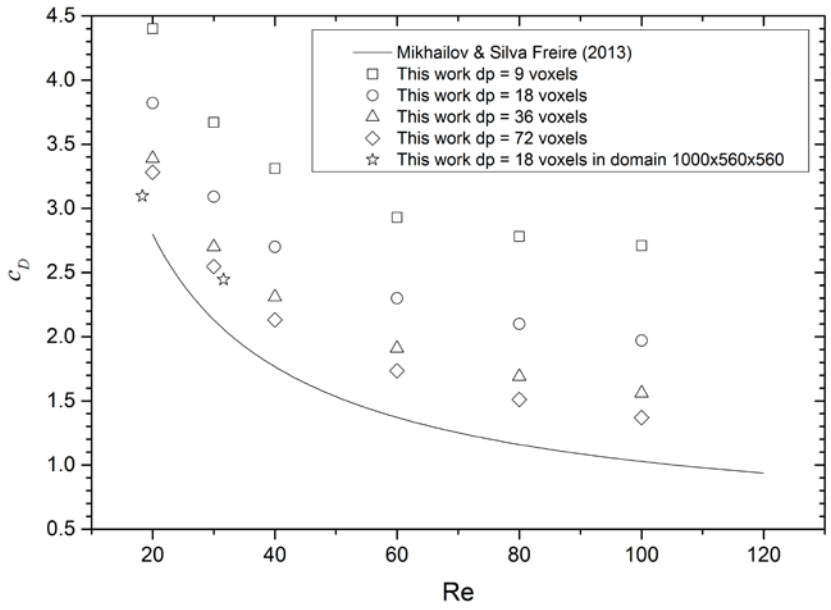

Figure 5-2 Flow past a fixed sphere c_D vs Re plot

Two additional attempts were run. The gap between the surface of the sphere and the boundary was increased 30 radii with the intention of mitigating the boundary effects. In Chapter 4 PBCs were tested and it was found that the wave propagation effect affected drag and a large number of iterations were required to initialise the fluid to a steady state. All the data points in Figure 5-2 were carried out using VBC, unlike PBC as configured in the reference papers (Owen et. al and Galindo-Torres). In order to reduce the PBC effect, the direction of the flow was increased to 1000 voxels in order to use PBC as in reference papers and observe the effects of using different BCs.

In order to further investigate the possible reasons giving such overestimated values, different attempts were carried out to observe the effect of varying parameters in the simulations and the use of VED in equation (3-64). The details of these attempts and the corresponding findings are presented next.

Keeping Re very close to 20, the sphere was repositioned along the X axis to observe the effect caused on c_D when the edges of the sphere were not aligned with the computational grid. Ten different positions were tested corresponding to fractional locations within 1 voxel length. The values obtained are presented in Table 5-3 below considering c_D = 2.8 for Re = 20.

Table 5-3 Values of c_D at different cell fractional positions

Position in X	c_D	Position in X	c_D
120.0	3.82	120.6	3.89
120.1	3.85	120.7	3.88
120.2	3.88	120.8	3.88
120.3	3.89	120.9	3.86
120.4	3.89	121.0	3.82
120.5	3.89		

It is inferred from the data provided by Galindo-Torres (2013) that τ was kept constant for all the simulations. However, to achieve higher Re, τ must have been modified. Similarly, only one value of body force to drive the fluid was reported by the author. For this reason there were two ways to proceed, one keeping τ constant as 0.8 and increase the fluid velocity to achieve the desired Re. The other one was to modify τ in order to achieve higher Re. It was observed that using τ = 0.8 did work to obtain a Re value close to 40, but not to achieve higher values because the system became numerically unstable. When modifying τ to be 0.6, higher Re values were obtained without finding numerical instabilities. The results for the two cases varying τ are presented in Table 5-4. In general, it was found that configuring VBC at the outlet showed reduced c_D values compared to PBC.

Table 5-4 Values of c_D obtained for a range of Re varying τ

Re	c_D (Mikhailov & Freire 2013)	[1] c_D DEM-LBM τ = 0.6 VBC 50000	[2] c_D DEM-LBM τ = 0.8 PBC 50000
20	2.712	3.732	3.924
30	2.120	3.014	3.890
40	1.739	2.642	4.949
60	1.355	2.264	unstable
80	1.137	2.081	unstable
100	1.016	1.982	unstable

Analysing the variables involved, force, fluid density and average fluid velocity are data retrieved from simulations. Knowing that numerical stability is related to mass conservation, the fluid density value should be always equal or close to 1 in the LBM environment. When fluid steady state was reached it was observed that indeed density was very close to 1 and also that the average fluid velocity in the domain was very close to the value set at the inlet. For example, the fluid velocity in LBM units configured for Re = 20 and τ = 0.8 was 0.11112, and the mean fluid velocity in the simulation was 0.111909. Nevertheless, the mean fluid velocity used in the calculations was further studied.

In Table 5-5 results of c_D are presented using different calculations of average fluid velocity. One column corresponds to calculations using the average fluid velocity over fluid and boundary nodes in X, Y and Z middle slices of the domain taken at the last LBM iteration, i.e. at steady state. The second one was similarly calculated but in this case the history of the data was considered, i.e. middle slice X, Y and Z data was saved every LBM iteration until reaching a steady state and then averaged. The final column corresponds to the calculation averaging all the fluid and boundary sites in the entire domain at steady state. Two c_D values are presented for every case, one calculating the projected area using the area in voxels, and one calculating the

[1] Data using VED
[2] Data without using VED

projected area using the VED = 0.07246 m instead of the original value d_p = 0.072 m. It was found that the closest value to the reference is the one calculated using VED and u_{f-avg} over middle slices every LBM iteration.

Table 5-5 Values of c_D for different u_{f-avg} (τ = 0.6, PBC, Re = 32, ref. c_D = 2.038)

Projected area calculation	c_D with u_{f-avg} over XYZ middle slices at final LBM iteration	c_D with u_{f-avg} over XYZ middle slices every LBM iteration	c_D with u_{f-avg} over entire domain at final LBM iteration
Using voxels	4.716	4.687	5.345
Using VED	4.685	4.656	5.309

According to Strack & Cook (2007), increasing the distance between the surface of the sphere and the boundary of the domain at least 30 radii would help to reduce significantly the effects on the drag calculation influenced by PBC. At first a cubic domain of 270 voxels was configured in order to avoid very large computational time for the simulations and first observe the effects of an increased gap between the lateral boundary wall and the surface of the sphere. Preliminary results are shown in Table 5-6. It was evident that for d_p = 18 voxels (as in the paper taken as reference) c_D was indeed smaller compared to previous simulations results. For this reason, an additional test was configured but this time having the recommended gap between the sphere and the boundary, increasing the cubic domain to 560 voxels. Thus, for a Re = 27.03, the expected c_D was 2.285 and the calculated one from simulations was 2.53, showing a significant improvement compared to initial calculations.

Table 5-6 Values of c_D for a sphere of d_p = 18 voxels in a cubic domain of 270 voxels

Re	c_D DEM-LBM	c_D Mikhailov & Freire (2013)
22.28	2.96	2.60
29.26	2.59	2.17
37.80	2.31	1.83
48.15	2.10	1.57
59.18	1.96	1.38
69.78	1.88	1.25
77.78	1.84	1.18
91.23	1.80	1.08
97.73	1.80	1.04
105.89	1.79	1.00

In the continuous effort to find the reason why the predicted values did not fit closer the reference curve, different papers in the literature were found. The two most valuable for the present work were the report of Pettyjohn & Christiansen (1948) presenting experimental correlations for drag on ellipsoids, cubes, octahedrons and tetrahedrons; and the correlation developed in Yow et al. (2005) based on an comprehensive research to obtain experimental data for a range of particle sphericity ψ and Re.

The way in which the sphere of 18 voxels diameter is represented in the present work is following the digitisation process as explained in Section 3.5.3. The sphericity of the 18 voxels digitised sphere is in fact 0.67; value that can be found in the plot reported by Pettyjohn & Christiansen (see Figure 5-3). It has been demonstrated that as the sphericity of a particle departs from 1, the corresponding drag coefficient of the particle appears to be above the curve of a perfect sphere with ψ = 1.

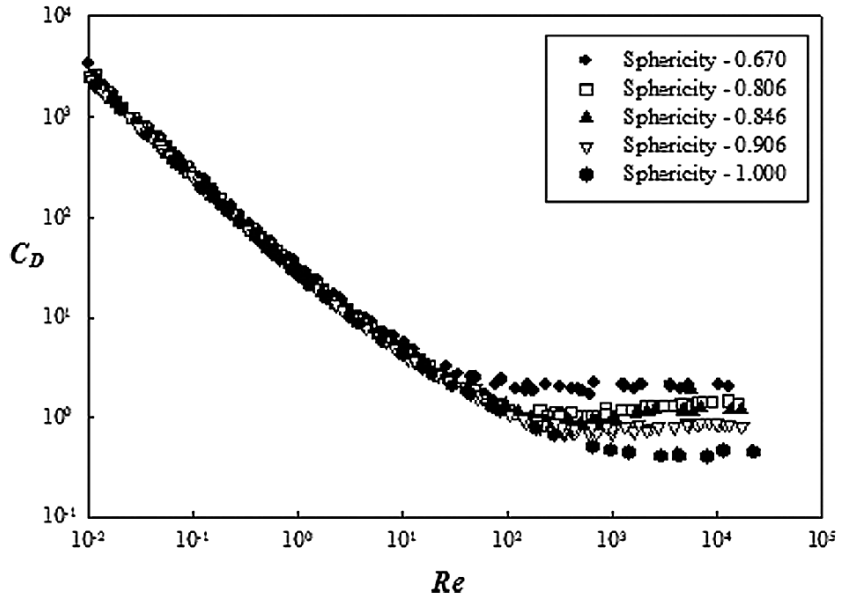

Figure 5-3 c_D vs Re plot in function of ψ (Pettyjohn & Christiansen (1948))

Having in mind the sphericity factor, the previous values obtained from DEM-LBM seem to be more sensible when taking into consideration the true sphericity of the sphere as found by Pettyjohn & Christiansen, and the correlation in Yow's work.

It makes sense to consider the nature of the digitised sphere in the FSI context since geometrical properties of particles interacting with fluids have an impact on the flow behaviour, such as the drag felt by the particle, the formation of vortices and the distribution of the boundary layer on the interface. Sphericity is a shape factor commonly used as a way of measuring how much a particle departs from a perfect spherical shape. In the DigiUtility tool some shape factors are calculated for every particle, including sphericity. Following Waddel's work (Waddel, 1934), the sphericity factor is a dimensionless value calculated as the ratio of the surface area of a sphere having the same volume of the particle in question to the actual surface area of the particle. The surface area of a digital particle is calculated considering all the square faces on the surface exposed to the fluid. The volume of a digitised particle can also be calculated easily considering all the voxels that form a particle.

The comparison of the previous values obtained with the correlation from Yow considering the sphericity factor is shown in Figure 5-4, where the maximum error found was 7.4% for Re ≈ 60 and 70. The comparison was made using data from simulations with a digital sphere of d_p = 18 voxels.

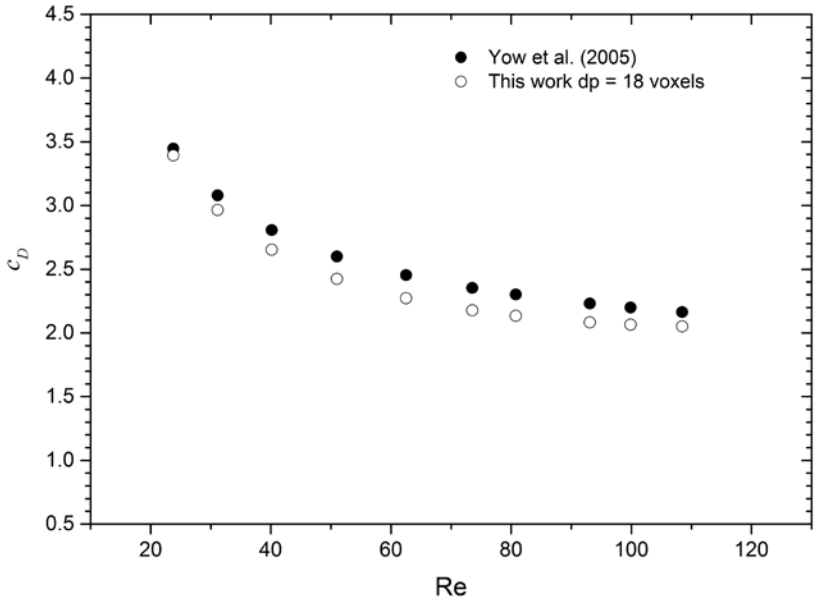

Figure 5-4 Flow past a fixed sphere c_D vs Re plot considering sphericity

It was found that sphericity of a digital sphere remains constant for large diameters (see Figure 5-5). Fluctuations were observed for d_p < 100 in the range (0.65, 0.68). This behaviour tells us that the inherent boundary effects of a digitised sphere have no further significant effect for particles with d_p > 100 in simulations carried out in this work.

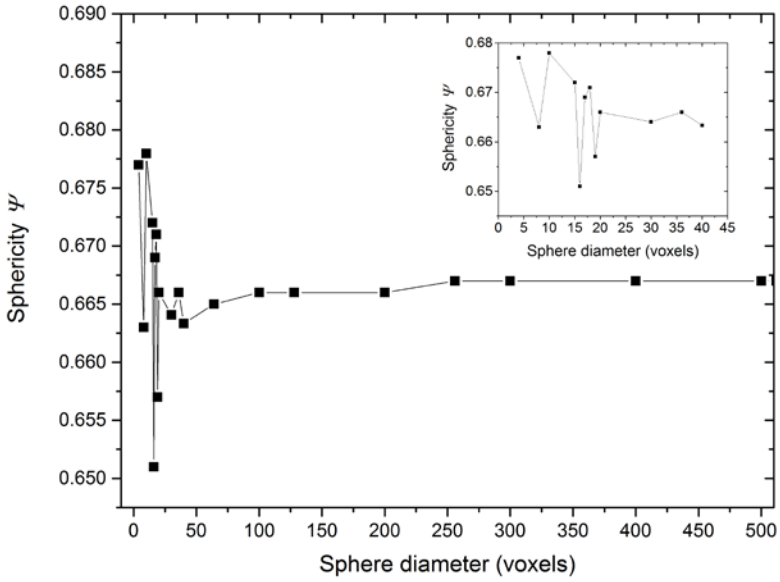

Figure 5-5 Sphericity of digitised spheres for different particle diameters

A sensitivity study was carried out (Guan et al. 2017, in press) running a significant number of simulations to assess the effect of increased d_p on results for c_D for an extended range of Re. The data obtained is presented in Figure 5-6.

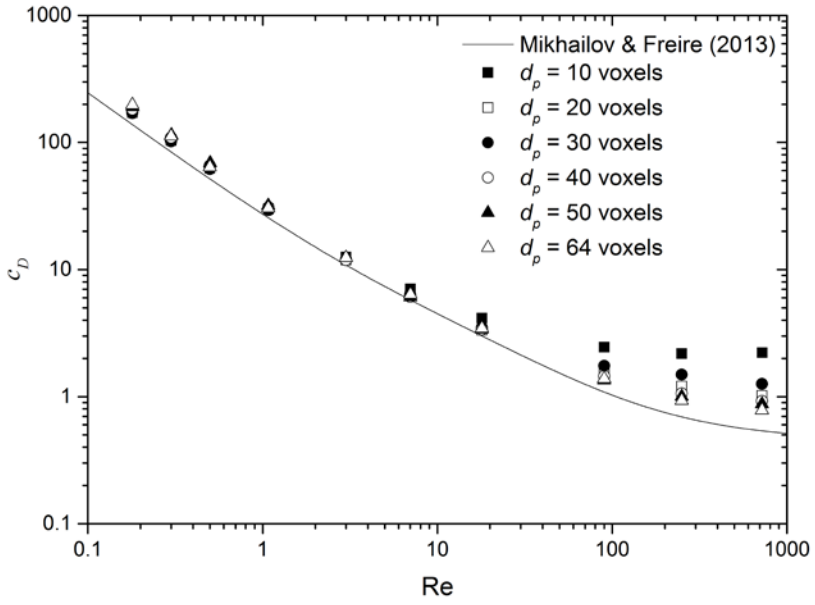

Figure 5-6 Sensitivity of drag coefficient to diameter of a digitised sphere

It is observed that increased resolution showed a better agreement with the reference curve. However the nature of the digital sphere entails a departure from the curve. This effect has been explained by the sphericity factor in Yow et al (2005). Once the comparison is made considering the sphericity, the values predicted showed a good agreement with a maximum relative error of 7.4%.

5.2. Flow past a circular cylinder

In order to test a non-spherical particle for the DEM-LBM coupling FSI on stationary walls, the flow past a cylinder configuration was selected. Cylindrical particles are present in different separation processes and have been subject of study in theoretical and experimental approaches. In other research areas, the flow around pipelines in offshore oil and gas industry is relevant, as well as in instrumentation where cylindrical-shape probes are immersed in a fluid flow.

The drag at which a cylinder is exposed is tested in this section for a Re = 100. The configuration used followed the studies reported in Li et al. (2009). The cylinder was placed at the centre of the domain with dimensions 2000x2000 LU. Such lengths were placed at 50 diameters away from the cylinder to ensure no wall effects affected the

calculations. VBC was configured in the direction of the flow. A relaxation parameter of 0.6 resulted in a fluid velocity of 0.0833 LU configured at the inlet.

The drag coefficient reported in Li et al. was 1.336 for Re = 100; the comparison with references therein showed similar values all falling in 1.3. The simulation carried out in this work resulted in a drag coefficient of 1.226, slightly underestimating the reported data with a relative error of 8.23%.

In order to extend the Re range, simulations were carried out configuring a smaller domain in order to run a number of simulations to obtain different data points. The intention of reducing the domain size was to save time, however in most of the cases it took several thousands of steps to achieve a steady state fluid before reading data. Figure 5-7 shows the c_D vs Re plot containing data points in the Re range 1 to 10^4.

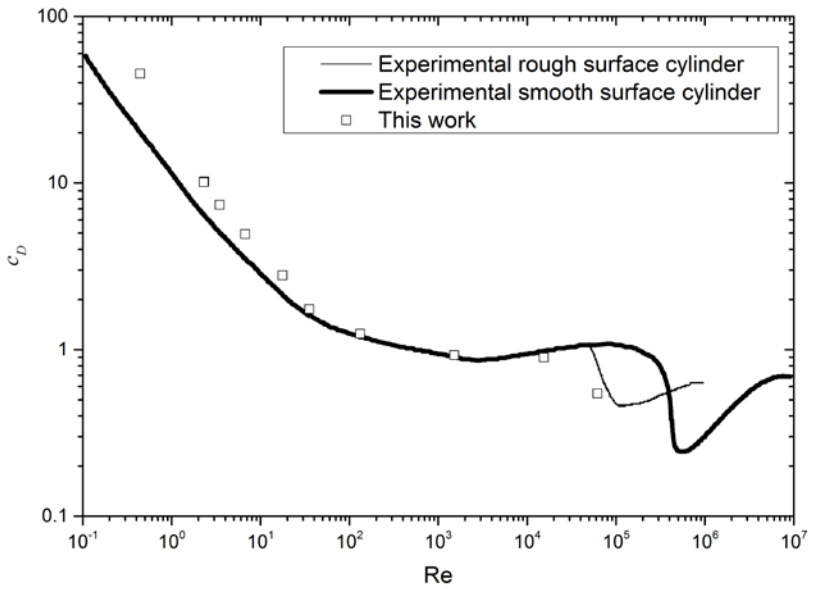

Figure 5-7 Flow past a cylinder drag coefficient at different Reynolds numbers

The first comparison was done with the common curve reported in the literature for a smooth surface cylinder. However, after observing the differences of the produced data points, analysing the nature of the digital representation of the cylinder, and considering the findings from the previous section, a further search in the literature led to a source providing the curve for a cylinder characterised by a rough surface (Schlichting 1979).

The predicted data points showed a good agreement compared to the reference curve, particularly for high Re, where the points followed the experimental rough surface cylinder curve. The accuracy of predictions at this stage was likely to be affected by flow separation expected at this fluid regime. During simulations vortices were developed with increasing frequency. The average fluid velocity plot reached a plateau but strong oscillations were observed due to vortices present in the fluid. A small range of velocities was available for calculations, which could have led to a better fit. However the mean value of the oscillations was taken into account.

5.3. Drag force on two interacting spheres as a function of interparticle distance

In this section a different test case involving two objects for the analysis of drag is presented. The interaction of two objects immersed in a fluid has been studied in various experiments; one of them is the case of fluid flow past two aligned particles. The case presented in a previous section for a single sphere is a well-established experiment to relate the drag force and the Reynolds number.

It has been shown that the drag force present at the interface on a single isolated particle is different than that one on a trailing sphere, and the local fluid around an isolated sphere displays well-known patterns. Experiments carried out in the past intended to show the effects produced on the drag force when the distance between two particles was modified.

The reference data for the configuration and comparison of results was obtained from an empirical correlation formulated from experimental data in Zhu et al. (1994). In this work it was showed experimentally that the drag force on the interface of a single isolated particle is different than the drag on a trailing sphere for an intermediate range of Re.

The drag force on two interacting spheres was evaluated and is presented in this section. The two spheres were labelled as *leading* and *trailing* sphere. The drag force on the latter was affected by the interparticle distance and the wake formed behind the leading sphere. Tests cases are presented varying the interparticle distance for a selected fixed Reynolds number.

For the system configuration, the dimensions of the domain had a particle to column ID ratio of 20/128 ≈ 0.15 (values in voxels). Different cases were configured for simulations, one for a single sphere and the rest for two spheres vertically aligned on the Z axis varying the distance between them. The interparticle distance l to particle diameter d_p ratios were 0.25, 0.75, 1, 2, 3, 5 and 7. All configurations were set trying to keep a fluid velocity that would give a Re ≈ 61. Both spheres were fixed with zero velocity and the fluid was initialised until reaching a steady state. The number of required LBM iterations was tested independently in DigiFlow to find the optimal number to achieve a steady-state fluid.

Figure 5-8 illustrates the configuration of the single sphere (far-left image), the two particles with l = 0 (second image from left to right), and different interparticle distances, showing the trailing particle on top/above the leading one.

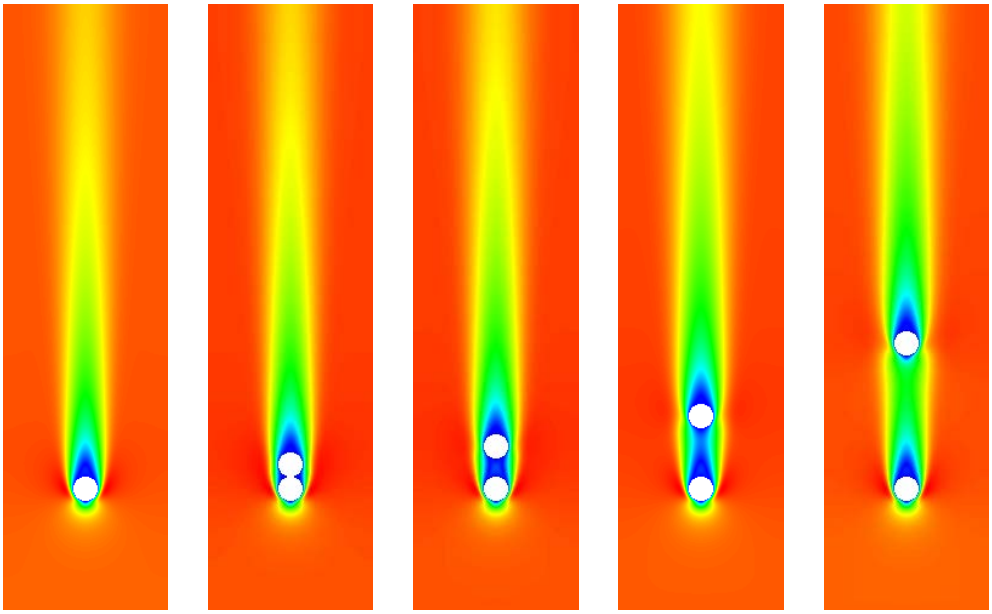

Figure 5-8 Leading (bottom) and trailing (top) spheres configurations for different l

The empirical equation presented in Zhu's work relates the drag on an isolated sphere F_{D_0} to the drag F_D on a trailing sphere in the two-interacting spheres configuration. The comparison of results from simulations with the empirical correlation from Zhu et al. (1994) is presented in Figure 5-9. Both the drag force and interparticle distance are presented in dimensionless form. It can be observed that the drag ratio increased exponentially as the interparticle distance increased as well. A low pressure wake was created behind the leading sphere, an effect seen by the trailing particle as reduced drag.

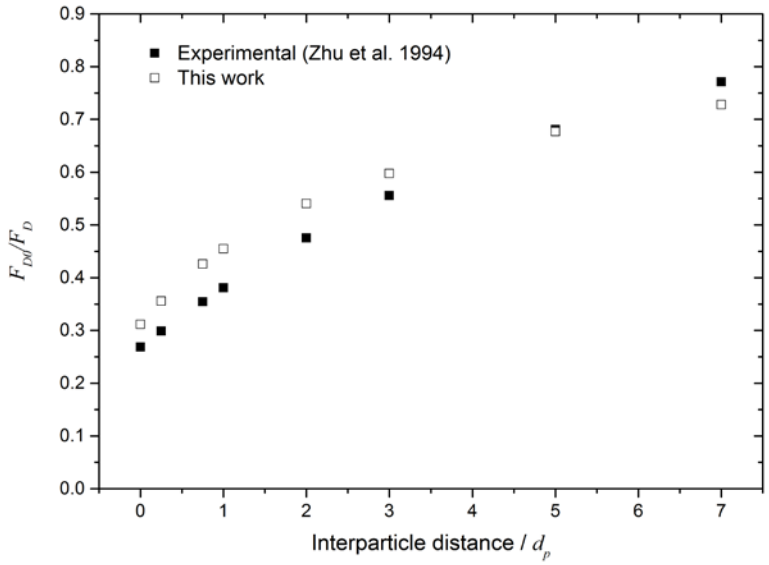

Figure 5-9 Drag ratio on trailing sphere in function of interparticle distance

In the experiment the fluid used was a mixture of water with glycerine containing the latter between 75 to 85 wt%. The glycerine content and fluid temperature were changed in order to achieve different viscosities and in turn, different Re. Since no specific values of fluid density and viscosity were given for determined Re, it was decided to use the mean value of the range reported. Thus, the values used for simulations were: fluid density at 20^0C with glycerine content of 80 wt% was 1208.5 kg/m^3 and viscosity of 0.065 kg/m s.

Although both spheres were fixed in their positions for every run, the complete set of simulations can be regarded as still frames in the drafting-kissing-tumbling (DKT) interaction (Dash & Lee 2015; Fortes et al. 1987). The fluid around the leading particle generates a wake behind it that acts as a shield ‘protecting’ the trailing sphere from the hydrodynamic drag. When the trailing sphere is far away from the wake, the drag ratio is equal to 1. This can be seen as a case in which both spheres are far enough from each other to have a local fluid around them without any other disturbance from neighbouring particles. As soon as the trailing sphere enters the tail of the wake, the drag force starts to decrease. When both spheres are subject to gravity, the effect of the wake results in a reduced drag on the trailing sphere. As both spheres settle down in the fluid, the reduced drag permits the trailing sphere to travel faster with a reduced drag opposing the vertical movement. As the trailing sphere approaches to the leading sphere reducing the interparticle distance, the drag on the trailing sphere is decreased.

5.4. Analytical test on a single sphere rising and sinking in a non-zero velocity fluid

The Brownian motion of particles, as well as particles settling and rising are processes of great interest given their presence in a wide range of applications such as chemical reactors, waste management and wells drilling. Particles rising and sinking in fluids (fluidisation and sedimentation) are cases that have been numerically, analytically and experimentally studied extensively in the literature (Gueslin et al. 2006; Shahi & Kuru 2016; Mercer et al. 1999; Derksen 2014; Di Felice 1996; Escudero & Heindel 2013; Ramos Caicedo et al. 2002). For the present work, the sink and rise of a single sphere is fundamental in the validation process. Mutual interactions at fluid-solid interfaces are a key calculation in the process of testing the DEM-LBM coupling carried out. Correct hydrodynamic force calculations will produce the accurate behaviour of the system under study; in turn, the correct representation of particles motion in the fluid will provide the necessary data to update the local fluid pattern surrounding every particle and observe the effects of such motion.

The cases presented in this section cover the actual interaction of solid objects immersed in a fluid when they are not fixed in the computational mesh, i.e. they are allowed to freely move mainly due to the hydrodynamic force exerted by the fluid and the gravity force.

Initial tests were carried out with a sphere of density 2650 kg/m^3. Since the maximum LBM fluid velocity is somewhat dictated by τ, the sphere density was reduced because if it was denser, a larger drag force would have been necessary to lift the sphere, meaning that a higher fluid velocity was required. For this reason and for the test purposes the sphere density was reduced to 1500 kg/m^3.

The tests carried out for single sphere were sink and rise in non-zero velocity fluid in plug flow, one-way and two-way modes. The same domain, fluid and sphere properties configured were common for all cases. Velocity BC was configured at the inlet (bottom wall) to drive the fluid upwards, depending on the magnitude of the velocity, the suspended sphere was expected to rise or sink.

The specific weight γ of a sphere in a fluid was the main parameter considered to decide the fluid velocity configured at the inlet. Linked to this parameter is the rate at which a sphere settles down in a fluid. Stokes (1851) found that the settling or terminal

velocity of a sphere is reached once the effective weight of the sphere is balanced with the viscous resistance of the fluid in which is travelling. In this way, the drag force experienced by a small sphere as it settles down in a fluid can be calculated from equation (4-2). Following this concept it is expected to observe a drag-gravity force balance once the sphere has reached its terminal velocity, stage at which the sphere does not accelerate anymore.

For the configuration of this test, the parameters of the sphere and the fluid were set first. Five different sphere diameters were tested: 1, 10 and 100 μm; 1 and 10 mm. Then the specific weight of the spheres was calculated and drag force determined using a fluid velocity that resulted in a value greater or lesser than the specific weight, depending on the expected behaviour to observe. In a simple but effective analytical way, $F_D > \gamma$ will have the effect of making the sphere rise in the fluid; whereas $F_D < \gamma$ will allow the sphere to continue settling down under gravity. As presented in Chapter 4, the plug flow mode allows the user to select one of the two fluid regimes available, *Stokes* or *Rayleigh* depending on the Reynolds number expected. A reference to select the plug flow mode was to consider Re at u_t for every sphere.

Before running the coupled simulation, the fluid was initialised configuring a relatively high number of LBM iterations as required to achieve a fully develop fluid in the system. The optimal number of iterations depended on the system configuration and dimensions, i.e. a large domain with many particles would require several more iterations compared to a small domain with only one particle. For the single sphere case, the system was first run in DigiFlow to find the optimal number of iterations at which a steady state flow was achieved. The advantage of using DigiFlow for this purpose was that a “live view” plot of the evolution of the fluid velocity could be monitored. Once a steady state fluid was achieved there were no more fluctuations in the fluid velocity plot and a straight horizontal line was observed indicating convergence. In this way the optimal number of initial LBM iterations was found and used in the coupled DEM-LBM configurations.

The same computational domain was used in all cases but varying the cell width to represent different d_p. From initial runs it was found that the smallest particles of d_p 1 and 10 μm were prone to move largely in X and Y directions instead of the expected vertical movement right after starting the coupled simulations. The reason was that right after the fluid is initialised, numerical noise was introduced in X and Y with

magnitudes comparable to values in Z direction. Such numerical noise was expected and comes from the LBM iterative cycle to initialise every fluid cell in the domain. When a fluid velocity was set in Z direction, a small drag was present in X and Y direction but usually of small value. However, when the cell width is reduced significantly to orders of magnitude 10^{-7} and 10^{-8} m, the presence of noise in X and Y becomes significant making the drag magnitude comparable to the principal one along Z direction. To overcome this problem and for the purpose of the test, the density of the two smallest particles was increased significantly in order to avoid the undesired sided-motion of the spheres and be able to assess the rising and sinking effect. A number of tests were carried out using different values before deciding for $5x10^{6}$ kg/m^{3}.

At this point it is important to mention that in plug flow case, the motion of the sphere was always vertical along the central axis; no sideways motion was observed. That is an unnatural movement but it was expected since the fluid in plug flow is homogeneous in every vertical cross section. Unlike plug flow simulations, one- and two-way coupling modes showed a sphere mainly travelling in vertical direction but with slight lateral and rotational movement as the sphere was sinking or rising. This is a more realistic behaviour and was expected since the local fluid around the sphere was affected by the presence (one-way) and velocity of the sphere (two-way), thus updating accordingly the drag forces on the surface of the sphere. The sideways motion was affected by the cell width, showing greater lateral displacements as the cell width value was reduced.

Once the sphere reached the top wall or hit the bottom wall, the bouncing distance was also affected by the cell width. The largest spheres (1 and 10 mm) tended to bounce less and remained very close to the bouncing region, whereas the smallest particles tended to move around much more on the top/bottom wall.

A sequence of images is presented in Figure 5-10 showing the sphere of 10 mm sinking in plug flow, one-way and two-way modes. Plug flow images do not display any fluid pattern because the configuration implemented in DigiDEM only required inputting the fluid velocity. The coupling with LBM was one of the steps further to implement fluid pattern visualisation in DigiDEM.

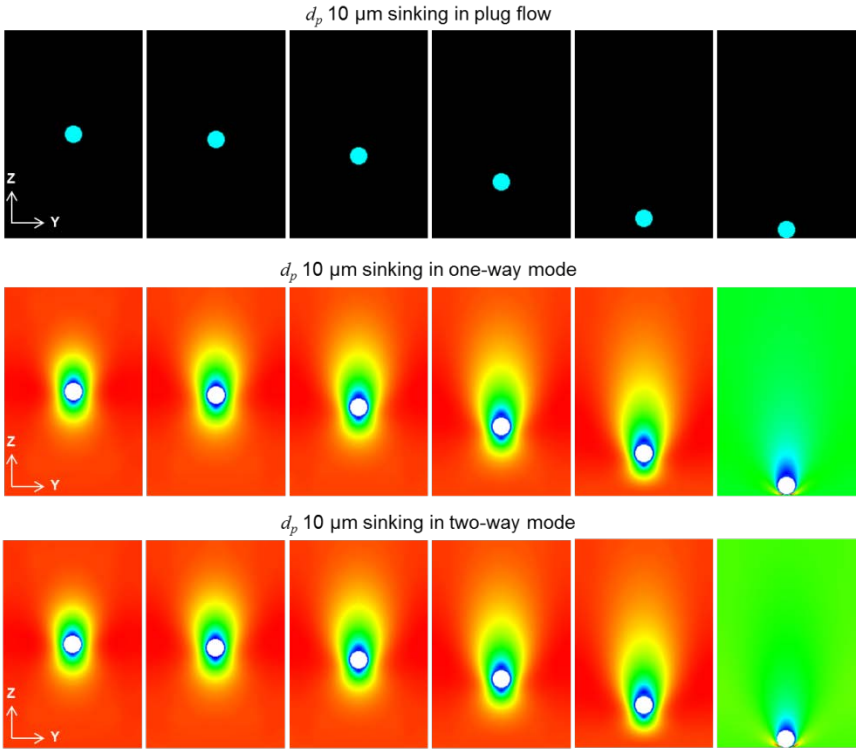

Figure 5-10 Sphere sinking in plug flow, one-way and two-way mode

When DEM-LBM was executed, the one-way coupling mode showed the sinking sphere expected behaviour. In two-way coupling mode a similar behaviour was observed but in this case the sphere took a few more steps to reach the bottom wall. This result was expected since in this mode the increasing velocity of the sphere is taken into account; drag on the sphere was proportionally increased as well and the overall effect was to slow down the sphere during settling down. Once the sphere landed on the bottom wall, the simulation was allowed to continue running to observe the behaviour of the sphere.

Additional configuration parameters and fluid velocities set at the inlet boundary to observe the rising and sinking behaviours are presented in Table 5-7.

Table 5-7 Configuration parameters for rising and sinking sphere tests

	d_p = 1 μm	d_p = 10 μm	d_p = 100 μm	d_p = 1 mm	d_p = 10 mm
Density (kg/m^3)	5x10^6	5x10^6	1500	1500	1500
Specific weight (N)	2.57x10^{-11}	2.57x10^{-8}	2.57x10^{-9}	2.57x10^{-6}	2.57x10^{-3}
u_f rising (m/s)	5x10^{-3}	5x10^{-1}	1x10^{-2}	2x10^{-1}	4.5x10^{-1}
u_f sinking (m/s)	1x10^{-3}	1x10^{-1}	1x10^{-3}	1x10^{-2}	1x10^{-1}
u_t (m/s)	2.72x10^{-3}	2.17x10^{-1}	2.63x10^{-3}	7.07x10^{-2}	4.15x10^{-1}

For one-way and two-way mode cases, the balance of forces yielded F_D values according to the u_f set. The behaviour was as expected showing that when F_D was smaller than the specific weight the sphere sank; when F_D had a greater value than specific weight the sphere rose.

The analytical tests helped not only to directly compare the results and behaviour from the different modes, but also to confirm that the physics are taking place as expected in the coupled system. Furthermore, moving boundaries were treated correctly and particle behaviour was governed by the forces involved, resulting in the corresponding particle motion observed. Additionally, when the sphere reached the solid top or bottom wall, a collision took place and bouncing was observed. The two smallest particles showed a greater motion near the walls due to the non-zero fluid velocities in X and Y directions being large enough to originate rotation and motion.

5.5. Spherical particles near contact rising and sinking in non-zero velocity fluid

The configuration presented in this section was critical since the actual particle-particle interaction of particles immersed in a fluid is of great relevance in the present study to represent FSI systems.

Initial tests of this configuration resulted in very large repulsive forces between two spheres near contact. As they approached to each other the remained in contact but after some time they ejected each other apart. An exhaustive and cyclic period of debugging and testing took place to address this problem. Contact forces were first isolated and analysed independently in large data sets to observe their behaviour.

Searching in the literature the problem of having two particles near contact in the LBM context, the work of Nguyen & Ladd (2002) was found. In their paper the authors discussed into detail the problem of small gaps between particles and an efficient way to treat the problem.

The problem is originated by the motion of the solid particle that results in a continuous re-mapping of fluid nodes. Even when time step may be small enough to freeze the system properties for calculations, the translation of a solid object with constant velocity modifies the volume fraction of boundary nodes, resulting in drag force fluctuations. The problem becomes more difficult when two particles approach each other to a distance between them smaller than the lattice width.

When two particles are close enough to the point that the gap between them is smaller than one lattice width, in LBM fluid sites are not present and are not available to create links for MEM. This results in artificial missing boundary nodes, which in turn leads to a loss of mass conservation. Additionally, the fluid between them cannot be resolved.

The solution proposed to avoid such scenario is the implementation of a hydrodynamic radius in LBM defined as $r_{hy} = r_p + \Delta$. This new 'layer' around the particle is the hydrodynamic boundary where the fluid velocity field matches the velocity of the particle for the no-slip BC (see Figure 5-11). In this way the lubrication force takes place at the hydrodynamic boundary.

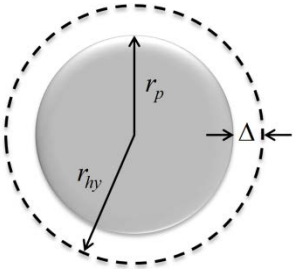

Figure 5-11 Representation of hydrodynamic boundary increased by Δ
(reproduced from Nguyen & Ladd 2002)

The actual distance Δ is very small, varying from 0 to $0.5\Delta x$. Once the hydrodynamic radius was implemented, the new boundary applied for all the particles in a domain for LBM. In DEM this was not applied because detection of overlaps between particles is required for contact force calculations. In DEM fractional overlap was implemented and tested. Previously contact force calculations were carried out at first volume overlap

detected; however, the minimum overlap to be detected was an entire voxel. With the fractional overlap implementation, volume overlaps taking place within a single voxel; i.e. Δx < 1, accounted for contact force calculations. This helped to smooth out the contact force evolution. Additionally, the first contact force value registered was not as large as compared to previous configurations.

The configuration in this test consisted of two spheres with their centres horizontally aligned and having only one lattice unit of space between them. The hydrodynamic force was originated by defining a velocity BC at the inlet to observe spheres rising and sinking. Both spheres shared the same properties of d_p 10 mm and density 1500 kg/m^3. They were located at the centre of the domain with initial zero velocity. The tests were carried out in the three available fluid modes, plug flow, one-way and two-way.

The fluid velocity used was configured to observe the spheres rising was 0.51 m/s; the corresponding one to observe them sinking was 0.09 m/s for the three fluid modalities. The Re_p observed were around 51 and 9 for sinking and rising cases respectively.

The behaviour of the spheres in every case was different. In plug flow cases the expected behaviours of rising and sinking were observed. However, both spheres moved in straight vertical motion, no rotation or trajectory deviations were observed. No contact between spheres was observed as well. In the plug flow context this behaviour made sense because the fluid velocity is applied only in one direction and is not affected by the presence of the spheres. The fluid superficial velocity was always constant and increased proportionally in every cross section occupied by the spheres.

The test for sinking in one-way mode did not show the spheres sinking; they rose instead. The fluid velocity was reduced and another test was run. This time the spheres came into contact and remained relatively static. Simulation was monitored for a longer period of time but no different behaviour was observed.

Two-way mode sinking test provided a better insight of the FSI taking place. The overall behaviour was as expected seeing both spheres sinking. However two effects were observed. In the beginning of the coupled simulation particles started to settle down under the balance of forces having a larger gravitational force compared to the hydrodynamic drag. As spheres travelled down, the local fluid was affected by the spheres in motion. The consequence of this was that the wall effect caused the impinging fluid to bounce back and push the spheres. Although not completely

symmetrical, both spheres felt the wall effect and the resulting effect brought both spheres into contact. Before contact the motion of the spheres seemed damped. After some time steps the spheres separated as they continued travelling towards the bottom wall of the domain. A second contact occurred and spheres separated again. Once they were close to the bottom wall, the wall effect was present coming from this wall. Two effects were observed, the spheres slowed down and the fluid going between the gap pushed the spheres further away. Figure 5-12 shows snapshots of the sinking configuration at different time steps for the three modes tested.

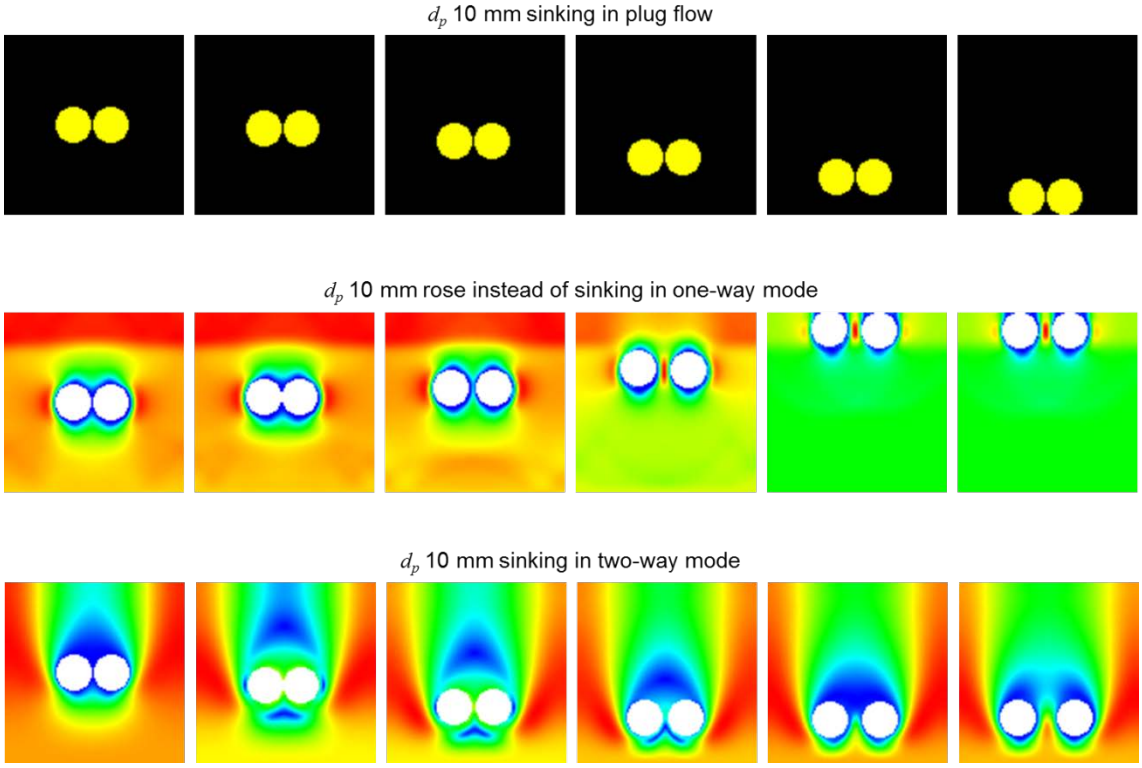

Figure 5-12 Two spheres near contact in non-zero velocity fluid

For the configurations with increased fluid velocity, one-way and two-way modes showed spheres travelling upwards towards the top wall. The difference between the two cases was that in one-way spheres became into contact and remained like that during rising and even after reaching the top wall. A longer run did not show the spheres coming apart. In two-way mode spheres touched only once when rising but separated after contact.

To the author's knowledge, 3D flow interactions at a mesoscale level have not been extensively studied experimentally and numerically. The number of studies is even more limited for combined DEM-LBM looking into the particular case configured in this

section. In Folkersma et al. (2000) and the references therein an insight into this configuration was reported. Studies at similar Re as used here were carried out using FEM and similar behaviours were observed in terms of repulsion and attraction between two spheres. However the distances were larger than the one considered here and the wall effect was not considered.

The results obtained from this section proved the efficacy of implementing the hydrodynamic radius for LBM calculations, which is useful in multi-particle systems where particles are in near contact. Moreover, the 3D test qualitatively showed the efficacy of coupled DEM-LBM to represent and simulate the evolution stages of two spheres near contact rising and sinking in a non-zero velocity fluid flow. The wall effect and the fluid flowing in the narrow gap between the particles governed the attraction and repulsion of the particles. The problem observed previously in which particles immersed in a fluid became into contact and large repulsive forces pushed them abruptly apart was corrected. The fluid was resolved between the spheres in a narrow space such as one lattice length, and particles interacted with each other and the fluid in a realistic way.

5.6. Terminal velocity of particles with sphericity different to 1

The terminal velocity of single particles with sphericity different to 1 has been studied by different authors (Chin et al. 1986; Gabitto & Tsouris 2008; Hazzab et al. 2008). In this section the work presented in Haider & Levenspiel (1989) is followed to compare the terminal velocity of different particles settling down in quiescent fluid for coupled DEM-LBM simulations. The intention is to use a number of different geometries other than traditional discs or spheres as used in the literature.

Haider & Levenspiel develop an empirical correlation fitting gathered data from experimentation reported in Pettyjohn & Christiansen (1948), Schmiedel (1928), Squires & Squires Jr. (1937) and Willmarth et al. (1964) who used cubic octahedrons, octahedrons, cubes, tetrahedrons, and disks. The equation developed to calculate the terminal velocity of a particle in function of its sphericity is:

$$u_t = \frac{\left[\frac{18}{d_*^2} + \frac{\left(2.3348 - 1.7439\psi\right)}{d_*^{0.5}}\right]^{-1}}{\left[\frac{\rho_f^2}{g\mu\left(\rho_p - \rho_f\right)}\right]^{1/3}} \tag{5-1}$$

where:

$$d_* = VED\left(\frac{g\rho_f\left(\rho_p - \rho_f\right)}{\mu^2}\right)^{1/3} \quad (5\text{-}2)$$

Equation (5-1) should only be used for particles displaying sphericities different of 1 but larger than 0.5, and for Re < 25000.

All the configurations presented in the following paragraphs were carried out only selecting the coupled DEM-LBM two-way mode, since this version is the one of interest because it takes into account the particle velocity to update the fluid field.

For the first simulation setup, a particle with ψ = 0.671, ρ_f = 2500 kg/m^3 and VED = 10.05 mm with initial zero velocity was placed suspended in a cylindrical column with quiescent fluid with water properties (ρ_f = 1000 kg/m^3 and μ = 0.001 kg/m s). The particle was initially placed in the fluid in the vertical centre line of the domain and 34 mm away from the top wall to avoid boundary effects. The lateral boundaries were configured as PBC and were apart 30 radii from the surface of the sphere.

Once the coupled simulation started, the particle settled down vertically subject to the gravitational force acting on it. Data collected at a determined interval is presented in Figure 5-13. The terminal velocity calculated from (5-1) for this sphericity was 0.066 m/s, equivalent to 119 in DEM units (solid line). The data points from the simulation show an asymptotic particle velocity evolution until a constant value of 114 DEM was achieved, having a relative error of 4.2%.

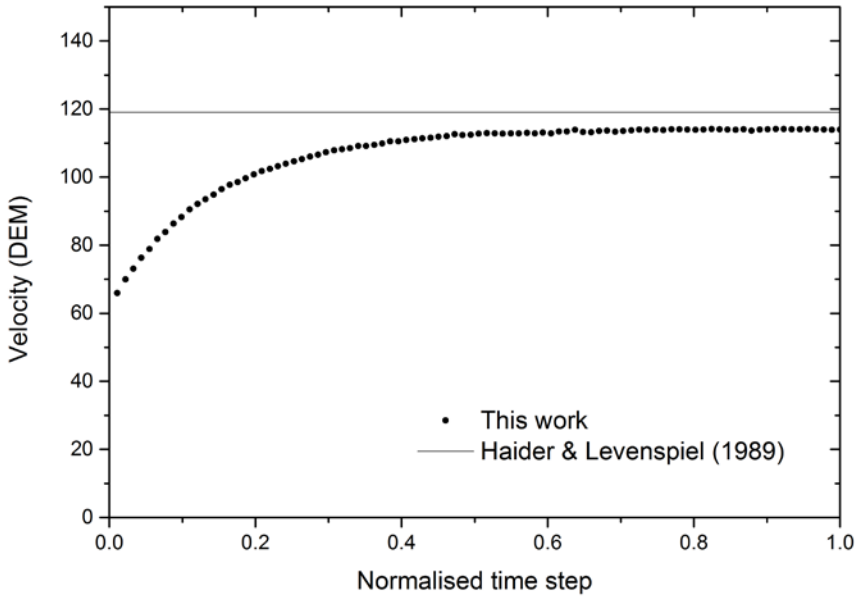

Figure 5-13 Terminal velocity of a particle with sphericity 0.671

A different particle with ψ = 0.806, ρ_f = 2540 kg/m^3 and VED = 12.41 mm was placed in a domain to run a similar test. In this case the domain was reduced to allow a faster run and attempt to configure more tests with non-spherical particles. The distance of the lateral walls to the surface of the particle was 9 radii. The calculated terminal velocity with (5-1) for this sphericity was 0.464 m/s, equivalent to 464 in DEM units. The predicted terminal velocity from coupled DEM-LBM simulation resulted in a much higher value of 523 DEM, representing a relative error of 11.28%.

For this case the wall effect did not seem to affect the particle's velocity. On the contrary, the particle reached a much higher u_t than expected. The narrower gap between the container walls and the particle did not result in an increased drag. Particle size and density were similar to the properties of the particle configured in the first part of this section. However, fluid viscosity was modified in this test in order to avoid numerical instabilities since the expected terminal velocity was approximately 10 times higher compared to the previous test.

A third configuration was tested considering a cylinder with I.D. to length ratio 0.33 and sphericity 0.636. The cylinder was allowed to settle down in stagnant fluid as carried out in experiments by Saito et al. (1984). In their work the authors found that experimental results showed that the cylinder settling behaviour for all cases can be described by the equation of simple harmonic motion.

Initial tests were carried out in coupled DEM-LBM one-way mode. The cylinder was placed in the domain with an angle of 45º between the horizontal plane and the vertical axis of the cylinder. A second run was configured having the cylinder vertically aligned with an angle of 90º. In the first run the cylinder showed rotation about its axis and reoriented itself to a stable horizontal position without showing any oscillation. The behaviour observed in one-way mode configuration indicated that effectively the initial position at which the cylinder was dropped originated a drag that resulted in the cylinder reoriented to a position in which less drag was 'felt'. The second run showed the cylinder settling down completely in vertical position without any rotation or turning. Since the initial position showed the smallest area perpendicular to drag, the cylinder remained in that position throughout the entire simulation. Let us remember that the two behaviours follow the characteristics of one-way mode in which the velocity of the particle has no influence on the local fluid around it. That is the reason why only hydrodynamic drag was the main factor reorienting (or not, for the second run), the cylinder to a more stable position.

The same test with the inclined cylinder at 45º was run in coupled DEM-LBM two-way mode, which is the most relevant in this thesis to test and the one that has particle velocity influencing the velocity field. The same domain and properties were used for this case.

Figure 5-14 shows on the far left image the initial position of the cylinder, which was inclined 45º. The idea was to observe the cylinder reorienting itself to a position in which less resistance would be 'felt' by the cylinder.

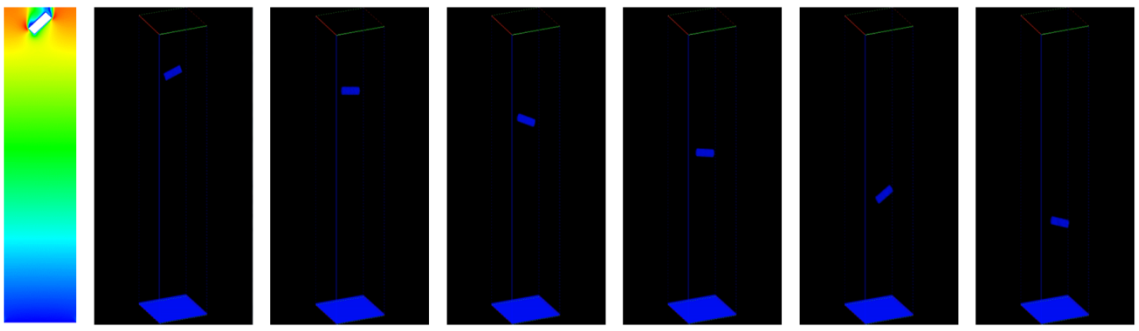

Figure 5-14 Snapshots of an inclined cylinder settling down in stagnant fluid

The images that follow in Figure 5-14 show different snapshots of the evolution of the simulation of the cylinder settling down. The behaviour observed was a constant reorientation in oscillatory mode of the cylinder. In the beginning the cylinder reached a

horizontal position (0º). That was because the lower end of the cylinder 'felt' a higher drag that slightly pushed that section of the cylinder compared with the upper end of the cylinder. Vortices forming behind the cylinder, i.e. at the upper end, also affected the reorientation motion. An oscillatory reorientation was observed as the cylinder was settling down. When the cylinder was close to the bottom solid wall, the cylinder remained in a more stable horizontal position until it hit the wall.

6. DEM-LBM model validation: Particles sedimentation and fluidisation

In this chapter different sedimentation and fluidisation cases were configured with the intention of extending the coupled DEM-LBM use to application cases involving a larger number of particles interacting with a single-phase fluid. In this way fundamental properties of suspensions and fluidised beds using spherical particles and irregular geometries were analysed.

Although particles sedimentation and fluidisation are simple examples of FSI systems, still a deeper analysis of the phenomenology taking place inside the system remains unknown. Moreover, numerical representations at a mesoscale level of multi-particle systems are necessary to understand changes in local fluid around interacting particles.

6.1. Particle sedimentation

Particle sedimentation is a process in which particles suspended in a fluid start to settle down and deposit at the bottom of a container. Particle sedimentation can be observed in river banks and coasts, in particle size analysis, particle separation, particle generation in oil and gas wells, corrosion sediments, chemical suspensions, etc.

In the following sections a number of cases for particles sedimentation are presented in the coupled DEM-LBM two-way mode following different configurations selected from the literature.

6.1.1. Drafting, kissing and tumbling behaviour of two settling spheres

The drafting, kissing and tumbling (DKT) behaviour is a well-known phenomenon observed in particle suspension flows and hindered settling. The DKT behaviour has been studied experimentally (Fortes et al. 1987; Joseph et al. 1987.; Dash & Lee 2015), and numerically (Feng et al. 1994). When two non-touching spheres of same diameter and density are vertically aligned and suspended in a column of stagnant fluid, at the moment they start to settle down the leading sphere creates a wake region behind itself. This region is characterised by a pressure reduction. If the trailing sphere is close enough to fall into the wake region, it will experience a smaller hydrodynamic

drag compared to the one 'felt' by the leading sphere. Since the trailing sphere is having less resistance to flow, it will accelerate until reaching the leading particle. At this stage the spheres are close to contact and it is known as the initiation of the *drafting* phase. As the distance between the spheres is reduced, the eventually touch, and this stage is known as *kissing* phase. During kissing the two spheres can be considered as a single particle, but after some time the spheres arrangement becomes unstable and the *tumbling* phase starts, characterised by the swapping of positions, i.e. the trailing sphere takes over the leading particle. After this, two possible behaviours could be observed: 1) the DKT takes place again, or 2) both spheres do not interact again and they simply settle down independently.

To configure the DKT test two spheres of diameter 10 mm were placed vertically aligned in the centre of the domain as shown in Figure 6-1 in image a). The distance between them was $2d_p$. For both spheres the initial velocity was zero and density 1500 kg/m^3.

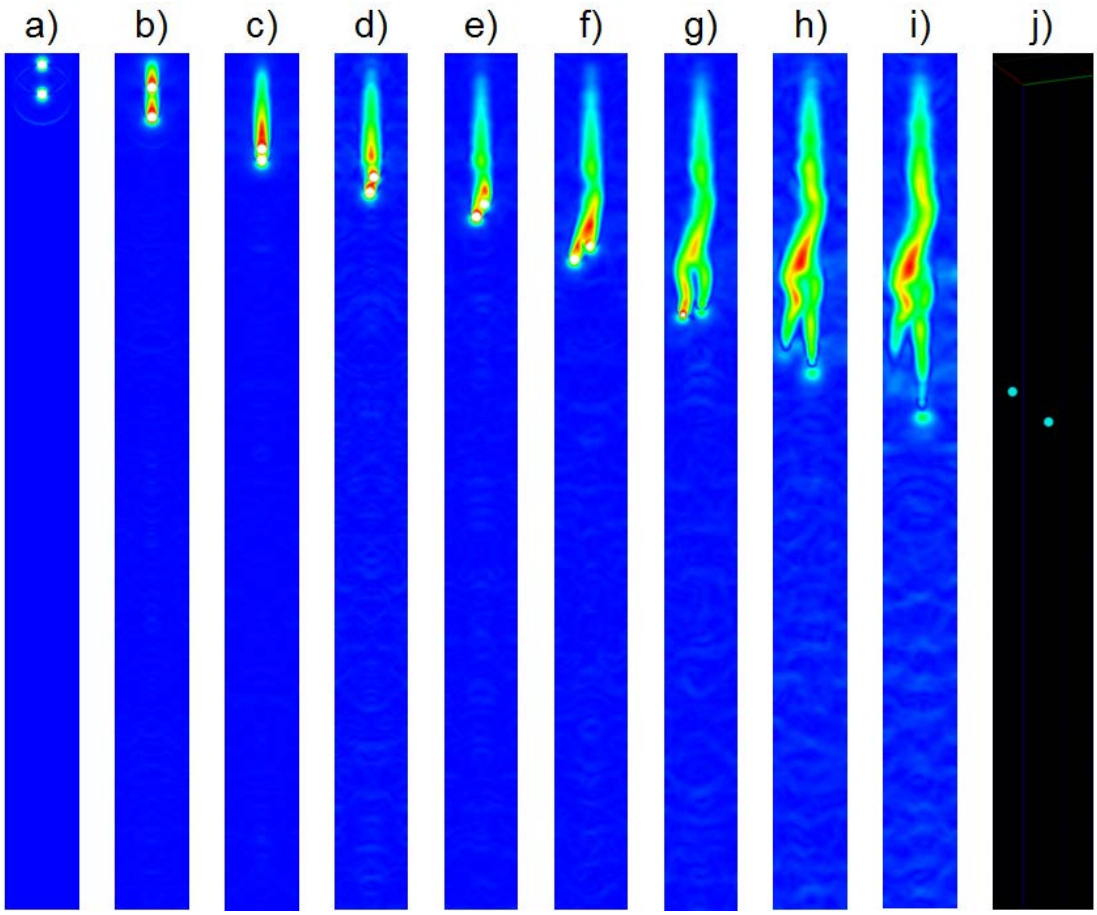

Figure 6-1 Snapshots showing the three characteristic stages of the DKT test

The complex dynamics can be observed in the sequence of images included in Figure 6-1. Before kissing both spheres travelled in the fluid in a vertical direction and eventually the trailing sphere reached the leading particle due to the wake effect previously explained. Once the particles touched, their unstable positions resulted in the trailing sphere moving towards the right boundary whereas the leading particle was observed to continue settling towards the left boundary. Rotational motion was registered, so even when the spheres visually seemed to be vertically aligned, a slight offset from the axial position led to a non-fully normal contact with the leading sphere.

After kissing, the tumbling stage took place and it is noticeable the change in positions in which the trailing sphere overtook the leading one. The rotational motion and asymmetric contact made the spheres to move in the –Y direction and separate from each other, that is the reason why the spheres were no longer seen in the screenshots dumped during simulation. However, the corresponding wakes of the spheres can be easily followed in the subsequent images. The last image j) in the sequence on the far right is a 3D view to locate the spheres. At this point spheres did settle down independently and no other DKT or interaction was observed.

As the trailing sphere approached the leading one during the drafting stage, the wake of the leading one was suppressed indicating that a continuous change of local flow took place and was well captured during the dynamic simulation. Similarly, the wake of the two spheres during kissing shown in image c) was that of a single particle, indicating the expected ‘one-long-body’ status during kissing. Images c) to f) showed the attraction, transition and repulsion regimes, categories described in Cao et al. (2015).

6.1.2. Symmetric array of mono-sized spheres settling down in stagnant fluid

In processes such as particles sedimentation and fluidisation, the particle-particle and particle-fluid interaction becomes more complex. Measuring or knowing the drag force and settling rate of individual particles is important to predict the system behaviour.

In this section a sedimentation configuration is presented for a case in which more than two particles are present in the system. The reference case for this test is an experimental correlation developed and discussed in Richardson & Zaki (1954) to find

the drag force on a single sphere in a suspension of mono-sized spheres symmetrically dispersed.

Although two configurations were studied by the authors, only one was considered for analysis in the present work to analyse the sedimentation of a larger number of spherical particles. The configuration of the array of spheres is shown in Figure 6-2; it consisted of particles of same size arranged in 5 squared layers of 9 spheres each, for a total of 45 mono-sized spheres in the system.

By varying the volumetric concentration of the suspension, four different cases were configured to allow suspensions settle down in stagnant fluid and compare the suspension settling velocity with the Stokes correlation.

In Richardson and Zaki, the settling velocity of a single particle was obtained from the Stokes equation (Stokes 1901). In the present work, the expected settling velocity of a single sphere was obtained using the Heywood tables to use it as a reference for the parameters to be configured in LBM. It is important to note that particles were added one by one since a symmetric arrangement should be attained, so particles could not have been added randomly. Only the addition of particles was time consuming, without considering the simulation time to run the sedimentation test. For that reason it was decided to keep the particle size constant and vary only the space between particles to obtain 4 different concentrations. Once the array of spheres was obtained, a coupled DEM-LBM two-way mode simulation was configured with the parameters shown in Table 6-1.

Table 6-1 Mono-sized sphere suspension configuration parameters

d_p (m)	0.01
ρ_p (kg/m^3)	2000
ρ_f (kg/m^3)	1000
v_f (m^2/s)	0.001
u_s (m/s)	0.051
τ	0.6

The experimental correction factor β found in Richardson & Zaki was $\beta = (1\text{-}C)^{-4.65}$. This factor can be found from the relation between the settling velocity of a sphere in an infinite fluid u_0 to the settling velocity of a single sphere in a suspension u_p.

Therefore, knowing the concentration of the suspension one can find β. From simulations, this factor can be obtained from the settling velocity of the suspension, which is relevant in this work to apply DEM-LBM to FSI applications.

The velocity u_p taken as reference corresponds to the particle located on the top row and middle column as seen Figure 6-2. The data was collected at the final step of a simulation of 1 second, time observed to be enough to allow spheres to settle down seeing the lower ones reach the bottom wall of the domain. The settling velocity fluctuation of the indicated particle is shown in Figure 6-3 for two different concentrations.

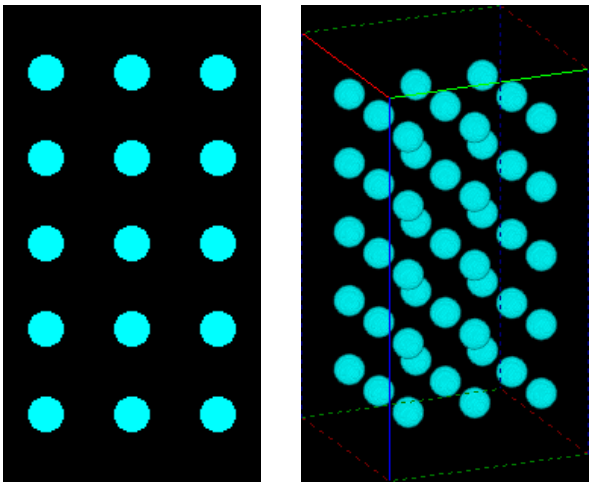

Figure 6-2 Array of spheres before sedimentation: 2D view (left) and 3D view (right)

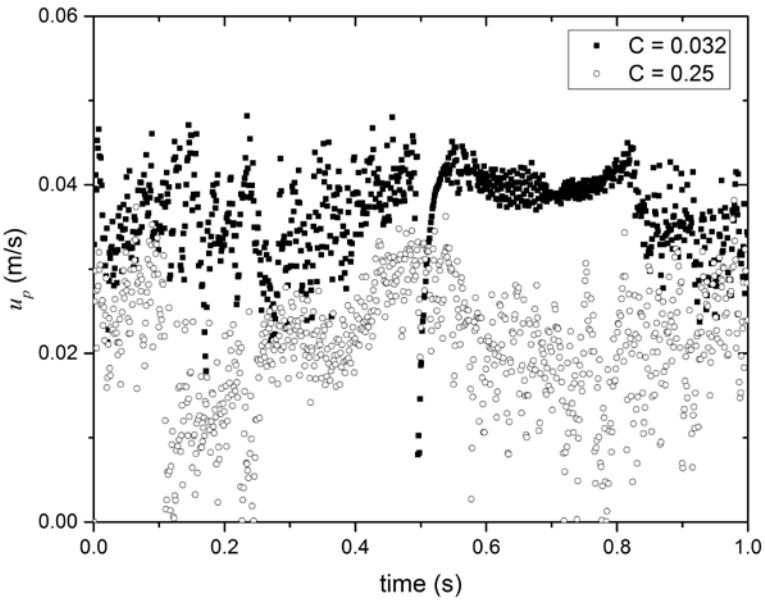

Figure 6-3 Sphere settling velocity evolution for two different concentrations C

The terminal velocity found for a single sphere with the characteristics described in Table 6-1 was 0.05 m/s. The velocity data for a single sphere settling down as part of a symmetric array of spheres is presented in Figure 6-3. It can be observed that for the small concentration (slightly larger domain with larger interparticle distance) the velocities of the particle were larger compared to the points corresponding to the higher concentration. Higher velocities for small concentration were observed since the particle had more space to travel vertically before experiencing the drag originated by the neighbouring spheres. Such drag was higher for the high concentration data set because the particles were much closer one from each other, resulting in the sphere experiencing the effects of fluid originated by the motion of neighbouring spheres settling down as well.

There is a marked drop in the sphere velocity for the small concentration case. In general, for the different concentrations simulated, the column in the centre of the array was the one showing the spheres falling less fast compared to the adjacent columns of spheres. That was because the middle column was surrounded by 8 columns of spheres all of them producing an increased drag largely affecting the spheres in the middle column. Moreover, when the lower layer of spheres touched the bottom wall, a fluid shock wave propagated upwards slowing down even more the velocity of the particles due to a further increased drag.

Settling velocity fluctuations observed were also originated by the wake generated from the immediate sphere settling down right below the sphere in the upper row. As in the DKT test discussed in the previous section, the wake generated by the leading sphere helped the trailing behind it to accelerate and increase its velocity. At the same time the local fluid from neighbouring spheres increased drag and slowed down the sphere. The same effect was observed for the spheres located in other rows in the array.

In Figure 6-4 the comparison of results obtained from Richardson & Zaki and predictions using data from simulations is presented. For the two arrays with low concentrations the data points show a good agreement with the reference data. However, the two points corresponding to higher concentrations depart from the reference data. That is because the velocity of the settling spheres from coupled DEM-LBM was smaller than the ones considered by Richardson & Zaki.

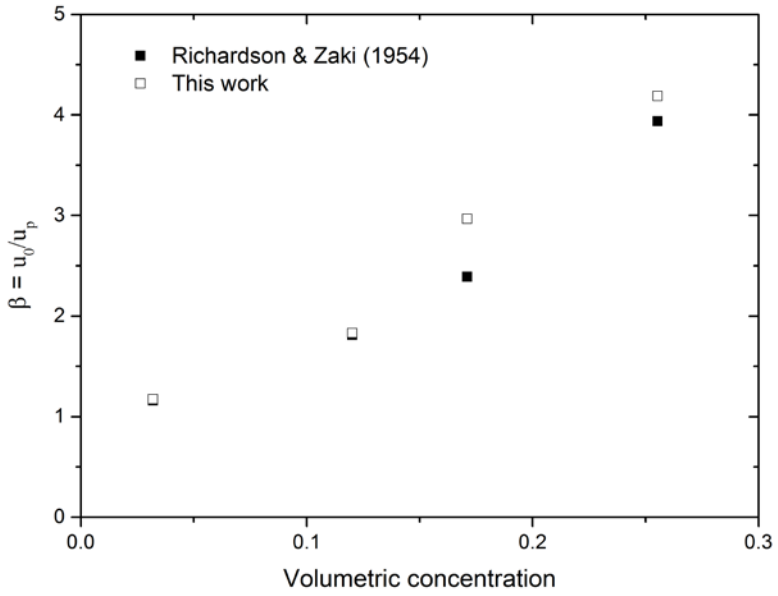

Figure 6-4 Comparison of β for different volume concentrations

In the experiments carried out and reported by Richardson and Zaki, the authors made some assumptions. For instance, they considered that the entire suspension settled down at a constant rate or velocity, and that a stable arrangement was maintained throughout the duration of their experiments. In the analysis carried out in this work the advantage of having available data from simulations was that it was possible to follow and track down relevant information of individual spheres such as the settling velocity. With this information it was possible to observe the settling velocity fluctuations due to local fluid velocities surrounding the sphere, and effects caused by neighbouring spheres, by the wall effect or by the spheres at the bottom row of the array near the solid wall. Higher concentrations had reduced space between particles, meaning that the drag originated by neighbouring spheres affected the settling velocity of adjacent spheres, resulting in a reduction of settling velocity as observed from predictions.

6.1.3. Mixed mono-sized spheres settling down in stagnant fluid

With the interest of assessing and applying the coupled DEM-LBM to more complex cases, the settling of many spheres randomly arranged at the top of a container was simulated. This configuration was decided to run in order to observe the behaviour of spherical particles in actual interaction while settling down in a stagnant fluid. Although this test is mainly qualitatively, it was necessary to include a configuration in which a more complex interaction between fluid and particles takes place. The addition of more spherical particles to the system was expected to significantly increase the number of

interactions between solid particles; interactions that in turn would modify the fluid pattern in the system and influence the drag on every particle.

A total of 900 spheres were added to the system, all of them with the same density of 2650 kg/m^3. The properties of the system and PSD followed a normal distribution with mean particle size 5 cm. The system was configured following a test presented in Owen et al. (2011) in which a qualitative case was set to observe the behaviour of spherical particles settling down in a stagnant fluid. Figure 6-5 below shows a cross section in the middle of the domain at three different stages.

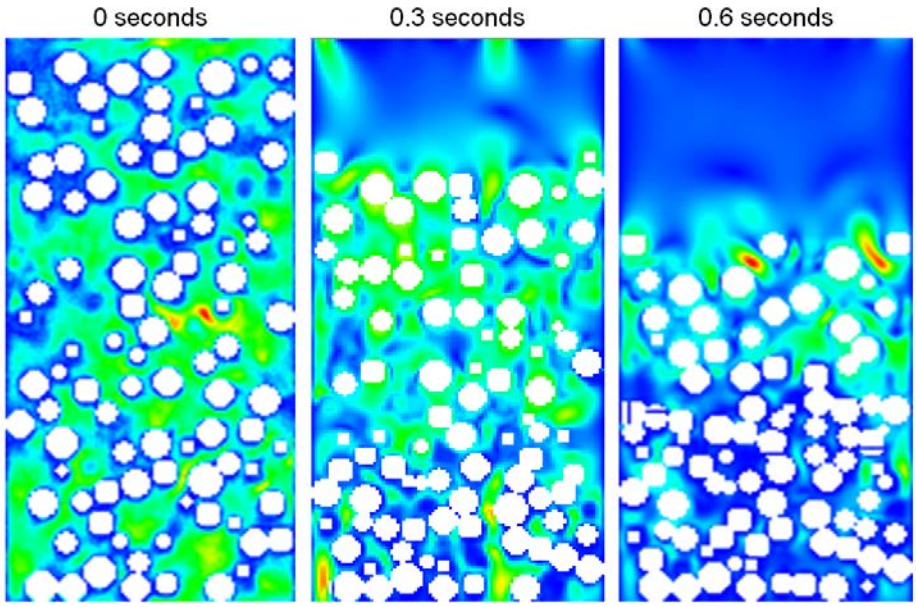

Figure 6-5 Spheres settling down in stagnant fluid at 0, 0.3 and 0.6 seconds

The image in the far left shows the initial state of the suspension with al spheres having zero velocity. The fluid was initialised and the coupled DEM-LBM two-way mode simulation started. PBC were used for all the walls in the domain following the configuration presented in the reference work. Due to the nature of LBM, the fluid pattern observed displays a range of velocities with high ones corresponding to warm colours, and low ones to small velocities. However the fluid velocities at initialisation are very small, of the order of 10^{-8} and/or 10^{-9}. The reason why is because they cannot be zero, to initialise the variables they should contain a non-zero value after the first LBM cycle is executed. For this reason the fluid pattern shown in the image at 0 seconds should not be confused or interpreted as a strict non-zero velocity fluid.

When the simulation time reached 0.3 seconds the execution was interrupted to capture the image presented in the middle. Although only a 2D cross section is presented in Figure 6-5, the bed height was monitored to confirm that the interface was indeed decreasing. Additionally a visual inspection of the entire domain was checked to corroborate that no sphere was still suspended above the suspension interface observed. The last image at 0.6 seconds shows the decreased suspension interface.

Different runs were executed before obtaining the one presented in this work. Initial runs were unsuccessful, spheres did not settle at first. After inspection it was found that when the spheres were first introduced into the domain, particles touching the upper boundary caused noise in the fluid sites. For this reason it was decided to move those spheres at the top wall 5 LU below to avoid any contact. This time the configuration showed the spheres settling down as previously presented. However, the similar problem was found in fluidisation configurations as presented in further sections in this chapter. The investigation of the effect of particles on boundaries is beyond the objectives set out in this work, but it is definitely an issue to look at in the future.

6.1.4. Sedimentation of particles with irregular geometries

Particles sedimentation was further studied but in this case a configuration using two different irregular geometries was included into the system. The intention was to use sand grains in the coupled DEM-LBM two-way mode in a more complex configuration with an increased number of particles.

The qualitative test intended to assess the sedimentation of sand grains under the influence of gravity; two configurations were set for this purpose. One of them included a cluster of particles intermixed, having 120 heavy large particles with VED 24 cm and density of 2650 kg/m^3, and 7200 small light particles with VED 8 mm and density of 1100 kg/m^3. All the particles started with a zero velocity and were allowed to settle down under the influence of gravity in two different environments, in vacuum and in stagnant fluid. The purpose of the test was to directly compare and observe the behaviour of the particles as they settled down. Figure 6-6 shows such comparison with snapshots taken at different intervals. For every part a) to h) two images are shown, being the left one with the particles settling down in vacuum, and the one on the right with the particles settling down in water.

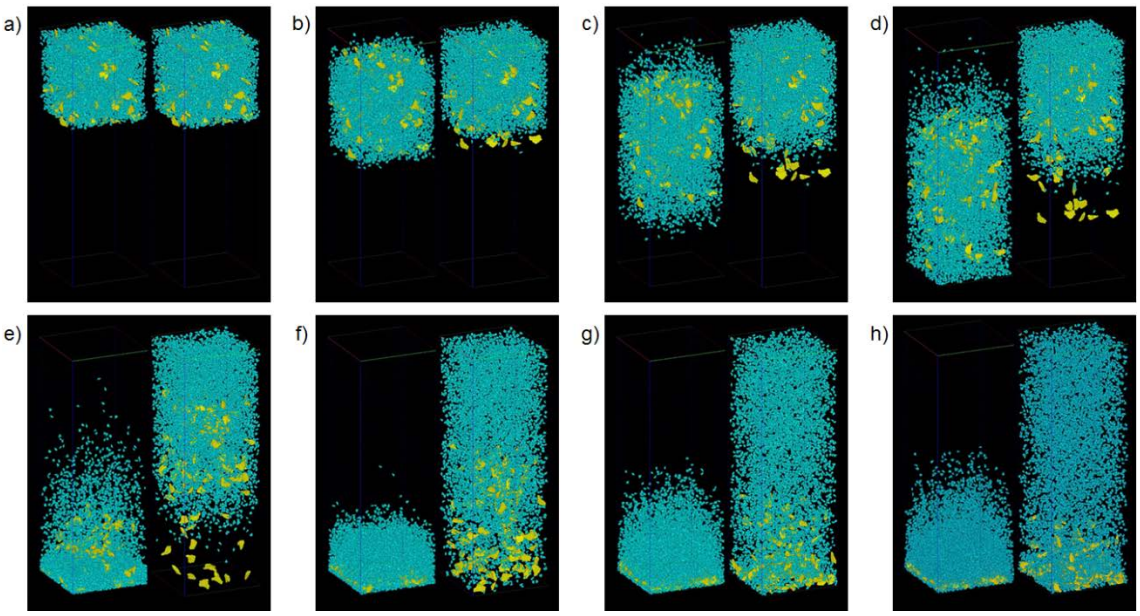

Figure 6-6 Sand grains sedimentation in vacuum (left) and water (right)

The sequence of images provides an insight into the effects and behaviour in both systems. In vacuum, particles seemed to fall together uniformly as a cluster; they fell down faster compared to the configuration with particles in fluid. That was expected and the reason is that no hydrodynamic force was present to slow down the particles. The only forces present were gravity and interparticle forces taking place among particles in contact. The sequence e) to g) for particles in vacuum shows the moment in which the particles reach the bottom region of the domain and the high rate of interparticle interactions caused the particles bouncing back.

For the same simulation time the particles settling down in stagnant fluid showed a different behaviour. The large and heavy particles were observed to settle down faster in comparison with the small ones. In images b), c) and d) it can be observed clearly how the yellow particles at the lower part of the cluster are the ones separating firstly. In h) almost all of them have reached the bottom of the domain. On the other hand, the smallest particles settled down slowly. Two effects were observed while the small particles travelled towards the bottom wall. One effect was hindered settling; the high concentration of small particles originated a high number of interactions. Similarly, the high concentration meant that particles had a large number of neighbouring particles interacting and modifying the fluid pattern around them, originating drag not only in the vertical direction but also in horizontal directions. Augmented drag was also produced by the motion of large particles settling down faster that caused fluid to be displaced

upwards. The overall behaviour observed was an increased particle segregation and hindered settling that slowed down the small particles as they travelled down.

Hindered settling is a phenomenon that has been studied extensively in experiments in order to understand the effect of concentration in suspensions of different solutes and solvents, and to develop a general settling law that could be applied based on measurable parameters. Even at low concentrations, it is difficult to follow trajectories and measure settling velocities of individual particles. The problem escalates in systems with large number of particles of order of microns interacting and forming aggregates of different size and shape.

6.2. Fluidisation of particles

Fluidisation is a process in which granular material is transformed from a static state into a dynamic fluid-like state by means of a fluid flowing upwards through the bed. When the fluid velocity is large enough the static particles commence to move and the overall behaviour observed is an expanding bed. As the flow of fluid increases, the pressure drop through the bed does as well. When the pressure drop through the bed becomes equal to the weight of the bed it is said that incipient fluidisation starts, and the fluid velocity at this point is known as minimum fluidisation velocity.

Depending on the fluid used to fluidise the bed two main phenomena would be observed. Gas fluidised beds are characterised by a bubbling or boiling behaviour in which gas pockets are formed and travel up through the bed until they burst at the top. As the bubbles rise they push aside the particles towards the walls of the container and they fall in the wake formed by the bubble. In liquid fluidised beds the characteristic behaviour observed is a uniform bed expansion showing particles recirculation near the walls of the container. At incipient fluidisation the upper layer of the bed would show a slight boiling-like behaviour.

A popular expression to study the pressure loss of a flow flowing through a packed bed is the Ergun equation (Ergun 1952), a relation between viscous energy loss and inertial loss proportional to the superficial velocity of the fluid. The parameters involved in this equation are pressure drop ΔP, bed height L, fluid viscosity μ_f, bed voidage ε, fluid superficial velocity u_f, particle diameter d_p, and fluid density ρ_f. The Ergun equation calculates the pressure drop along a packed bed for a given fluid velocity as:

$$\frac{\Delta P}{L} = \frac{150\mu(1-\varepsilon)^2 u_f}{d_p^2 \varepsilon^3} + \frac{1.75(1-\varepsilon)\rho_f u_f^2}{d_p \varepsilon^3} \tag{6-1}$$

In (6-1) the first term in the summation represents the laminar regime component and the second term corresponds to the turbulent regime. In the laminar regime the pressure gradient increases linearly with velocity, whereas in turbulent regime the pressure drop is independent of fluid viscosity but is increased with the quadratic fluid velocity.

For calculations involving non-spherical particles, the VED times the sphericity ψ must substitute the sphere diameter, where VED is obtained from:

$$VED = \frac{(6V_p)}{A_p} \tag{6-2}$$

where V_p is the volume of the non-spherical particle and A_p is the surface area of the non-spherical particle.

If a PSD forming the packed bed is to be taken into consideration, the Sauter mean diameter (SMD) should be used:

$$SMD = \frac{\sum_{i=min}^{i=max}\left(N_i^3 d_{p_i}^{\ 3}\right)}{\sum_{i=min}^{i=max}\left(N_i^2 d_{p_i}^{\ 2}\right)} \tag{6-3}$$

where N is the number of particles having a specific diameter d_{p_i}, and i is the diameter in the size distribution.

In fluidised beds and reactors it is important to know beforehand the range of fluid velocities that will produced fluidisation and entrainment. The Ergun equation is a practical equation used to determine a critical value known as the *minimum fluidisation velocity* u_{mf}. At this fluid velocity it is considered that the net weight of the packed bed is balanced with the upward force of the fluid on the cross sectional area of the bed, i.e. the bed is being supported by the fluid but the bed itself is not being fluidised yet. In this way, the upward force is defined as:

$$\Delta P \cdot A \tag{6-4}$$

And the volume of particles in the packed bed is given by:

$$(1-\varepsilon)AL \tag{6-5}$$

The net gravitational force on the particles is:

$$(1-\varepsilon)(\rho_p - \rho_f)ALg \tag{6-6}$$

Balancing and reducing (6-4) with (6-6) yields the pressure drop through the bed expected at u_{mf}:

$$\Delta P = (1-\varepsilon)(\rho_p - \rho_f)Lg \tag{6-7}$$

In the particular case of a bed generated with small particles d_p ≤ 0.1 mm, if the flow velocity is different of zero but the bed is not fluidised yet, the flow conditions at this level imply a relatively small Re < 10 and the Ergun equation is reduced to (6-8) to find u_{mf} :

$$u_{mf} = \frac{(\rho_p - \rho_f)g d_p^2 \varepsilon^3}{150\mu(1-\varepsilon)} \tag{6-8}$$

Once the bed experiences incipient fluidisation, further increment of fluid velocity will see a linear increase on pressure drop; bed height and voidage will be modified as well. The determination of u_{mf} is carried out experimentally from a u_f vs ΔP plot. Initially the packed bed is fixed and the fluid velocity flowing through the bed is increased in steps. Every time the fluid velocity is increased, a stabilisation period of time should be allowed to reach a steady flow in the entire bed for that specific velocity. In water fluidised beds, the increase in velocity results in a uniform bed expansion. Once the bed reaches its maximum possible height, the pressure drop does not increase anymore. At this point a plateau for pressure drop is observed in a u_f vs ΔP plot (see Figure 6-7). The minimum fluidisation velocity is found precisely where the pressure drop does not increase anymore.

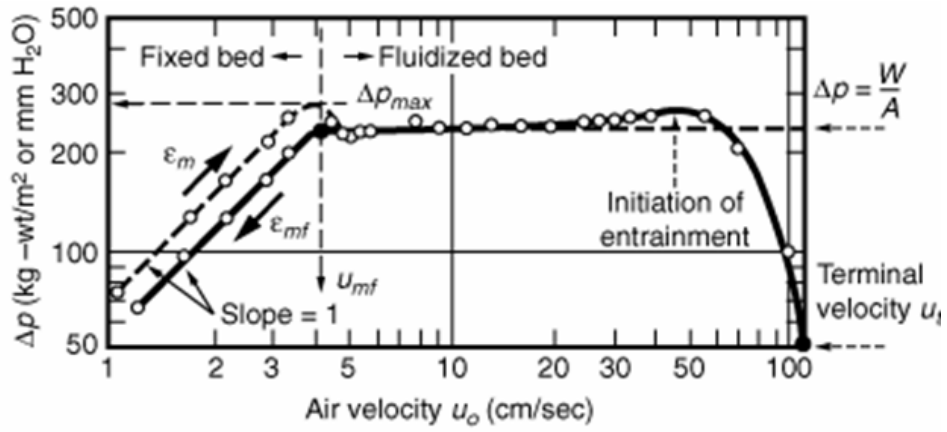

Figure 6-7 Experimental plot to find minimum fluidisation velocity (Kunii & Levenspiel 1991)

6.2.1. Fluidisation of packed beds of spherical particles

In order to simulate a fluidised system, the first step was to start with a small domain with a few particles in order to quickly assess the qualitative behaviour and numerical stability of the simulation. To do so, a cubic domain containing 46 mono-sized spheres resting at the bottom with zero-velocity was configured to observe particle fluidisation with water. The density of the spheres was 1200 kg/m^3 and the fluid velocity used was 0.01 LU (equivalent to 0.06 m/s). Snapshots of the simulation at 0 s and 2 s are presented in Figure 6-8.

The main aspects to test were that the superficial fluid velocity would be large enough to lift the spheres without causing any numerical instability; also to observe the expected behaviour without solid particles colliding and bouncing back with very large velocities. Another important aspect assessed was that the simulation would run for a relatively long period of time without presenting numerical instabilities due to large oscillations of the DDFs that could arise from particle velocities after collisions.

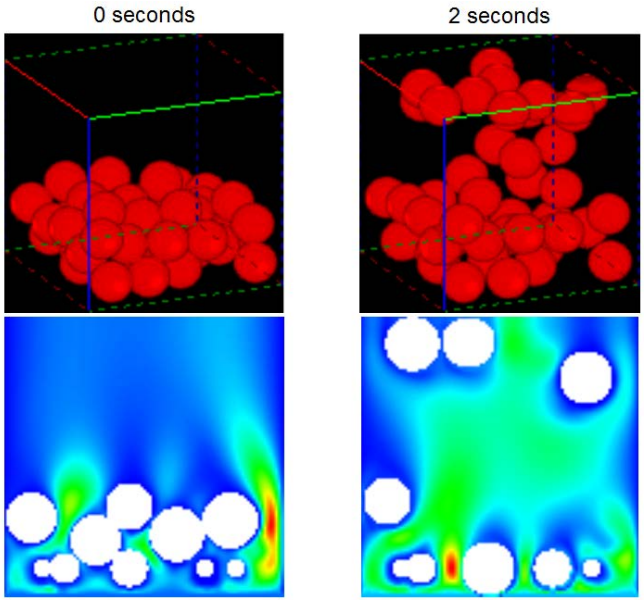

Figure 6-8 Water fluidisation of 46 spheres in a cubic domain

Figure 6-9 shows the superficial velocity in the axial Z direction at the centre of the cubic domain. The fluid velocity configured in LBM units was 0.01 LU; fluctuations observed correspond to the increment of fluid velocity when fluid flows through narrow interstices between the particles or around them.

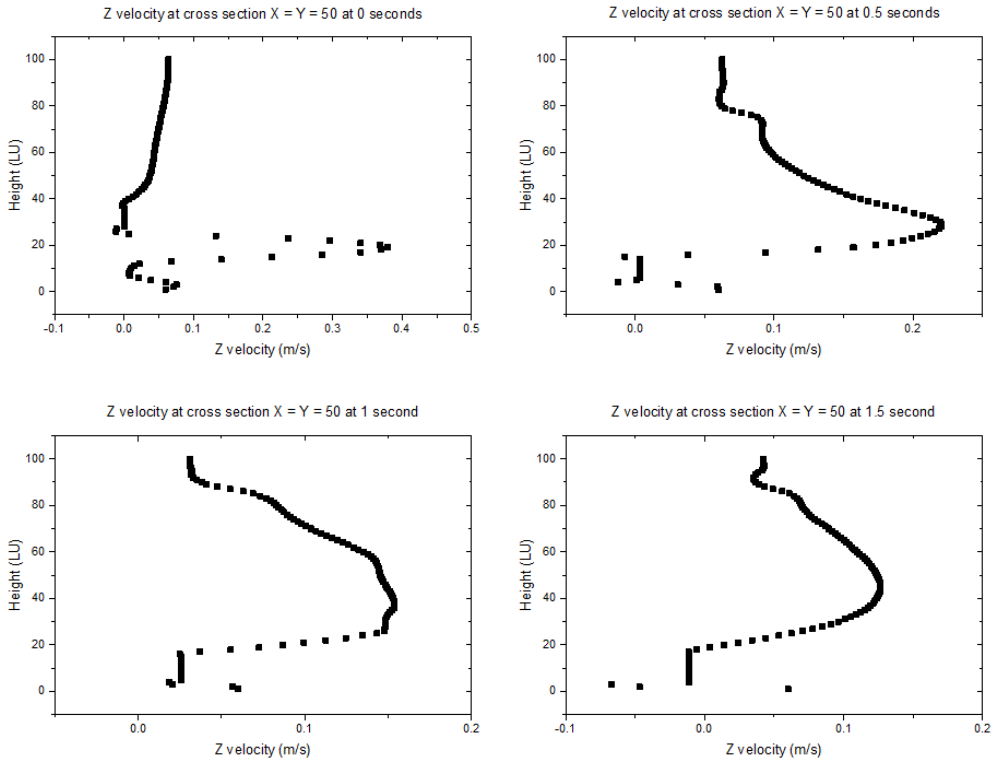

Figure 6-9 Fluid velocity in Z direction at different times in a domain with 46 spheres

After observing fluidisation and numerical stability for the fluid velocity given, a larger system was configured building a bed of mono-sized spheres in a domain with dimensions X, Y, and Z of 200x200x500 LU with 2500 spheres with d_p = 10 mm. For a number of attempts the bed was not fluidised at all. In theory, the velocity found using the Ergun equation should have originated incipient fluidisation. A larger initial velocity was used but numerical instabilities were found originated by DDFs large fluctuations beyond permissible values.

A specific test was carried out to assess the axial superficial velocity at different heights in the system, within the bed and above it. It was observed that the velocity at the bottom dropped down up to 10 times, so the inlet velocity to be configured should be higher than the calculated from Ergun equation in order to achieve such velocity during the simulation.

A new attempt was carried out reducing the domain height from 500 to 300 LU containing 1200 spheres. The calculated u_{mf} with the Ergun equation was around 4.3×10^{-5} LU, but the fluid velocity configured at the inlet was 10^{-3} LU because it was expected to drop significantly according to the previous test carried out. The relaxation parameter was reduced to 0.51 and the boundary in the direction of the fluid was configured as VBC. After initialising the fluid until reaching a steady state, the superficial velocity of the fluid near the bottom was of the order 10^{-4}; then the coupled DEM-LBM simulation was started.

The simulation stability, bed height and superficial velocity of the fluid were parameters monitored every second in simulation time. The bed expanded steadily as it can be seen from data collected and presented in Table 6-2.

Table 6-2 Bed height change in fluidised bed of spheres

Time (s)	Bed height (LU)	Superficial velocity near the bottom of the bed (LU)
0	240	4.0×10^{-4}
1	253	1.4×10^{-4}
2	265	1.3×10^{-4}
3	274	2.0×10^{-4}
4	281	2.8×10^{-4}
5	278	3.2×10^{-4}
6	295	6.0×10^{-4}

The simulation provided a better insight not only about the dynamics of the system but also helped to understand how simulation parameters and configuration in a much larger domain affected the behaviour of the system. The fluid velocity at the inlet had to be increased one order of magnitude to observe bed expansion. However, the configuration parameters also played an important role since fluid velocity cannot be larger than 0.01 LU. In order to reach such fluid velocity, the relaxation parameter has to be reduced close to 0.5, but the inherent nature of LBM dictates that instabilities are expected when τ is reduced significantly close to this value.

To fluidise large particles like the ones in this test (10 mm), the minimum fluidisation velocity from the Ergun equation was 2.6×10^{-3} m/s. Even such a small velocity caused some difficulties in LBM before the optimal parameters were configured. To observe a fully fluidised bed the system domain should be increased as well as velocity but it is difficult to ensure if the simulation would remain numerically stable.

An issue was detected and it was present in one sedimentation case as well. To illustrate the problem Figure 6-10 shows a simulation sequence of 2D cross sectional images at the middle of the domain from 0 to 6 seconds.

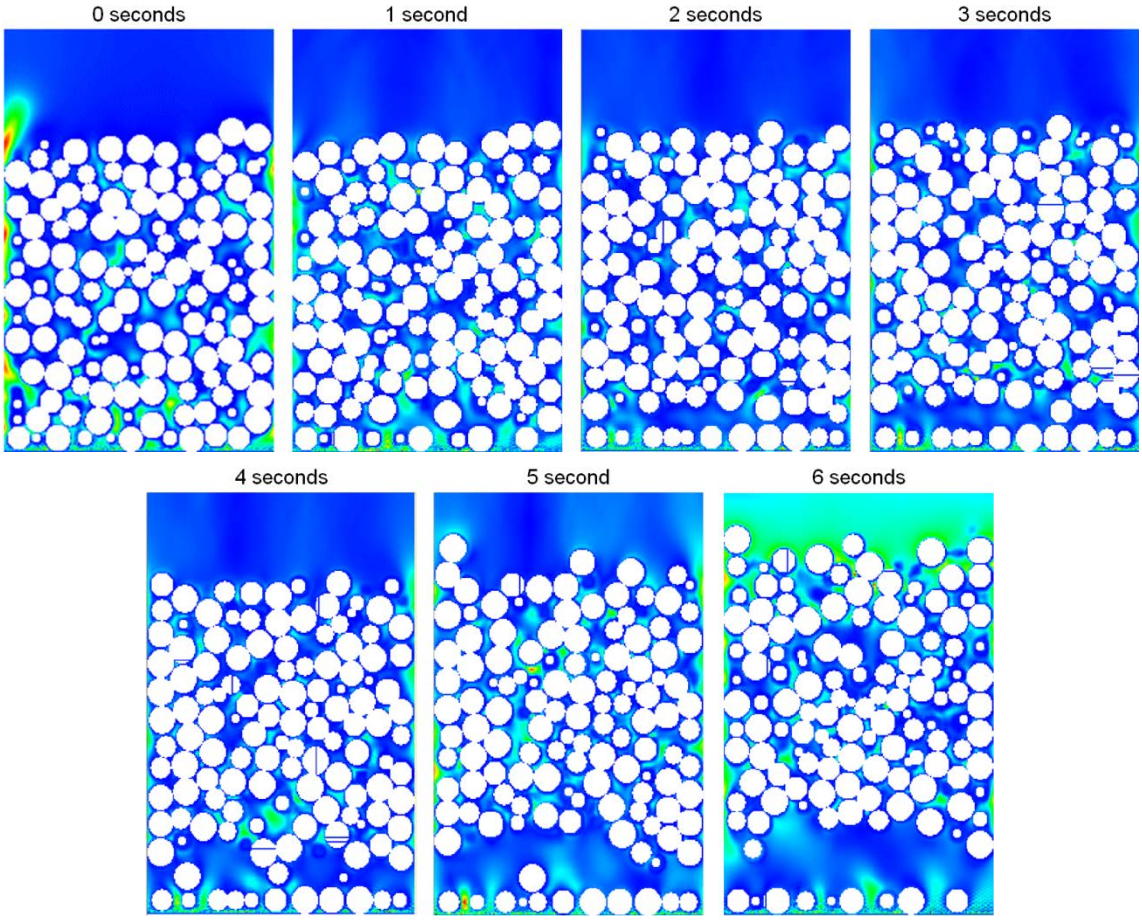

Figure 6-10 Water fluidised bed of 10 mm mono-sized spheres

It can be observed that the bottom layer of spheres did not show any sphere rising up. Although they seemed to move sideways, vertical motion did not take place. As in the sedimentation case, the spheres in contact with the bottom boundary were the ones that did not fluidise. The local fluid around them and drag force on each one of them was large enough and comparable to the actual fluidised spheres, confirming that calculations were indeed correct and worked for the majority of the spheres in the system but the ones in contact with the bottom were the exception.

The objective was to observe fluidisation of a larger number of spheres in a 3D domain. Considering the minimum fluidisation velocity and the properties of the bed, the fluid velocity was configured at the inlet. However, from preliminary tests it was observed that the fluid velocity was reduced up to 10 times after initialisation. For this reason a greater value was configured at the input, expecting it to drop but not to be smaller than u_{mf}. After the analysis of the effects on fluid velocity, the selected fluid velocity configured worked successfully to observe spheres rise and produce a bed expansion,

achieving the primary objective of the test. However, the spheres at the bottom of the domain did not rise and that is an issue that must be looked at in future work.

The increased value in fluid velocity at the inlet compared to the Ergun equation value calculated may differ from the following reason. Ergun equation contains the voidage factor which is assumed to be homogeneous through the entire bed. In reality that is not the case, voidage in the bulk region might be homogeneous but at the bottom and top of the bed voidage fluctuations are present. For instance, at the bottom of the bed voidage might have a smaller value compared to other section of the bed. In most of the fluidisation experiments the 'hump' observed in the fluidisation curve provides evidence of the necessary increase of flow rate to overcome frictional forces among the particles, which might be higher at the bottom of the bed, particles that are also supporting the upper layers of the bed.

6.2.2. Fluidisation experiments

The fluid flow through a bed of glass beads (Ballotini) was experimentally assessed in two columns using water and air. A bed rig located in one laboratory in the Faculty of Engineering at the University of Leeds was used to run fluidisation tests. The packed bed characteristics and behaviour were observed at different fluid velocities. The equipment used is shown in Figure 6-11; the main properties of the system are listed in table 6-3.

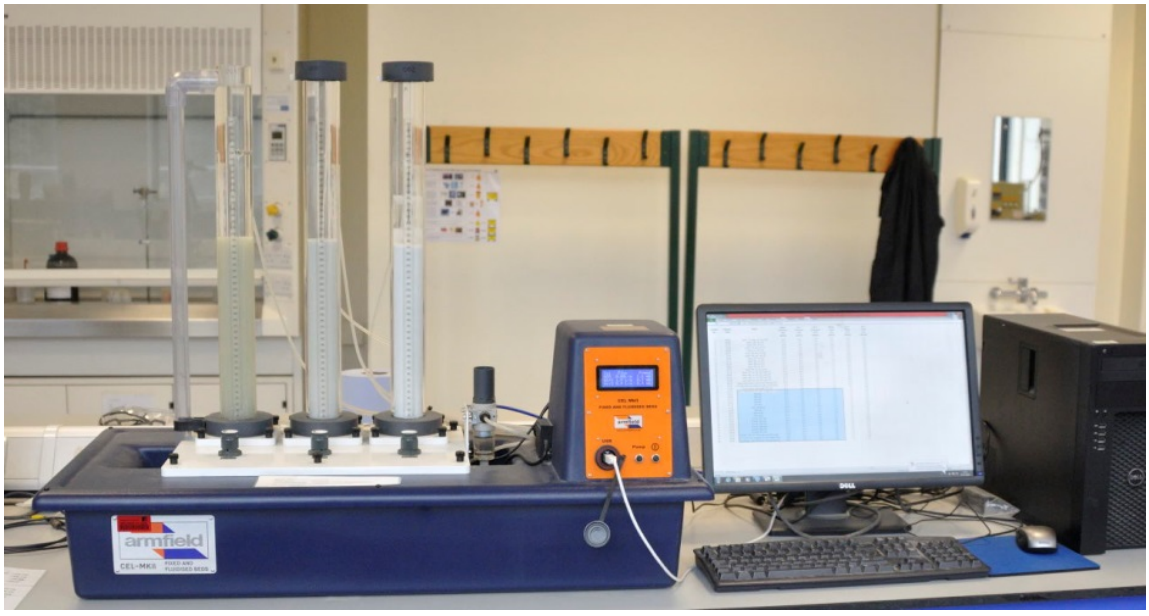

Figure 6-11 Experimental setup for bed fluidisation tests

Table 6-3 Packed bed properties

Particle diameter (μm)	625
Particle density (g/cm^3)	2.5
Fixed bed height (mm)	315
Mass of packing (g)	150.57
Volume of packing (cm^3)	97
Theoretical bed voidage	0.38

The fluid flow was controlled starting from zero and slowly incremented. Data such as pressure drop and fluid flow was registered directly to a computer. Bed height was read directly from the tube after 5 minutes of allowing the fluid flow to stabilise through the bed for every flow rate registered.

Water fluidised bed – the behaviour observed was that the initial fluid velocity increment produced a reduction in bed height. This was attributed to the flow moving the particles and allowing them to accommodate filling in some voids. This effect is similar to slightly tapping or shaking the bed to allow some spheres to settle down and reposition. Further increment on fluid velocity produce a “boiling” effect at the top layer of the bed, showing some particles being slightly fluidised bouncing on neighbouring ones, indicating incipient fluidisation. The velocity steps from this point to the one where actual bed expansion is observable correspond to the small hump in Figure 6-7 which is interpreted as the extra energy required to overcome the overall frictional forces between particles and created by the wall. Once the packed bed was loose and particles were moving, the pressure drop did not increase anymore. The full bed was expanded showing a homogeneous behaviour. The corresponding plot is shown in Figure 6-12(a), which includes also the defluidisation curve. It has been discussed (Asif & Ibrahim 2002) that the defluidisation curve produces more consistent data and accurate value of u_{mf} compared to data from a fluidisation curve, in which fluidisation conditions strongly depend on the initial structure of the bed and cohesive forces between the particles. In this way, the u_{mf} found was 0.00375 m/s.

Air fluidised bed – Since the fluid density is much smaller compared to that of water, higher velocities were required to observe bed expansion. No bubbling effect was

observed at incipient fluidisation; the effect was more like bursts seeing a few individual particles jumping quickly. When the fluid velocity was increased, the characteristic pockets in gas fluidised beds were easily observed rising up through the bed. Bed height oscillated since pockets pushed particles away, and the bed height was registered as the average of the minimum and maximum reading for every fluid velocity step. The corresponding curve is shown in Figure 6-12(b) finding u_{mf} at 0.442 m/s.

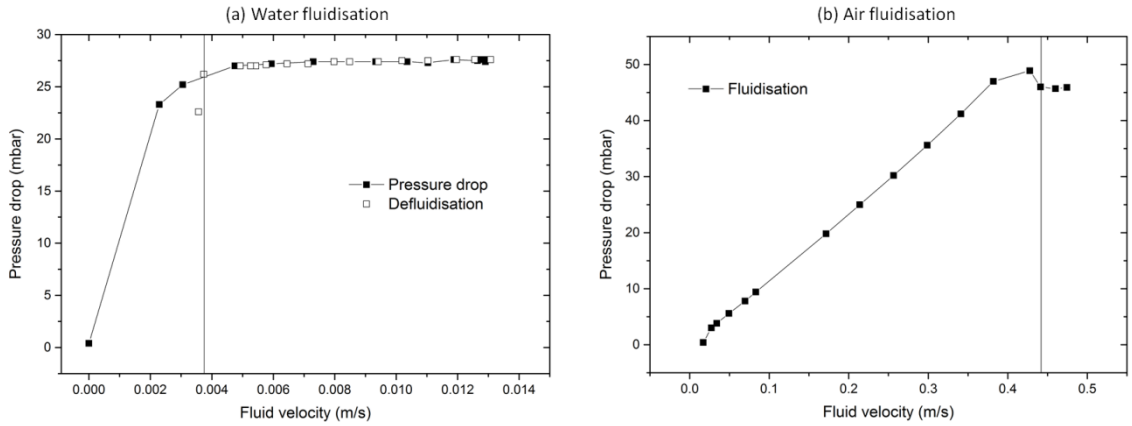

Figure 6-12 Results from fluidisation experiments with (a) water and (b) air

Experimental fluidised bed systems commonly are carried out using tube I.D. in the range of 50 to 100 mm and particle size in the range of hundreds of microns (Asif & Ibrahim (2002); Girimonte et al. (2016)), yielding aspect ratios close to 100 or more. In order to reproduce experimental configurations in simulations according to the available computational capabilities, the first feature to consider is the particle size in LU. Since the maximum particle overlap allowed in DigiDEM is 10%, a minimum of 10 LU is recommended for the smallest axis of any particle.

Having this value as reference, the following example is presented to describe the difficulties encountered to represent identical physical properties and dimensions of fluidised bed systems into the DEM-LBM computational environment.

The physical dimensions of the fluidisation system used to carry out experiments are presented in Table 6-4. Representing a Ballotini sphere with a diameter of 10 LU results in Δx = 6.25x10^{-5} m; then the domain dimensions were calculated having this parameter as reference.

Table 6-4 Fluidised bed physical properties

	Physical dimension	Digital dimension (voxels)
Particle size	625 μm	10
Column ID	50 mm	800
Bed height	300 mm	4800
Bed expansion	100 mm	1600
Tube length	600 mm	9600

From the previous table it was calculated that the domain dimensions should be I.D. 800 and height at least 6400 voxels, resulting in 4.096×10^9 nodes. A system domain of this magnitude is simply not possible to configure considering the current available computational capabilities. For instance, a computational domain tested composed of 3.136×10^8 nodes, required about 82 GB of memory to run, leaving less than 2 MB of memory available, and taking about two weeks to reach a steady-state fluid initialisation only (not coupled DEM-LBM execution). For this reason, the feasibility of representing an entire bed matching the physical dimensions was very challenging.

However, for simulation purposes and depending on the features to evaluate or the desired behaviour to observe, in some cases it is not strictly necessary to achieve a maximum bed expansion as observed in fluidisation experiments. For instance, only a fraction of the bed height can be used if the minimum fluidisation velocity is the parameter to be found. In experiments of gas fluidised beds carried out by Cranfield & Geldart 1974, Gunn & Hilal 1997, and Rao et al. 2010, the effect of bed height on minimum fluidisation velocity was tested. Having as reference Re at u_{mf}, the authors varied the initial bed height for a fixed I.D. According to their findings reported, the experiments did not show a significant increase in the fluid velocity. Different bed configurations and particle size were tested and the authors reported similar results in relation to the effect of static bed height on u_{mf}. The effect of bed height in water fluidised beds has not been extensively studied. However, Peng et al. (2016) recently reported on CFD-DEM simulations carried out following experimental configurations of a water fluidised bed. The original dimensions of the bed were reduced in order to be able to implement the system in the computational environment and run it in a

reasonable time scale. Their results from numerical simulations on segregation and dispersion of a binary system showed good agreement compared to experimental results. In Doroodchi et al. (2012) it was shown that as long as the I.D. to d_p ratio is above 10, the wall effect is still minimised.

To evaluate the effect of modifying system dimensions on the voidage of packed beds, a sensitivity analysis was carried out reducing symmetrically the dimensions of a cubic domain of 480 voxels. Similarly, the height of a column was reduced from 800 to 4 smaller heights. The results are presented in Table 6-5.

Table 6-5 Sensitivity analysis of DEM bed dimensions on bed voidage

Domain dimensions in XYZ (voxels)	ε
160x160x800	0.486
160x160x640	0.487
160x160x480	0.492
160x160x320	0.473
160x160x160	0.579
480x480x480	0.480
320x320x320	0.478
160x480x160	0.479
160x320x160	0.494

From the voidage column in the previous table it is evident that reducing a cubic domain a third of its size (480 to 320) did not modify significantly the voidage (from 0.480 to 0.478). However reducing a cubic domain two thirds showed an increased voidage that cannot be neglected. For the case of modifying only the bed height (4 top rows in Table 6-5), reducing three fifths the height of the bed still attained a voidage value close to the original one. From the evidence found in the literature, and from the bed voidage analysis carried out in digital packed beds, it was decided to reduce the dimensions of the static bed to carry out fluidisation simulations.

A column of particles was generated trying to mimic the properties and features from the experiment previously described in this section. However, given the large difference of particle size to I.D., the dimensions of the domain required to be of several thousands of LU. A smaller bed was then generated but small particles of order of microns did not fluidise. Attractive forces were present and were found to be

predominant; clusters of particles were observed forming through the bed. When the velocity was increased, the relaxation parameter had to be reduced significantly being very close to 0.5. This configuration is not advisable but it was tested. Unfortunately, numerical instabilities were observed after a few steps of running the coupled simulation.

With the intention to observe a fully fluidised bed and knowing the particle size and configurations used in previous simulations showing incipient fluidisation, a bed with spherical particles of 5 mm diameter was configured as in Wen & Yu (1966). The cylindrical column of spheres is shown in Figure 6-13. The vertical and horizontal lines observed are of the same length and were placed to help visualise the bed height changes. The sequence of images shows different snapshots of the bed at incipient fluidisation. The top layer of particles behaved as observed in experiments carried out; however when fluid velocity was increased further no obvious bed expansion was observed.

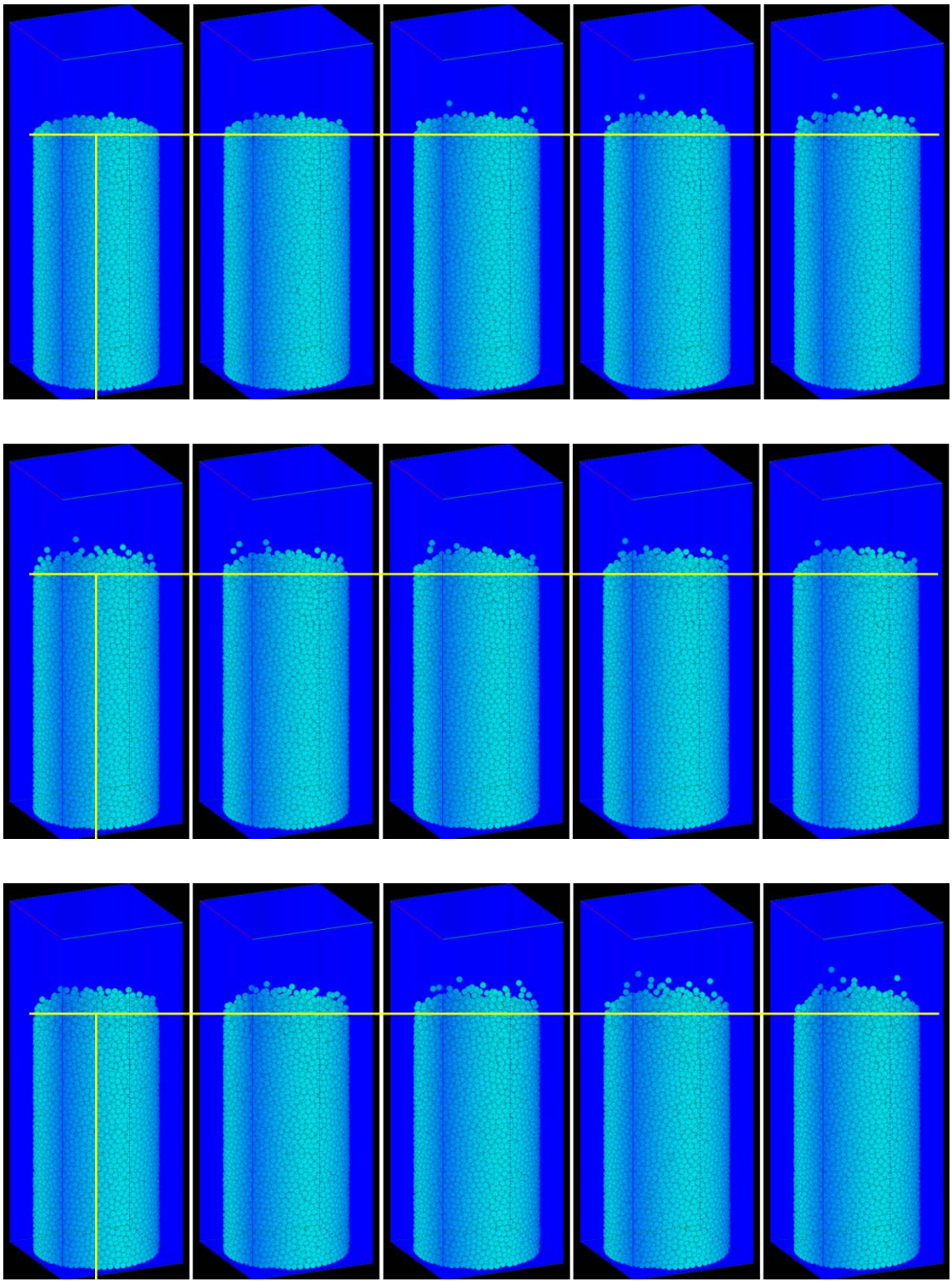

Figure 6-13 Bed column of spheres fluidised with water at incipient fluidisation

.

6.2.3. Air fluidised bed of spherical particles

A bed of spheres was configured to be fluidised as presented in Third & Müller (2013). The analytical minimum fluidisation velocity was found from the Ergun equation and compared to predictions from a CFD-DEM model. The bed constructed in this work with DEM follows the detailed information provided in the paper aforementioned. The main properties of the system and configuration parameters are listed in Table 6-6. Fluid properties of air at normal conditions were configured.

Table 6-6 Air fluidised bed system properties and configuration parameters

Δx (m)	$5x10^{-5}$
d_p (m)	$9x10^{-4}$
Particle density (kg/m^3)	1000
Fluid density (kg/m^3)	1.14
Fluid viscosity (m^2/s)	$1.58x10^{-5}$
Fluid velocity at inlet (m/s)	0.3034
Bed voidage	0.39
Total number of spheres	6239
Bed dimensions L x H x W (m)	0.028 x 0.0261 x 0.0054
τ	0.51

Three different particle diameters were used following the distribution reported in the paper. In Table 6-6 only one size is reported corresponding to a sphere of 18 LU in diameter; the other two dimensions correspond to ±1 voxel.

The initial bed height was the same as reported in the reference paper; however the bed voidage obtained in DigiDEM was 0.4, close to the value reported of 0.42. The difference was regarded to be influenced by the particle size distribution and specific number of particles added. Nevertheless, the generated structure was a fair approximation to the bed reported by Third & Müller.

The minimum fluidisation velocity predicted by the authors using the Ergun equation was 0.27 m/s and was confirmed in the present work to be 0.2755 m/s for the bed described in Table 6-6. For simulations in the present work, the fluid velocity configured was 0.3 m/s; the simulation was allowed to run for a number of steps and stopped at

different intervals to collect data. The bed height fluctuation is presented in Figure 6-14, indicating that the bed expanded approximately $2d_p$ but no more.

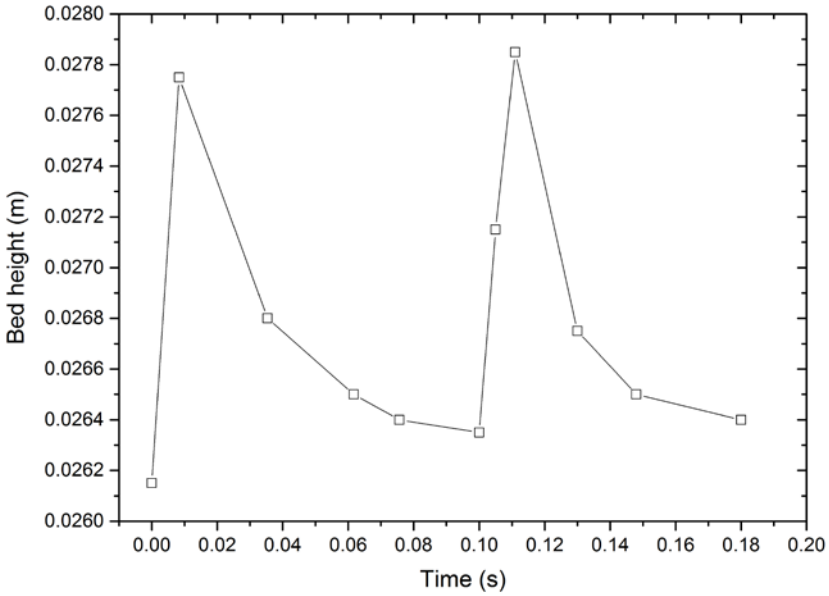

Figure 6-14 Bed height oscillation during air fluidisation at fluid velocity 0.3 m/s

The behaviour observed in the plot is a slight increase in bed height but not a full bed expansion. This rapid increase and decrease of bed height indicates that only some particles were fluidised at the top layer of the packed bed. This is a characteristic behaviour of air fluidised beds reaching incipient fluidisation that was visually verified from the images dumped during the simulation execution and also compared to images and videos produced during experimentation as discussed in section 6.2.2.

6.2.4. Fluidisation of particles with irregular geometries

A packed bed was prepared following a similar configuration as the one in the previous section but in this case sand grains were configured to be fluidised with air. The Ergun equation was used to calculate the minimum fluidisation velocity but including into the equation the sphericity factor multiplying the VED in order to account for particle shape. Initially the velocity calculated resulted in u_{mf} = 0.456 m/s. The relaxation parameter was set as 0.51, yielding a u_{mf} = 0.0048 in lattice units. Then the fluid velocity configured as BC at the inlet was slightly increased to 0.007 LU.

Execution started and the simulation was run for a number of steps. Bed height increment was not observed and the simulation was stopped to collect data. The

parameter checked was the fluid velocity in Z direction. It was found that in the middle axial plane normal to the flow direction the mean fluid velocity was indeed higher (0.006 LU) than the calculated minimum fluidisation velocity. However, fluid sites near the top and bottom of the bed presented fluid velocities all lesser than 0.004 LU.

The execution was allowed to run for more steps to give more time to observe any change in bed height. However, it did not occur and it was decided to increase the fluid velocity to 0.015 LU, equivalent to 1.422 m/s. This fluid velocity produced fluidisation of particles as observed in Figure 6-15.

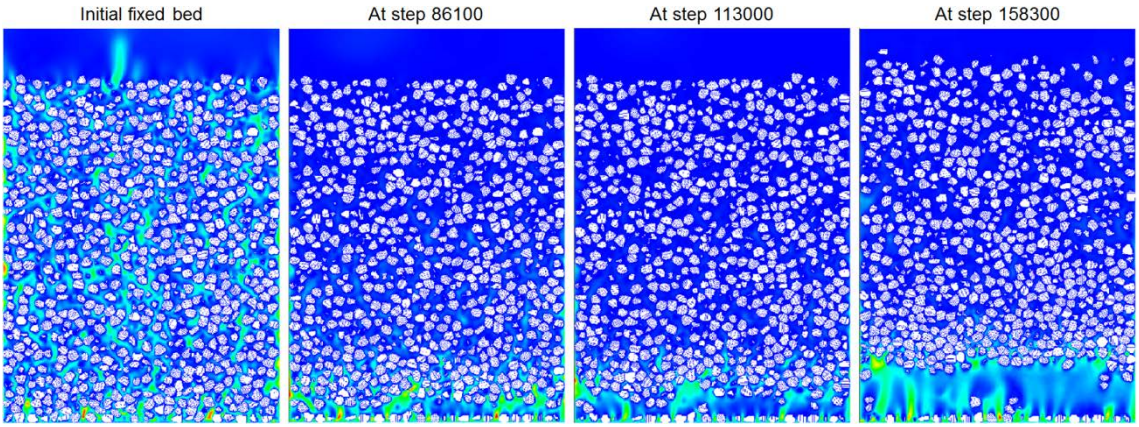

Figure 6-15 Bed height evolution in an air fluidised bed of sand grains

From the snapshot observed in the far-right image (step 158300), the fluid velocity at the bottom of the system was between 0.008 and 0.009 LU, i.e. higher than the calculated u_{mf}. In the sequence of images from left to right it is observed the formation of larger voids among particles, especially at the bottom. The particles in the lower part of the bed seemed to be pushed upwards by what it is interpreted as a pocket. Smaller voids were observed in the lower section indicating that the particles were still being pushed upwards. However the particles in the upper region reached the maximum height touching the top wall and the bed was not fluidised further. The domain height was restricted for time-execution reasons. Even when the system domain was kept relatively small, reducing further the height of the empty space above the bed reduced significantly the computational memory to about 3.5 GB required for the coupled simulation. Additionally, the purpose of this configuration did not require having a large empty space for the bed to be fully fluidised since it was prepared to find u_{mf} and not to observe the maximum bed height.

At the bottom wall of the domain a layer of particles was not fluidised at all. Even when fluid velocity and individual drag force were large enough to move the particles, they seemed to remain inert. A similar behaviour was observed in fluidisation configurations using spheres. The reasons should be studied in future work looking at the velocity BC configuration and how to treat solid nodes in contact with the boundary during fluid initialisation. A similar effect was observed for the packed bed of spheres in a domain of 200x200x300 LU previously presented in section 6.2.1 (see Figure 6-10). This is a problem to look at further in future work.

A small cubic domain was configured with two types of sand grains differing in size and density. The main objective of this configuration was to leave a small empty gap between the bottom of the bed and the bottom wall. The reason of leaving such gap was to test the fluidisation effects on particles that are not in direct contact with the boundary. In sedimentation and fluidisation configurations it was found that particles in contact with the walls, whether top or bottom wall, did not show any vertical movement after fluid initialisation. Figure 6-16 shows a sequence of images dumped during simulation.

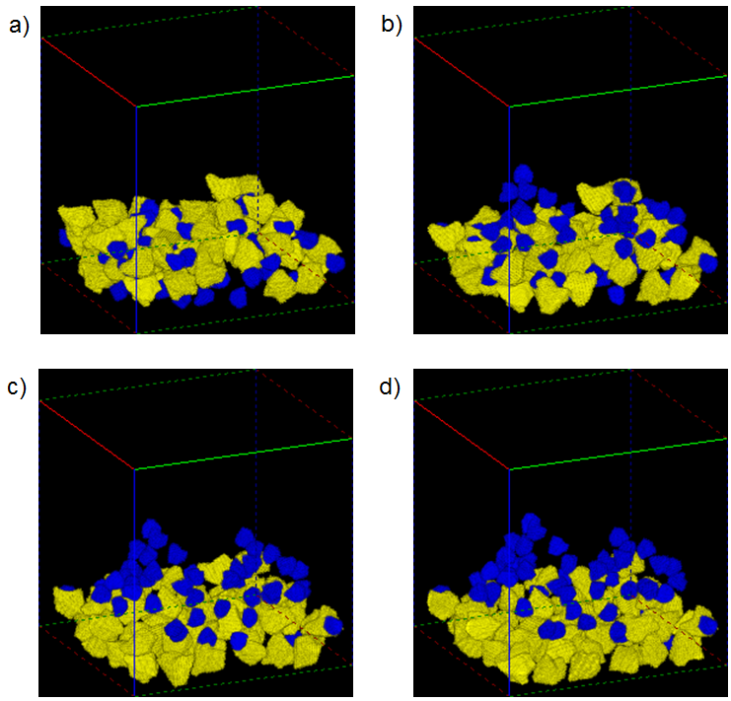

Figure 6-16 Fluidisation and segregation of sand particles

The bed configured was similar to the one used in section 4.3.2, this with the intention of additionally assessing the segregation behaviour observed previously in plug flow configuration but in this case with the coupled DEM-LBM two-way mode.

The fluid was initialised first following a similar analysis of force balance to fluidise the small particles and allow the bigger ones to remain at the bottom of the domain. Once the coupled DEM-LBM execution started, the behaviour observed was that the small particles (blue) started to move upwards, whereas the larger ones (yellow) settled down through the small gap that was left empty intentionally.

Although a simple test, the behaviour observed confirms that fluidisation is taking place correctly at small scale, for configurations in which the particles are not in contact with the bottom wall and when particle size is of the order of millimetres. More importantly simulations are numerically stable even when tau was reduced to 0.51 or 0.6. However, future work must address and test cases for smaller particles of the order of microns in a fully fluidised bed to extend the application of the coupled code to a wider range of configurations.

7. Conclusions and suggestions for future work

In this chapter the main conclusions and findings in this thesis are summarised. The discussion derives from the work carried out and reported in the previous chapters, namely Chapters 4, 5 and 6. Suggestions for further work are discussed in the second part of this chapter.

7.1. Conclusions

Two modules currently available in the DigiPac software as stand-alone DEM and LBM solvers were coupled in this work by means of a computational algorithm. The implementation was based on the momentum exchange method and the immersed boundary method for digital particles. The correct exchange of information between the two solvers permitted running coupled simulations to represent and study selected fluid-structure interaction systems.

Through X-ray microtomography complex geometries were digitised and implemented into DEM-LBM coupled simulations. Initial validation of the coupling was carried out to detect errors and carry out debugging tasks. Derived from these tasks, improvements were carried out to the user's interface with the corresponding adaptations for the new features implemented in the code, modifications for better visualisation of the system, and data dumping for data collection and analysis.

An important challenge was dealing with moving boundaries immersed in a fluid. Combining IBM with the concepts of partial saturated cells and hydrodynamic radius helped to mitigate drag force oscillations originated by the continuous covering and uncovering of fluid cells as solid particles translated in the fluid. In this way numerical stability was ensured.

Analytical calculations were used to obtain fluid velocities that would balance the specific weight of a particle immersed in a fluid and the drag force originated by a fluid in motion. The behaviour observed followed the predictions of unbalanced forces and the particle rose and sank as expected. Furthermore, the particle was allowed to interact with solid walls and with a neighbouring particle to fully test the coupling algorithm. The effects produced by particle shape into the local fluid and the overall

behaviour of FSI systems was also observed, having a larger impact in systems such as sedimentation and fluidisation with multiple particles.

The flow past a sphere test showed a resolution dependence. The data predicted from simulations followed closely the Cd vs Re curve reported in the literature, but showed a slight departure from the reference curve as Re increases. When the sphericity factor was taken into consideration, the values showed a good agreement within a maximum relative error of 7.4%. The inherent staircase-like boundary of solid particles originates drag force oscillations around the particle, and flow around angled corners resulted in variations in fluid pattern and potential development of small eddies. The effects of digital particles were observed as well in different configurations such as the terminal velocity of a non-spherical particle settling down in a column of quiescent water and the flow past a cylinder. The former configuration showed an asymptotic convergence to the reference value, whereas the later followed closely data corresponding to a rough-surface cylinder.

Results obtained from Configurations of 3D multi-particle systems, such as fluidisation and sedimentation in which particles are in near contact, proved the efficacy of the DEM-LBM coupling. A number of tests showed the evolution of interacting particles in non-zero velocity fluids. With the hydrodynamic radius concept implemented in LBM the initial problem observed in which particles immersed in a fluid became into contact and large repulsive forces pushed them abruptly apart was corrected. The fluid was resolved between the spheres in narrow spaces, i.e. one lattice length.

The sedimentation of two interacting spheres known as DKT configuration was a good representation to effectively test the capabilities of the coupled DEM-LBM model. The simulation followed the behaviour observed from experiments as reported in the literature for attraction and repulsion originated by the wake of the leading particle, and tumbling after the trailing particle catches up. Sedimentation of a symmetric array of spheres and randomly mixed particles were simulated successfully. Segregation was observed in a case configured with particles with different size and density. Hindered settling was also observed causing the slow settling of the small particles.

In simulations of fluidisation of particles it was detected that the fluid velocity configured at the inlet generally dropped up to 10 times. Therefore the fluid velocity had to be increased but the relaxation parameter had to be reduced. This behaviour was not

observed for configurations in which the total number of particles in the system was of the order of hundreds. Incipient fluidisation of spherical and irregular geometries was observed in larger domains in which thousands of particles were included in the system. Smaller domains with a small number of particles showed particles to rise upwards beyond the initial height of the fixed bed.

A case on permeability of rocks was studied combining XMT with LBM. The advantage of using digital images was to implement realistic structures into LBM simulations of fluid flow through porous media. The ability of XMT to detect closed pores was very important to account their volume into voidage calculations. Although the samples were expected to display a homogeneous permeability and pore structure, the range of smaller pores (nanopores) was not detected due to limited resolution of the XMT system. However, pore interconnection was observed to play an important role in permeability and identifying its properties and characteristics helped to understand and compare predictions with estimations from the literature. The XMT-LBM technique was considered as an alternative method for permeability and pore structure analysis, and it is not claimed to be a substitution for current methods studying these properties.

7.2. Suggestions for future work

During the evolution of this work specific configurations provided an initial insight of the capabilities of the DEM-LBM coupling implemented. Areas of improvement and further investigation were detected and future work is suggested for the following cases:

The dependency on bed height for configurations of fluidisation of particles has to be inspected in coupled DEM-LBM simulations. According to the results analysed, small beds showed particles travelling further up to the top wall of the domain. However, for beds with a large number of particles, incipient fluidisation was observed but not fully fluidisation. It is reasonable to consider that the more contacts a particle has, the more friction restricts its motion. However, artificial forces seemed to be generated once the fluid was initialised, resulting in particles coming together forming clusters, especially for small particles of the order of microns. Future work is suggested to look into this problem to test cases involving smaller particles of the order of microns in a fully fluidised bed to extend the application of the coupled code to a wider range of particle size.

In sedimentation of particles tests the ratio between particle size to container diameter was challenging to implement in coupled DEM-LBM. Supernatants are observed after several minutes, which in computational time translates into days and even weeks. For this reason the overall domain size had to be reduced proportionally (keeping constant the concentration of the suspension) in order to generate a reasonable sized domain to run a long-time simulation. However, particles did not settle down in stagnant fluid in reduced domains. This problem should be looked as well for small particles of order of microns.

In fluidisation of particles cases particles resting at the bottom wall of the domain were not fluidised at all. Even when the fluid velocity and individual drag force were large enough to move the particles, they seemed to remain inert. It was detected that only the particles touching the bottom wall showed this behaviour. A similar effect was observed in sedimentation configurations when particles were in contact with the top wall. The reasons originating this behaviour should be investigated looking at the velocity BC configuration and how to treat solid nodes in contact with the boundary during fluid initialisation.

References

Abdelhamid, Y. & El Shamy, U., 2014. Pore-scale modeling of surface erosion in a particle bed. *International Journal for Numerical and Analytical Methods in Geomechanics*, 38, pp.142–166.

Abell, A., Willis, K. & Lange, D., 1999. Mercury Intrusion Porosimetry and Image Analysis of Cement-Based Materials. *Journal of colloid and interface science*, 211(1), pp.39–44. Available at: http://www.sciencedirect.com/science/article/pii/S0021979798959860.

Aidun, C.K., Lu, Y. & Ding, E.-J., 1998. Direct analysis of particulate suspensions with inertia using the discrete Boltzmann equation. *Journal of Fluid Mechanics*, 373(1998), pp.287–311.

Al-Mdallal, Q.M., 2015. Numerical simulation of viscous flow past a circular cylinder subject to a circular motion. *European Journal of Mechanics, B/Fluids*, 49(PA), pp.121–136. Available at: http://dx.doi.org/10.1016/j.euromechflu.2014.08.008.

Almedeij, J., 2008. Drag coefficient of flow around a sphere: Matching asymptotically the wide trend. *Powder Technology*, 186(3), pp.218–223.

Alonso-Marroquín, F., 2008. Spheropolygons: A new method to simulate conservative and dissipative interactions between 2D complex-shaped rigid bodies. *EPL (Europhysics Letters)*, 83(1), p.14001. Available at: http://stacks.iop.org/0295-5075/83/i=1/a=14001.

Al-Raoush, R. & Alsaleh, M., 2007. Simulation of random packing of polydisperse particles. *Powder Technology*, 176(1), pp.47–55.

Asif, M. & Ibrahim, A.A., 2002. Minimum fluidization velocity and defluidization behavior of binary-solid liquid-fluidized beds. *Powder Technology*, 126(3), pp.241–254.

Asmar, B.N. et al., 2002. Validation tests on a distinct element model of vibrating cohesive particle systems. *Computers and Chemical Engineering*, 26(6), pp.785–802.

Awile, O. et al., 2012. Fast neighbor lists for adaptive-resolution particle simulations.

Computer Physics Communications, 183(5), pp.1073–1081.

Beaudoin, J.J., 1985. Effect of water and other dielectrics on subcritical crack growth in portland cement paste. *Cement and Concrete Research*, 15(6), pp.988–994. Available at: http://www.sciencedirect.com/science/article/pii/0008884685900894.

Beetstra, R., van der Hoef, M.A. & Kuipers, J.A.M., 2006. A lattice-Boltzmann simulation study of the drag coefficient of clusters of spheres. *Computers and Fluids*, 35(8–9), pp.966–970.

Bernal, J.D., 1964. *The Bakerian Lecture, 1962: The structure of liquids*, Proc. Royal Society.

Berryman, J.G. & Blair, S.C., 1987. Kozeny–Carman relations and image processing methods for estimating Darcy's constant. *Journal of Applied Physics*, 62(6).

Bertei, A. et al., 2014. Modified collective rearrangement sphere-assembly algorithm for random packings of nonspherical particles: Towards engineering applications. *Powder Technology*, 253, pp.311–324. Available at: http://dx.doi.org/10.1016/j.powtec.2013.11.034.

Bhatnagar, P.L., Gross, E.P. & Krook, M., 1954. A Model for Collision Processes in Gases. I. Small Amplitude Processes in Charged and Neutral One-Component Systems. *Physical Review*, 94(3), pp.511–525. Available at: http://link.aps.org/doi/10.1103/PhysRev.94.511.

Blasius, H., 1907. *Grenzschichten in Flussigkeiten mit kleiner Reibung*. University of Gottingen.

Bogner, S., Mohanty, S. & Rüde, U., 2015. Drag correlation for dilute and moderately dense fluid-particle systems using the lattice Boltzmann method. *International Journal of Multiphase Flow*, 68, pp.71–79. Available at: http://dx.doi.org/10.1016/j.ijmultiphaseflow.2014.10.001.

Bolton, A.J., Maltman, A.J. & Fisher, Q., 2000. Anisotropic permeability and bimodal pore-size distributions of fine-grained marine sediments. *Marine and Petroleum Geology*, 17(6), pp.657–672.

de Bono, J.P. & McDowell, G.R., 2015. An insight into the yielding and normal compression of sand with irregularly-shaped particles using DEM. *Powder Technology*, 271, pp.270–277. Available at: http://dx.doi.org/10.1016/j.powtec.2014.11.013.

Borquist, E., Thapa, S. & Weiss, L., 2016. Experimental and lattice Boltzmann simulated operation of a copper micro-channel heat exchanger. *Energy Conversion and Management*, 117, pp.171–184. Available at: http://dx.doi.org/10.1016/j.enconman.2016.02.066.

Bossa, N. et al., 2015. Micro- and nano-X-ray computed-tomography: A step forward in the characterization of the pore network of a leached cement paste. *Cement and Concrete Research*, 67, pp.138–147. Available at: http://dx.doi.org/10.1016/j.cemconres.2014.08.007.

Van Brakel, J. & Heertjes, P.M., 1977. Capillary rise in porous media. Part I. a problem. *Powder Technology*, 16(1), pp.75–81. Available at: http://www.sciencedirect.com/science/article/pii/0032591077850249.

Brumby, P.E. et al., 2015. Coupled LBM–DEM Micro-scale Simulations of Cohesive Particle Erosion Due to Shear Flows. *Transport in Porous Media*, 109(1), pp.43–60. Available at: "http://dx.doi.org/10.1007/s11242-015-0500-2.

Bux, J. et al., 2015. In situ characterisation of a concentrated colloidal titanium dioxide settling suspension and associated bed development: Application of an acoustic backscatter system. *Powder Technology*, 284, pp.530–540. Available at: http://dx.doi.org/10.1016/j.powtec.2015.07.028.

Cai, J. & Huai, X., 2010. Study on fluid-solid coupling heat transfer in fractal porous medium by lattice Boltzmann method. *Applied Thermal Engineering*, 30(6–7), pp.715–723. Available at: http://dx.doi.org/10.1016/j.applthermaleng.2009.12.001.

Cao, C. et al., 2015. Simulating the interactions of two freely settling spherical particles in Newtonian fluid using lattice-Boltzmann method. *Applied Mathematics and Computation*, 250, pp.533–551. Available at: http://dx.doi.org/10.1016/j.amc.2014.11.025.

Carman, P.C., 1937. Fluid flow through granular beds. *Transactions of the Institute of Chemical Engineering*, 15, pp.155–166.

Catalano, P. et al., 2003. Numerical simulation of the flow around a circular cylinder at high Reynolds numbers. *International Journal of Heat and Fluid Flow*, 24(4), pp.463–469.

Caulkin, R. et al., 2006. An investigation of packed columns using a digital packing algorithm. *Computers and Chemical Engineering*, 30(6–7), pp.1178–1188.

Chakraborty, J., Verma, N. & Chhabra, R.P., 2004. Wall effects in flow past a circular cylinder in a plane channel: A numerical study. *Chemical Engineering and Processing: Process Intensification*, 43(12), pp.1529–1537.

Chapman, S., 1916. On the law of distribution of molecular velocities, and on the theory of viscosity and thermal conduction, in a non-uniform simple monotomic gas. *Phil. Trans. R. Soc. A*, 216, pp.279–348.

Chen, L. et al., 2014. A comparative study of lattice Boltzmann methods using bounce-back schemes and immersed boundary ones for flow acoustic problems. *International Journal for Numerical Methods in Fluids*, 74, pp.439–467.

Chen, Y. et al., 2013. Momentum-exchange method in lattice Boltzmann simulations of particle-fluid interactions. *Physical Review E - Statistical, Nonlinear, and Soft Matter Physics*, 88(1).

Chen, Y., Third, J.R. & Müller, C.R., 2015. A drag force correlation for approximately cubic particles constructed from identical spheres. *Chemical Engineering Science*, 123, pp.146–154. Available at: http://dx.doi.org/10.1016/j.ces.2014.10.002.

Chin, A.D.A. et al., 1986. A shape-modified size correction for terminal settling velocity in the intermediate region. *Powder Technology*, 48(1), pp.59–65.

Cho, H., Jeong, N. & Sung, H.J., 2013. Permeability of microscale fibrous porous media using the lattice Boltzmann method. *International Journal of Heat and Fluid Flow*, 44, pp.435–443. Available at: http://dx.doi.org/10.1016/j.ijheatfluidflow.2013.07.013.

Chu, K.W. et al., 2011. CFD-DEM simulation of the gas-solid flow in a cyclone separator. *Chemical Engineering Science*, 66(5), pp.834–847.

Chung, Y.C. & Ooi, J.Y., 2011. Benchmark tests for verifying discrete element modelling codes at particle impact level. *Granular Matter*, 13(5), pp.643–656.

Cleary, P.W. & Sawley, M.L., 2002. DEM modelling of industrial granular flows: 3D case studies and the effect of particle shape on hopper discharge. *Applied Mathematical Modelling*, 26(2), pp.89–111.

Comer, J.K. & Kleinstreuer, C., 1995. A numerical investigation of laminar flow past nonspherical solids and droplets. *ASME J Fluids Eng*, 117, pp.170–175.

Comisky, J.T., Newsham, K.E. & Rushing, J.A., 2007. A comparative study of capillary-pressure-based empirical models for estimating absolute permeability in tight gas sands. *Society of Petroleum Engineers*, SPE 110050.

Connington, K. et al., 2009. Peristaltic particle transport using the lattice Boltzmann method. *Physics of Fluids*, 21(5), p.53301. Available at: http://dx.doi.org/10.1063/1.3111782.

Cook, B., Noble, D. & Williams, J., 2002. A Coupled DEM-LB Model for the Simulation of Particle-Fluid Systems. In *Discrete Element Methods*. American Society of Civil Engineers, pp. 161–166. Available at: http://dx.doi.org/10.1061/40647(259)29.

Cook, B.K. et al., 2000. Direct simulation of particle-laden fluids. *American Rock Mechanics Association*, 1.

Cranfield, R.R. & Geldart, D., 1974. Large particle fluidisation. *Chemical Engineering Science*, 29(4), pp.935–947.

Cui, X. et al., 2014. Coupled DEM-LBM simulation of internal fluidisation induced by a leaking pipe. *Powder Technology*, 254, pp.299–306.

Cui, X. et al., 2012. The Effect of Initial Bed Height on the Behaviour of a Soil Bed Due to Pipe Leakage Using the Coupled DEM-LBM Technique. In *Discrete Element Modelling of Particulate Media*. The Royal Society of Chemistry, pp. 51–58. Available at: http://dx.doi.org/10.1039/9781849735032-00051.

Cui, Y. & Sommerfeld, M., 2015. Forces on micron-sized particles randomly distributed on the surface of larger particles and possibility of detachment. *International Journal of Multiphase Flow*, 72(SEPTEMBER 2012), pp.39–52.

Cundall, P.A., 1988. Formulation of a three-dimensional distinct element model-Part I. A scheme to detect and represent contacts in a system composed of many polyhedral blocks. *International Journal of Rock Mechanics and Mining Sciences and*, 25(3), pp.107–116.

Cundall, P.A. & Strack, O.D.L., 1979. A discrete numerical model for granular assemblies. *Géotechnique*, 29(1), pp.47–65.

d'Humières, D., 1992. Generalized lattice Boltzmann equations. *Rarefied Gas Dynamics: Theory and Simulations, Prog Astronaut Aeronaut*, 159, pp.450–458.

Dal Ferro, N. et al., 2012. Coupling X-ray microtomography and mercury intrusion porosimetry to quantify aggregate structures of a cambisol under different fertilisation treatments. *Soil and Tillage Research*, 119, pp.13–21. Available at: http://dx.doi.org/10.1016/j.still.2011.12.001.

Dash, S.M. et al., 2014. A flexible forcing three dimension IB-LBM scheme for flow past stationary and moving spheres. *Computers and Fluids*, 95, pp.159–170. Available at: http://dx.doi.org/10.1016/j.compfluid.2014.02.025.

Dash, S.M. & Lee, T.S., 2015. Two spheres sedimentation dynamics in a viscous liquid column. *Computers & Fluids*, 123, pp.218–234. Available at: http://www.sciencedirect.com/science/article/pii/S004579301500331X.

Delaney, G.W. et al., 2015. DEM modelling of non-spherical particle breakage and flow in an industrial scale cone crusher. *Minerals Engineering*, 74, pp.112–122. Available at: http://dx.doi.org/10.1016/j.mineng.2015.01.013.

Delaney, G.W. et al., 2012. Testing the validity of the spherical DEM model in simulating real granular screening processes. *Chemical Engineering Science*, 68(1), pp.215–226. Available at: http://dx.doi.org/10.1016/j.ces.2011.09.029.

Derksen, J.J., 2014. Simulations of hindered settling of flocculating spherical particles. *International Journal of Multiphase Flow*, 58, pp.127–138. Available at:

http://dx.doi.org/10.1016/j.ijmultiphaseflow.2013.09.004.

Domínguez, J.M. et al., 2010. Neighbour lists in smoothed particle hydrodynamics. *International Journal for Numerical Methods in Fluids*, 67(12), pp.2026–2042.

Dong, K., Wang, C. & Yu, A., 2015. A novel method based on orientation discretization for discrete element modeling of non-spherical particles. *Chemical Engineering Science*, 126, pp.500–516. Available at: http://dx.doi.org/10.1016/j.ces.2014.12.059.

Doroodchi, E. et al., 2012. Fluidisation and packed bed behaviour in capillary tubes. *Powder Technology*, 223, pp.131–136. Available at: http://www.sciencedirect.com/science/article/pii/S0032591011004050.

Dullien, F.A.L., El-Sayed, M.S. & Batra, V.K., 1977. Rate of capillary rise in porous media with nonuniform pores. *Journal of Colloid and Interface Science*, 3, pp.496–506.

Dünweg, B. & Ladd, A.J.C., 2009. Lattice Boltzmann Simulations of Soft Matter Systems. *Advances in Polymer Science*, 221(1), pp.89–166.

Džiugys, A. & Peters, B., 2001. An approach to simulate the motion of spherical and non-spherical fuel particles in combustion chambers. *Granular Matter*, 3(4), pp.231–266.

Edmundson, H.P., 1969. Theory of self-reproducing automata. *Information Storage and Retrieval*, 5(3), p.151.

Enskog, D., 1917. *Kinetische Theorie der Vorgänge in mässig verdünnten Gasen*.

Ergun, S., 1952. Fluid flow through packed columns. *Chemical Engineering Progress*, 48, pp.9–94.

Escudero, D. & Heindel, T.J., 2013. Minimum fluidization velocity in a 3D fluidized bed modified with an acoustic field. *Chemical Engineering Journal*, 231, pp.68–75. Available at: http://dx.doi.org/10.1016/j.cej.2013.07.011.

Eshghinejadfard, A. et al., 2016. Direct-forcing immersed boundary lattice Boltzmann

simulation of particle/fluid interactions for spherical and non-spherical particles. *Particuology*, 25, pp.93–103. Available at: http://dx.doi.org/10.1016/j.partic.2015.05.004.

Eshghinejadfard, A., Janiga, G. & Thévenin, D., 2015. Calculation of the permeability in porous media using the lattice Boltzmann method. *Conference on Modelling Fluid Flow (CMFF'15)*, 0, pp.1–11. Available at: http://dx.doi.org/10.1016/j.ijheatfluidflow.2016.05.010.

Fadlun, E.A. et al., 2000. Combined immersed-boundary finite-difference methods for three-dimensional complex flow simulations. *Journal of Computational Physics*, 161(1), pp.35–60. Available at: http://www.sciencedirect.com/science/article/pii/S0021999100964842.

Farr, R.S., 2013. Random close packing fractions of lognormal distributions of hard spheres. *Powder Technology*, 245, pp.28–34. Available at: http://www.sciencedirect.com/science/article/pii/S0032591013002660.

Farsi, A. et al., 2016. Simulation and characterisation of packed columns for cylindrical catalyst supports and other complex-shaped bodies. In *The 7th International Conference on Discrete Element Methods*. pp. 1–10.

Di Felice, R., 1996. A relationship for the wall effect on the settling velocity of a sphere at any flow regime. *International Journal of Multiphase Flow*, 22(3), pp.527–533.

Feng, J., Hu, H.H. & Joseph., D.D., 1994. Direct simulation of initial value problems for the motion of solid bodies in a Newtonian fluid. Part 1. Sedimentation. *J. Fluid Mech.*, 261, pp.95–134.

Feng, Y.T., Han, K. & Owen, D.R.J., 2010. Combined three-dimensional lattice Boltzmann method and discrete element method for modelling fluid-particle interactions with experimental assessment. *International Journal for Numerical Methods in Engineering*.

Feng, Z.G. & Michaelides, E.E., 2004. The immersed boundary-lattice Boltzmann method for solving fluid-particles interaction problems. *Journal of Computational Physics*, 195(2), pp.602–628.

Filippova, O. & Hänel, D., 1997. Lattice-Boltzmann simulation of gas-particle flow in filters. *Computers & Fluids*, 26(7), pp.697–712.

Finney, J.L., 1976. Fine structure in randomly packed, dense clusters of hard spheres. *Materials Science and Engineering*, 23(2–3), pp.199–205.

Folkersma, R., Stein, H.N. & Van De Vosse, F.N., 2000. Hydrodynamic interactions between two identical spheres held fixed side by side against a uniform stream directed perpendicular to the line connecting the spheres' centres. *International Journal of Multiphase Flow*, 26(5), pp.877–887.

Fortes, A.F., Joseph, D.D. & Lundgren, T.S., 1987. Nonlinear mechanics of fluidization of beds of spherical particles. *Journal of Fluid Mechanics*, 177(1987), pp.467–483. Available at: http://journals.cambridge.org/article_S0022112087001046\nhttp://journals.cambridge.org/action/displayAbstract?fromPage=online&aid=393062&fileId=S0022112087001046\nhttp://journals.cambridge.org/action/displayFulltext?type=1&fid=393063&jid=FLM&volumeId=177&.

Foteinopoulou, K., Karayiannis, N.C. & Laso, M., 2015. Monte Carlo simulations of densely-packed athermal polymers in the bulk and under confinement. *Chemical Engineering Science*, 121, pp.118–132. Available at: http://dx.doi.org/10.1016/j.ces.2014.08.021.

Fraige, F.Y., Langston, P.A. & Chen, G.Z., 2008. Distinct element modelling of cubic particle packing and flow. *Powder Technology*, 186(3), pp.224–240.

Franke, U. et al., 2006. Wave tank study of particulate organic matter degradation in permeable sediments. *Limnology and Oceanography*, 51(2), pp.1084–1096.

Frisch, U., Hasslacher, B. & Pomeau, Y., 1986. Lattice-gas automata for the Navier-Stokes equation. *Physical Review Letters*, 56(14), pp.1505–1508.

Fusi, N. & Martinez-Martinez, J., 2013. Mercury porosimetry as a tool for improving quality of micro-CT images in low porosity carbonate rocks. *Engineering Geology*, 166, pp.272–282. Available at: http://dx.doi.org/10.1016/j.enggeo.2013.10.002.

Gabitto, J. & Tsouris, C., 2008. Drag coefficient and settling velocity for particles of

cylindrical shape. *Powder Technology*, 183(2), pp.314–322.

Galindo-Torres, S.A., 2013. A coupled Discrete Element Lattice Boltzmann Method for the simulation of fluid-solid interaction with particles of general shapes. *Computer Methods in Applied Mechanics and Engineering*, 265, pp.107–119. Available at: http://dx.doi.org/10.1016/j.cma.2013.06.004.

Gan, M. et al., 2004. Predicting packing characteristics of paticles of arbitrary shapes. *KONA*, 22, pp.82–93.

Girimonte, R., Vivacqua, V. & Formisani, B., 2016. Extension of the model of binary fl uidization to beds con fi ned in a packing of coarse spheres. *Powder Technology*, 297, pp.275–282. Available at: http://dx.doi.org/10.1016/j.powtec.2016.04.034.

Goldstein, D., Handler, R. & Sirovich, L., 1993. Modeling a no-slip flow boundary with an external force field. *Journal of Computational Physics*, 105(2), pp.354–366. Available at: http://www.sciencedirect.com/science/article/pii/S0021999183710818.

Gómez-Carracedo, A. et al., 2009. Fractal analysis of SEM images and mercury intrusion porosimetry data for the microstructural characterization of microcrystalline cellulose-based pellets. *Acta Materialia*, 57(1), pp.295–303.

Goyal, N. & Derksen, J.J., 2012. Direct simulations of spherical particles sedimenting in viscoelastic fluids. *Journal of Non-Newtonian Fluid Mechanics*, 183–184, pp.1–13. Available at: http://dx.doi.org/10.1016/j.jnnfm.2012.07.006.

Green, D.W. & Perry, R.H., 2008. Perry's Chemical Engineers' Handbook, Eighth Edition. *Perry's Chemical Engineers' Handbook, Eighth Edition*. Available at: https://accessengineeringlibrary.com:443/browse/perrys-chemical-engineers-handbook-eighth-edition/p200139d899706_4001.

Guan, Y. et al., Lattice Boltzmann simulation of flow past a non-spherical particle. *Advanced Powder Technology*. Available at: http://www.sciencedirect.com/science/article/pii/S0921883117301309.

Gueslin, B. et al., 2006. Flow induced by a sphere settling in an aging yield-stress fluid. *Physics of Fluids*, 18(10), pp.1–8.

Gunn, D.J. & Hilal, N., 1997. The expansion of gas-fluidised beds in bubbling fluidisation. *Chemical Engineering Science*, 52(16), pp.2811–2822.

Haider, A. & Levenspiel, O., 1989. Drag coefficient and terminal velocity of spherical and nonspherical particles. *Powder Technology*, 58, pp.63–70.

Han, K., Feng, Y.T. & Owen, D.R.J., 2007. Coupled lattice Boltzmann and discrete element modelling of fluid-particle interaction problems. *Computers and Structures*, 85(11–14), pp.1080–1088.

Han, Y. & Cundall, P.A., 2013. LBM-DEM modeling of fluid-solid interaction in porous media. *International Journal for Numerical and Analytical Methods in Geomechanics*, 37, pp.1391–1407.

Hardy, J., Pomeau, Y. & de Pazzis, O., 1973. Time evolution of a two dimensional model system. I. Invariant states and time correlation functions. *Journal of Mathematical Physics*, 14(12).

Hazzab, A., Terfous, A. & Ghenaim, A., 2008. Measurement and modeling of the settling velocity of isometric particles. *Powder Technology*, 184(1), pp.105–113.

He, X. & Doolen, G., 1997. Lattice Boltzmann Method on Curvilinear Coordinates System: Flow around a Circular Cylinder. *Journal of Computational Physics*, 134, pp.306–315.

He, X. & Luo, L.S.L.-S., 1997. Theory of the lattice Boltzmann method: From the Boltzmann equation to the lattice Boltzmann equation. *Physical Review E*, 56(6), p.6811. Available at: http://link.aps.org/doi/10.1103/PhysRevE.56.6811.

Hertz, H., 1896. *Miscellaneous papers*, Macmillan and Co., Ltd.

Heywood, H., 1962. No Title. *Symp. Interaction between Fluids Particles*, Inst. Chem, p.1.

Higuera, F.J., Succi, S. & Benzi, R., 1989. Lattice Gas Dynamics with Enhanced Collisions. *EPL (Europhysics Letters)*, 9(4), p.345. Available at: http://stacks.iop.org/0295-5075/9/i=4/a=008.

Hogue, C. & Newland, D., 1994. Efficient computer simulation of moving granular particles. *Powder Technology*, 78, pp.51–66.

Holdich, R., No Title. *Filtration & Separation*. Available at: http://www.filtration-and-separation.com/settling/settling.htm.

Holdich, R.G., 2002. *Fundamentals of Particle Technology*, Mindland Information Technology and Publishing.

Hölzer, A. & Sommerfeld, M., 2009. Lattice Boltzmann simulations to determine drag, lift and torque acting on non-spherical particles. *Computers and Fluids*, 38(3), pp.572–589. Available at: http://dx.doi.org/10.1016/j.compfluid.2008.06.001.

Hooper, J.D. & Wood, D.H., 1984. Fully developed rod bundle flow over a large range of Reynolds number. *Nuclear Engineering and Design*, 83(1), pp.31–46.

Huettel, M. & Rusch, A., 2000. Transport and degradation of phytoplankton in permeable sediment. *Limnology and Oceanography*, 45(3), pp.534–549.

Huettel, M., Ziebis, W. & Forster, S., 1996. Flow-induced uptake of particulate matter in permeable sediments. *Limnology and Oceanography*, 41(2), pp.309–322. Available at: http://dx.doi.org/10.4319/lo.1996.41.2.0309.

Ido, Y., Sumiyoshi, H. & Tsutsumi, H., 2016. Simulations of behavior of magnetic particles in magnetic functional fluids by using hybrid method of lattice Boltzmann method, immersed boundary method and discrete particle method. *Computers & Fluids*, 0, pp.1–10. Available at: http://linkinghub.elsevier.com/retrieve/pii/S0045793016301232.

Ishak, M.H.H., Abdullah, M.Z. & Abas, A., 2016. Lattice Boltzmann method study of effect three dimensional stacking-chip package layout on micro-void formation during encapsulation process. *Microelectronics Reliability*, 65, pp.205–216. Available at: http://dx.doi.org/10.1016/j.microrel.2016.07.002.

Izquierdo, S., Martínez-Lera, P. & Fueyo, N., 2009. Analysis of open boundary effects in unsteady lattice Boltzmann simulations. *Computers and Mathematics with Applications*, 58(5), pp.914–921.

Jia, T. et al., 2012. Dynamic simulation of granular packing of fine cohesive particles with different size distributions. *Powder Technology*, 218, pp.76–85.

Jia, T., Zhang, Y. & Chen, J.K., 2011. Dynamic Simulation of Particle Packing With Different Size Distributions. *Journal of Manufacturing Science and Engineering*, 133(2), p.21011. Available at: http://manufacturingscience.asmedigitalcollection.asme.org/article.aspx?articleid=1470776.

Jia, X. et al., 2007. Validation of a digital packing algorithm in predicting powder packing densities. *Powder Technology*, 174(1–2), pp.10–13.

Jia, X. & Williams, R.A., 2001. A packing algorithm for particles of arbitrary shapes. *Powder Technology*, 120(3), pp.175–186.

Jin, F. et al., 2011. Probability-based contact algorithm for non-spherical particles in DEM. *Powder Technology*, 212(1), pp.134–144. Available at: http://dx.doi.org/10.1016/j.powtec.2011.05.003.

Jing, L. et al., 2016. Extended CFD–DEM for free-surface flow with multi-size granules. *Int. J. Numer. Anal. Meth. Geomech.*, 40, pp.62–79.

Jones, A.M. & Knudsen, J.G., 1961. Drag coefficients at low reynolds numbers for flow past immersed bodies. *AIChE Journal*, 7, pp.20–25.

Jones, F.O. & Owens, W.W., 1980. A laboratory study of low-permeability gas sands. *Journal of Petroleum Technology*, 32, pp.1631–1640.

Joseph, D.D. et al., *Nonlinear mechanics of fluidization of spheres, cylinders and disks in water* 1987th ed., SIAM.

Karabelas, S.J. et al., 2012. High Reynolds number turbulent flow past a rotating cylinder. *Applied Mathematical Modelling*, 36(1), pp.379–398. Available at: http://dx.doi.org/10.1016/j.apm.2011.07.032.

Katz, A.J. & Thompson, A.H., 1987. Prediction of rock electrical conductivity from mercury injection measurements. *Journal of Geophysical Research*, pp.599–607.

Katz, A.J. & Thompson, A.H., 1986. Quantitative prediction of permeability in porous rock. *American Physical Society, Phys. Rev. B*, 34, pp.8179–8181.

Khabbazi, A.E., Ellis, J.S. & Bazylak, A., 2013. Developing a new form of the Kozeny-Carman parameter for structured porous media through lattice-Boltzmann modeling. *Computers and Fluids*, 75, pp.35–41. Available at: http://dx.doi.org/10.1016/j.compfluid.2013.01.008.

Klemm, A., Kimmich, R. & Weber, M., 2001. Flow through percolation clusters: NMR velocity mapping and numerical simulation study. *Phys. Rev. E*, 63, p.41514.

Kollmannsberger, S. et al., 2009. Fluid-Structure Interaction based on Lattice Boltzmann and p-FEM: Verification and Validation. *Proceedings of the …*, pp.1–4. Available at: http://www.inf.bv.tum.de/wwwold/papers/uploads/paper_0634.pdf.

Korevaar, M.W. et al., 2014. Integrated DEM-CFD modeling of the contact charging of pneumatically conveyed powders. *Powder Technology*, 258(May), pp.144–156.

De Korte, A.C.J. & Brouwers, H.J.H., 2013. Random packing of digitized particles. *Powder Technology*, 233, pp.319–324. Available at: http://dx.doi.org/10.1016/j.powtec.2012.09.015.

Krueger, B., Wirtz, S. & Scherer, V., 2015. Measurement of drag coefficients of non-spherical particles with a camera-based method. *Powder Technology*, 278, pp.157–170. Available at: http://dx.doi.org/10.1016/j.powtec.2015.03.024.

Kruggel-Emden, H. et al., 2008. A study on the validity of the multi-sphere Discrete Element Method. *Powder Technology*, 188(2), pp.153–165. Available at: http://dx.doi.org/10.1016/j.powtec.2008.04.037.

Kunii, D. & Levenspiel, O., 1991. *Fluidization Engineering (Second Edition)*, Butterworth-Heinemann.

Ladd, A.J.C., 1994a. Numerical simulations of particulate suspensions via a discretized Boltzmann equation. Part I. Theoretical foundation. *Journal of Fluid Mechanics*, 271(1), p.285-. Available at: http://journals.cambridge.org/abstract_S0022112094001771.

Ladd, A.J.C., 1994b. Numerical simulations of particulate suspensions via a discretized Boltzmann equation. Part II. Numerical results. *Journal of Fluid Mechanics*, 271, p.311-. Available at: http://arxiv.org/abs/comp-gas/9306005.

Laín, S. & Sommerfeld, M., 2007. A study of the pneumatic conveying of non-spherical particles in a turbulent horizontal channel flow. *Brazilian Journal of Chemical Engineering*, 24(4), pp.535–546.

De Lange Kristiansen, K., Wouterse, A. & Philipse, A., 2005. Simulation of random packing of binary sphere mixtures by mechanical contraction. *Physica A: Statistical Mechanics and its Applications*, 358(2–4), pp.249–262.

Langston, P.A. et al., 2004. Distinct element modelling of non-spherical frictionless particle flow. *Chemical Engineering Science*, 59(2), pp.425–435.

Langston, P. & Kennedy, A.R., 2014. Discrete element modelling of the packing of spheres and its application to the structure of porous metals made by infiltration of packed beds of NaCl beads. *Powder Technology*, 268, pp.210–218. Available at: http://dx.doi.org/10.1016/j.powtec.2014.08.018.

Lemieux, M. et al., 2008. Large-scale numerical investigation of solids mixing in a V-blender using the discrete element method. *Powder Technology*, 181(2), pp.205–216.

Lewis, R.W. et al., 2005. A combined finite-discrete element method for simulating pharmaceutical powder tableting. *International Journal for Numerical Methods in Engineering*, 62(7), pp.853–869.

Li, H. et al., 2004. Force evaluations in lattice Boltzmann simulations with moving boundaries in two dimensions. *Phys. Rev. E*, 70(2), p.26701. Available at: http://link.aps.org/doi/10.1103/PhysRevE.70.026701.

Li, J. et al., 2004. Flow of sphero-disc particles in rectangular hoppers - A DEM and experimental comparison in 3D. *Chemical Engineering Science*, 59(24), pp.5917–5929.

Li, S.. & Ng, K.-L., 2003. Monte Carlo study of the sphere packing problem. *Physica A: Statistical Mechanics and its Applications*, 321(1–2), pp.359–363. Available at:

http://www.sciencedirect.com/science/article/pii/S0378437102017983.

Li, X. & Ng, T.-T., 1995. Contact detection algorithms for three-dimensional ellipsoids in discrete element modelling. *International Journal for Numerical and Analytical Methods in Geomechanics*, 19, pp.653–659.

Li, Y. et al., 2009. Prediction of vortex shedding from a circular cylinder using a volumetric Lattice-Boltzmann boundary approach. *European Physical Journal: Special Topics*, 171(1), pp.91–97.

Liao, S.J., 2002. An analytic approximation of the drag coefficient for the viscous flow past a sphere. *International Journal of Non-Linear Mechanics*, 37(1), pp.1–18.

Lisjak, A. & Grasselli, G., 2014. A review of discrete modeling techniques for fracturing processes in discontinuous rock masses. *Journal of Rock Mechanics and Geotechnical Engineering*, 6(4), pp.301–314. Available at: http://dx.doi.org/10.1016/j.jrmge.2013.12.007.

Lochmann, K., Oger, L. & Stoyan, D., 2006. Statistical analysis of random sphere packings with variable radius distribution. *Solid State Sciences*, 8(12), pp.1397–1413.

Lu, G., Third, J.R. & Müller, C.R., 2015. Discrete element models for non-spherical particle systems: From theoretical developments to applications. *Chemical Engineering Science*, 127, pp.425–465.

Luo, L.S. et al., 2011. Numerics of the lattice Boltzmann method: Effects of collision models on the lattice Boltzmann simulations. *Physical Review E - Statistical, Nonlinear, and Soft Matter Physics*, 83(5).

Machado, R., 2012. Numerical simulations of surface reaction in porous media with lattice Boltzmann. *Chemical Engineering Science*, 69(1), pp.628–643.

Di Maio, F. & Di Renzo, A., 2005. Modelling Particle Contacts in Distinct Element SimulationsLinear and Non-Linear Approach. *Chemical Engineering Research and Design*, 83(11), pp.1287–1297. Available at: http://linkinghub.elsevier.com/retrieve/pii/S026387620572832X.

Mansouri, M. et al., 2009. A 3D DEM-LBM approach for the assessment of the quick condition for sands. *Comptes Rendus - Mecanique*, 337(9–10), pp.675–681. Available at: http://dx.doi.org/10.1016/j.crme.2009.09.010.

Maosong, T. et al., 2004. Estimation of permeability of shaly sand reservoir from induced polarization relaxation time spectra. *Journal of Petroleum Science and Engineering*, 45(1–2), pp.1–10.

Marinack Jr., M.C. & Higgs III, C.F., 2015. Three-dimensional physics-based cellular automata model for granular shear flow. *Powder Technology*, 277, pp.287–302. Available at: http://dx.doi.org/10.1016/j.powtec.2015.02.057.

Mccullough, J.W.S. et al., 2016. Lattice Boltzmann methods for the simulation of heat transfer in particle suspensions. *International Journal of Heat and Fluid Flow*, 62, pp.150–165. Available at: http://dx.doi.org/10.1016/j.ijheatfluidflow.2016.11.005.

McNamara, G.R. & Zanetti, G., 1988. Use of the boltzmann equation to simulate lattice-gas automata. *Physical Review Letters*, 61(20), pp.2332–2335.

Mei, R., Yu, D. & Shyy, W., 2002. Force evaluation in the lattice Boltzmann method involving curved geometry. *Phys Rev E*, 65, p.41203.

Mercer, T. et al., 1999. Hindered settling of particulate dispersions. *Journal of Magnetism and Magnetic Materials*, 193(1–3), pp.284–287.

Mikhailov, M.D. & Freire, A.P.S., 2013. The drag coefficient of a sphere: An approximation using Shanks transform. *Powder Technology*, 237, pp.432–435. Available at: http://dx.doi.org/10.1016/j.powtec.2012.12.033.

Mirtich, B., 1997. V-Clip: Fast and robust polyhedral collision detection. *ACM Transactions on Graphics*, 17, pp.177–208.

Mishra, B.K. & Rajamani, R.K., 1992. The discrete element method for the simulation of ball mills. *Applied Mathematical Modelling*, 16, pp.598–604.

Mueller, G.E., 1997. Numerical simulation of packed beds with monosized spheres in cylindrical containers. *Powder Technology*, 92(2), pp.179–183.

Munjiza, A., 2004. *The combined finite-discrete element method*, Wiley.

Mussa, A., Asinari, P. & Luo, L.S., 2009. Lattice Boltzmann simulations of 2D laminar flows past two tandem cylinders. *Journal of Computational Physics*, 228(4), pp.983–999. Available at: http://dx.doi.org/10.1016/j.jcp.2008.10.010.

Navvab Kashani, M. et al., 2016. A new method for reconstruction of the structure of micro-packed beds of spherical particles from desktop X-ray microtomography images. Part A. Initial structure generation and porosity determination. *Chemical Engineering Science*, 146, pp.337–345. Available at: http://dx.doi.org/10.1016/j.ces.2016.02.031.

Nguyen, N.Q. & Ladd, A.J.C., 2002. Lubrication corrections for lattice-Boltzmann simulations of particle suspensions. *Physical Review E - Statistical, Nonlinear, and Soft Matter Physics*, 66(4), pp.1–12.

Noble, D.R. & Torczynski, J.R., 1998. A lattice-boltzmann method for partially saturated computational cells. *International Journal of Modern Physics C*, 9(8), pp.1189–1201.

Nolan, G.T. & Kavanagh, P.E., 1992. Computer simulation of random packing of hard spheres. *Powder Technology*, 72(2), pp.149–155.

Oakeshott, R.B.S. & Edwards, S.F., 1994. Perturbative theory of the packing of mixtures and of non-spherical particles. *Physica A*, 202(3–4), pp.482–498.

Oger, L. et al., 2008. Study of the collision of one rapid sphere on 3D packings: Experimental and numerical results. *Computers and Mathematics with Applications*, 55(2), pp.132–148.

Owen, D.R.J., Leonardi, C.R. & Feng, Y.T., 2011. An efficient framework for fluid-structure interaction using the lattice Boltzmann method and immersed moving boundaries. *International Journal for Numerical Methods in Engineering*, 87, pp.66–95.

Pan, C., Hilpert, M. & Miller, C.T., 2001. Pore-scale modeling of saturated permeabilities in random sphere packings. *Phys. Rev. E. Stat. Nonlin. Soft Matter Phys.*, 64.

Papatzacos, P., 1989. Cellular Automaton Model for Fluid Flow in Porous Media. *Com plex Systems*, 3, pp.383–405. Available at: http://www.complex-systems.com/pdf/03-4-5.pdf.

Peng, S. et al., 2012. Using X-ray computed tomography in pore structure characterization for a Berea sandstone: Resolution effect. *Journal of Hydrology*, 472–473, pp.254–261. Available at: http://dx.doi.org/10.1016/j.jhydrol.2012.09.034.

Peng, Z. et al., 2016. Segregation and dispersion of binary solids in liquid fluidised beds: A CFD-DEM study. *Chemical Engineering Science*, 152, pp.65–83.

Perkins, E. & Williams, J.R., 2001. A fast contact detection algorithm insensitive to object sizes. *Engineering Computations*, 18, pp.48–62.

Peskin, C.S., 1977. Numerical analysis of blood flow in the heart. *Journal of Computational Physics*, 25(3), pp.220–252. Available at: http://www.sciencedirect.com/science/article/pii/0021999177901000.

Pettyjohn, E.S. & Christiansen, E.B., 1948. Effect of particle shape on free settling rates of isometric particles. *Chem. Eng. Progr.*, 44, pp.157–172.

Pitter, R.L., Pruppacher, H.R. & Hamielec, A.E., 1973. A numerical study of viscous flow past a thin oblate spheroid at low and intermediate reynolds numbers. *J Atmos Sci*, 30, pp.125–134.

Pournin, L. & Liebling, T.M., 2005. A generalization of distinct element method to tridimensional particles with complex shapes. *Powders and Grains 2005*, 2(1), pp.1375–1478. Available at: http://infoscience.epfl.ch/record/77616.

Prestininzi, P., Lombardi, V. & Rocca, M. La, 2016. Curved boundaries in multi-layer Shallow Water Lattice Boltzmann Methods: bounce back versus immersed boundary. *Journal of Computational Science*, 16, pp.16–28. Available at: http://www.sciencedirect.com/science/article/pii/S1877750316300151.

Purcell, W.R., 1949. Capillary pressures - Their measurement using mercury and the calculation of permeability therefrom. *Society of Petroleum Engineers*, 1.

Qian, Y.H., D'Humières, D. & Lallemand, P., 1992. Lattice BGK Models for Navier-Stokes Equation. *EPL (Europhysics Letters)*, 17, pp.479–484. Available at: http://stacks.iop.org/0295-5075/17/i=6/a=001.

Qiu, L.-C., 2015. A Coupling Model of DEM and LBM for Fluid Flow through Porous Media. *Procedia Engineering*, 102, pp.1520–1525. Available at: http://www.sciencedirect.com/science/article/pii/S1877705815003057.

Qu, L. et al., 2013. Quantitative numerical analysis of flow past a circular cylinder at Reynolds number between 50 and 200. *Journal of Fluids and Structures*, 39, pp.889–9746. Available at: http://dx.doi.org/10.1016/j.jfluidstructs.2013.02.007.

Ramos Caicedo, G. et al., 2002. Minimum fluidization velocities for gas-solid 2D beds. *Chemical Engineering and Processing*, 41, pp.761–764.

Rao, A. et al., 2010. The effect of column diameter and bed height on minimum fluidization velocity. *AIChE Journal*, 56(9), pp.2304–2311.

Reimers, C.E. et al., 2004. In situ measurements of advective solute transport in permeable shelf sands. *Continental Shelf Research*, 24(2), pp.183–201.

Rezaee, R., Saeedi, A. & Clennell, B., 2012. Tight gas sands permeability estimation from mercury injection capillary pressure and nuclear magnetic resonance data. *Journal of Petroleum Science and Engineering*, 88–89, pp.92–99. Available at: http://dx.doi.org/10.1016/j.petrol.2011.12.014.

Richardson, J.F. & Zaki, W.N., 1954. The sedimentation of a suspension of uniform spheres under conditions of viscous flow. *Chemical Engineering Science*, 3(2), pp.65–73. Available at: http://www.sciencedirect.com/science/article/pii/0009250954850159.

Rigby, S.P. et al., 2011. Improving the interpretation of mercury porosimetry data using computerised X-ray tomography and mean-field DFT. *Chemical Engineering Science*, 66(11), pp.2328–2339. Available at: http://dx.doi.org/10.1016/j.ces.2011.02.031.

Rong, L.W., Dong, K.J. & Yu, A.B., 2013. Lattice-Boltzmann simulation of fluid flow through packed beds of uniform spheres: Effect of porosity. *Chemical Engineering*

Science, 99, pp.44–58.

Rothman, D.H., 1988. Cellular-automaton fluids: a model for flow in porous media. *Geophysics*, 53, pp.509–518.

Saha, A.K., 2004. Three-dimensional numerical simulation of the transition of flow past a cube. *Phys. Fluids*, 16, pp.1630–1646.

Saito, F., Kamiwano, M. & Aoki, R., 1984. Free settling of a non-spherical particle in a stagnant liquid. *Particulate Science and Technology*, 2(3), pp.247–258. Available at: http://www.tandfonline.com/doi/abs/10.1080/02726358408906409.

Sarkar, S., van der Hoef, M.A. & Kuipers, J.A.M., 2009. Fluid-particle interaction from lattice Boltzmann simulations for flow through polydisperse random arrays of spheres. *Chemical Engineering Science*, 64(11), pp.2683–2691.

Schlichting, H., 1979. *Boundary layer theory* 7th ed., New York: McGraw-Hill, Inc.

Schmiedel, J., 1928. No Title. *Phyzik Z.*, 29.

Schmitt, M. et al., 2013. Characterization of pore systems in seal rocks using Nitrogen Gas Adsorption combined with Mercury Injection Capillary Pressure techniques. *Marine and Petroleum Geology*, 39(1), pp.138–149. Available at: http://dx.doi.org/10.1016/j.marpetgeo.2012.09.001.

Scott, D.G. & Kilgour, D.M., 1969. The density of random close packings of spheres. *Applied Physics 2*, pp.863–866.

Sexton, M.B. et al., 2014. Sheared disk packings as a model system for complex dynamics. *Physica A: Statistical Mechanics and its Applications*, 394, pp.312–319. Available at: http://www.sciencedirect.com/science/article/pii/S0378437113009217.

Shahi, S. & Kuru, E., 2016. Experimental investigation of the settling velocity of spherical particles in Power-law fluids using particle image shadowgraph technique. *International Journal of Mineral Processing*, 153, pp.60–65. Available at: http://dx.doi.org/10.1016/j.minpro.2016.06.002.

Shih, W.C.L. et al., 1993. Experiments on flow past rough circular cylinders at large Reynolds numbers. *Journal of Wind Engineering and Industrial Aerodynamics*, 49(1–3), pp.351–368.

Singha, S. & Sinhamahapatra, K.P., 2010. Flow past a circular cylinder between parallel walls at low Reynolds numbers. *Ocean Engineering*, 37(8–9), pp.757–769. Available at: http://dx.doi.org/10.1016/j.oceaneng.2010.02.012.

Smagorinsky, J., 1963. General circulation experiments with the primitive equations. *Monthly Weather Review*, 91(3), pp.99–164. Available at: http://dx.doi.org/10.1175/1520-0493(1963)091<0099:GCEWTP>2.3.CO.

Soontrapa, K. & Chen, Y., 2013. Mono-sized sphere packing algorithm development using optimized Monte Carlo technique. *Advanced Powder Technology*, 24(6), pp.955–961. Available at: http://dx.doi.org/10.1016/j.apt.2013.01.007.

Squires, L. & Squires Jr., W., 1937. No Title. *Trans. Am. Inst. Chem. Eng.*, 33.

Stokes, G.G., 1901. *Mathematical and Physical Papers*, Cambridge: Cambridge University Press. Available at: https://www.cambridge.org/core/books/mathematical-and-physical-papers/A9396EB3FAAC5388877253302BEF05D2.

Stokes, G.G., 1851. On the effect of the internal friction on the notion of pendulums. *Camb. Philos. Trans.*, 9, pp.8–106.

Strack, O.E. & Cook, B.K., 2007. Three-dimensional immersed boundary conditions for moving solids in the lattice-Boltzmann method. *International Journal for Numerical Methods in Fluids*, 55, pp.103–125.

Succi, S., 2015. Lattice Boltzmann 2038. *EPL (Europhysics Letters)*, 109(5), p.50001. Available at: http://stacks.iop.org/0295-5075/109/i=5/a=50001?key=crossref.25d788b03338660330490f90eaae331f.

Suikkanen, H. et al., 2012. Modelling packing of spherical fuel elements in pebble bed reactor using DEM. In *Discrete Element Modelling of Particulate Media*. The Royal Society of Chemistry, pp. 175–183.

Sukop, M.C. & Thorne Jr., D.T., 2007. *Lattice Boltzmann modeling. An introduction for geoscientists and engineers*, Springer.

Suzuki, M. et al., 2008. Study of the Wall Effect on Particle Packing Structure Using X-ray Micro Computed Tomography. *Advanced Powder Technology*, 19(2), pp.183–195. Available at: http://openurl.ingenta.com/content/xref?genre=article&issn=0921-8831&volume=19&issue=2&spage=183.

Swanson, B.F., 1981. A simple correlation between permeabilities and mercury capillary pressures. *Journal of Petroleum Technology*, 33.

Third, J.R. & Müller, C.R., 2013. Coupled LBM-DEM simulations of gas-fluidized beds. *AICHE 2013 Annual Meeting*.

Tsakiroglou, C.D. & Payatakes, A.C., 1990. A new simulator of mercury porosimetry for the characterization of porous materials. *Journal of Colloid And Interface Science*, 137(2), pp.315–339.

Tsakiroglou, C.D. & Payatakes, A.C., 2000. Characterization of the pore structure of reservoir rocks with the aid of serial sectioning analysis, mercury porosimetry and network simulation. *Advances in Water Resources*, 23(7), pp.773–789.

Tsutsui, T., 2008. Flow around a sphere in a plane turbulent boundary layer. *Journal of Wind Engineering and Industrial Aerodynamics*, 96(6–7), pp.779–792.

Tueckmantel, C. et al., 2012. Single- and two-phase fluid flow properties of cataclastic fault rocks in porous sandstone. *Marine and Petroleum Geology*, 29(1), pp.129–142.

Turnbull, J.C. et al., 2017. Atmospheric monitoring of carbon capture and storage leakage using radiocarbon. *International Journal of Greenhouse Gas Control*, 56, pp.93–101. Available at: http://www.sciencedirect.com/science/article/pii/S1750583616305473.

Vidal, D. et al., 2009. Effect of particle size distribution and packing compression on fluid permeability as predicted by lattice-Boltzmann simulations. *Computers and Chemical Engineering*, 33(1), pp.256–266.

Vollmari, K., Jasevičius, R. & Kruggel-Emden, H., 2016. Experimental and numerical study of fluidization and pressure drop of spherical and non-spherical particles in a model scale fluidized bed. *Powder Technology*, 291, pp.506–521.

Waddel, H., 1934. The coefficient of resistance as a function of Reynolds number for solids of various shapes. *J. Franklin Inst.*, 217.

Wang, L., Guo, Z.L. & Mi, J.C., 2014. Drafting, kissing and tumbling process of two particles with different sizes. *Computers and Fluids*, 96, pp.20–34.

Wang, L., Xu, W. & Xu, A., 2012. Three-dimensional cellular automata based particle flow simulations of mechanical properties of talus deposit. *Journal of Rock Mechanics and Geotechnical Engineering*, 4(4), pp.375–384. Available at: http://www.sciencedirect.com/science/article/pii/S1674775515302055.

Wang, M. et al., 2017. Numerical modelling of fluid-induced soil erosion in granular filters using a coupled bonded particle lattice Boltzmann method. *Computers and Geotechnics*, 82, pp.134–143. Available at: http://dx.doi.org/10.1016/j.compgeo.2016.10.006.

Washburn, E.W., 1921. *The dynamics of capillary flow*, Phys. Rev.

Weber, E. et al., 2010. Comparison of X-ray micro-tomography measurements of densities and porosity principally to values measured by mercury porosimetry for carbon-carbon composites. *Carbon*, 48(8), pp.2151–2158. Available at: http://dx.doi.org/10.1016/j.carbon.2009.11.047.

Wen, C.Y. & Yu, Y.H., 1966. Mechanics of fluidization. *Chemical Engineering Progress Symposium Series*, 62, pp.100–111.

White, F., 1991. *Viscous fluid flow* 66th ed., McGraw-Hill.

Williams, J.R. & Pentland, A.P., 1992. Superquadratics and modal dynamics for discrete elements in interactive design. *Engineering Computations*, 9, pp.115–127.

Willmarth, W.W., Hawk, N.E. & Harvey, R.L., 1964. No Title. *Physics of Fluids*, 7.

Wilson, A.M., Huettel, M. & Klein, S., 2008. Grain size and depositional environment as predictors of permeability in coastal marine sands. *Estuarine, Coastal and Shelf Science*, 80(1), pp.193–199.

Wolfram, S., 2002. *A new kind of science*, Wolfram Media.

Yazdchi, K. & Luding, S., 2011. On the Validity of the Carman-Kozeny Equation in Random Fibrous Media. *Particle-Based Methods II: Fundamentals and Applications*, pp.264–273. Available at: http://doc.utwente.nl/80382/\npapers3://publication/uuid/2E83E83C-7830-4A04-81F9-B0758FAA9AF3.

Yin, X., Le, G. & Zhang, J., 2012. Mass and momentum transfer across solid-fluid boundaries in the lattice-Boltzmann method. *Physical Review E - Statistical, Nonlinear, and Soft Matter Physics*, 86(2).

Yow, H.N., Pitt, M.J. & Salman, a. D., 2005. Drag correlations for particles of regular shape. *Advanced Powder Technology*, 16(4), pp.363–372. Available at: http://www.sciencedirect.com/science/article/pii/S0921883108608110.

Yu, D. et al., 2003. Viscous flow computations with the method of Lattice Boltzmann Equation. *Prog. Aerospace Sci*, 39(5), pp.329–338. Available at: http://www.sciencedirect.com/science/article/pii/S0376042103000034.

Yuan, Y. et al., 2016. Two typical structure patterns in jammed monodisperse disk packings at high densities. *Physica A: Statistical Mechanics and its Applications*, 461, pp.747–755. Available at: http://www.sciencedirect.com/science/article/pii/S0378437116303053.

Yuan, Y. & Rahman, S., 2016. Extended application of lattice Boltzmann method to rarefied gas flow in micro-channels. *Physica A: Statistical Mechanics and its Applications*, 463, pp.25–36. Available at: http://dx.doi.org/10.1016/j.physa.2016.06.123.

Zhang, D., Papadikis, K. & Gu, S., 2016. A lattice Boltzmann study on the impact of the geometrical properties of porous media on the steady state relative permeabilities on two-phase immiscible flows. *Advances in Water Resources*, 95, pp.61–79.

Available at: http://dx.doi.org/10.1016/j.advwatres.2015.12.015.

Zhao, D. et al., 2006. Three-dimensional discrete element simulation for granular materials. *Engineering Computations*, 23(7), pp.749–770.

Zhao, T. et al., 2015. A composite particle model for non-spherical particles in DEM simulations. *Granular Matter*, pp.763–774.

Zhiyin, Y., 2015. Large-eddy simulation: Past, present and the future. *Chinese Journal of Aeronautics*, 28(1), pp.11–24. Available at: http://www.sciencedirect.com/science/article/pii/S1000936114002064.

Zhou, J., Ye, G. & van Breugel, K., 2010. Characterization of pore structure in cement-based materials using pressurization-depressurization cycling mercury intrusion porosimetry (PDC-MIP). *Cement and Concrete Research*, 40(7), pp.1120–1128. Available at: http://dx.doi.org/10.1016/j.cemconres.2010.02.011.

Zhu, C., Liang, S.C. & Fan, L.S., 1994. Particle wake effects on the drag force of an interactive particle. *International Journal of Multiphase Flow*, 20(1), pp.117–129.

Zhu, H.P. et al., 2008. Discrete particle simulation of particulate systems: A review of major applications and findings. *Chemical Engineering Science*, 63(23), pp.5728–5770.

Zhu, H.P. et al., 2007. Discrete particle simulation of particulate systems: Theoretical developments. *Chemical Engineering Science*, 62(13), pp.3378–3396.

Zhu, H.P. & Yu, A.B., 2006. A theoretical analysis of the force models in discrete element method. *Powder Technology*, 161(2), pp.122–129.

Ziegler, D.P., 1993. Boundary conditions for lattice Boltzmann simulations. *Journal of Statistical Physics*, 71, p.1171-.

Zobel, N. et al., 2012. Influence of the wall structure on the void fraction distribution in packed beds. *Chemical Engineering Science*, 71, pp.212–219. Available at: http://dx.doi.org/10.1016/j.ces.2011.12.029.

Zou, Q. & He, X., 1997. On pressure and velocity boundary conditions for the lattice

Boltzmann BGK model. *Physics of Fluids*, 9(6), p.1591. Available at: http://arxiv.org/abs/comp-gas/9611001\nhttp://scitation.aip.org/content/aip/journal/pof2/9/6/10.1063/1.869307.

Zou, R.P. & Yu, A.B., 1995. The packing of spheres in a cylindrical container: the thickness effect. *Chemical Engineering Science*, 50(9), pp.1504–1507.

Appendix A

Permeability in sandstone: comparison of methodologies and literature with combined XMT-LBM

A case was investigated to compare permeability predictions from simulations with data from mercury intrusion porosimetry (MIP). Five different sandstone samples were kindly provided by Dr Anren Li from *Rock Deformation Research Ltd* at the moment of carrying out the tests in this appendix. The samples were labelled as S1, S2, S3, S4 and S5. A brief description of MIP is introduced first including relevant concepts and theory behind this technique to later present findings and discussion about results obtained.

It is important to note that at the time of printing this thesis, the experimental data of porosity and permeability from MIP, and porosity data from SEM was not published. For that reason the experimental data was not included for comparison in the results section. However, the extensive work carried out led to a methodology and studies that are considered worth to discuss and present. Discussion will include MIP and SEM qualitative comparisons but data was not actually included in tables and figures.

There were two data sets provided including values of porosity and permeability; one includes direct measurements of permeability through permeametry technique and volume-based porosity estimations based on SEM images. The other data set comes from MIP raw data to predict permeability and porosity by means of empirical equations behind the software used with the equipment; such equations are presented in a further section. In this way, figures comparing results will include information from these two data sets plus values obtained using LBM for permeability predictions.

The procedure for sample digitisation, image post-processing and analysis was very similar for each one of the five samples. A brief description of the steps followed is listed below:

- Samples were reduced in size to about 2 to 3 mm^3; coarse sand paper was used to give a raw cubic shape, then fine sand paper helped to smooth out all the faces of the sample
- Scans were carried out obtaining 1440 projections for each sample; once finished, volume reconstruction was performed using the scanner proprietary software

- Post-processing of the digitised volumes in DigiUtility was carried out (i.e. air from the background was removed conserving only the voxels forming the rock sample)
- Post-processed images were compared at the same scale with the corresponding SEM image in order to visually compare the pore network. Four sub-volumes of dimensions 300x200x200 voxels were extracted from each sample
- Porosity, mean empty space (1000 points), and tortuosity (1000 random points, 100 repetitions per point, bounce back probability factor 0.5, maximum number of steps 1000) were calculated in DigiUtility for each one of the sub-volumes
- Sub-volumes were imported in DigiFlow to perform fluid flow simulations and permeability calculations. The parameters configured were τ = 1 and b_f = 0.001 for all tests
- Data gathering and analysis

The image post-processing stage required the application of a number of software tools to achieve an appropriate sample definition of the features of interest, in this case the correct visualisation of the pores within the sample. In most cases sample enhancing was necessary to distinguish the region of interest and discard non-relevant voxels. In digital images, pores are interpreted as air as well as the empty space surrounding the sample. These groups of pores were removed from the digital volumes.

Three-dimensional digital images are compounds of cubes known as voxels; each voxel has a particular numerical value in an 8-bit RGB scale assigned depending on attributes such as colour and brightness. Reduction of noise in the image can be done by applying filters, which basically modify the value of every voxel based on a function involving the values of neighbouring voxels. To smooth the image a Gaussian filter (low pass filter) was used; in some cases a median filter was also used to preserve the object edges, or filters to reduce the noise. The correct filter to apply depends on the results observed; the user could apply repeatedly the same filter if necessary or a combination of them until the desired features are emphasised. The kernel or total number of neighbouring voxels involved in a filtering function can be selected by the user to produce different results.

Two different thresholdings were applied to the digitised images to remove air voxels setting their individual values to 0. For instance, in Figure A-1 a 2D projection of sample S2 is observed where the white space corresponds to air. From left to right, the original XMT image is presented; to the right, the image after applying threshold 1; and far on the right, the image after applying a different threshold 2. The difference between

these two thresholdings is basically the range of voxels set to 0, i.e. for thresholding 1 the range of voxel values cut off was [124, 255]; in thresholding 2 the range was [120, 255]. Although the range difference seems to be small, it has an important impact once the filters and thresholding are applied to the entire volume. Pore size and shape are modified when voxels are removed; this directly affects the overall porosity of the sample. The bigger the volume, the larger number of voxels that can be potentially removed applying a small range thresholding.

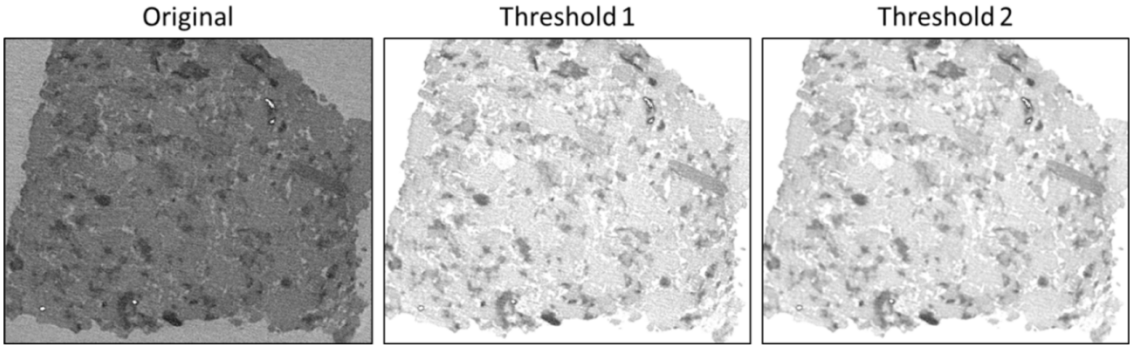

Figure A-1 Comparison of a 2D projection before and after applying thresholding

All five rock samples were scanned at resolution 1.5 μm/pixel; after applying the aforementioned thresholdings, 4 different sub-volumes of lengths in 300x200x200 voxels in X, Y and Z directions were extracted from each volume to evaluate permeability. The longest length was configured as the fluid flow direction in simulations. Porosity and permeability values from the four sub-volumes were averaged and presented as final results. SEM images were available and helped to compare digitised images after applying thresholding to visually assess the pores in every sample.

Figure A-2 shows a cross section of sample S2 with thresholding 2 applied in which the blue, red and yellow squares indicate the location where three sub-volumes were extracted. A fourth sub-volume was extracted from the blue squared location but at a different height. The corresponding coordinates of every sub-volume are shown below the image. Although the locations of every square differ from sample to sample, the same procedure was followed for all the five samples.

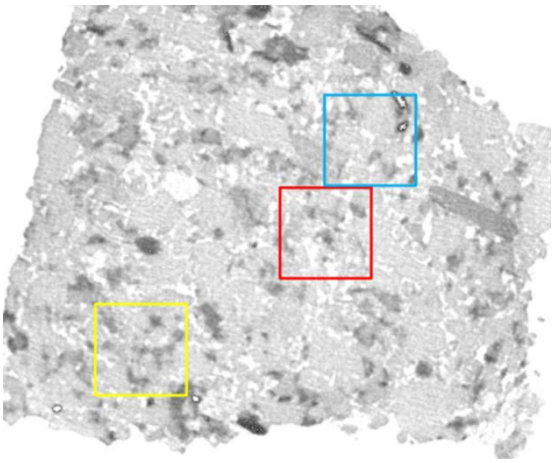

Figure A-2 XY cross section of sample S2 showing locations of 3 sub-volumes

Coordinates:

Sub-volume 1: x [600 800], y [400 600], z [450 750] – Red square

Sub-volume 2: x [200 400], y [660 860], z [200 500] – Yellow square

Sub-volume 3: x [700 900], y [200 400], z [200 500] – Blue square

Sub-volume 4: x [700 900], y [200 400], z [600 900] – Blue square at different height

Mercury intrusion porosimetry technique - The MIP technique is widely used in the characterisation of rock samples obtaining parameters such as pore-size distribution, pore volume and porosity; in bio medics in the characterisation of tricalcium phosphate granules; in the petrochemical industry to obtain the pore volume of catalyst substrates such as silica and alumina zeolites; in studies of oil and gas reservoirs; in aquifers pollution studies; and in pharmacy to assess the quality of tablets produced under different compression values, just to mention a few.

The MIP technique is based on the progressive intrusion of a non-wetting liquid, commonly mercury, at controlled high pressures into a sample by means of a porosimeter. The sample to be analysed is placed in a small chamber connected to a glass capillary stem, both chamber and capillary filled with mercury. In the first intrusion steps, the largest pores are filled in. As the applied pressure is increased, the smallest pores would experience mercury intrusion. As mercury is introduced, its volume is monitored by changes in capacitance between a metal cladding on the outer surface of the glass stem and the mercury column inside it. The pressure increments together with the corresponding cumulative volume are the raw data produced from MIP tests.

The pressure used to control mercury intrusion is a measured parameter; once this data is obtained, the volume of mercury intruded related to pressure is known. Both parameters help to evaluate pore volume, pore size and porosity of the sample.

The concept of 'wetting' is relevant for MIP experiments. Wetting can be seen as the affinity of a liquid for a solid surface. When adhesive forces in the interface are predominant, the liquid will spread across the solid surface thus resulting in a wet surface. If cohesive forces are predominant, the liquid may behave as a stationary sphere-shaped droplet, case in which the liquid is known as non-wetting. A way of measuring the wetting is the contact angle θ between the solid surface and the tangent to the liquid droplet as seen in Figure A-3. A wetting liquid will show contact angles smaller than 90°, whereas a non-wetting liquid shows values of $90° < \theta < 180°$.

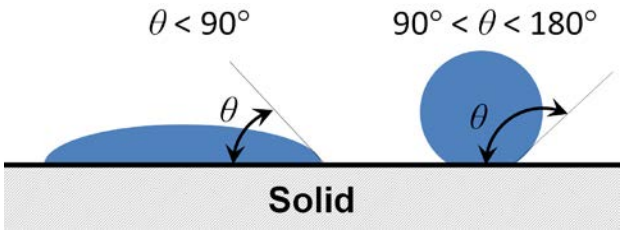

Figure A-3 Wetting (left) and non-wetting liquid (right)

In MPI, mercury (Hg) is the non-wetting liquid used for intrusion into the pores. Pressures greater than ambient pressure must be applied to mercury in order to force it into the pores as shown in Figure A-4.

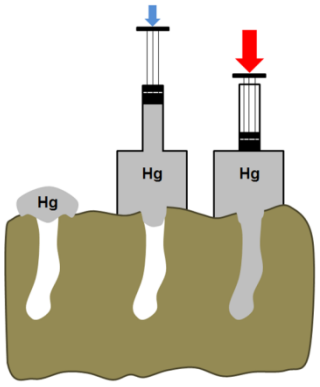

Figure A-4 Representation of mercury intrusion in a pore

As pressure is applied, the mercury intrusion starts; firstly the larger pores are filled in with mercury. Thereafter, the pressure is increased progressively, measuring the volume of mercury intruded through changes in capacitance between a metal shield on

the outer part of a capillary glass and the mercury column length in the capillary tube. The continuous increment in pressure causes the fill of smaller pores, whether they are inter-particle or intra-particle pores, making evident the inverse proportional relationship between pressure and pore size, i.e. more pressure is needed to fill smaller pores. For example, commercial porosimeters pressure range can go from 50 to 60000 psi, the highest pressure corresponding to pores of 0.003 μm diameter.

The Washburn equation (Washburn 1921) is used in MIP since it relates the applied pressure to pore diameter indicating that the pressure required to force a non-wetting liquid into a capillary pore is inversely proportional to the diameter of such capillary, and directly proportional to the liquid angle of contact with the surface and its surface tension. According to this equation, for a capillary of small radius, it will be necessary to apply more than one atmosphere of pressure differential to the non-wetting liquid to enter the capillary filled with atmospheric pressure. From the pressure-versus-intrusion data produced from an experiment, volume and pore size distribution are generated based on the Washburn equation:

$$P = -\frac{4\gamma\cos\theta}{D_P} \tag{A-1}$$

where P is the applied pressure on the liquid for intrusion; γ is the surface tension of liquid; θ is the contact angle of intruded liquid; and D_P is the pore diameter. The minus sign in (A-1) is to cancel with $\cos\theta$. Since the MIP technique is performed under vacuum, P begins at zero. The contact angle of mercury with most of solids is approximately 140°; the surface tension of mercury is ≈ 0.48 N/m, thus yielding a simple expression to calculate pore diameter in function of applied pressure:

$$D_P = \frac{1.47}{P} \tag{A-2}$$

Although MIP technique based on (4-2) has been proven a powerful and widely used tool for qualitatively analysis of porous structures and for practical representation of pore distributions, one of its drawbacks is the assumption of pores within the structure as cylindrical tubes. This may result in differences between analysis and real measurements. The technique measures the pore entrance or throat but not the real inner size of the pore. Additionally, mercury will not enter in closed pores, and the

overall porosity of the sample may be underestimated. To better understand this effect, a representation is shown in Figure A-5.

In Figure A-5-a) the ideal case for pore size calculation with equation (A-2) is depicted; at initial low pressure P_1 the largest pore with diameter d_1 is filled. When pressure is increased a different range of pores smaller than d_1 is filled; thus, pores within the range $d_2 < d_1$ are filled at P_2. If pressure is further increased to P_3, the smallest pores with diameter d_3 are filled. Figure A-5-b) shows the case where the same volume of mercury is intruded in the pore as in case a) but only until P_3 is reached. The same figure reveals a phenomenon known as ink-bottle effect due to the similar shape of a pore with narrow throat at the top and wider opening below. The consequence of this pore shape is a potential overestimation in the total number of pores with small diameters. When P_1 (corresponding to d_1) is applied at the pore entrance at the top, no mercury is intruded. Applying P_2 would not cause any effect either; but when P_3 is applied the whole pore would be filled. In this case, a plot of pore diameter vs total volume intruded will show a large volume of mercury intruded for small pores of diameter d_3.

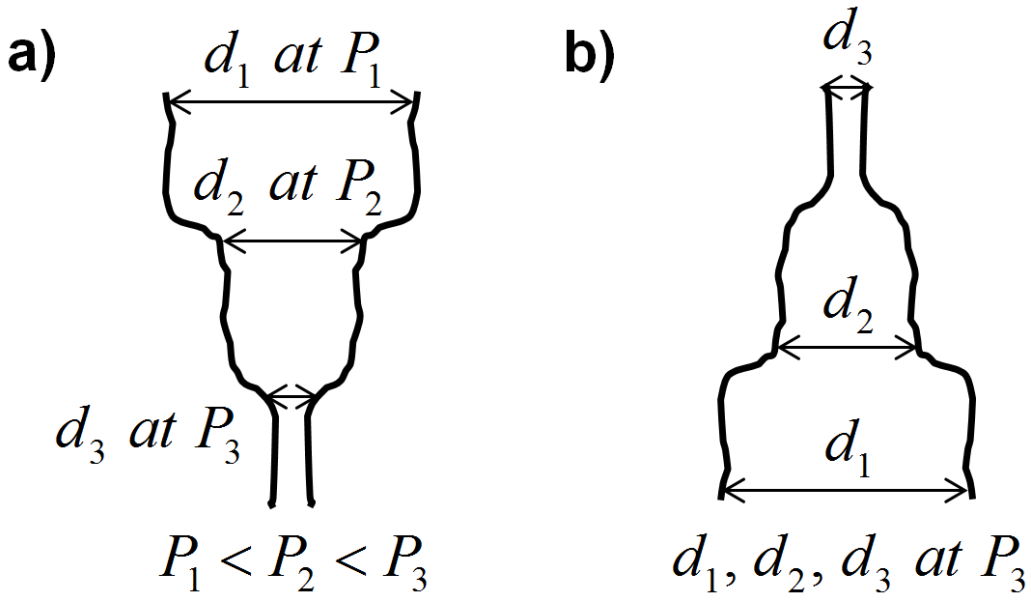

Figure A-5 Non-cylindrical pores and ink-bottle effect

From the total volume intruded, the length of the sample is consider as the height of the cylinder-like pores within the sample, resulting in an unrealistic total number of pores of

size d_3. It is important to bear in mind that pores are not always straight and the ideal interpretation of cylindrical pores neglects pore connections and tortuous pore paths.

To overcome the phenomenon just described, decreasing pressures can be included in the analysis as well after mercury has been completely intruded into the sample. The curve produced is called “extrusion curve” which differs from the intrusion curve due to hysteresis because there is mercury entrapment in ink-bottle shaped pores and there is no internal force pushing the mercury out of the pores. The difference between the two curves helps to better characterise pore shape.

Porosity calculations and permeability predictions from combined XMT-LBM technique - In this section the combined XMT-LBM technique for characterisation of five rock samples provided is presented. Additional calculations to obtain permeability and porosity from MIP raw data were made but unfortunately are not presented for the reasons stated at the beginning of section 4.2.4. The results were further compared with different permeability estimations found in the literature.

The resolution of 1.5 µm/pixel at which samples were digitised constrained the consideration of the entire pore size range. This meant that the smallest pore size was 1.5 µm, leaving out a pore range from samples having a minimum pore size of the order of 10^{-3} µm. For this reason it was sensible for the study to compare porosity at the same level, i.e. to delimit data from MIP to calculate the corresponding porosity down to a pore size limit. Two curves resulted from the restriction of minimum pore size to 1.5 and 4.5 µm.

Unlike MIP technique that misses out pores where Hg cannot enter, one of the advantages of XMT digitisation technique is the capability to capture and visualise closed pores (see Figure A-6). This image is rendering the pore network of sub-volume 2 from sample S5. The white arrows indicate closed pores that MIP definitely cannot access but they are visible in the digitised version of the structure and ultimately account for the overall porosity. The XMT porosity yielded higher values when compared with the corresponding MIP curves limited to 1.5 and 4.5 µm. Even though these pores do not contribute to permeability, whether measured or predicted by LBM, they do contribute in proportion to the porosity calculation from XMT.

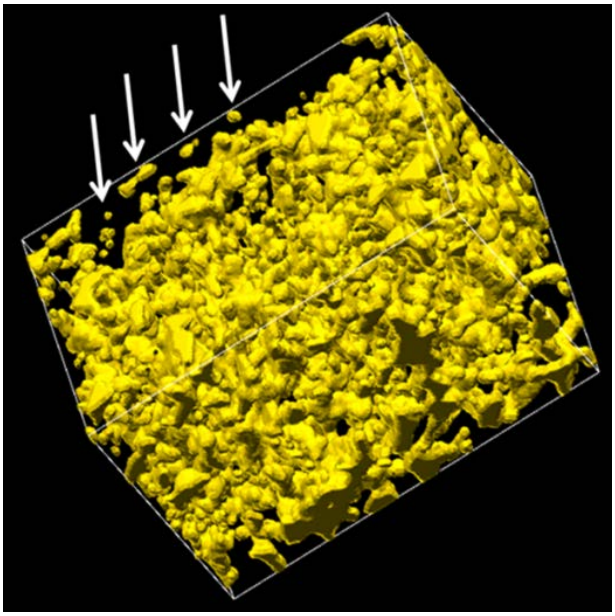

Figure A-6 Visible closed pores within sample S5 sub-volume 2

Comparing the two data sets provided, MIP porosities were larger than SEM porosities, which can be attributed to the fact that SEM only considers a small region of the sample and is an averaged value over a selected number of 2D images. However, when comparing XMT curve with SEM curve, porosity values of samples S1, S3 and S4 were very close to each other, indicating a good match of porosity since through SEM it is also possible to detect closed pores as in XMT. On the other hand, XMT porosities were lower when comparing with MIP curve; this effect was expected because XMT did not capture the range of smallest pores below image resolution limitation.

Although possible, it is difficult to assert that the total volume corresponding to closed pores detected in XMT images is equivalent to the volume of all the pores with pore-throats smaller than 1.5 µm. If truth, it will be fair to simply claim so in order to overcome the fact that this range of small pores is not accounted in the digitised image. For instance, a significant number of undetected small pores are needed to fit in only one closed pore in XMT image which in theory could balance the overall porosity. Therefore, to make a direct comparison it was necessary to know the volume of all the pores smaller than 1.5 µm and the volume of closed pores in XMT image.

In order to further assess the effect of these closed pores on porosity, different tasks were carried out including pore volume comparison assuming homogeneous pore network throughout the rock samples and using only MIP pore size data limited to 1.5

µm and 4.5 µm. Closed pores were removed in XMT volumes in the attempt to keep only all the interconnected pores and understand how this reduced porosity compares to MIP data.

Porosity from MIP was compared with small and large sub-volumes of every sample, and the same sub-volumes without closed pores present. From MIP raw data, the sample volume is known as well as the total volume of mercury intruded at the end of the test and the cumulative volume in every pressure step measurement. With this data, the corresponding fraction of pore volume captured in XMT sub-volumes was compared with data considering all the Hg volume intruded, Hg volume intruded to a limit of 4.5 µm and Hg volume intruded to a limit of 1.5 µm. To ensure that the volume size of selected sub-volumes is representative of the original volume scanned, porosities from larger volumes were obtained from the rock samples.

Figure A-7 presents three XMT porosity curves. The curve corresponding to small sub-volumes was labelled as XMT (small); the curve for large sub-volumes was labelled as XMT (large). Small sub-volumes had dimensions 300x200x200 LU, whereas large sub-volumes varied in size according to the original size of the digitised volume. The samples' shapes were irregular, so the largest possible sub-volumes obtained were (all in LU) S1: 500x500x450; S2: 700x650x1200; S3: 600x800x875; S4: 400x600x1100 and S5: 550x1000x1000.

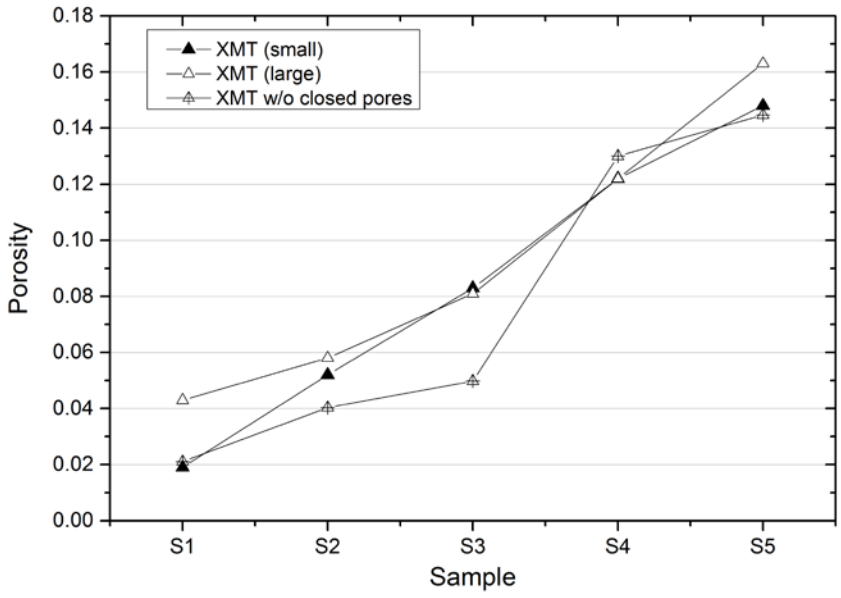

Figure A-7 Porosity comparison including XMT sub-volumes without closed pores

Sample S1 porosity was higher in the large volume; this is attributed to a marked irregularity in pores and long cracks observed that directly affected overall porosity. In sample S5-large wide pores were observed in some areas that likely contributed to porosity increase. Sample S3 showed a significant reduction in porosity when the closed pores were removed. Such behaviour was observed to have an impact on permeability calculated from MIP, curve in which sample S5 showed the lowest permeability. XMT curves with closed pores (small and large) seem to have a smoother transition between samples whereas the curve showing porosities w/o closed pores presents a notorious change for sample S3.

Matching SEM and MIP porosities with DEM generated structures - Porous structures were generated with DigiDEM using digitised sand grains. To match low porosities reported by SEM and MIP, large overlaps were allowed among particles with the solely intention of reproducing tight structures and compare permeability trends in case that XMT sub-volume would have had porosities similar to the reported ones from MIP and SEM.

In Figure A-8 two plots are presented, on the left-hand side the case matching SEM porosities, and on the right-hand the case matching MIP porosities. For these specific plots there are two Y axes having independent scaling, one for permeability and the other for porosity to directly observe the relationship between the two parameters.

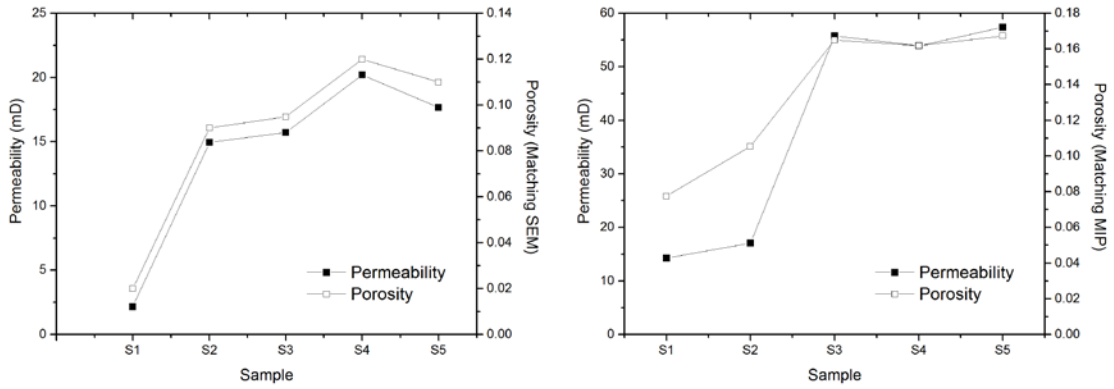

Figure A-8 SEM (left) and MIP (right) porosities from structures generated in DigiDEM

Within the small range of porosities it was expected to have a linear relationship as observed in Figure A-8, in which it is evident that a reduction in porosity followed a reduction in permeability. That is the ideal case but in reality, permeability is influenced greatly by large pores and their interconnectivity. For instance, MIP permeability curve showed a different trend compared to its corresponding porosity curve. MIP

permeability estimation is based on an empirical equation (A-3) presented in a further section. The difference between two measuring techniques suggested that there is a range of low permeabilities in which MIP technique may not be accurate when its predictions were compared with measured values. MIP overestimated permeability for samples S1 and S2 with differences of 3 and 1 order of magnitude respectively.

Figure A-9 compares permeability curves from the sub-volumes presented previously with the DEM structures generated matching SEM and MIP porosities. The XMT sub-volumes curve followed the trend of measured data but predictions overestimated measured data up to 3 orders of magnitude for S1; 2 orders of magnitude for S2 and S3, and 1 order of magnitude for S4 and S5.

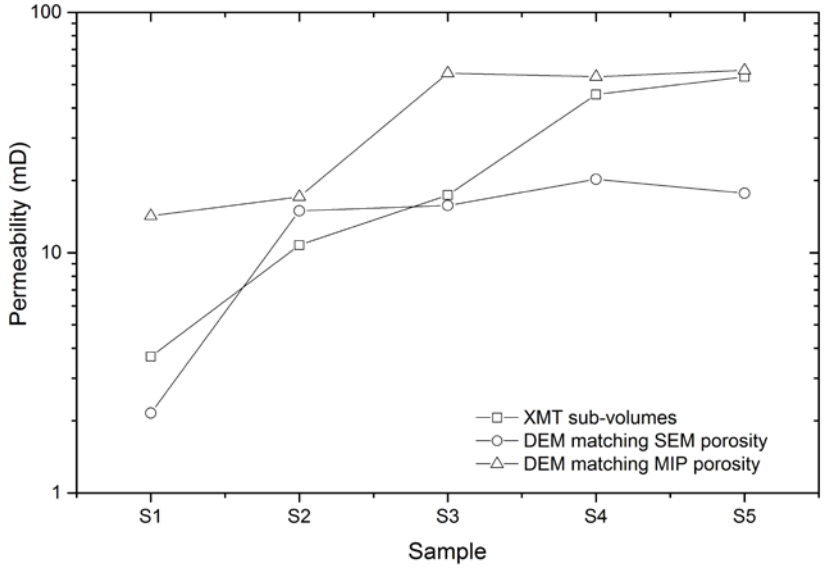

Figure A-9 Permeability comparison among DEM-SEM, DEM-MIP and XMT

In order to check consistency and repeatability of permeability predictions, larger volumes were used in fluid flow simulations. Since calculations were time consuming only one sample was selected for this test. A cubic volume of dimensions 400 LU^3 was tested with fluid flowing in X, Y and Z directions. A larger volume of dimensions 800x300x300 LU was also used with fluid flowing only in the longest direction. The predictions showed consistency between them but still overestimated permeability by similar orders of magnitude. In this case, the test helped to discard the idea that small sub-volumes had an effect in over predictions, and sample homogeneity was confirmed.

A different factor was thought to lead to overestimated permeability predictions. This was the possibility that closed pores may have been opened unintentionally at the moment of extracting the corresponding XMT sub-volumes. For this reason a pore network analysis was carried out.

A methodology was designed to thoroughly study and classify the types of pores present in the sub-volumes and their proportion. The intention was to identify only the open pores that go from end to end (through pores) and semi-open pores in the flow direction. Four categories were defined, explained below and depicted in Figure A-10:

- Closed pore. A cluster of empty voxels that is neither in contact with any wall, nor in contact with a neighbouring pore
- Semi-open pore. A cluster of empty voxels in contact with one of the walls in the flow direction
- Open or through pore. A cluster of empty voxels in contact with both walls in the flow direction
- Other. A cluster of empty voxels in contact with one or two walls in a non-flow direction

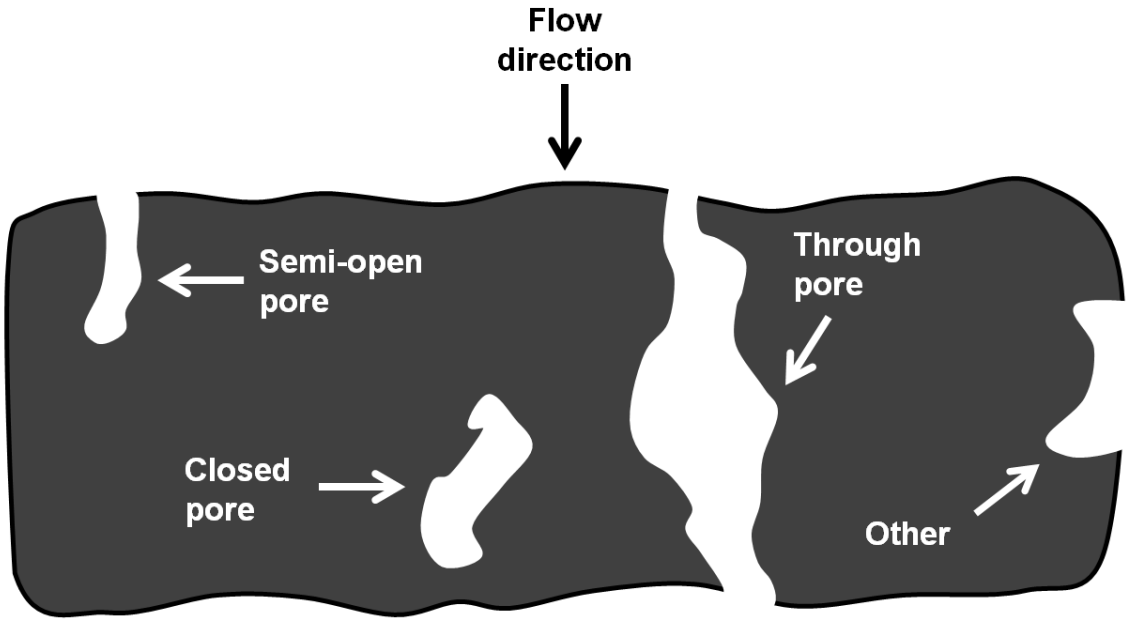

Figure A-10 Clasification of pores present within a structure

After obtaining the pore classification for each sample sub-volume, fluid flow simulations were carried out in samples containing only semi-open pores. One order of

magnitude reduction for tightest samples S1 and S2 was observed, bringing closer the prediction curve to the measured one.

After a comprehensive pore analysis it was found that two different voxels corresponding to two different pores touching at their vertices showed high velocity fluid flow. This meant that semi-open pores at one end of the sample actually were through pores when in diagonal contact with other semi-open pores reaching the opposite end of the sample.

The reason is due to LBM nature allowing PDFs streaming to neighbouring cells including diagonal directions. For this reason, artificial structures with different square-shaped-entry pores were generated with the intention of evaluate their contribution to permeability predictions.

The structures tested consisted of: a) six through pores, b) six through pores and two semi-open pores, and c) six through pores and 1 diagonal pore as presented in Figure A-11. Permeability predictions are compared in Table A-1.

Table A-1 Porosity, velocity and permeability of through, semi-open and diagonal pores

Structure	Porosity	Fluid velocity (LU)	Permeability (mD)
a)	0.24	0.00525	887.04
b)	0.28	0.00527	890.42
c)	0.28	0.00528	892.22

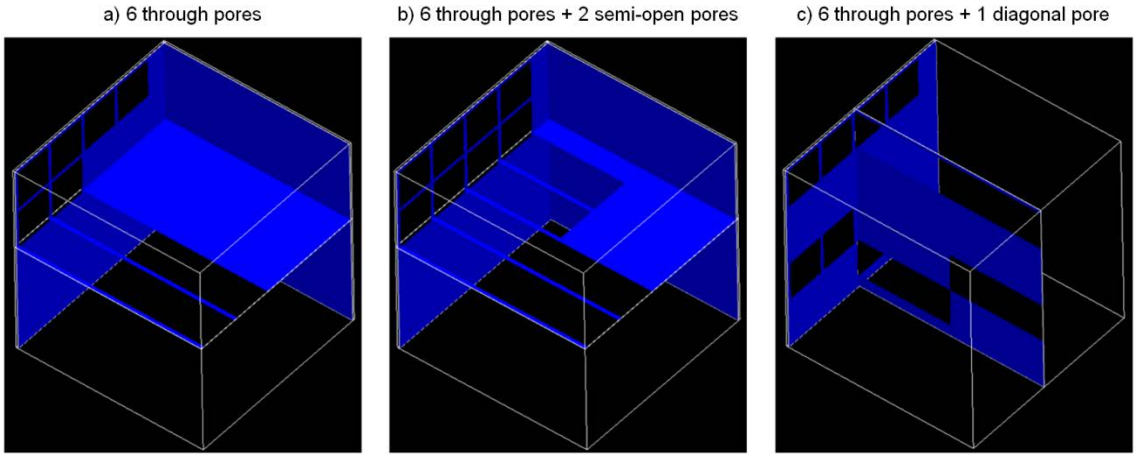

Figure A-11 Pores used to test permeability contribution according to its clasification

According to the results the contribution of through pores is minor and cannot be conclusive to show evidence that the difference of 3 or 2 orders of magnitude is caused by these pores. However, it is known that pore interconnection has a significant impact on permeability. The more interconnections among pores, the more increase in permeability. What is not clear in the literature and from experiments is to what extent permeability is increased, and what is the pore size classification of interconnections leading to an increased permeability.

In order to further investigate permeability calculations, in the following paragraphs relevant permeability estimation techniques found in the literature are discussed and used to compare previous findings with calculations using these different techniques.

Katz and Thompson model - The permeability estimation theory behind MIP is based on laboratory measurements carried out by Katz & Thompson (1986). Their permeability model is described by:

$$k = \frac{1013}{226} L_c^2 \frac{\sigma}{\sigma_0} \qquad \text{(A-3)}$$

The permeability k is a function of a critical or characteristic length L_c which corresponds to a pore diameter found at a threshold Hg intrusion pressure. Such pressure is found from the intrusion volume vs pressure plot where the curve shows a steepest section. The threshold pressure can be calculated beforehand or the MIP user can define a fixed value before carrying on with the tests. The characteristic length can also be found from the cumulative Hg saturation vs pressure curve where an inflection from concave upwards to concave downwards is observed. From the raw data it was confirmed that the pressure threshold was fixed by the MIP user to be 14 psia for the five samples; given this pressure, a corresponding diameter was assigned to be L_c using the Washburn equation.

The sigma ratio in equation (A-3) is another output data known as conductivity formation factor. In this model is described as the ratio of rock electrical conductivity σ at 100% brine saturation to the brine conductivity σ_0 in the pore space. The constant 1013 in equation (A-3) is used to convert permeability in μm^2 to milidarcies (mD); the constant 226 was derived in Katz & Thompson (1987) paper from assumptions of percolation theory and fractal dimension.

Purcell model - Other methodologies exist based on Poiseuille tube models for MIP in which the total flow through a rock is equal to the summation of the flow in individual tubes of different diameters. Purcell (1949) presented a work in which an equation was formulated to relate permeability to porosity in porous structures according to experimental data generated. The relation found was presented as:

$$k = Cf\varepsilon \sum_{S_{Hg}=0\%}^{S_{Hg}=100\%} \frac{S_{Hg_i}}{\left(P_{Hg_i}\right)^2} \qquad \text{(A-4)}$$

where k is permeability in mD; C is a constant used to convert units when pressure P_{Hg} is input in psia; f is a constant lithology factor that depends on the rock type and pore network; sample porosity ε; and S_{Hg} is the mercury saturation increment.

Purcell based his model in experimental tests carried out on 27 sandstones showing moderate to high permeability, thus finding a factor f = 0.216. Comisky et al. (2007) tested a larger number of samples in a wider range of permeabilities finding f = 0.15. The problem of using this factor directly in (A-4) is that this equation was designed based on a smaller range of permeabilities and as such, the permeability will be underestimated.

Swanson model - This estimation of permeability was founded from a power law relationship between permeability and the Swanson parameter (Swanson 1981) defined as the bulk rock Hg saturation in % divided by the mercury capillary pressure in psia.

$$k = aS^b \qquad \text{(A-5)}$$

Swanson found the parameters to be a = 399 and b = 1.691 for permeability k in mD. The maximum ratio of mercury saturation to pressure S was found from the capillary pressure curve. Swanson proposed that this maximum point takes place when the pore network is filled with Hg and the corresponding capillary pressure reflects the effective interconnected pores that predominate in the sample and control the fluid flow. Although several authors have proposed different values for these parameters, Comisky et al. confirmed that the original Swanson's values better fit low permeability data.

Large sets of data from MIP were analysed and used in the equations from the models previously presented to obtain the corresponding permeability estimations. The results were compared with those ones from combined XMT-LBM technique proposed in this work. In the following sections the findings are presented and discussed.

It is important to point out that two different threshold pressures were considered since the output MIP dataset reported a fixed value of 14 psia, but the pressure vs %Hg volume intruded curves showed a different value. For example, the corresponding curve for sample S1 showed a threshold pressure at 600 psia. The corresponding threshold pressures of the rest of the samples were obtained in the same way: S2: 250; S3: 150; S4: 55 and S5: 50 psia.

After analysing the results using the datasets corresponding to the above threshold pressures and the user-fixed pressure from MIP data (14 psia), it was found that a better agreement was achieved when using the pressures obtained from the corresponding pressure vs %Hg volume intruded plots. Table 4-7 shows the comparison of the values previously obtained with XMT-LBM with the calculations using the different estimations introduced. MIP permeability was calculated considering a fixed L_c for all the samples. Figure A-12 presents the curves corresponding to values reported in Table A-2.

Table A-2 Values of permeability from XMT-LBM and estimations

	Permeability (mD)				
Method	S1	S2	S3	S4	S5
Predicted (XMT-LBM)	3.696	10.746	17.4	45.511	54.031
Katz et al. (1986)	0.001	0.0017	0.004	0.069	0.208
Purcell (1949) f = 0.216	0.0015	0.008	0.033	0.261	0.468
Swanson (1981)	0.125	0.015	0.008	0.037	0.098

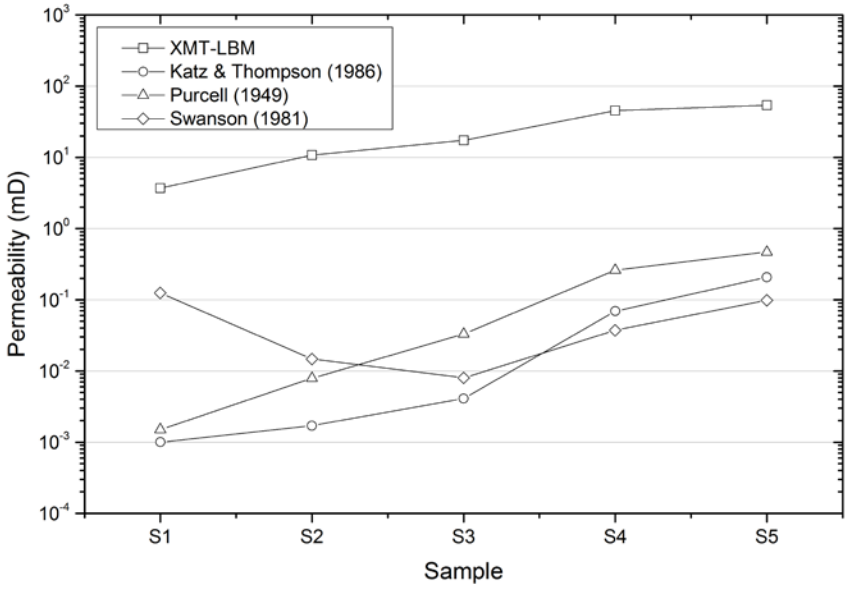

Figure A-12 Comparison of permeability values from different methodologies used

Samples used for porosity and permeability studies are commonly taken from the same core extracted. Although homogeneity is expected between neighbouring samples, differences in porosities and permeabilities reported may become apparent when cores have been stored for long periods of time and are dried and not prepared correctly, i.e. carrying out a proper cleaning work and water-vapour pressure equilibration test. Similarly, the duration of tests may have an impact on the results.

For MIP tests Jones & Owens (1980) recommended a minimum confining stress of 1000 psi for tight samples in order to close micro fractures in the sample. Tests using a higher stress may result in undesired effects such as crushed pore throats, which in turn would result in fines generation that might close some pores and reduce porosity. Data provided from MIP tests showed a maximum stress of 60000 psi applied to every sample, which is a confining stress much higher than those ones observed in in situ reservoirs. These may cause an increase in scatter rather than major deviations of the permeability trend. The precision of measurements in MIP depends on the pressure steps and the time each pressure is kept constant to allow mercury reach a steady status. From the raw data, the steps yielded a precision of about 14%.

Results using estimations from Katz & Thompson, Purcell and Swanson showed underestimation of permeabilities compared to MIP and measured data. Katz & Thompson and Purcell estimations showed better agreement for points following the trend of measured data. However, differences still showed a variation of 1 or 2 orders

of magnitude for samples S2 to S5. Swanson's curve followed the permeability trend of MIP data, the values were underestimated though.

Pores present within the sample before MIP tests could have been closed during mercury intrusion when increasing the effective stress. If in MIP tests pores were closed due to high stress Hg intrusion, that could have resulted in lower permeability measurements compared to predictions because in simulations the flow did not close pores. The rock samples scanned were not the same used in MIP tests because those ones were contaminated. That means that samples scanned did not suffer additional stress and potentially, no artificial closure of open pore.

Appendix B

Boundary layer solution for laminar flow on a plate

Paul Richard Heinrich Blasius (Blasius 1907) described a steady two-dimensional laminar boundary layer formed by a constant and unidirectional incompressible flow on a semi-infinite plate with zero pressure gradient. The free stream velocity *U* at the inlet is constant, meaning that *dU/dx = 0*. As the fluid flows, the effect of the presence of the plate propagates outwards into the fluid, and the boundary layer thickness becomes broader. This boundary layer thickness is represented by *δ* in Figure B-1, and refers to the distance across a boundary layer perpendicular from the wall to a point where the flow velocity has essentially reached the free stream velocity.

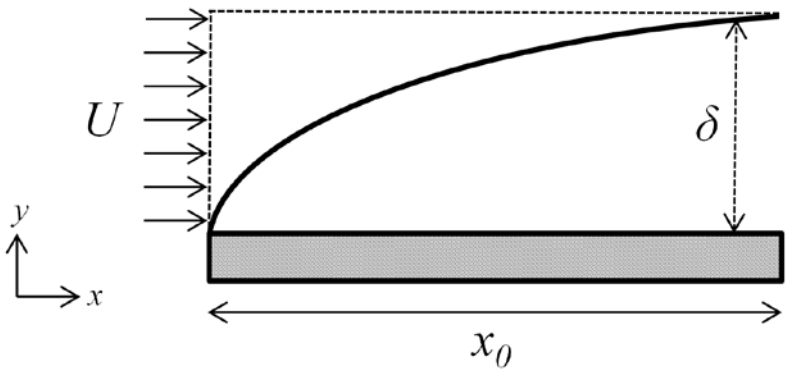

Figure B-1 Representation of the boundary layer thickness δ

For laminar boundary layers over a flat plate with a steady incompressible flow with constant viscosity, the governing equations of the Blasius solution are:

$$\frac{\partial u}{\partial x}+\frac{\partial v}{\partial y}=0\,,\; u\frac{\partial u}{\partial x}+v\frac{\partial u}{\partial y}=\nu\frac{\partial^2 u}{\partial y^2} \qquad \text{(B-1)}$$

Where *u* and *v* are the corresponding *x* and *y* components of the velocity field, and ν is the kinematic viscosity of the fluid. The set of boundary conditions is:

1. At $y = 0 \rightarrow u = v = 0$

2. As $y \rightarrow \infty$ then $u = U$ for all *y* at $x = 0$

Blasius introduced a variable to combine the two independent quantities x and y into one non-dimensional independent variable know as similarity variable η. This variable was conceptualized from the assumption that the laminar flow on a flat plate looks the same, i.e. looks similar, regardless of how close or how far it is observed.

$$\eta = y\sqrt{\frac{U}{\nu x}} \tag{B-2}$$

The Blasius velocity profile is presented in Figure B-2. It is considered that at $\eta = 5$ the ratio u/U is 0.992, and at this point the boundary layer edge is located. Substituting $\eta = 5$ in equation (B.2):

$$5 = y\sqrt{\frac{U}{\nu x}} \tag{B-3}$$

and solving for y, which is equal to δ:

$$\delta = \frac{5x}{\sqrt{\mathrm{Re}}} \tag{B-4}$$

In this way, for a given fluid kinematic viscosity and a point along the flat plate, the boundary layer can be found.

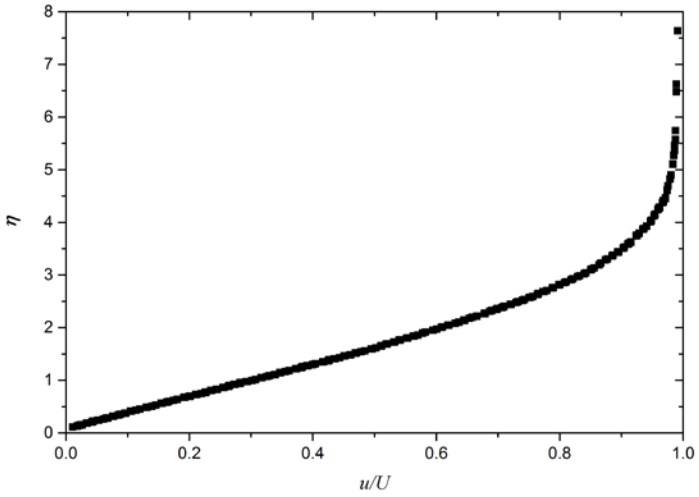

Figure B-2 Blasius velocity profile for laminar flow over a flat plate

A steady two-dimensional laminar fluid flow on a semi-infinite plate with zero pressure gradient was configured to test the boundary layer in LBM as in the Blasius solution.

The configuration parameters are presented in Table B-1. For a given viscosity of the fluid, and a fluid velocity, the corresponding boundary layer was analysed from the LBM simulation. The fluid velocity profile is observed in Figure B-3. The interface of the boundary layer is located at the upper edge of the layer in yellow.

Table B-1 Configuration parameters for laminar flow over a flat plate test in LBM

pw (m)	0.001
kinematic viscosity of water ν (m^2/s)	10^{-6}
velocity at inlet U (m/s)	0.001
τ	0.6
viscosity (LBM)	0.03333
velocity at inlet U (LBM)	0.03333
Δt_{LBM}	3.33×10^{-2}

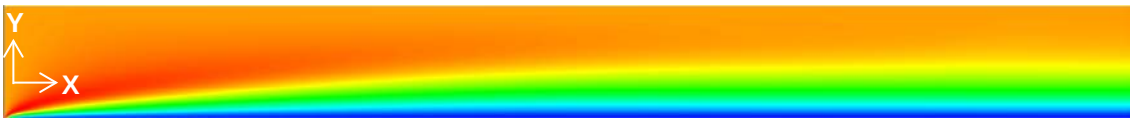

Figure B-3 Configuration in LBM of a 2D laminar flow on a semi-infinite plate

At different positions in *x* the height of the boundary layer was registered; the data points are presented in Figure B-4.

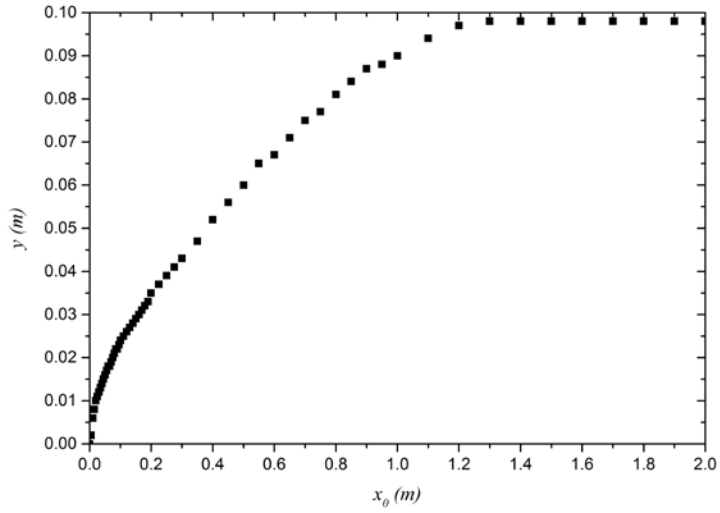

Figure B-4 Blasius velocity profile for laminar flow over a flat plate